Si nanostructures thin films for 3rd generation of solar cells

R.P. Nalini

université de Caen Basse-Normandie

CIMAP

UNIVERSITÉ de CAEN BASSE-NORMANDIE

U.F.R. Sciences

ECOLE DOCTORALE: Structure, Information, Matière et Matériaux

THESE

Présentée par

M^{elle} Pratibha Nalini RAMESH SUNDAR

le 26 septembre 2012

en vue de l'obtention du

DOCTORAT de L'UNIVERSITÉ de CAEN

Spécialité: Milieux denses, matériaux et composants

Titre

Films minces à base de Si nanostructuré pour des cellules photovoltaïques de 3ème génération.

Membres du Jury

M^{me}. Caroline BONAFOS	Chargé de Recherche, CEMES, Toulouse	Rapporteur
M. Herve RINNERT	Professeur des Universités, Institut Jean Lamour, Nancy	Rapporteur
M. Philippe PAREIGE	Professeur des Universités, GPM, Université et INSA de Rouen	Examinateur
M. Julien CARDIN	Ingénieur de Recherche, CIMAP, ENSICAEN, Caen	Examinateur
M. Christian DUFOUR	Professeur des Universités, CIMAP, ENSICAEN, Caen	Co-directeur de thèse
M. Fabrice GOURBILLEAU	Directeur de Recherche CIMAP, ENSICAEN, Caen	Directeur de thèse

Acknowledgement

Three years of PhD has been special three years of my life with enriching experiences and I thank the Lord Almighty for His immense blessings.

I express my most sincere gratitude to my thesis director Dr. Fabrice Gourbilleau for all that he has done to make me feel comfortable inside and outside the lab, for the valuable discussions, guidance and the time spent in nurturing me from a PhD student to a young researcher. I thank my thesis co-director, Prof. Christian Dufour for the care he took to make sure I understand all that I do and for his major role he played with patience on the theoretical part of my thesis. I am grateful to Dr. Julien Cardin who was equally involved as my thesis directors, for the enthusiasm that he passed on, for the clear explanations and for all the valuable support he rendered in completing the thesis work.

My special thanks to the Jury members, Dr. Caroline Bonafos, Prof. Hervé Rinnert and Prof. Philippe Pareige for their careful analysis of this work, their constructive criticism, valuable suggestions and for their appreciation which are encouraging.

I extend my heartfelt gratitude to Dr. Larysa Khomenkova, for being instrumental from the beginning till the end of this thesis work in making it successful. I thank her for her friendship, useful discussions, and the valuable time she spared for me along with Dr. Vladimir Khomenkov.

I acknowledge Prof Xavier Portier, Philippe Marie, Michael Boisserie, Olivier Debieu, Patrick Voivenel, Cedric Frilay for some of the measurements they performed and likewise Dr. Etienne Talbot, Manuel Roussel, Dr. Marzia Carrada for the collaborative works. I thank all my colleagues, technicians, dear friends in the CIMAP laboratory for the lively times, friendship, support and encouragement, and also my previous and present officemates for the healthy discussions. I thank Geeta for her company during these three years and I also appreciate the pleasant times spent with the Indian community in Caen.

I would also like to thank my family members for sending me to France despite crucial situations at home, their prayers and blessings, constant support and motivation without which I would not have pursued this degree. I also express my heartfelt thanks to my dear friends in India and in France, all my teachers, and the church for the various helps they have rendered academically, emotionally or physically through the years.

R. Pratibha Nalini

Contents

List of Figures

List of Tables

LIST OF ABBREVIATIONS

APT	Atom Probe Tomography
CA	Classical Annealing (1h-1100°C)
FG	Forming Gas
FTIR	Fourier Transform InfraRed spectroscopy
LTA	Long Time Annealing (1h)
ML	MultiLayer
NRSN	Nitrogen-Rich Silicon Nitride
PL	PhotoLuminescence
PV	PhotoVoltaic
QCE	Quantum Confinement Effect
QD	Quantum Dots
Si-np	Silicon nanoparticles
SRSN	Silicon-Rich Silicon Nitride
SRSO	Silicon-Rich Silicon Oxide
STA	Short Time Annealing (1min-1000°C)
TEM	Transmission Electron Microscope
XRD	X-Ray Diffraction
XRR	X-Ray Reflectivity

Introduction

State of the art

In the quest for new renewable sources of energy, the focus of research today is on cost-effective photovoltaic technologies with higher levels of efficiency. The second generation thin film solar cells were promising compared to the first generation of bulk solar cells in reducing the manufacturing costs. But, the efficiencies are lower since the thin films in general cannot absorb efficiently the solar spectrum without light trapping mechanisms. The combination of the third generation solar cell concepts and the second generation thin film materials has been identified as a solution to economically meet the global energy needs. The major targets of the third generation photovoltaics (PV) are:

- to reduce the cost from 1$/watt of second generation PV to 0.50-0.20 $/watt by increasing the efficiency and lowering the material need.
- to overcome the power loss mechanisms in single bandgap solar cells using approaches that effectively absorb photons below and above the bandgap of the solar cell material.

Tandem cell is one of the third generation concepts that enables to absorb a wide range of solar spectrum by stacking individual cells with different bandgaps. The wide availability of the non-toxic Si, and its compatibility with the already existing technologies make "All-Si tandem cell" an attractive approach. Silicon, being an indirect semiconductor is not an ideal material in reducing the cost of solar cells because it requires about 125 micron thickness to absorb 90% of solar radiation, while in a direct bandgap material such as GaAs about 1 micron is sufficient. The discovery of quantum confinement effect in Si nanostructures resolves this problem arising from conventional c-Si solar cells, and therefore can be efficiently incorporated in a tandem cell. The bandgap engineering is achieved by stacking quantum wells (QW) or quantum dots (QD) of Si with dielectric barriers which are also based on Si-compounds such as SiO_2, Si_3N_4 or SiC. With increasing QD density, the effective

bandgap increases. Consequently, the absorption and emission properties are also enhanced which are promising for photovoltaic as well as photonic applications. The main challenge lies in optimizing the dielectric barrier thickness to provide confinement for the formation of QDs as well as carrier transport.

Prior to integration of these materials in a tandem cell device, preliminary investigations of the Si QW or QD in each of these dielectric matrices become a necessary part of research. In this context, this thesis aims at studying Si QW or QD in SiO_2 and Si_3N_4 matrices in monolayered [Si-rich SiO_2 (SRSO) and Si-rich Si_3N_4 (SRSN)] and multilayered [SRSO/SiO_2 and SRSO/SRSN] configurations.

Major objectives of this thesis

For Si-based thin films to be incorporated in a third generation solar cell device, this thesis focuses on four major issues which are:

Material growth technique: Among the various methods available for the fabrication of Si nanostructures, we use the sputtering technique for thin film growth in our laboratory. Increasing the density of Si-QDs is one of the most effective way to enhance the optical and electrical properties required for a solar cell device that takes advantage of Si QDs. Therefore, the first major objective of this thesis is to increase the Si excess incorporation in the material during the growth process that would form Si-QDs upon suitable high temperature annealing.

Thermal budget: Decreasing the thermal budget (either the temperature or time of annealing) required for the formation of Si-QDs would be attractive. Therefore, the second major objective of this work is to explore ways of favoring the formation of Si-QDs even in the as-grown state, and also to analyse various temperature/time of annealing towards possible lowering of the thermal budget.

Material properties: Photoluminescence (PL) measurements are indicative of the possibility to create excitons in the material that facilitate absorption and electrical transport in a future PV device. Achieving significant emission is a challenge, and understanding the origin of these emission becomes the next important challenge. Therefore, the third major objective of this work is to obtain size controlled Si-QDs, analyse the structural properties of the material and to understand the influence of the materials microstructure on optical properties.

Optical and geometrical effects on emission: Besides the inherent material properties depending on the Si-QD density, various other factors such as the angle of incidence of the incident light, its profile inside the thin film structure with regard to thickness and refractive indices of the material etc., may affect the optical properties. These effects have to be considered with a special attention during device fabrication,

as the thickness of the film, the pattern thickness, electronic density and incident light profile influences the emission intensity. Therefore, the fourth major objective of this work is to analyse the emission behaviour of the thin films, contributed by factors other than Si-QDs using simulations.

Sketch of this thesis

This thesis work is separated into five chapters.

Chapter 1 details the global energy needs, the various solar cell concepts - their advantages and limitations, and the Si-based strategies. This Chapter outlines the current research status on Si nanostructures for photovoltaics and highlights the important results that serve as a platform for further research.

Chapter 2 elaborates the principle, details of the equipments used and the working of various experimental techniques employed in our laboratory for the growth and characterization of the thin films.

Chapter 3 focusses on understanding the temperature dependent sputtering mechanism and optimizing the deposition parameters of Si-rich Silicon Oxide (SRSO) materials. The structural and optical properties of SRSO monolayers and SRSO/SiO_2 multilayers are investigated. The role of SiO_2 sublayer as a diffusion barrier in multilayers is analysed.

Chapter 4 focusses on optimizing the deposition parameters of silicon nitride materials that are nitrogen rich, stochiometric or silicon rich. Monolayers of silicon nitride and SRSO/SRSN multilayers are analyzed for structural and optical properties. Special emphasis is laid on understanding the emission behaviour of the material.

Chapter 5 deals with understanding the influence of optical and geometrical effects on the experimentally obtained photoluminescence using theoretical models.

Chapter 1

Role of Silicon in Photovoltaics

1.1 Energy needs in the global scenario

The growth of industrialization and sophistications in the human life-style have enormously increased the global energy demands. The fossil fuels such as coal, oil and natural gas have been the major source of electricity from the last two centuries, owing to its affordability. Though 85% of today's energy needs are satisfied by burning fossil fuels, it is accompanied with two major environmental footprints: 1) Depletion of natural resources, and 2) CO_2 emission of about 26.7 billion tons into the atmosphere each year [Internet 01]. As a result of CO_2 emission, there is an increase in the global mean surface temperature and the sea level. According to a report on climate changes [IPCC 07], it is estimated that the temperature has increased by 1.8-4.0°C in the 20th century, due to global warming. Though the production and consumption of renewable energies like solar, wind, ocean, biomass, geothermal resources, and biofuels have increased over the years, it accounts to only 15% of the global energy consumption as per 2007 statistics (Fig. 1.1). Hence, the world faces an urge towards maximum utilization of renewable resources to meet the global energy needs. The enormous quantity of non-polluting energy from the Sun has gained attention as one of the major alternative energy source leading towards a sustainable development. Despite being an abundant source of energy, only 0.015% of world's electricity comes from the solar energy [Crabtree 07] due to the lack of efficient technology to harness and store the solar radiation.

In general, solar energy can be harnessed and utilized for energy generation by two different approaches [Internet 02]:

1. Solar Thermal Approach, which deals with the direct usage of Sun's radiation as heat such as in passive water heaters.

2. Solar Photovoltaic (PV) Approach, which deals with the usage of semicon-

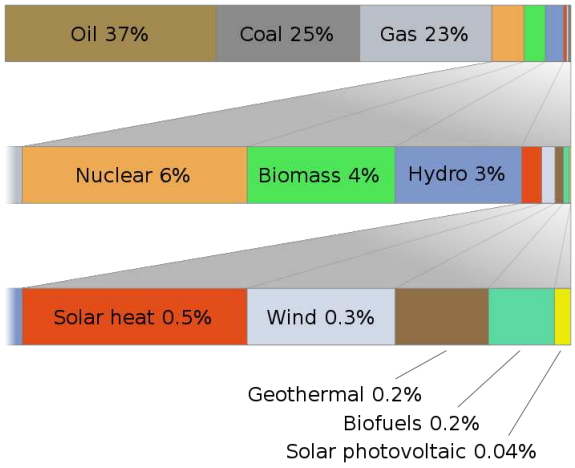

Figure 1.1: World energy consumption-2007 Statistics [Internet 03].

ductors to convert light into electric energy. Solar PV can be effectively used to power isolated homes in remote places.

The sustainability and availability of the solar energy serves as a motivation to achieve cost-effective PV devices with high efficiency, by developing novel materials.

1.2 Solar Photovoltaics

1.2.1 A brief history of PV cells

The solar photovoltaic approach generates power using solar panels, which are made up of a large number of solar cells. It works on the principle discovered by Edmond Becquerel in 1839 known as the photovoltaic effect, which is the production of current in a material on illumination. A century later, Russel Ohl discovered the presence of a p-n junction in Silicon, by observing that one area of the material offered more resistance to current flow than the other, when heated or illuminated. He reasoned this junction formation to be a contribution from segregation of impurity in recrystallized silicon (Si) melts during the growth of monocrystalline Si rods. This discovery of p-n junction resulted in the first PV devices in 1941 [Ohl 41a, Ohl 41b]. In 1952, conversion efficiency of about 1% was achieved by controlling the location of junction formation, which was a major problem in the earlier devices [Kingsbury 52]. In 1954, the first modern solar cell developed at the Bell laboratories using the silicon p-n junction, increased the efficiency to 6% which is the first milestone in the PV research industry [Chapin 54]. The wide usage of PV cells for space applications resulted in modifications of the device structures by placing contact grids on the top surface and this resulted in a further increase of efficiency to 14% [Mandelkorn 62]. Eversince, a lot of materials have been investigated for PV applications and presently

mono-, poly- and amorphous silicon, cadmium telluride, and copper indium gallium selenide/sulfide (CIGS) have become the most used materials.

1.2.2 Three Generations of PV cells

The major challenges faced by the PV industry are the high costs of production for a relatively low efficiency[1]. To overcome this challenge, PV cells are categorized into three generations on their genealogical basis, and all three are being currently investigated towards profitable development. Figure 1.2 shows a consolidated representation of the conversion efficiencies and cost of the three generations of PV cells.

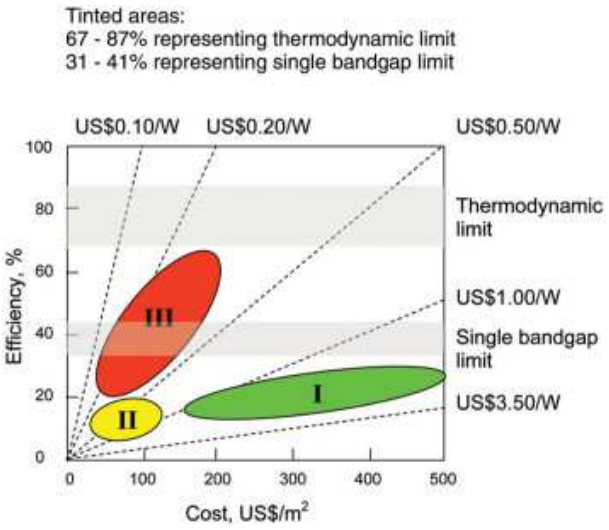

Figure 1.2: Consolidated representation of conversion efficiencies and cost of the three generations of PV cells [Conibeer 07].

The first generation PV cells are largely based on mono- or polycrystalline Si and has the major share of over 85% commercial production. Laboratory efficiencies of 23-24.7% [Green 93, Green 01a] and commercial module efficiencies lying between 14-19% [Parida 11] have been reported from these cells. The main drawback of first generation cells arises from the indirect bandgap nature of Si which necessitates a thick active layer which is at least 50 µm thick for efficient absorption [Chopra 04]. In general, about 300-500 µm thick layer is used for a solar cell, which accounts to about 28% of the module cost. The sophisticated procedures for high temperature processing to obtain highly purified electronic grade silicon for a device, combined with the need for large material area has made these solar cells expensive with about US$ 3.50/W.

The second generation PV cells aim at reducing the production costs by

[1]Efficiency = Maximum electrical power/ Incident optical power

alternate fabrication techniques and by reducing the material requirements. This is achieved by depositing thin films (1-2 µm thick) of the semiconductor PV material on glass, silicon or ceramic substrates. Though the costs are reduced to reach US$ 1/W, the efficiencies are lower than the first generation solar cells. Cell efficiencies of 12-20%, prototype module efficiencies of 7-13% and production module efficiencies of 9% have been reported from these cells [Internet 04]. The most successful materials used in second generation solar cells are cadmium telluride (CdTe), copper indium gallium selenide (CIGS), amorphous silicon and micromorph silicon (combination of crystalline and amorphous Si).

The third generation PV cells aim at enhancing the performance of the second generation thin film technology in terms of efficiency (targeting 30-60%) while maintaining a low production cost (targeting $<$ US$ 0.20/W). It aims at producing future large scale affordable devices using different approaches like tandem cells [Marti 96, Green 06], multiple exciton generation [Nozik 01], hot carrier solar cells [Ross 82] etc. A more detailed discussion on the third generation PV will be dealt in the forthcoming sections.

1.3 Silicon in photovoltaic industry

Traditionally, inorganic semiconductors are used as PV materials. A typical solar cell contains one or more light-absorbing semiconductor layers that form a charge-separating junction (Fig. 1.3). This can be either a homojunction as in Silicon or a heterojunction with other materials. An ideal solar cell material must be a readily available, non-toxic, direct band-gap material with bandgaps between 1-1.7 eV in addition to its high photovoltaic efficiency and long term stability [Goetberger 02]. Besides, the solar cell material must also possess high absorption coefficients of 10^4-10^5 cm^{-1} in the wavelengths between 350 - 1000 nm (1.24-3.54 eV), a high quantum yield[2] for the excited carriers, a long diffusion length and a low recombination velocity [Poortmans 06]. The economical and ecological aspects such as the abundant availability in earth's crust with low toxicity make Si to be the most important choice as a PV material. The compatibility of Si materials with the already existing CMOS microelectronic technology, their maturity in the industry, simple well established processing techniques and mechanical strength become an added advantage for their usage in the PV industries.

[2]Quantum yield = Number of photons emitted/Number of photons absorbed

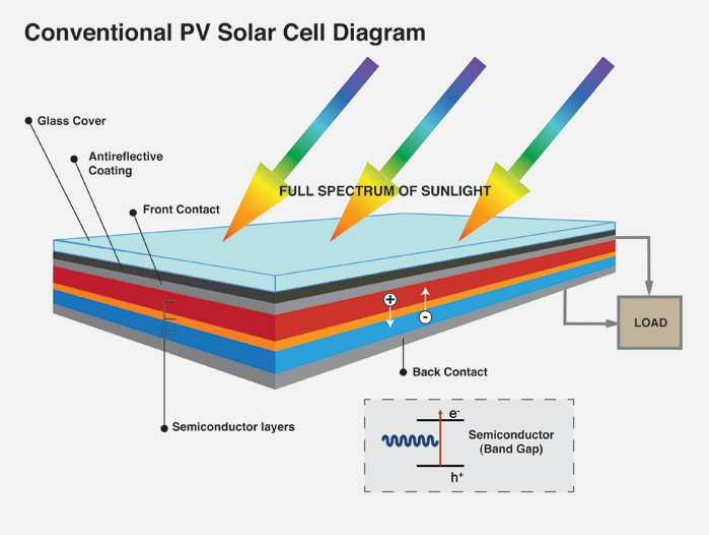

Figure 1.3: A typical solar cell architecture [Internet 05].

1.3.1 Crystalline Silicon- Advantages and Drawbacks

Crystalline Silicon (c-Si) is a mature candidate in the PV technology owing to its long usage, high efficiencies and excellent stability. Hence, the production of solar cells was and is still largely based on c-Si, which is also called as the solar grade Si. In a classical p-n type solar cell, the incident photons ($h\nu$) create the photocarriers (electron-hole pairs) in each zone 1, 2 and 3 represented in figure 1.4.

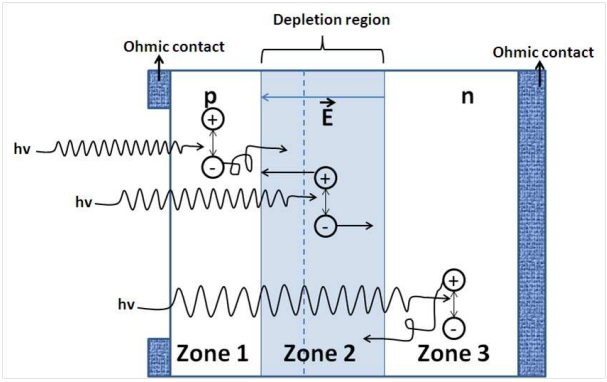

Figure 1.4: Schematic representation of photocurrent mechanism in a p-n junction.

The n-region are rich in electrons and the minority photocarriers (holes) diffuse to the depletion region where they are subjected to the electric field. They then diffuse to zone 1, where the holes are a majority and this would constitute the photocurrent arising from the diffusion of holes. Similarly, the minority carriers (electrons) in p-region contribute to photocurrent due to the electron diffusion. Besides these,

in the depletion zone the photocarriers dissociate due to an internal electric field and are sent to n-region or p-region accordingly contributing to a directly generated photocurrent. Thus the photocurrent of a solar cell is a sum of the three components: photocurrent due to diffusion of holes, photocurrent due to the diffusion of electrons and directly generated photocurrent in the depletion region. Thus it can be seen that the diffusion of the minority carriers plays a vital role in the photocurrent of the device. In c-Si wafers, the minority carrier diffusion lengths, L_{diff} are sufficiently high to transport the minority carriers by diffusion to the junction. But, c-Si being an indirect semiconductor requires 100 µm thick layer to absorb 90% of light whereas 1µm of GaAs is sufficient to achieve the same level of absorption being a direct semiconductor.

Conventionally the band structure of a semiconductor is represented by the E-k diagram (Fig. 1.5), where E is the energy of an electron or a hole at the band edge with wave vector k in the first Brillouin zone. The difference between the highest point in the valence band and the lowest point in the conduction band gives the bandgap (E_g) of the material. When these two points do not lie at the same position of k as in the case of Si, the semiconductor is said to possess an indirect bandgap.

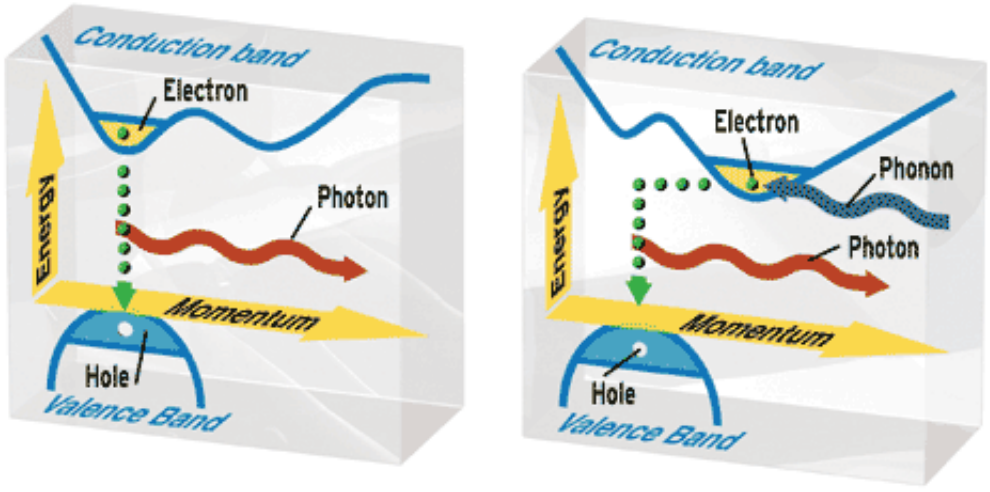

Figure 1.5: Energy vs. momentum (E-k diagram) of Direct and Indirect bandgap semiconductors [Coffa 05]. ILLUSTRATION: JOHN MACNEILL.

Bulk c-Si is an indirect bandgap semiconductor (E_g = 1.1 eV), and hence the recombination of electron in the conduction band with the hole in the valence band requires the participation of a third particle, which is the phonon (lattice vibrations) with a wavevector equal to the initial conduction band state. The probability of

occurance of this three body event is lower than a direct electron-hole recombination in direct bandgap material. The total conservation of energy and momentum of phonon and exciton, leads to the low absorption and emission behaviors in indirect semiconductor materials. This explains the requirement of a thick c-Si as the active layer for efficient absorption as compared to direct bandgap materials. Therefore, reducing the material thickness by exploring the possibilities to tailor its bandgap, would be a possible solution to lower the production costs which is the goal of a second generation PV cell.

1.3.2 Amorphous Silicon - Advantages and Drawbacks

Amorphous Si (a-Si) was identified as a material relevant for solar cells as early as 1969 [Chittick 69] and a systematic study was reported by 1972 [Spear 72]. By 1976, the first solar cell based on a-Si was reported by Carlson [Carlson 76]. In its native form, a-Si is not a material suitable for PV due to the disorder in the material with a high density of dangling bonds ($>10^{19}$ cm^{-3}), unless passivated with hydrogen. It was shown that in a-Si with 5-20 at% hydrogen, the dangling bond density reduces to 10^{15}-10^{16} cm^{-3} [Street 78, Chopra 04]. Among the various reasons for broadening of bandtails in a-Si, the short range order in the material and/or defects can be considered important. The bandtails and the dangling bonds causes relaxation in the transition rules such that it behaves as a direct bandgap semiconductor with a bandgap about 1.7 eV [Wronski 02, Pieters 08].

Even after hydrogen incorporation, a-Si:H still possesses neutral silicon dangling bonds. Their associated electronic levels in the bandgap act as deep traps and recombination centers which are observed in photoluminescence [Street 78], optical absorption [Jackson 82] or transient photoconductivity [Street 82] and follow various recombination dynamics as illustrated (Fig. 1.6).

Depending on the alloying process, the bandgap of a-Si can also be tailored between 1.4 eV and 1.8 eV, which seems promising towards reducing the material requirements. On the other hand, the light induced degradation, popularly known as the Staebler Wronski effect (SWE) challenged a-Si:H supremacy despite its attractive features, over c-Si [Staebler 77]. The new additional recombination centers and the dangling bonds that appear on illumination affect the electronic characteristics such as the lifetime of carriers. Though the SWE decreases the efficiency of a-Si based solar cells upon illumination, this process of defect formation is reversible when a-Si sample is annealed above 150°C and the cell's efficiency stabilizes at a value below the initial efficiency [Staebler 80]. But, even without the SWE, the initial efficiency of a-Si:H is lower (9-15%) than c-Si (14-23%).

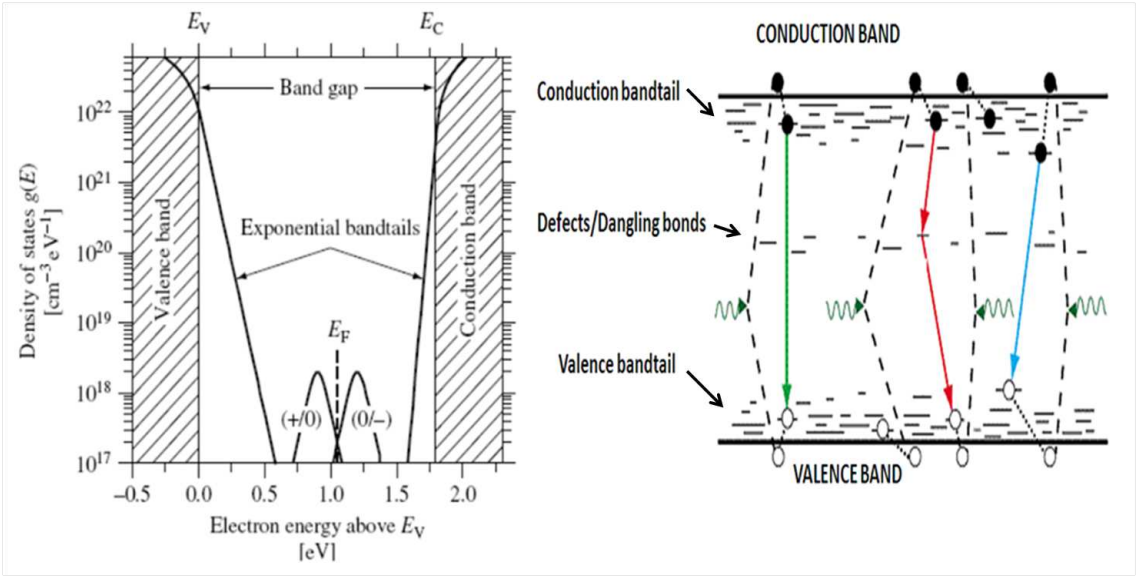

Figure 1.6: Electronic levels of a-Si:H and an illustration of few possible recombination paths [Miroslav , Boehme 10].

Amorphous-Si materials have low carrier mobilities (μ) and short carrier lifetimes (τ) thereby making the L_{diff} very small (0.1-0.2 μm in a-Si vs. $\sim$ 100 μm in c-Si) [Hegedus 97, Balber 98]. Therefore, a-Si based solar cells always use p-i-n structure in contrast to the classical p-n diode structure used in c-Si solar cells. The width of the depletion region is increased by placing an intrinsic layer (i) between the p and n regions in order to prevent recombination of free carriers within the cell. The electric field in the i layer increases depending upon the voltage bias across the device and increases the generated photocurrent. The high field in the intrinsic region also sweeps the diffused photocarriers to the contacts before they recombine. Thus, the photocurrent in a-Si p-i-n structures are largely dependent on field assisted drift rather than the minority carrier diffusion processes. The main advantage of a-Si as compared to c-Si lies in the incorporation of thin film technology to a-Si, due to better absorption arising from bandgap modifications that leads to potentially cheaper production. But, the low efficiencies and poor electrical transport of a-Si solar cells comes as their major limitation.

1.3.3 Alternate configurations of c-Si and a-Si for solar cells

In order to increase the efficiency of a-Si based thin film solar cells, various configurations of a-Si have been investigated. The usage of a-Si in a multijunction solar cell/tandem cell has been the most popular choice over the years. Different junction devices with appropriately graded bandgap can be placed in a stack to form a multijunction device. The top junction absorbs the higher energy photons and

transmits the lower energy photons to be absorbed by the bottom junction. In the 1980s, remarkable advancements have been made in studying amorphous Si based structures like silicon carbide, silicon nitride etc. It was seen that the multijunction tandem structures of a-Si such as a-silicon carbide/a-Si heterojunctions, a-Si/poly-Si and amorphous Si/germanium alloys [Folsch 95, Guha 02] could reduce the light induced degradation [Guha 99] and improve the efficiency of the solar cells. Up to three junctions have been in production for a-Si:H [Yang 94].

Another promising configuration is based on microcrystalline silicon (μc-Si). The possibility of producing μc-Si was discovered as early as 1968 [Veprek 68]. But it was only in 1990s, that the hydrogenated microcrystalline Si (μc-Si:H) was pioneered as a new thin film material for PV by Institute of Microtechnology, University of Neuchatel, and 7% efficiency was achieved [Meier 94b]. Despite similar deposition conditions and hydrogen incorporations as in a-Si, microcrystalline-Si materials exhibit properties similar to those of c-Si and are immune to the light induced degradation (SWE). The bandgap E_g of μc-Si is similar to c-Si, which necessitates a thick active layer when compared to a-Si:H. These observations led to the discovery of hybrid cells also called as micromorph tandem, which is the combination of a microcrystalline bottom cell with a-Si top cell [Meier 94a].

About the same time, when research on μc-Si:H was initiated, Sanyo introduced the first HIT (Heterojunction with Intrinsic Thin layer) solar cells using a-Si and c-Si. HIT solar cells improve the boundary characteristics and reduce the power generation losses by forming impurity-free i-type amorphous silicon layers between the crystalline base and p- and n-type amorphous silicon layers. Conversion efficiencies above 20% have been reported from HIT solar cells, which are modified from their crystalline counter part (Fig. 1.7) [Taguchi 00].

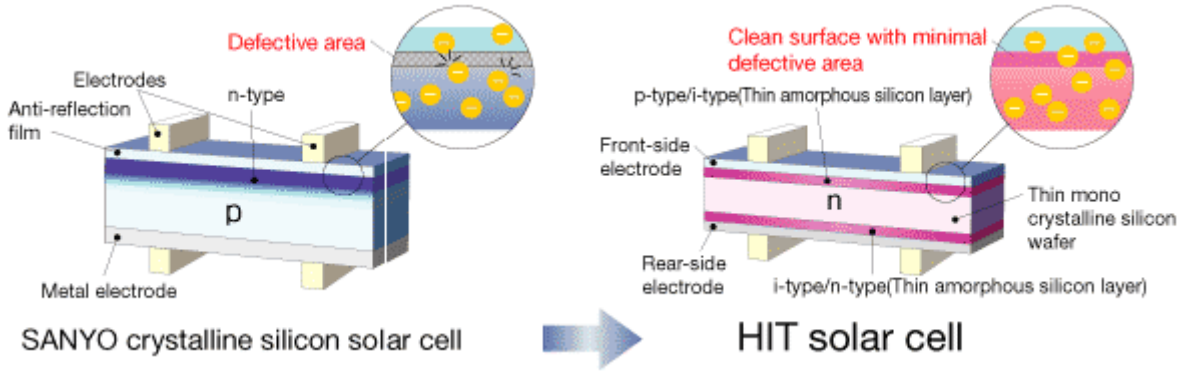

Figure 1.7: Sanyo's transition from traditional solar cell to HIT solar cell [Internet 06].

The present silicon solar cell design has evolved significantly from the simple single junction device, by incorporating passivation of the surfaces, light trapping

and sophisticated anti-reflection coatings in addition to its tandem or micromorph configurations. This helps in efficient light absorption in all the wavelength range (energy range) accessible to silicon and ensure that each absorbed photon leads to a carrier quantum yield equal to 1 [Ginley 08]. The present thin film based PV technology is focussed towards exploring silicon nanostructures that offer promising solutions to overcome the drawbacks of bulk c-Si and a-Si.

1.4 Advent of quantum effects in silicon nanostructures

The major obstacle to the performance, efficiency and cost of Si-based solar cells, as can be observed from the discussions in the previous sections, is the indirect bandgap nature of bulk Si. Over 90% of the solar radiations that reaches the earth's atmosphere contain photons with energies ranging from 0.5-3.5 eV and only those photons which have energies equal to/higher than the bandgap of a semiconductor are absorbed (Fig. 1.8a). The fundamental losses of the incident solar spectrum in a solar cell are represented in figure 1.8b. Photons with energies below the semiconductor bandgap are not absorbed while those with energies above the bandgap are thermalized after being absorbed, (i.e. the created electrons and holes lose their excess kinetic energy in the form of heat during relaxation (Fig. 1.8b)).

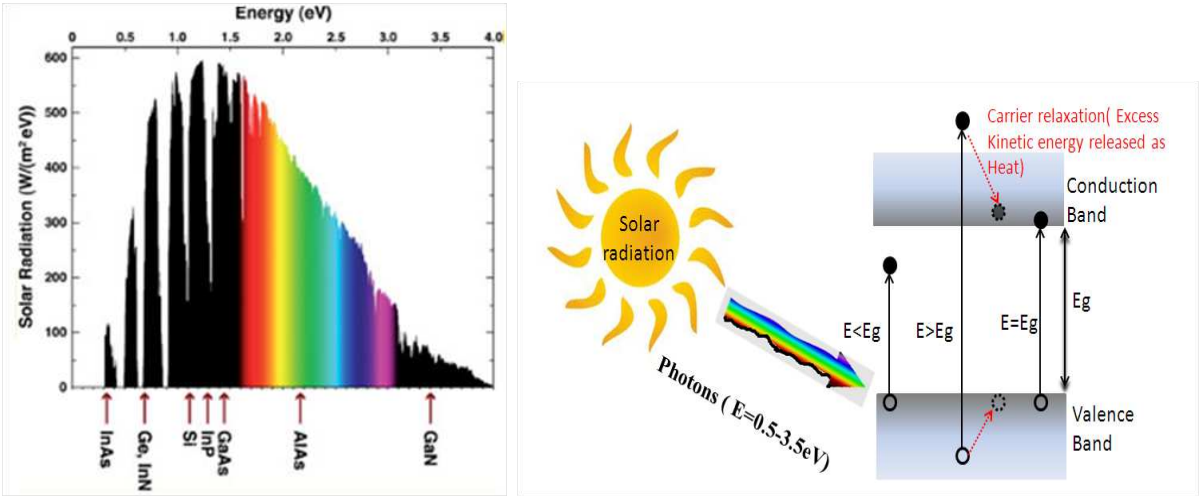

(a) AM 1.5 solar spectrum. Arrows indicate the bandgaps of some semiconductors.

(b) Solar cell losses.

Figure 1.8: Incident solar spectrum adapted from [Brown 09] and schematic representation of fundamental losses in a solar cell.

Such carriers, termed as hot electrons and hot holes, contribute significantly in limiting the conversion efficiency of single bandgap cells based on bulk Si to the

Shockley-Queisser limit of 31% [Shockley 61]. The possible solution to these problems would be in attaining a semiconductor with a tunable direct bandgap structure insensitive to SWE, which is almost completely achieved in quantum confined Si.

1.4.1 Quantum Confinement Effect (QCE)

QCE refers to the dramatic size dependent effects that the semiconductors like Si show when their charge carriers (electron-hole pairs = excitons) are spatially confined in nanometer sized volumes. At these dimensions, the bulk properties of the solid becomes severely distorted and the behaviour of a confined exciton follows 'a particle in a box' model [Brus 83]. The simplest case of this model concerns the 1D system which represents a situation where a particle of mass m is confined by two walls of infinite potential energy at $x = 0$ and $x = L$. The particle is free to move within this space and possesses non-zero discrete energy levels. After mathematical derivations by solving Schrödinger equation, the permitted energy levels for a 1D model is given as

$$E_n = n^2h^2/8mL^2 \text{ for n=1,2,3...} \qquad \text{Eqn (1.1)}$$

Applying the same principles to a particle confined in 3D (i.e.) confined in x, y and z directions by potential wells at L_x,L_y and L_z, the energy levels are given as

$$E_{n_x,n_y,n_z} = (h^2/8m)\left[(n_x^2/L_x^2) + (n_y^2/L_y^2) + (n_z^2/L_z^2)\right] \qquad \text{Eqn (1.2)}$$

From equations (1.1) and (1.2), it can be seen that the size of the box has an inverse relationship with the energy of the particle. Thus, as the size of the box shrinks which indirectly refers to the particle size, there is an enhancement in the energy gap. This is the reason behind the enlargement of bandgap as the particle size decreases in nanometric particles which becomes more pronounced below a particular limit specific to the particle, known as the exciton Bohr radius (typically < 10 nm). The particles with radii larger than this limit are said to be in the 'weak confinement regime' and those that have radii smaller than the exciton Bohr radius are said to be in the 'strong confinement regime'. Another associated phenomena with the exciton confinement is the breakdown of momentum conservation rule. When the excitons are confined by a box, it follows the Heisenberg's uncertainity principle and their position in k space is blurred. Therefore, there is an overlap between the tail of electron and hole wavefunctions even in an indirect bandgap semiconductor, giving rise to quasi-direct transitions (Fig. 1.9a). The optical quasi-direct transitions without the intervention of phonons are similar to the case of

a direct bandgap semiconductor [Gnutzmann 74] and increases the probability of radiative recombinations. Thus, QCE leads to strong variations in the optical and electronic properties of a material.

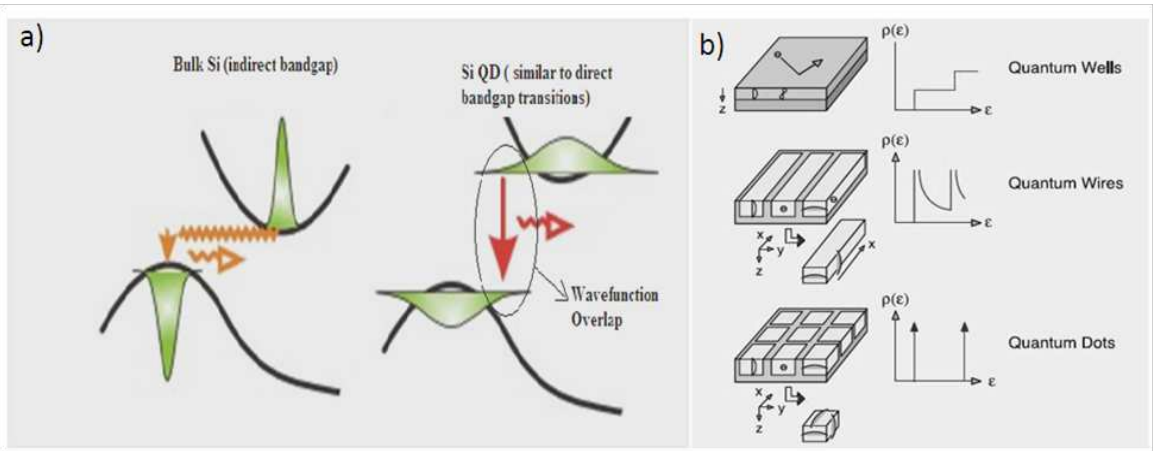

Figure 1.9: (a) The consequence of Quantum Confinement Effect, and (b) the density of states of structures confined in 1D, 2D and 3D.

The confinement of excitons in a semiconductor in one, two or three spatial dimensions are termed as quantum wells, quantum wires or quantum dots respectively (Fig. 1.9b).

1.4.2 Silicon nanostructures

The quantum confinement effects (QCE) in three dimensionally confined semiconducting crystals was identified in the early 1980s [Ekimov 81]. About the same time investigations began on the Si nanostructures confined along one direction (quantum wells) and QCE were witnessed [Abeles 83, Ibaraki 84, LeComber 85]. Quantum well refers to a structure in which a low bandgap material is sandwiched between layers of higher bandgap which act as potential barriers. If the higher bandgap layer is sufficiently thick, it provides a high potential barrier and each well is electronically isolated without the overlap of electronic wavefunctions. Such alternated wells and barriers are collectively referred as multiple quantum wells. On the other hand, if the barrier thickness is sufficiently low, there is an overlap of wavefunctions and efficient charge transport is possible normal to the layers. These structures behave like direct bandgap material and are termed superlattices. In general, it was reported if the barrier thickness is 4 nm or below, miniband formation occurs leading to inter-well electronic coupling in a superlattice [Peterson 88].

A deep investigation on the QCE in Si and its applicability towards optoelectronic devices began in the 1990s stimulated by the discovery of size dependent

luminescence from 2D confined porous Si [Canham 90]. Porous Si can be prepared by anodic etching or strain etching of single c-Si wafers in hydroflouric acid. Porous Si from these etching procedures initially consists of hydrogen terminated silicon nanowires (2D confined) or interconnected small silicon nanocrystals. An additional oxidizing step isolates the silicon nanocrystals from the surrounding matrix resulting in a three dimensionally confined quantum dot (QD) structures . The QDs are normally estimated to have a characteristic size between 2-8 nm with no preferential orientation [Palma 02], and through observations it was seen that a very broad dispersion of QD sizes between 3-30 nm is possible [Cullis 97].

The major consequences of quantum confinement in Si which are promising for solar cell applications are as follows:

1. Increase in the optical bandgap with reducing dimensions which leads to size tunable absorption and emission (Fig. 1.10a). Using the theory of linear combination of atomic orbitals within the tight binding approach, the optical gap to a good approximation follows the semi-empirical formula as given in [Delerue 93],

$$E_g(eV) = E_{go}(eV) + \left(\frac{3.79}{d(nm)^{1.39}}\right) \qquad \text{Eqn(1.3)}$$

where E_g and E_{go} are the bandgaps of quantum confined and bulk Si respectively.

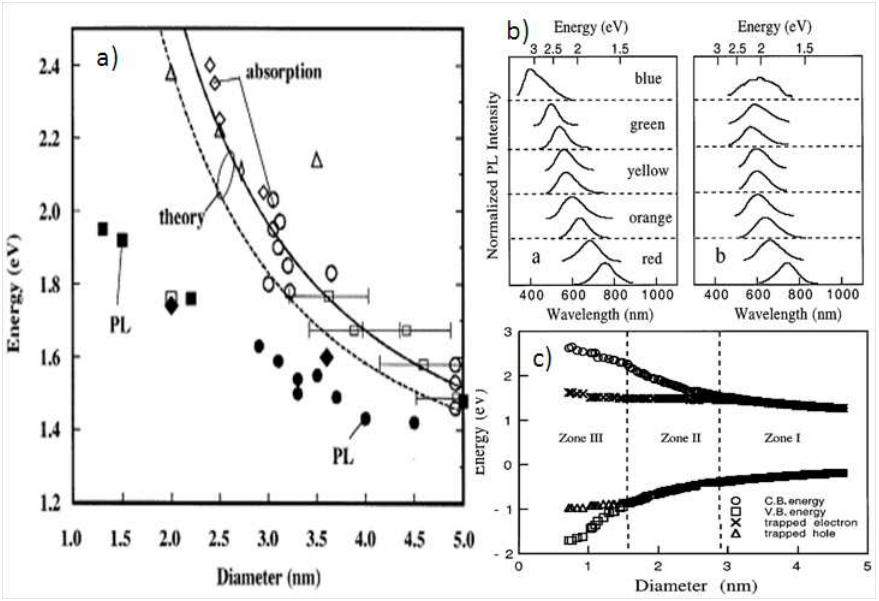

Figure 1.10: (a) Compilation of optical bandgaps of silicon crystals and porous Si obtained from absorption(unfilled symbols) and luminescence (filled symbols) [Delerue 99], (b) Size dependent photoluminescent spectra observed from porous Si with different porosities before and after exposure to air, and (c) Electronic states as a function of cluster size and surface passivation [Wolkin 99].

2. Strong increase in the radiative recombination efficiency of Si nanostructures, due to the associated shifts in energy and momentum that increase the overlap between the electron and hole wavefunctions in k space. Figure 1.10b shows the size tunable emission from red to blue with increasing order of porosities before and after exposures to air.

3. Increase in the influence of surface states lying within the bandgap, due to the increased surface to volume ratio in Si nanostructures. This influence of surface states manifests itself in optical and electronic properties and hence suitable passivation of surfaces is required to tune the properties. The recombination mechanism in Si nanostructures leading to size-dependent PL is reported to be an influence of the type of surface passivation [Wolkin 99]. A hydrogen passivated material is dominated by recombination via free exciton states for all the sizes whereas a sample exposed to air and passivated by oxygen exhibits a more complicated mechanism. Figure 1.10c represents the three zones leading to three kinds of recombination mechanism in oxygen passivated Si nanostructures which are through 'free excitons', 'trapped electron and a free hole' and 'trapped excitons' respectively. This also explains the less pronounced shift of few curves in figure 1.10b after exposure to air indicating passivation of dangling bonds by the fomation of Si=O resulting in recombination via trapped excitons if the particle sizes are in zone III.

1.4.3 Third Generation Solar Cell Approaches

The size tunability and the associated changes in the bandgap of Si nanostructures gave birth to new Si based solar cell approaches to increase the efficiencies beyond the Shockley-Queisser limit [Green 01b, Nozik 02]. The solar cells based on these approaches (Fig 1.11) were collectively named as the Third Generation Solar Cells by Martin Green [Green 01c].

The major objectives and approaches of third generation solar cells are summarized in table 1.1. Besides the list in the table, there are also other approaches like Multiband (impurity) band solar cells, Up/Down conversion /Photoluminescent down shifting of incident solar photons etc, few of which are discussed below.

Tandem cell : Tandem PV devices are the most well established and best developed concept so far. They are formed by stacking multiple p-n or p-i-n junctions with decreasing bandgap values along the direction of the incident light. The higher bandgap material placed at the top, absorbs the high energy photons it can most efficiently convert while the lower energy photons are absorbed in the subsequent layers. Taking advantage of the quantum confinement in Si, "All-Si tandem cell"

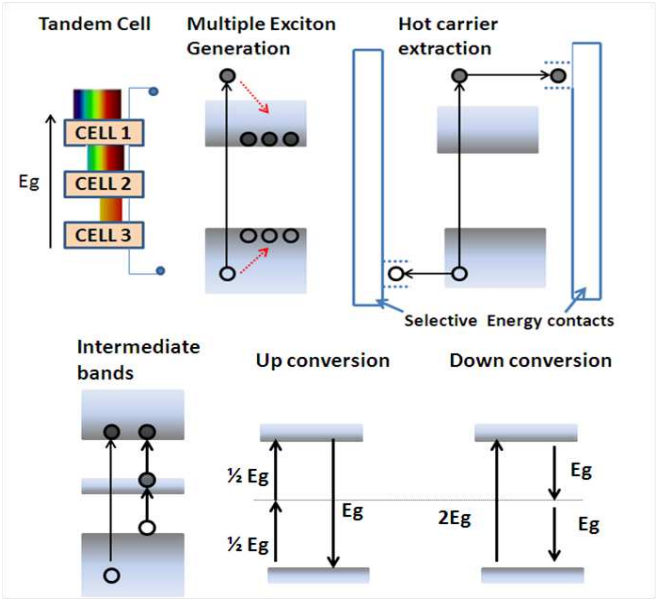

Figure 1.11: Schematic representation of third generation solar cell principles.

concept was proposed [Green 06] considering the stability, compatibility and availability of all the stacked materials required for the cell. Si nanostructures embedded in barriers such as silicon oxide (SiO_2), silicon nitride (Si_3N_4) and silicon carbide (SiC) possess high absorption coefficients and short diffusion lengths allowing their incorporation in a tandem cell [Green 05, Conibeer 06]. Though other approaches promise higher theoretical efficiencies, tandem cell approach is the only successfully demonstrated approach so far.

Impurity, Intermediate and Multi bandgap solar cell : In order to absorb the sub-bandgap photons, recent attempts have been made on Impurity Photovoltaic effect (IPV), by introducing an impurity level in the semiconductor band gap. Finding a suitable wide band gap semiconductor combined with a efficient radiative impurity is the major challenge [Beaucarne 02]. Intermediate Band Solar Cells (IBSC) is a related concept characterized by the existence of a narrow band often called the "intermediate band" formed by the QD arrays within the forbidden band gap [Luque 97]. IBSC with many bands are very promising photovoltaic devices (theoretical maximum efficiency-87%) and are known as multiband solar cells [Green 02]. It is very difficult to produce such solar cells, because a significantly high quantum dot density ($\sim 10^{19} cm^{-3}$) is needed to form the intermediate band and there is no successful demonstration of IBSC yet. Recently, some attempts have been made to obtain the intermediate band structure using InAs quantum dot arrays embedded in GaAs [Luque 05], Si/SiO_2 superlattices [Jiang 06a], and Si QDs [Kurokawa 06, Quan 11].

Approach	Objective	Principle	Efficiencies Expected/ Achieved
Tandem Cells	Utilise a wide range of solar spectrum	Stacking of multiple bandgaps in the solar cell	Infinite stack of bandgaps (Expected)-66% and Using three stacks (Achieved)-40.7%
Intermediate band gap solar cells (IBSC), Multiband solar cells	Absorb energies lesser than semiconductor bandgap	Impurity Photovoltaic Effect. Placing an intermediate band in the forbidden energy gap of semiconductor	Intermediate band located at 0.36eV below the conduction band or above the valence band-Expected-54% [Quan 11] Theoretical-(IBSC)63% (multiband)87% [Luque 97, Green 02]
QD solar cell (Multiple Exciton Generation-MEG); hot carrier solar cells	Prevent thermalization losses of high energy photons	Electron-Hole pair multiplication in QDs or extract the carrier before it cools down	Two excitons per photon at a threshold of $2E_g$(Expected) 42- 44% [Hanna 06, Nozik 08]
Up-Down conversion	Prevent losses of sub-bandgap and above bandgap photons	Up-conversion: Absorb two or more sub-bandgap photons and emit one above bandgap photon Down conversion: Absorb above bandgap photons and emit several low energy photons	Up-conversion: About 48% under 1Sun (estimated) Down conversion: About 38-40% (optimum efficiency for a bandgap of solar cell around 1.5 eV)[Trupke 02a]

Table 1.1: Third Generation Photovoltaics- Objectives and Approaches.

Multiple Exciton Generation (MEG) : Also called as carrier multiplication, it refers to the generation of multiple electron-hole pairs from the absorption of a single photon [Ellingson 05]. In this process, an electron or a hole with kinetic energy greater than the semiconductor bandgap produces one or more additional exciton pairs. This is achieved either by applying an electric field or by absorbing a photon with energy at least twice that of semiconductor bandgap energy. In QDs since there is a formation of discrete electronic states, the cooling rates of hot carriers can be decreased [Nozik 08] and Auger processes are enhanced due to the decrease in distance between the excitons. These aid the production of multiple excitons in QDs as compared to the bulk semiconductors. In relation with the present scenario, MEG has been reported in different semiconducting QDs such as PbSe, PbS, PbTe, CdSe, InAs and Si [Beard 07]. Very recently, highly efficient carrier multiplication and enhancement in the luminescence quantum yield have

been observed in Si nanocrystals in SRSO and in p-Si, which are promising for Si-based PV [Timmerman 11].

Hot Carrier Solar Cells : This is another approach to overcome the thermalization losses. Hot carrier solar cells (HCSC) attempt to minimise the loss by extracting the hot carriers at elevated energies in a narrow energy range. The underlying concept is to decrease the cooling rate of photoexcited carrier and to allow the collection of hot carriers [Ross 82, Wurfel 97, Konig 10]. HCSC is necessarily constituted of a hot carrier absorber layer where the carrier cooling is delayed and an energy selective carrier extraction through contact layer. This selective energy contact is usually made up of small quantum dots with high resonant state energy for resonant tunneling. Experiments using double barrier electron-tunneling structures, with a single layer of Si QDs have been reported [Jiang 06b]. However, the problem in decreasing the carrier cooling rate remains as an obstacle to the efficient demonstrations of HCSC.

Up-Down conversion : The process in which at least two sub-bandgap photons are absorbed to emit one above bandgap photon is called as up conversion. The process of absorbing at least twice the energy of semiconductor bandgap and emitting two photons is called as down conversion. An up converter layer can increase the current by absorbing the below bandgap photons which are generally not absorbed. A down converter layer can increase the current by converting photons in the ultraviolet range into a large number of photons in the visible range. Nanostructures of Si are efficient light emitters and hence can be used as a photoluminescent down shifter (PDS) layer, through which high energy photons are absorbed to emit low energy photons. The principles are similar to that of IBSC and MEG with slight modifications in the configurations. The possibility of using porous Si, Si nanocrystals and rare-earth doped nanostructures for these purposes have been reported [Wang 92, Trupke 02a, Svrcek 04, Timmerman 08, Miritello 10].

1.5 Si Quantum Dots (QDs) in Photovoltaics

Third generation PV approach takes advantage of the quantum confinement effect and it can be seen from the previous section that Si QDs can be utilised in all the approaches. Si QDs have a wide range of applicability in a solar cell device due to their optical and/or electrical properties. Among those, the most important applicability of Si QDs includes the active layer in a simple p-n junction [Cho 08, Hong 10, Hong 11] or intrinsic layer in p-i-n junction device, selective energy contacts, photoluminescent down shifter layers, and a tandem cell's active layers in all the cascaded p-n junctions or p-i-n junctions. In this context, it becomes im-

portant to control the formation of Si QDs in various hosts, and their corresponding optical and electronic properties. Hence, this section deals with a brief discussion on the widely used configurations of Si-QDs explored thus far towards PV applications.

1.5.1 Porous Silicon (p-Si)

Porous Si is the first investigated form of Si-QDs, ever since the discovery of size tunable visible luminescence in the material. The surface of p-Si is highly textured which enhances light trapping and reduces the reflection losses. The possibility of having a wide particle size distribution among the QDs helps in the tunability of the p-Si bandgap. This can be utilized to absorb a wide range of solar spectrum. But the high resistivity of the material leads to problematic electric transport. Besides, the poor thermal and mechanical stability of the material challenges [Nguchi 93, Ruiz 94] its endurance to high temperature processing steps usually ranging between T=1000°C to T_{melt}=1400°C, the melting temperature of Si [Reber 99, Bergmann 99] in solar cell fabrications. The emission properties of p-Si is not stable during storage in air due to various causes such as desorption of hydrogen or SiH_x complexes [Prokes 92, Weng 93, Zoubir 94], oxidation processes [Stevens 93, Xiao 93], absorption of water and other substances from the atmosphere [Cullis 97, Canham 91].

1.5.2 Si Quantum Dots embedded in dielectric hosts

In order to overcome the drawbacks of p-Si while taking advantage of the quantum confinement effects observed in it, alternative means of synthesizing Si QDs were investigated. Embedding Si QDs in wide bandgap insulators is one of the most convincing solution to obtain strong quantum confinement. Various techniques for the growth of Si-rich layers have been employed such as ion implantation [Min 96, Bonafos 04], chemical vapour deposition [Lin 00], pulsed laser deposition [Chen 04], plasma enhanced chemical vapour deposition [Iacona 00], magnetron sputtering/co-sputtering [Seifarth 98, Gourbilleau 01], evaporation in ultra-high vacuum [Miska 10] etc. Subsequent annealing treatments allow the formation of nanoclusters or crystals from the Si excess in the Si-rich layers. Since the goal is to concentrate on an all-Si tandem cell, the forthcoming discussions are restricted to the Si QDs embedded in its dielectric compounds such as oxide, nitride or carbide, the oxide dielectric providing the strongest confinement of all (Fig. 1.12).

(a) Si QDs in SiO_2: Silicon oxide with silicon excess are termed as Silicon Rich Silicon Oxides or Silicon Rich Oxides and are often denoted by any of these : SRSO/SRO/SiO_x where x<2. In this thesis, the notation SRSO is generally used and occasionally SiO_x. Si QDs embedded in SiO_2 is the most widely investigated

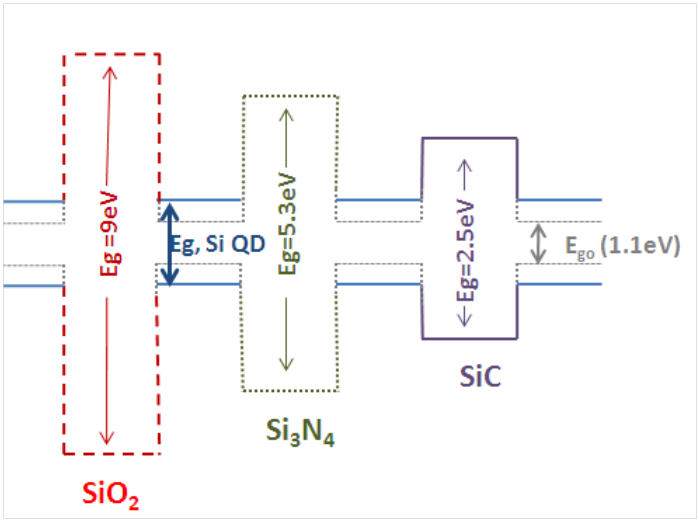

Figure 1.12: Energy diagram of bulk Si, Si QDs and their potential insulating barrier materials.

material to overcome the shortcomings of p-Si. Similar to p-Si, size dependent luminescence was observed in these configurations also with combined advantages of mechanical robustness, compatibility with silicon tehnology and chemical stability for potential applications. The origin of luminescence has opened a debate and various experimental and theoretical studies attribute it to processes such as quantum confinement effects in silicon nanocrystals [Schuppler 95], silicon oxide: its defect centers and siloxene derivatives etc.[Deak 92, Duan 95, Cooke 96, Qin 93]. Crystallized Si QDs have high stability against the photo-induced degradation and stronger light absorption in the lower wavelengths (higher energies). There is also an increase in the short circuit current due to the absorption of high energy UV photons within the SRSO film. This is attributed to the PL re-emitted as red light that reaches the active p-n junction thereby increasing the photocurrent of the solar cell [Lopez 11]. The surface passivation of the material often leads to a reduction in the number of non-radiative centers and allows achievement of efficient photoluminescence. In contrast to p-Si, it is reported that the spectral band caused by exciton recombination in Si crystallites does not change practically during aging [Baran 05]. The electrical properties of SRSO depend on Si concentration and the QD size [Aceves 96, Aceves 99] and various mechanisms are proposed for carrier transport such as Fowler-Nordheim, Poole-Frenkel, direct or elastic tunnelling models [Kameda 98, Salvo 01, Kahler 01].

(b) Si QDs in Si_3N_4 or Si-Rich silicon nitride (SRSN): The silicon nitride films are compatible with silicon technology and have been used as antireflection coatings as well as passivation layers in crystalline silicon solar cells [Aberle 01]. The

carrier tunnelling probability between the quantum dots can be increased due to the lower bandgap of Si_3N_4 ($\sim$5 eV) as compared to SiO_2 ($\sim$ 9 eV) [Green 05]. It has been reported that the Si QDs form at a faster rate and at a lower annealing temperature as compared to SRSO [Negro 06] and efficient photoluminescence have been observed from SRSN films [la Torre 06, Lelievre 07] which are reported to be blueshifted when compared to Si QDs in SiO_2 (Fig. 1.13 from [Yang 04]). High carrier mobility and relaxed interdot separation of 3-4 nm as compared to 1-2 nm in SiO_2 has been estimated from Si QDs in Si_3N_4 leading to better conduction property of the device [Jiang 06a]. Under blue/green light it is reported that Si QDs in silicon nitride show about 14 times enhanced absorption than bulk Si and a photocurrent which is about 4 times higher than that of bulk Si solar cells [Kim 09]. The carrier mobility in silicon nitride containing QDs is attributed to direct tunnelling process and is dependent on the Si QD density [Jiang 04]. Hence enhancing the density of Si QDs in Si_3N_4 has an added advantage of using this material in the active layers of a solar cell. Besides, Si QDs embedded in Si_3N_4 antireflection layer of solar cells can be used as luminescent converters to enhance photovoltaic conversion in the blue region of the spectrum [Trupke 02a, Trupke 02b]. Apart from such promising advantages of this material, the processes of luminescence mechanism and defect formations is less understood than in the case of SiO_2. The Si QD size, and their surface passivation cannot be directly deduced from photoluminescence because silicon nitride matrix itself exhibits a strong visible luminescence which is attributed by several authors to nitrogen and silicon levels in the silicon nitride bandgap [Deshpande 95, Gritsenko 99].

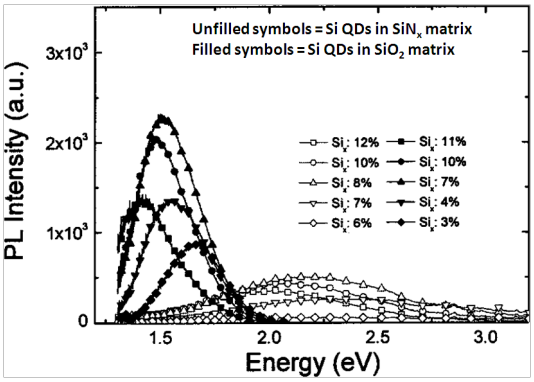

Figure 1.13: Comparison of luminescence peak positions between Si QDs embedded in SiO_2 and SiN_x (SRSN) matrices[Yang 04].

(c) Si QDs in SiC: SiC is another important successful material used in solar cells in its amorphous thin film form as p-type window layers and buffer layers in p-i-n configurations. Though very few works have been reported with Si QDs embedded

in SiC, the lower bandgap ($\sim$2.5 eV) compared to the other two dielectrics discussed above, offers several advantages [Cho 08, Song 08b]. The lower barrier of the SiC increases the tunnelling probability among the QDs and also promotes effective luminescence. The confined energy levels of Si QDs in SiC is quite similar to that of Si QDs in oxide matrix [Kurokawa 06]. Efforts relating to developing a multi-band configuration of Si QDs in SiC [Chang 10] and doping for enhanced conductivity [Lim 08, Cho 08] have been taken up recently which would help significantly in the design of PV devices. Depending on the composition of SiC, the QDs vary in shape, some joining together to form an extended crystal. It is reported that depending upon the stochiometry, SiC QDs are formed instead of Si QDs [Cho 07]. It also has to be mentioned that the segregation and formation of Si QDs in SiC are more difficult that the other two dielectrics mentioned above. Though investigations on Si QDs in SiC are still at a preliminary level, the results obtained thus far show the potential use of this material in solar cells.

1.5.3 Si Quantum Dots in multilayers

The successful incorporation of Si QDs in various dielectric matrices and its various optoelectronic properties reflect the advantages of quantum confinement in Si for PV devices, with increased mechanical strength as compared to the p-Si. But the size dispersion of the QDs in these materials, complicate the understanding of the material properties [Credo 99]. Moreover, with increase in time and temperatures of annealing, the nanocrystals (QDs) agglomerate and form bigger crystals (Fig. 1.14). As a consequence, the material behaves similar to bulk Si with indirect bandgap nature, due to the loss of quantum confinement effect. Nanocrystals with a narrow size distribution are required to produce a solar cell with a controlled bandgap energy. Therefore multilayer approaches were adopted to maintain a uniform size distribution with a precise control over Si QDs size and distribution as represented in figure 1.14.

Usually a multilayer is formed by sandwiching Si QDs between stochiometric insulating layers that serve as barriers. The most investigated configuration is the SRSO/SiO_2 multilayers (MLs) proposed by F. Gourbilleau and M. Zacharias [Gourbilleau 01, Zacharias 02], due to the relatively well understood mechanisms of luminescence and electric transports. Since the tunneling probability depends on the insulating barrier height, Si_3N_4 or SiC is expected to provide a better carrier transport. Substantial research efforts are being taken up, in enhancing the carrier transports, both in the well understood SRSO/SiO_2 MLs, and in the alternative

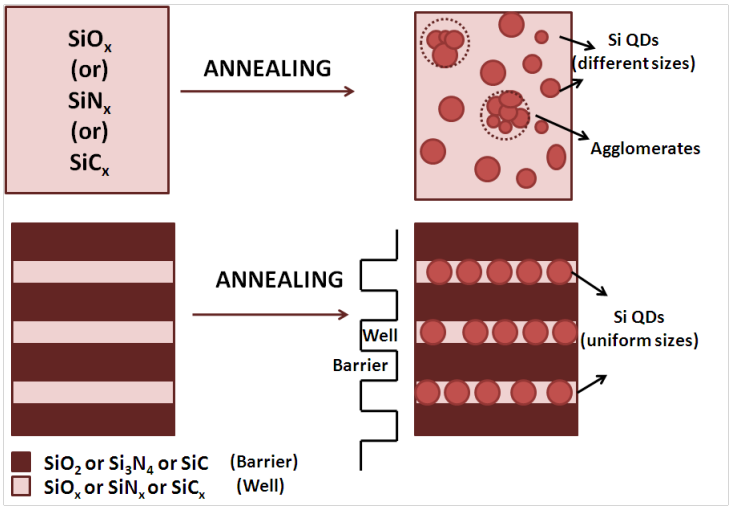

Figure 1.14: Formation of QDs with size dispersion in monolayers and with size control in multilayers.

SRSO/Si_3N_4 or SRSO/SiC MLs. The investigations aiming at exploring the possibile potentials of these alternative MLs for PV applications are still at their infancy. The present research scenario concentrates on understanding silicon nitride based MLs, though parallely a couple of reports on SiC based MLs have also begun to appear from the past few years [Song 08a]. Focusing on silicon nitride based MLs, configurations like SRSO/Si_3N_4 [Di 10], Si-rich-Si_3N_4/Si_3N_4 [So 11] and Si-rich-Si_3N_4/SiO_2 [Delachat 09] have been proposed for the purpose and hardly a couple of reports [Conibeer 10], as of today, are available on the optical and electrical properties of such materials.

1.6 Purpose and Aim of the thesis:

The motivation of this research work is to extend the CMOS compatible Si technology to the advanced Third Generation PV concepts that promise a futuristic world of sustainability. It is remarkable that both the essential parts of a solar cell- the Sun (Solar energy), and the PV material Silicon, are abundant resources available in nature. The quantum confinement effect in Si has tremendously benefitted the PV research sector, and achieving high efficiencies beyond Shockley-Queisser limit is no longer confined to theoretical studies. In order to fully utilise the inherent capabilities of the Si QDs in a PV device, a deep understanding of the material properties and addressing the present challenges is important. Investigating Si QDs in various configurations and hence novel Si QD based materials with tunable bandgap, absorption, luminescence and electrical properties are important to approach a step closer towards device applications.

Background of this thesis: A new method of depositing SRSO/SiO_2 MLs by using hydrogen instead of the usually used oxygen was demonstrated in our laboratory by reactive magnetron sputtering approach [Gourbilleau 00, Gourbilleau 01]. The influence of various parameters like deposition temperature, hydrogen rate, annealing temperatures [Portier 03, Chausserie 05] etc. on the formation of Si-nanoparticles (Si-np) and their emission,absorption and electrical properties were investigated [Gourbilleau 09, Maestre 10]. A high density of Si-nanoparticles (10^{18} np/cm^3) was achieved as can be seen from the EFTEM image (Fig. 1.15) and opto-electronical investigations were performed on such layers for solar cell applications. High values of resistance obtained till now on these kind of layers, require further investigations and optimizations before their incorporation in a device.

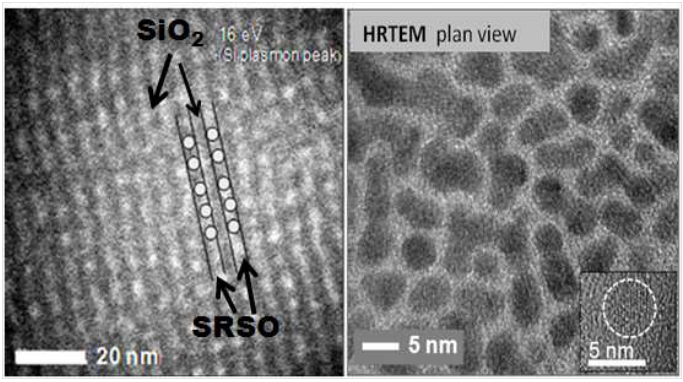

Figure 1.15: Microstructural images of SRSO/SiO_2 superlattice showing the formation of Si-nanoparticles [Gourbilleau 09].

In this context, **the four major objectives of this thesis** are:

1. Enhancing the already reported [Maestre 10] Si-np density by (i) varying the deposition parameters and the sputtering approaches, and (ii) investigating post fabrication processes on Si-rich Silicon oxide and silicon nitride layers in mono- and multilayered configurations

2. Decreasing the thermal budget for the formation of Si-np.

3. Demonstrating the advantages of SRSO/SRSN MLs over SRSO/SiO_2 MLs, with more emphasis on the absorption and emission properties.

4. Gaining insight on photoluminescence properties with experimental and theoretical analyses, for further developments towards device integrations.

Chapter 2

Experimental techniques and analytical methods

The synthesis of Si nanostructures in various dielectric matrices has been successfully demonstrated by many research groups using a variety of techniques such as ion implantation, PECVD, sputtering, laser ablation etc., as mentioned in chapter 1. Among these, our group (NIMPH team) specializes in RF magnetron sputtering. Multilayers of SRSO alternated by their oxide or their nitride are our prime subjects of investigation. But before proceeding to the multilayers, it is important to choose the growth parameters of each sublayers. Hence, single layers of these materials (SRSO, SiN_x and SiO_2) were grown to extract informations such as composition, deposition rate, structural and optical properties depending on the fabrication conditions. This chapter details the principle, description and elaboration of the sputtering technique, and the various characterization tools used for investigation.

2.1 Thin film fabrication

The fabrication of thin films using Physical Vapour Deposition (PVD) can be broadly categorized into two groups:

1) thermal evaporation, in which the target material placed in a vacuum chamber boils, evaporates and finally condenses to deposit a thin film, and

2) sputtering.

The forthcoming discussions are restricted to the latter with more emphasis on magnetron sputtering which is one of the variant techniques that work under the principle of sputtering.

2.1.1 Radiofrequency Magnetron Reactive Sputtering

Principle

The phenomena of sputtering consists of striking the source material (the target) with fast moving, inert gas ions (eg. Ar) which transfer momentum to the target species (electrons, atoms, molecules) and eject them out.

The positive ions of the plasma (from ionized Ar) are accelerated towards the negatively charged target and impinge on its surface. Some of the bombarding ions are reflected back and are neutralised, while some have sufficient energy to reach the substrate and are back scattered. The secondary electrons are also emitted during this process and they may cause further ionisation of the neutralised species. Due to the law of conservation of energy, when these electrons return to ground state, the energy gained by the neutral gas atom is released as photons which keep the plasma glowing. The main intention of sputtering is to direct the ejected species towards the substrate with sufficient energy and mobility, because if they collide with other atoms in the plasma, the energy is diminished and their path is modified. The incident species with sufficient mobility diffuse to join with other species at the substrate and grow until they coalesce to form a continuous film [Wagendristel 94]. The mobility of the incident atoms arriving at the substrate is highly dependent on sputtering parameters such as the power applied, pressure in the chamber, temperature, distance between the target and the substrate etc.

The energy required to initiate and sustain the plasma was initially provided by a DC power supply to create a discharge and ionise the gas. But the principle of DC discharge is ineffective for an insulating target, because no current can pass through it. As a consequence, charge build-up occurs and stops the process. In order to overcome this shortcoming of a DC power supply, RF power system was developed. For frequencies up to 50 kHz, the ions are mobile enough to reach the electrodes at each half cycle of the AC power. This leads to alternative sputtering of the substrate and the target which cancels the global transport of matter. At high frequencies typically used for sputtering (13.6 MHz), new phenomena occur:

1. The ions remain practically motionless in the RF field due to their mass as compared to the electrons, and do not involve themselves in sputtering.

2. The electrons in high frequency field acquire sufficient energy to cause ionization of the effective plasma.

3. At such high frequencies, the target behaves as a conductive one.

Thus, the use of RF sputtering enables any material to be sputtered. A matching impedence network is always required with RF sputtering in order to absorb

maximum power into the plasma.

(a) Reactive sputtering : The principle of introducing a reactive gas (g) such as H_2, N_2, O_2 into the chamber and forming a thin film through chemical reactions between the sputtered species and gaseous plasma is known as reactive sputtering. Oxide and nitride films are often formed by reactive sputtering and the stochiometry of the film can be tuned by controlling the relative flow rates of the inert and reactive gases. The desired compound is formed at the substrate, depending on the power and the surface reactivity. In this thesis, the total gas flow was fixed at 10 standard cubic cm/min (sccm) while changing the ratio of the gas flow (in sccm) between the reactive gas and Ar. The equivalent partial pressure (mTorr) in the chamber displayed by the pressure indicator for a given gas flow (sccm) was used to calculate the reactive gas rate ($r_g\%$) in percentage by,

$$r_g(\%) = [P_g/(P_g + P_{Ar})] * 100 \qquad \text{Eqn (2.1)}$$

where P_g represents the partial pressure of reactive gas, g (g may be H_2, N_2 or O_2 depending on the process) and P_{Ar} represents the partial pressure of Argon.

(b) Effect of magnetron : Magnetron sputtering uses the principle of applying a magnetic field to the conventional sputtering target in order to obtain more efficient ionization of the plasma even at low pressures. The magnets placed behind and sometimes at the side of the target capture the escaping electron and confine them to the immediate vicinity of the target. This confinement provided by the magnet is illustrated in the sputter process shown in figure 2.1. Due to the increased confinement as compared to a conventional DC system, the plasma density often increases at least by an order of magnitude. This results in fast deposition rates at low pressures. However the major limitation of using magnetron is that the target erodes inhomogeneously due to the non-uniform magnetic field.

Experimental set-up and working

The samples for this work were deposited using AJA Orion 5 UHV sputtering unit from AJA international [AJA 1] which has multiple magnetron sources aimed at a common focal point (Confocal sputtering). The substrate is placed in the vicinity of this focal point and is kept under rotation to ensure uniform deposition of the film. The sputtering chamber was maintained under vacuum of 10^{-7}- 10^{-8} mTorr using a turbo-molecular pump coupled to the primary pump. The substrate and the target which function as the anode and the cathode repectively, are placed facing each other in the sputtering chamber and an inert gas (Ar) is introduced. Applying the RF power and introducing a pressure controlled gas flow leads to the presence

of plasma in the chamber. Figure 2.1 illustrates the various processes that occur during a magnetron sputtering using a schematic diagram of the process.

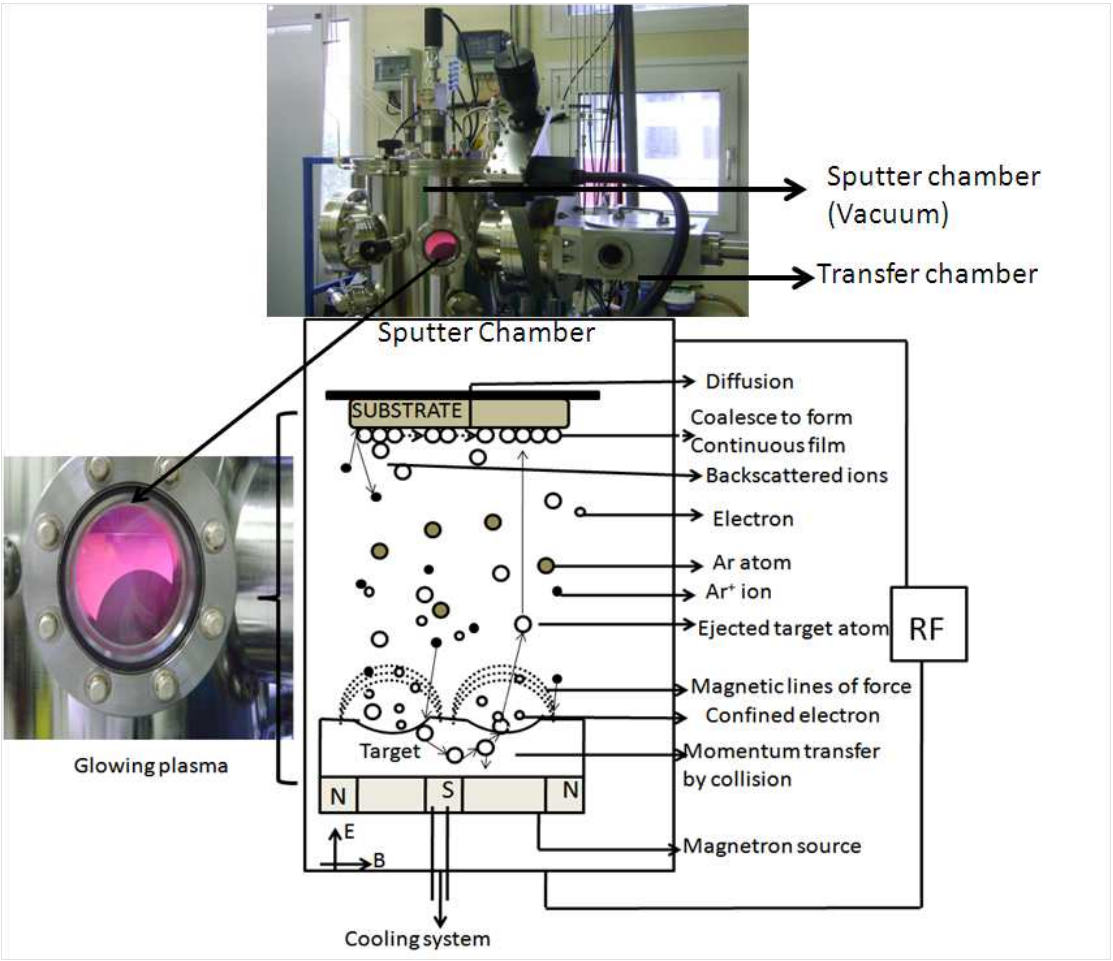

Figure 2.1: Photo of the AJA Sputter chamber with glowing plasma and the diagrammatic representation of various processes during sputtering.

Two halogen lamps provide heat to the rear side of the sample holder and helps to maintain the temperatures between ambient and 850°C. Therefore the samples can be deposited at any of these temperatures.

2.1.2 Sample preparation

All the samples were deposited on a 2 inch boron doped Si wafer with 5-15 $\Omega.cm$ resistivity provided by SILTRONIX [Siltronix 1]. Few samples were also grown on a fused silica substrate to facilitate characterization through optical spectroscopy. The three methods of deposition techniques used in this thesis (reactive sputtering, co-sputtering and reactive co-sputtering) are illustrated in figure 2.2.

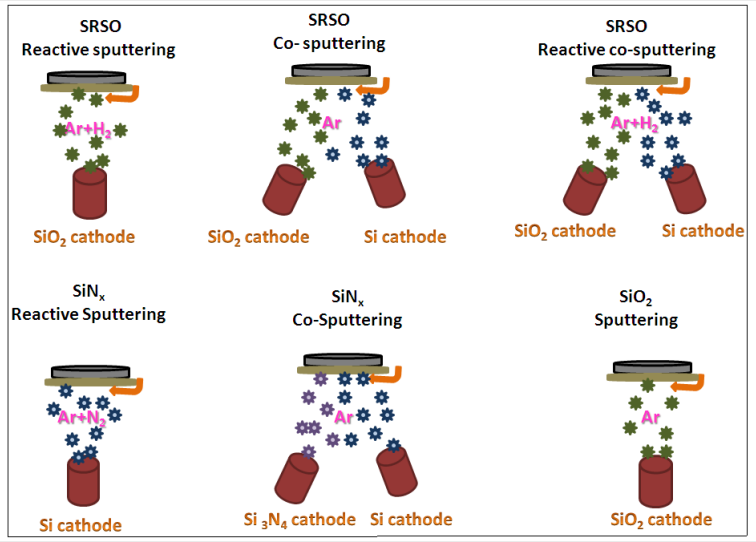

Figure 2.2: Illustration of sample fabrication methods.

Silicon Rich Silicon Oxide (SRSO)

Three different methods to introduce Si excess were employed for the fabrication of SRSO.

Reactive magnetron sputtering: the SRSO layers were grown by sputtering a pure SiO_2 target in a mixture of hydrogen and Ar plasma. The hydrogen-rich plasma favors Si excess in the SiO_2 sublayer by the reduction reactions with oxygen species [Gourbilleau 01]. The hydrogen gas rate, r_H (%) was varied between 4.6-57% in order to analyze the balance between deposition and etching. The RF power density on the SiO_2 cathode was maintained at 7.4 W/cm^2.

Magnetron co-sputtering: the SRSO layers were grown by simultaneously sputtering the SiO_2 and Si targets in a pure Ar plasma. The RF power density on SiO_2 cathode was fixed at 7.4 W/cm^2 while that on Si cathode was varied between 1.62-2.96 W/cm^2 to analyze the effect of excess Si incorporation.

Reactive magnetron co-sputtering: this method is a combination of the above mentioned methods. Both the targets, SiO_2 and Si were sputtered simultaneously in hydrogen-rich plasma in order to witness an increase in the excess Si incorporation obtained from the earlier used methods. The power of SiO_2 was fixed as before, and r_H was fixed at 26%, while the power density on the Si cathode was varied between 1.62-2.96 W/cm^2.

Silicon-rich silicon nitride (SiN_x)

Two different approaches were used for the synthesis of silicon nitride as illustrated in figure 2.2.

Reactive method: Si cathode is sputtered while introducing nitrogen into the Ar plasma to obtain Si-rich silicon nitride (SRSN). A sample of N-rich silicon nitride (NRSN) was obtained by sputtering a Si_3N_4 target in N-rich plasma.

Co-sputtering method: this approach involves the simultaneous co-sputtering of Si_3N_4 and Si cathodes. The power density on Si_3N_4 was fixed at 7.4 W/cm^2 and that on Si cathode was varied between 0-2.96 W/cm^2 in order to see the effect of excess Si incorporation.

Silicon dioxide (SiO_2)

Silicon dioxide layer was deposited by sputtering SiO_2 cathode under pure Ar plasma. As in the previous cases, the RF power density on the SiO_2 cathode was maintained at 7.4 W/cm^2.

The single layers and the multilayers of SiO_2, SRSO and SiN_x were synthesized using the growth methods described above. The composition of the layers were varied using appropriate deposition conditions such as temperature, pressure, RF power density monitored using a computer software provided by AJA International. To deposit at a desired temperature a ramp time was fed in the program to reach the temperature and a dwell time of 1 hour was fixed for stabilization (to reach a uniform temperature over the substrate) before the deposition takes place. The substrate was kept under rotation with a speed of 20 revolutions/minute to ensure homogeneous deposition and the substrate-target distance was fixed at 38 cm.

2.1.3 Thermal treatment

All the deposited layers were subjected to thermal treatments in order to favour phase-separation, crystallization and passivation of the defects (vacancy, dangling bonds, etc.) in the material. All the samples were annealed under the nitrogen atmosphere and the temperatures of annealing was varied between 400-1100°C depending on the requirement. A couple of multilayers were also subjected to annealing under the forming gas atmosphere between 380°C-500°C. The effect of the annealing time and temperatures of different kinds of layers were analyzed.

2.2 Structural and Optical Characterization

The samples in this thesis have been analyzed structurally and optically using one or many of the following techniques: Fourier Transform Infrared Spectroscopy, X-

Ray Diffraction, X-Ray Reflectivity, Electron Microscopy, Raman spectroscopy, ellipsometry, photoluminescence spectroscopy. An insight on the structural and compositional details of the as-deposited and the annealed films can be extracted from microscopic images, characteristic vibrational frequencies of specific elements in the film, refractive indices, the material's absorption and emission behaviours etc., resulting from the above mentioned characterization techniques.

2.2.1 Fourier Transform Infrared Spectroscopy (FTIR)

Principle

FTIR spectroscopy is a powerful tool to investigate the chemical bonds present in a molecule. Molecular bonds vibrate at specific frequencies depending on the elements and the types of bond they possess. When the incident IR light interacts with the molecules, they absorb light at these specific frequencies that are characteristic of their structure. The molecules can vibrate in any of the following ways: symmetrical and asymmetrical stretching, scissoring, rocking, wagging and twisting as indicated in figure 2.3. The resulting absorption spectrum yields both qualitative as well as quantitative information on the chemical bonds and their concentration in the material, respectively.

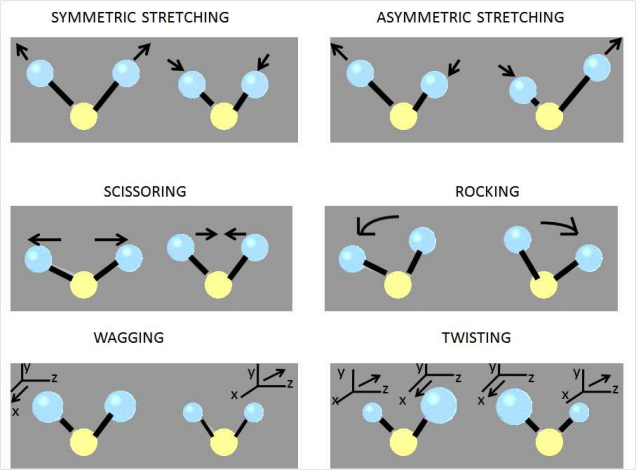

Figure 2.3: Different types of molecular vibrations.

Experimental set-up and working

FTIR measurements were performed using Thermo Nicolet Nexus 750-II. The spectra were recorded in wavelength ranging between 400 to 4000 cm^{-1} with a resolution of 2 cm^{-1} at room temperature. The apparatus has two light sources: He-Ne monochromator (633 nm) and a lamp with tungsten filament that generates light

between 2.5-25 µm. The former is used for alignment and the latter interacts with the sample. In the FTIR set-up, the IR radiation is guided through a Michelson's interferometer (Fig. 2.4a) with a moving mirror. An interferogram consisting of light intensity versus optical path is recorded by the detector with each movement of the mirror. This data from the interferogram is converted into the spatial domain using fourier transformation (Fig. 2.4b). The contributions from the reference substrate and other atmospheric components such as CO_2 and water were subtracted from the spectrum to analyse the structural composition of the deposited material.

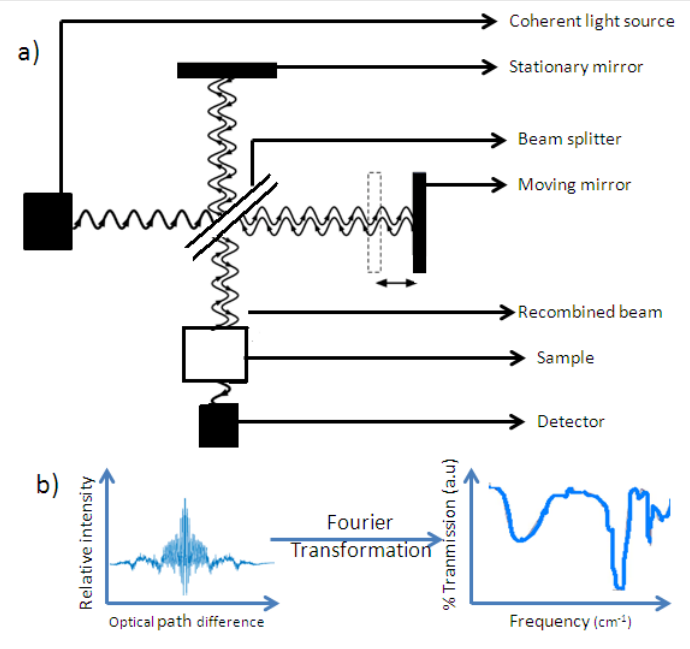

Figure 2.4: (a) Schematic representation of FTIR set-up and (b) Interferogram to Fourier transformed spectra.

Typical spectra of SiO_2 obtained in two different angles of incidence are presented in figure 2.5 as a representative of the main absorption features analysing methodology which will be followed for all the other samples in this thesis.

The spectrum recorded in normal incidence enables to visualise the transverse optical modes as shown in figure 2.5a. The spectra of SiO_2 is characterized by three major absorption bands TO_2, TO_3 and TO_4 corresponding to Si-O-Si rocking, symmetric stretching and asymmetric stretching modes respectively. Each transverse optical mode (TO) has an associated longitudinal optical mode (LO), and this is called as the LO-TO splitting. LO modes cannot be seen through FTIR in normal incidence but can be detected if measured in oblique incidence (Fig. 2.5b) [Berremann 63]. In this thesis, Brewster incidence of 65° is chosen for viewing the LO modes. Besides these vibrations, there is a fourth vibrational splitting known as

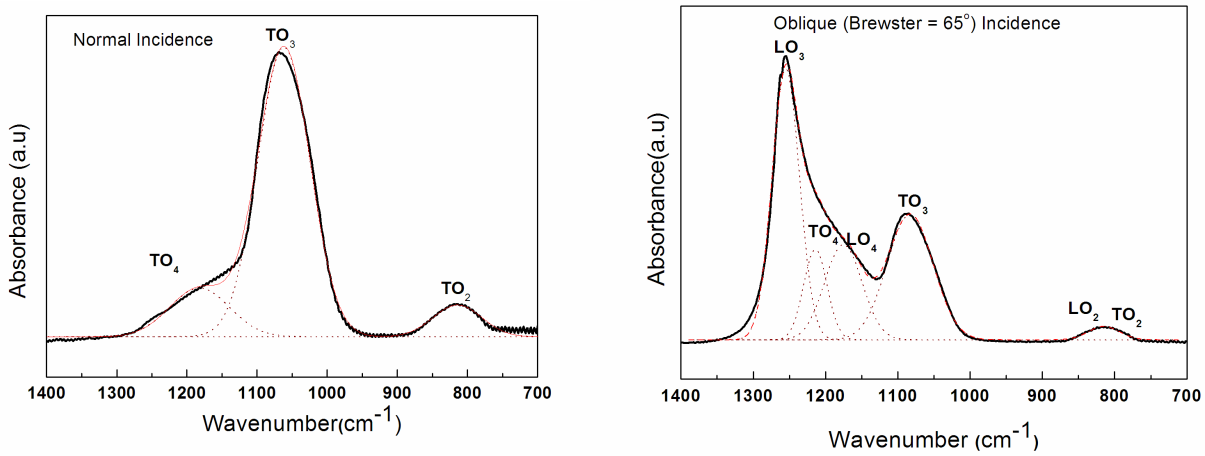

(a) Normal Incidence. **(b)** Oblique (Brewster) Incidence.

Figure 2.5: Typical FTIR spectra of SiO_2 which is decomposed into three and five gaussians in the normal incidence and Brewster incidence spectra respectively.

LO_4-TO_4, which is assigned to disorder-induced mode in the SiO_2 matrix [Kirk 88]. The presence of these vibrational modes are sometimes overlapping and hence a curve fitting within the range of interest was perfomed using gaussian functions to resolve the peaks and estimate their positions.

Table 2.1 summarizes the characteristic vibrational frequencies of SiO_2 as compiled from [Lehmann 83, Pai 86, Innocenzi 03].

Peak position (cm^{-1})	Vibrational Modes
460	TO_1Si-O rocking
507	LO_1 Si-O rocking
810	TO_2 Si-O symmetric stretch
820	LO_2 Si-O symmetric stretch
1080	TO_3 Si-O antisymmetric stretch (adjacent O atoms in phase)
1256	LO_3 Si-O antisymmetric stretch
1150-1200	LO_4-TO_4 Si-O antisymmetric stretch (adjacent O atoms out of phase - disorder induced mode).

Table 2.1: Characteristic FTIR vibrational frequencies of SiO_2.

Informations extracted in this thesis

- The different types of bonds such as Si-O, Si-H, Si-N, Si-ON, N-H etc., are detected from the position of the longitudinal and transverse optic modes.

The ratio of intensities between the TO and LO modes, and the shift of the peak positions yield informations about the quality and composition of the film. Using these informations, the stress, defect, Si content and the elemental presence in a given layer can be estimated.

- The Si excess in SRSO, which represents here the amount of isolated Si in SiO_x matrix, can be estimated from the TO_3 peak position. The position of TO_3 peak and the ratio of oxygen to silicon ($x = O/Si$) can be related by the following formula [Ono 98]:
  $v_{TO3} = 900 + 90x$ Eqn (2.2).
  From, this the atomic percentage of excess silicon in SRSO is calculated using the formula below:
  Si_{excess}at. $\% = [(2 - x)/(2 + 2x)]100$ Eqn (2.3)
  It has to be remembered that the Si excess obtained from FTIR would not include the Si atoms that have started nucleating or agglomerating during the deposition process. This is because the homopolar bonds are inactive to IR radiations. Hence the Si excess obtained from FTIR is an underestimation of the total excess present in the material.

- The evolution of the phase-separation process and the structural relaxation towards a more ordered material can be observed from the FTIR spectra. For example, the TO_3 peak position shifts towards high wavenumbers indicating that the SiO_x becomes more oxygen rich (approaching SiO_2) together with the nucleation of Si particles.

2.2.2 X-Ray Diffraction (XRD)

Principle

X-ray diffraction is a technique that reveals detailed information about the chemical composition and crystallographic structure of materials. When waves interact with a periodic structure whose repeat unit has dimensions similar to the incident wavelength, diffraction occurs through constructive interference phenomena. Hence if a X-ray beam of wavelength lambda (λ) is in the order of few angströms similar to the interatomic distances of crystalline solids, they get diffracted if certain geometrical requirements are satisfied. This is given by the Bragg's law and is expressed as,

$$2dsin\theta = n\lambda \quad \text{Eqn (2.4)}$$

where d is the interatomic distance, θ is the angle between the incident ray and the scattering planes, n is an integer, and λ is the X-ray wavelength. According

to equation 2.4, when X-ray beam strikes on a crystal at an angle θ, constructive interference occurs only when the distance travelled by the X-rays scattered from successive planes differs by an integer n of the wavelength and results in the diffraction pattern. In our case, the thin films are usually composed of randomly oriented nanocrystals and figure 2.6 shows a pictorial representation of Bragg's diffraction from one of the diffracting nanocrystal. Each orientation of the crystal results in a diffraction peak at different angles (which is usually measured as 2θ in the experiments for practical purposes), characteristic to the crystallographic structures of the material.

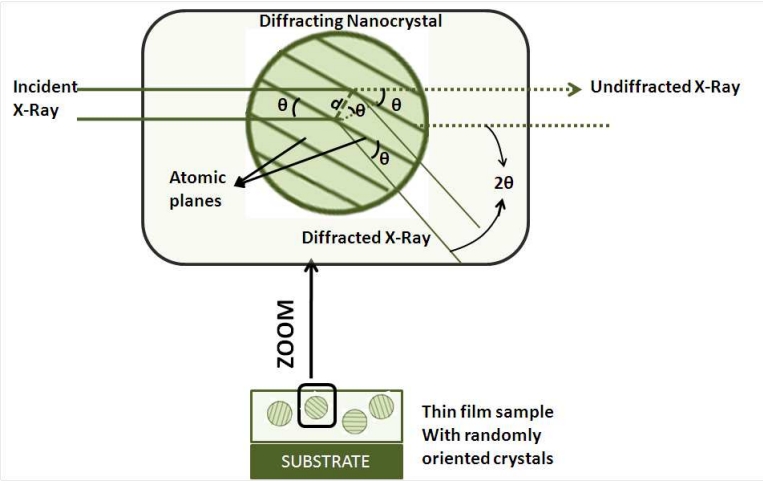

Figure 2.6: Pictorial representation of Bragg's law.

Experimental set-up and working

The experiments were performed in grazing incidence using a Philips XPERT instrument equipped with a copper anode to generate X-rays with $\lambda = 1.5406$ and 1.5444 angströms corresponding to the Cu-$K_{\alpha 1}$ and $K_{\alpha 2}$ lines respectively. Figure 2.7 shows a schematic representation of the experimental set-up in grazing geometry.

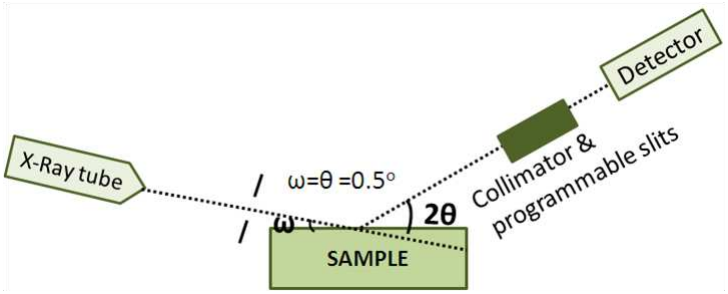

Figure 2.7: XRD- Illustration of working principle and experimental set-up.

Grazing incidence XRD is a technique suitable for the analysis of thin films since

the penetration of X-rays into the substrate is minimized and a large volume of the thin film can be investigated by increasing the X-ray path. Hence, Bragg's peaks arise only from the surface structure. The Cu X-rays generated by the X-ray tube are collimated and directed on the sample. The intensity of the diffracted X-rays are recorded. The grazing angle of incidence is fixed at $\omega = \theta = 0.5°$ and the angle between the incident beam and the detector varies between from 2θ =10°-90°.

Informations extracted in this thesis

- The amorphous or crystalline natures of the thin films are investigated from the absence/presence of the diffraction peaks.
- An estimation of crystalline volume in the material can be obtained. Figure 2.8 shows a typical spectrum obtained from a Si-based multilayer with the diffraction peaks (hkl) corresponding to (111), (220) and (311) planes of Si nanocrystals.

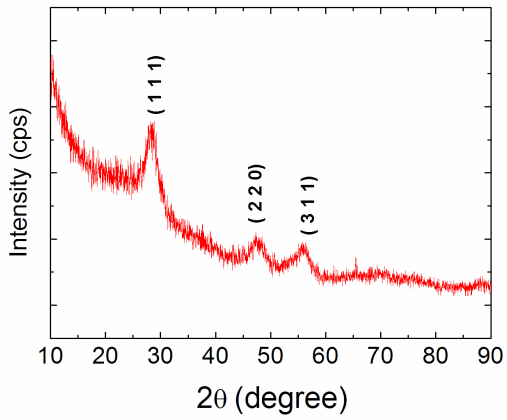

Figure 2.8: A typical example of XRD spectrum taken from Si-based multilayer containing Si nanocrystals.

- In some cases, the grain size of crystalline volume from the diffraction peak corresponding to Si (111) plane was estimated using the Scherrer's formula,
  Grain size = $(K\lambda)/(\beta cos\theta)$ Eqn (2.5)
  where K (= 0.9) is a constant known as the shape factor, λ (=1.5406 angström) is the wavelength of X-ray, θ is the Bragg's diffraction angle converted to radians and β is the full width at half maximum of the diffraction peak under

investigation. This value is obtained by subtracting instrumental width β_{inst} from the experimental width β_{exp} after perfoming curve fitting using Gaussian functions on the (111) peak. Thus $\beta = \beta_{exp}^2 - \beta_{inst}^2$ where:

$$\beta_{inst} = (0.15/cos\theta) + 0.07 \qquad \text{Eqn (2.6)}$$

2.2.3 X- Ray Reflectivity (XRR)

Principle

X-Ray Reflectivity is a non-contact technique that enables determination of film thicknesses ranging between 2-200 nm with a precision of 10-30 nm. The process of total reflection of X-rays from solid samples with flat and smooth surfaces and interfaces forms the basis of XRR technique. Since the refractive index of X-rays is slightly lower than 1, a beam of incident X-rays impinging on a flat surface can be totally reflected if the angle of incidence remains below a critical angle θ_c. This is called as total external reflection. The reflectivity decreases at larger angles of incidence ($\theta > \theta_c$). If the surface is not ideally flat and possesses some roughness, the X-rays are scattered and the reflected intensity deviates from that predicted by Fresnel reflectivity. The interface roughness gives rise to a progressive damping of the interference fringes. Thus from an analysis of the reflected intensity, we can extract the electron density profile, the total thickness in a monolayered sample or sublayer thicknesses in a multilayered sample. This technique does not work effectively if there is no sufficient contrast in the electronic density (in the refractive indices) of the different sublayers in a multilayer film and yields information only on the pattern thickness.

Experimental set-up and working

The same apparatus used for XRD is used for XRR with a slight change in the configuration (Fig. 2.9). As seen from the figure, two modes of measurement are possible with XRR: (i) Specular reflection and (ii) Non-specular reflection.

(i) In specular reflection, both the X-ray beam and the detector move at an angle θ from the surface. This is known as the $\theta - \theta$ measurement. The rotation of the detector is controlled through a programmable slit. The incident angle moves between 0-2° in steps of 0.001°. The spectrum of specular reflectivity shows two regions discussed as follows:

Region 1: Where θ is less than the critical angle θ_c, there is a total reflection on the sample surface and the detector receives the maximum intensity. The value of

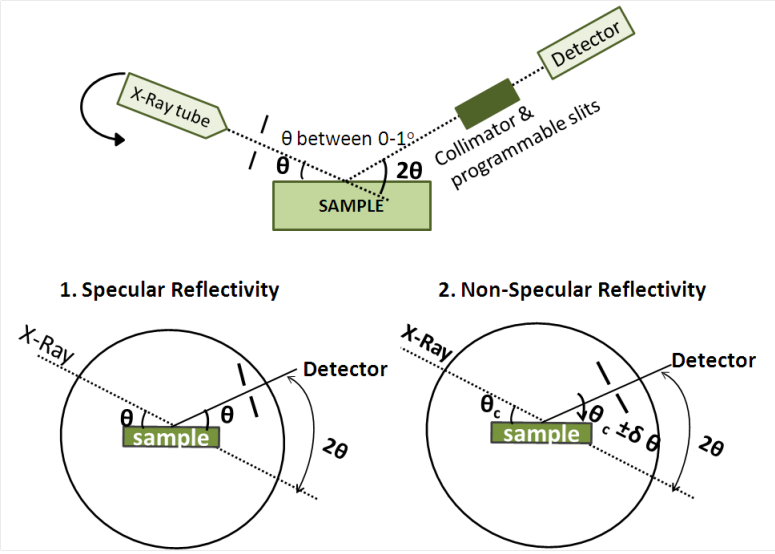

Figure 2.9: Schematic diagram of XRR set-up and the two modes of measurement.

this critical angle gives access to the index of refraction of the surface layer by the law of Snell-Descarte ($\cos\theta_c$ =n).

Region 2: When θ is greater than θ_c, a part of the incident beam is transmitted into the layer where it undergoes multiple reflections leading to the formation of interference. Since the substrate is optically denser than the film, a phase difference occurs at the film surface and the substrate. The interference fringes lead to maxima and minima in the spectra. The difference between two successive maxima in the reflectivity spectra yields information on the thickness (d) of the film or the sublayers forming the film from the following formula,

$$d = \frac{\lambda}{2\sqrt{sin^2\theta_{k+1} - sin^2\theta_k}} \qquad \text{Eqn (2.7)}$$

where λ= 1.54Å and θ_{k+1} and θ_k represent the position of two successive maxima in the reflectivity spectra. Similar calculations are done using a computer simulation in the laboratory that allows estimation of the sample thickness. For $\theta > \theta_c$, the surface roughness causes a sharp decrease in the reflected intensity and the other roughnesses below the surface (example: at the interfaces) reduces the amplitude of the reflected peaks. If the contrast in the electronic densities of the sublayers are high enough, then their individual thicknesses can be estimated from the resulting XRR spectra as mentioned above. In the case of our samples, we can estimate only the pattern thickness. A typical XRR spectra obtained from a 14 patterned SRSO/SRSN ML grown with 4 nm SRSO and 5 nm SRSN of similar refractive indices is shown in figure 2.10 from which the total thickness and the pattern thickness (4 nm+5 nm) is estimated to a high degree of accuracy. From equation 2.7 it can

be seen that large θ (here, θ is used to denote the term $\sqrt{sin^2\theta_{k+1} - sin^2\theta_k}$) corresponds to small thicknesses and hence from large θ we estimate the smaller pattern thickness and from small θ the total thickness.

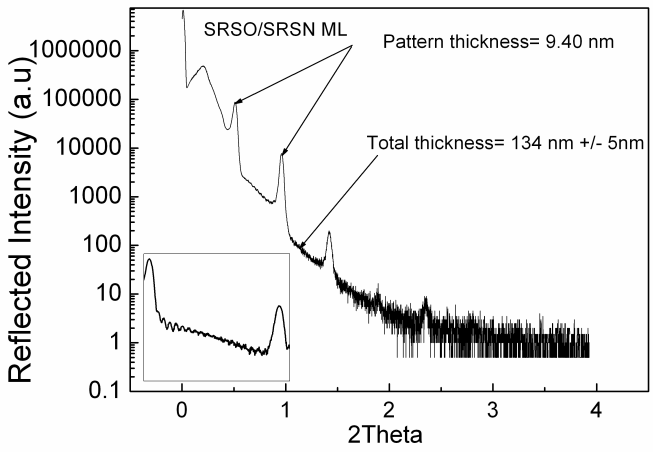

Figure 2.10: A typical XRR spectrum obtained from SRSO/SRSN ML with a zoom of the interferences leading to total thickness determination in the inset.

(ii) In non-specular mode, the reflection is obtained by fixing the incident beam at θ_c and moving the detector slightly around θ_c , ($\theta_c \pm\delta\theta$). Rotating the detector around the critical angle enables detection of the scattered beams from a rough surface. High angular resolution is needed to separate the scattered beams from the reflected ones.

All the samples investigated in this thesis were analyzed using XRR in specular reflection mode.

Informations extracted in this thesis

- The thickness of each pattern in a multilayer film.
- The total thickness of the film.

2.2.4 Raman Spectroscopy

Principle

Raman spectroscopy is a complementary technique of FTIR and is very sensitive to homopolar bonds. Raman spectroscopy is a vibrational spectroscopic technique that relies on the principle of scattering of a monochromatic light by molecular vibrations and phonons. This scattering is classified into two parts: Elastic (Rayleigh) and

Inelastic (Raman and Brillouin) scattering. A part of the photons is re-radiated at the incident energy and this is known as Rayleigh scattering. Few photons are scattered due to interaction with optical and acoustical phonons in the material and are termed as Raman and Brillouin scattering respectively. The energy shift of the Raman scattered light towards high (Anti-stokes) and low (Stokes) frequencies yield information on the vibrational modes in the measured sample. Figure 2.11 illustrates the Raman shift of the scattered light.

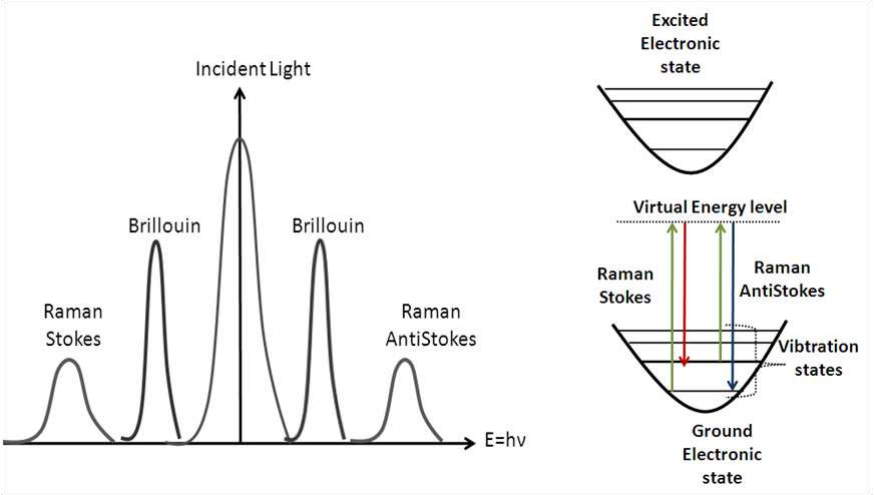

Figure 2.11: Illustration of scattering of light and Raman shift.

Experimental set-up and working

A Raman system typically consists of four major components:

- Excitation source (Laser),
- Sample illumination system and light collection optics,
- Wavelength selector (Filter or Spectrophotometer),
- Detector (Photodiode array, CCD or PMT).

The schematic diagram of a Raman spectrometer is as shown in figure 2.12.

The sample under investigation is illuminated with a laser beam. The scattered light is collected with a lens and is sent through a notch filter which removes the scattered light that is of the frequency of the laser beam. Only the light that has an energy shift (Raman shifted light) passes through the filter. The movable grating disperses the light and the different wavelengths are collected by a charged couple device (CCD) camera. Raman spectrometer from Jobin Yvon equipped with Ar

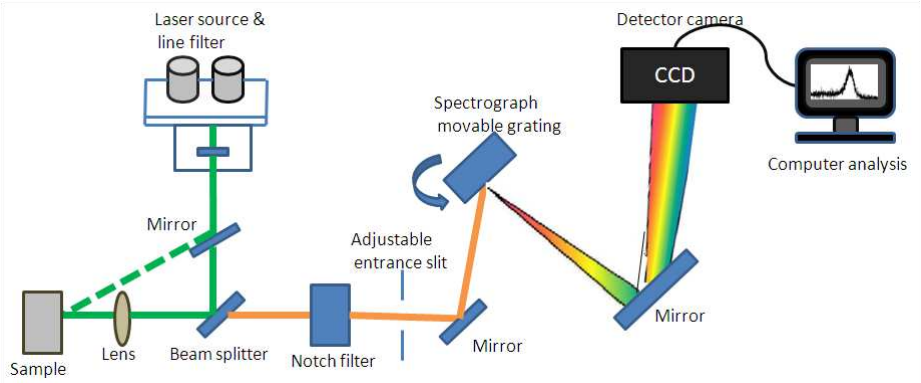

Figure 2.12: Raman spectrometer-Schematic representation.

laser was used for measurements on some of the ML samples deposited on a quartz substrate, in order to avoid the confusions between Si contribution from the sample and the Si substrate that has a peak around 521 cm^{-1}. The laser beam at 532 nm was incident on the sample, and most of the measurements were performed with a low power density of 0.14 MW/cm^2 in order to avoid any influence of laser heating. Few measurements were also performed by varying the power densities between 0.14-1.4 MW/cm^2 to see if there were any laser induced annealing on the microstructure of the sample. Figure 2.13 shows a typical Raman spectra obtained from Si and fused silica substrates.

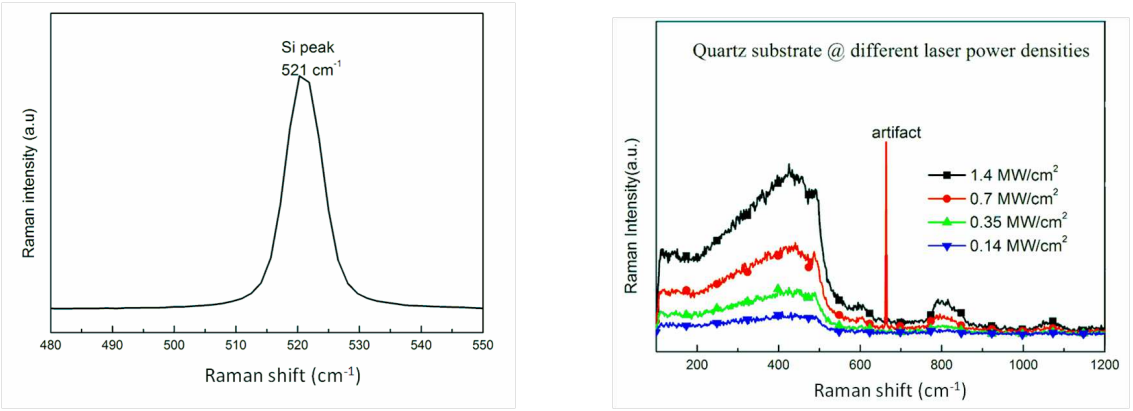

(a) Si monocrystalline substrate

(b) Fused silica substrate.

Figure 2.13: Typical Raman spectra of the substrates used in this thesis.

Informations extracted in this thesis

- The peak intensity gives information on the volume of crystalline phase of Si.
- The shift of the baseline at higher wavenumbers in the Raman spectra is indicative of photoluminescence.

- The influence of laser power density on the microstructure of the sample is investigated for possible laser annealing.

2.2.5 Electron Microscopy

Microstructural analyses were done using High Resolution Transmission Electron Microscope (HR-TEM) and Energy-Filtered Transmission Electron Microscope (EF-TEM)[1]. The principle and working of these instruments are as detailed below and the schematic diagram is shown in figure 2.14.

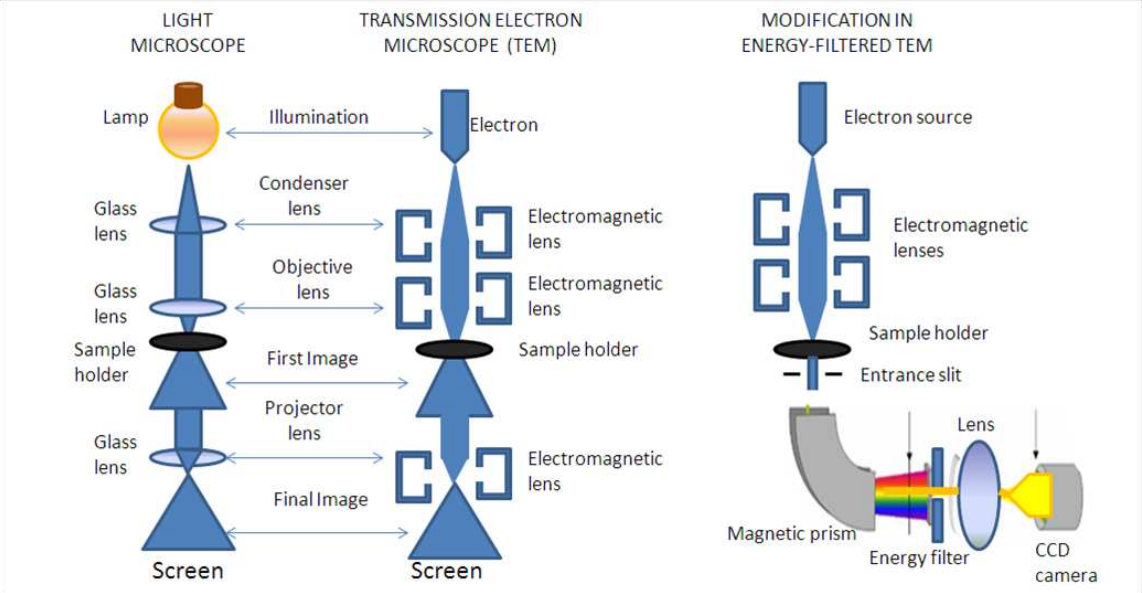

Figure 2.14: Schematic representation of light microscope, transmission electron microscope (TEM) and energy filtered TEM (EFTEM).

High Resolution Transmission Electron Microscope

Principle

Transmission electron microscopy (TEM) technique is the most powerful one to investigate at the nanometer scale the structural properties of nanocrystals. It works on the same principle of a light microscope (optical microscope), the only difference being the utilization of electrons instead of photons. TEMs use electrons as 'light source' and their much lower wavelength makes it possible to obtain resolutions that are a thousand times better than with a light microscope.

[1] All the HRTEM observations were made by Prof X. Portier (CIMAP) and EFTEM observations by Dr. M. Carrada, CEMES, Toulouse, France.

Experimental set-up and working

An electron beam, is produced by thermionic emission from a LaB_6 crystal or from a tungsten filament on application of current, and a potential difference generated extracts the electrons. Electrons can also be produced using a field emission gun with a tungsten tip when subjected to intense electric field. This electron beam propagates in vacuum to illuminate the sample to be analyzed. In our laboratory JEOL 2010F set-up, the latter method is used. Instead of glass lenses focusing the light in the light microscope, the TEM uses electromagnetic lenses to focus the electrons into a very thin beam. The electron beam then interacts while travelling through the sample. Depending on the density of the material present, some of the electrons are scattered and disappear from the beam. At the bottom of the microscope the unscattered electrons hit a fluorescent screen, which gives rise to a 'shadow image' of the sample with its different parts displayed in varied darkness according to their density. The image is then captured with a CCD camera for analysis. It is possible to observe either the image area exposed under the electron beam (image mode) or its associated diffraction pattern (diffraction mode). The diffraction pattern also gives information on the orientation of the substrate during the observation. In Image mode, two types of contrast can be viewed. A diaphragm placed in the focal plane of the objective lens is used to select the electrons diffracted in a particular direction and this image is called dark field. The image from transmitted beam, is known as the bright field image.

Informations extracted in this thesis

- The crystallization and size of the Si-nps can be visualised.
- The total thickness of the sample, and individual sublayer thickness in a multilayer can be obtained.

Energy Filtered Transmission Electron Microscope

Principle

Imaging Si nanoparticles in a SiO_2 (or Si_3N_4) matrix by "traditional" TEM is not straightforward. Si nanocrystals exhibit only weak amplitude and phase contrast because of the small differences in atomic number and density between Si and SiO_2. For this reason, it is impossible to image individual Si-nps by conventional TEM (defocused bright field or Fresnel contrast) as it is usually done for example for Ge-nps in SiO_2. In the case of crystalline particles HR-TEM or dark field (DF) imaging can

be used. In both these cases the images are orientation dependent, consequently only a fraction of the particles in the observed zone can be imaged at the same time. Moreover, the nanocrystal sizes determined by HR-TEM are generally underestimated, small nanocrystals have lower probability to be seen than big ones, and this probability is dependent on the observed region thickness. Energy-Filtered Transmission-Electron Microscopy (EFTEM) is the most appropriate technique to image Si-nps in a silica matrix, independently from their amorphous or crystalized state, and from their orientation. Hence EFTEM allows accurate measuring of the nanoparticles sizes and densities. EFTEM is an imaging technique based on electron energy loss spectroscopy (EELS). In this case the imaging is a sort of chemical mapping of the observed zone: instead of using differences in the atomic number and density, the differentiation between Si and SiO_2 is obtained by a difference in their electronic properties, i.e. their plasmon energies. The plasmons (collective oscillations of valence electrons) signature is observed in the low-energy-loss domain of the EELS. For Si and SiO_2 the plasmon energies are different and can be easily distinguished: their values are 16.7 and 22.5 eV, respectively. EFTEM consists in directly forming the image of the area of interest with electrons which have suffered the Si plasmon energy loss.

Experimental set-up and working

EFTEM was carried out at CEMES Toulouse on a cross-sectional specimens using a field emission TEM, FEI Tecnai™ F20 microscope operating at 200 kV, equipped with a corrector for spherical aberration and a TRIDIEM Gatan Imaging Filter (GIF). The EFTEM images are formed with the electrons that are selected by a slit placed in the energy-dispersive plane of the spectrometer with a width of 4 eV centred at an energy position of 17 eV (Si-plasmon energy). On these images, the accuracy is equal to +/−0.5 nm for ncs size, and 30% for ncs density.

The EF-TEM study was carried out on selective SRSO/SRSN MLs to witness the presence of amorphous Si-np and estimate their density. The EFTEM images were obtained by inserting an energy-selecting slit at the Si (17 eV) and at the SiO_2 (23 eV) plasmon energy, with a width of ± 2 eV.

Informations extracted in this thesis

- Even the amorphous clusters are witnessed in EF-TEM images. Therefore Si nanoparticle density can be extracted from the EF-TEM image by considering the good observed volume using the thickness maps associated with every image if the nanoparticles are separated.

- The presence of Si from SiO_2 or silicon nitride can be distinguished.

2.2.6 Atom Probe Tomography

Priniciple

Atom probe tomography (APT) is a powerful 3D chemical microscope whose principle relies on the field evaporation of the surface atoms from the specimen prepared in the form of a sharp tip, and their identification by time-of-flight mass spectrometry. Surface atoms are evaporated using electric pulses V_p added to the DC voltage V_0 and are collected on a position sensitive detector. The time of flight of each evaporated ion between the electric pulse and the impact on the detector is measured. This measurement permits to calculate the mass to charge ratio:

$$\frac{m}{n} = \frac{2EL^2}{t^2}(V_o + V_p) \qquad \text{Eqn (2.8)}$$

where m is the mass of the evaporated ion (in kg), n its electronic charge, L the distance between the tip and the detector (in m) and t the time of flight of the ion (in s). This calculation permits to identify the chemical nature of evaporated ions.

Experimental set-up and working

APT analyses were carried out at Groupe de Physique des Matèriaux, Université et INSA de Rouen on a Laser Assisted Wide-Angle Tomographic Atom Probe (LAWATAP). The radius of curvature of the sharp tip specimen must be smaller than 50 nm in order to create a high electric field. This is carried out with a focused ion beam (FIB) instrument. The Ga^+ ion beam is able to etch samples and nanoscaled structures can be extracted from bulk materials. In order to prevent any Ga ions implantation or sample degradation, a sacrificial platinum layer is deposited before every milling step (approximately 400 nm). This deposition is realized directly in the FIB instrument using the gas injection system. The three step method which is commonly used to obtain a tip from the chunk state is illustrated figure 2.15.

The first step consists of etching a thin lamella of 2-4 μm of the sample (Fig. 2.15a). Successive milling operations are operated on the chunk in order to extract posts. The second step consists in micromanipulating and mounting extracted posts on the top of a stainless steel needle using a Pt weld (Fig. 2.15b). During the final step, the post is submitted to an annular milling. The post is located along the axis of the ion beam which due to annular motion successively cut concentric circles of the sample. By reducing the diameter of these circles, the post is thickened into a sharp tip with a curvature radius lower than 50 nm (Fig. 2.15c-e). To prevent ion

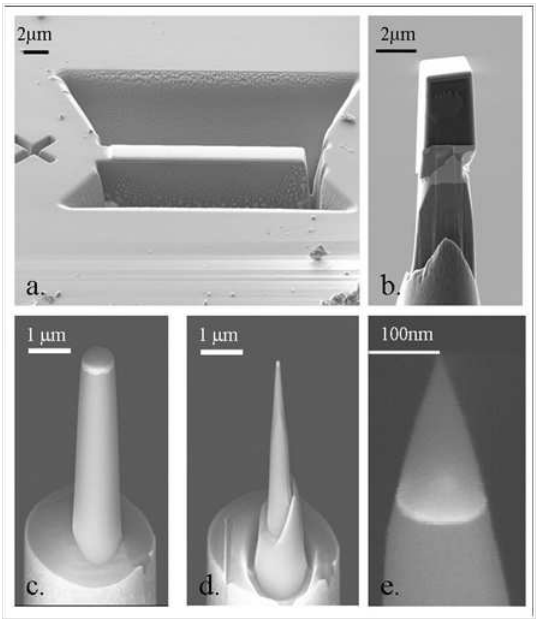

Figure 2.15: (a). Extraction of a silicon post using the Lift-out method. The sample has been milled with the help of a FIB in order to extract a strip of material. (b). The strip is shaped in a post and welded onto a steel needle (platinum weld). (c-e). Successive annular milling steps permit to obtain a very sharp tip which curvature radius does not exceed 50nm. (Images from M. Roussel, GPM Rouen)

beam damage and Ga implantation in our SRSO/SiO_2 layers, the final milling is performed at a low accelerating voltage (2 kV).

The specimen is placed under high vacuum (≈10-13 Bar), at low temperature (80°K), and at a high positive voltage ($V_0 \approx$ 5-15 kV. Therefore, an intense electric field is created at the apex of the tip (several $V.nm^{-1}$). Instead of electric pulses the ionization and the field evaporation of the surface atoms are triggered by the superposition UV (343 nm) femtosecond laser pulses (50 nJ, 350 fs, 100 kHz).

Informations extracted in this thesis

- Using some geometrical arguments and knowing the position of the impact of an ion on the detector permits to calculate its position on the specimen, before the evaporation. These data enable the 3D reconstruction of the sample at the atomic scale. Therefore the formation and location of Si-np is known

- The density of Si-np is estimated.

2.2.7 Spectroscopic Ellipsometry

Principle

Ellipsometry is a non-destructive optical technique used to analyze the dielectric properties of a material, such as the complex refractive index ($\widetilde{n} = n - ik$), and thickness. This technique is applicable to thin films with thicknesses ranging between few nanometers to about 50µm, depending upon which the accuracy differs.

The electric field E of the incident light is resolved into two components, one parallel to the incident plane and the other perpendicular, denoted as E_{ip} and E_{is} respectively. Similarly the reflected light components are represented as E_{rp} and E_{sp}. These components of the incident and reflected light are related using Fresnel's reflection coefficients expressed as,

$$r_p = E_{rp}/E_{ip} \; ; \; r_s = E_{rs}/E_{is} \qquad \text{Eqn (2.9)}$$

The ratio (ρ) of these reflection coefficients is conventionally written in the following form,

$$\rho = r_p/r_s = \tan \Psi . \exp (i\Delta) \qquad \text{Eqn (2.10)}$$

This ratio is a complex number which can be expressed using the ellipsometric angles Ψ and Δ that decribes the amplitude component and the phase shift component of the reflection coefficients, respectively. Since the Fresnel coefficients are dependent on multiple variables such as the complex refractive index, thickness, wavelength and angle of incidence, from an analysis of the ellipsometric spectra the optical constants of the dielectric sample under study can be obtained.

Experimental set-up and working

The reflection coefficients are recorded using a Jobin-Yvon ellipsometer (UVISEL). The ellipsometry set-up (Fig. 2.16) consists of,

- an unpolarized light source with a broad spectral range (Xenon lamp)
- a polarizer
- a phase modulator which dephases the parallel and perpendicular components of the electric field
- the sample holder
- an analyzer and a detector consisting of a monochromator and a photomultiplier tube.

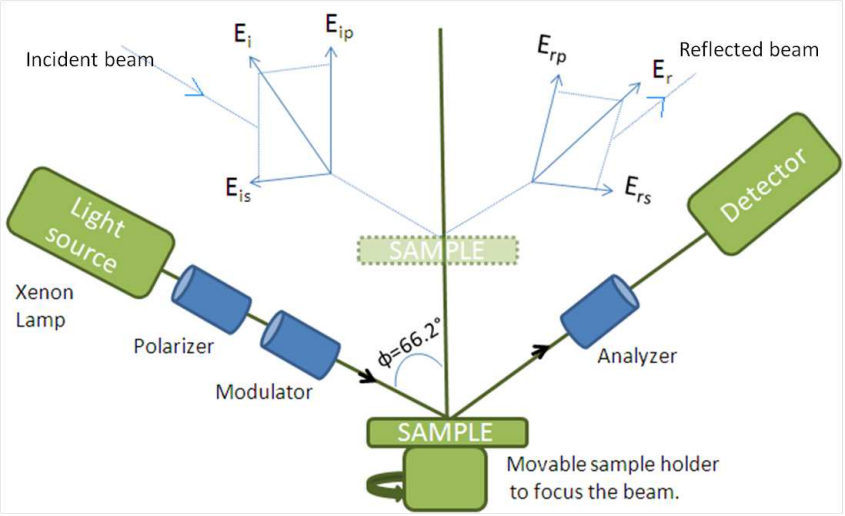

Figure 2.16: Schematic diagram of principle and experimental set-up of an ellipsometer.

The measurements were done at an angle of incidence Φ fixed at 66.2°, between 1.5-4.5 eV with a resolution of 0.01 eV. The unpolarized incident light is linearly polarized when it passes through the polarizer operated at a fixed angle of 45°. A quartz modulator fixed at normal incidence, phase modulates the linearly polarized beam and this beam interacts with the sample (Si substrate with the dielectric layer, in our case). The light after undergoing multiple reflections leave the layer under the same exit angle as the incidence angle and passes through a rotating analyzer operated at 45°. The analyzer measures the reflectance from all the phases and a photodetector records the intensity of this phase modulated light which is a measure of Ψ and Δ. The data acquistion is done for each sample using ELLI42 software provided by the seller, in the measured energy range. The optical parameters of the thin film are obtained by making a model that fits the measured spectra with the theoretical ones. Ellipsometry thus is a non contact method to determine the thickness in contrast to the tedious sample making procedures for microscopic analysis.

Modelling the spectra: Ellipsometry is a model dependent method. The modelling of the samples is done using a DeltaPsi software provided by Jobin Yvon [ellipso 1], which estimates the thickness, the optical constants of the sample etc. A dispersion model of n and k as a function of energy known as the "new amorphous model" derived from the Forouhi-Bloomer model [Forouhi 86] is used so as to fix the initial values of the optical constants: n_∞, ω_j, Γ_j, ω_g and f_j. The phenomenon of dispersion depends upon the complex refractive indices of materials which are a function of various parameters related as follows:

$$n(E)=n_\infty + \frac{B(\omega-\omega_j)+C}{(\omega-\omega_j)^2+\Gamma_j^2} \qquad \text{Eqn (2.11)}$$

$$k(E) = \frac{f_j(\omega - \omega_g)^2}{(\omega - \omega_j)^2 + \Gamma_j^2} \qquad \text{Eqn (2.12)}$$

$$k(E) = 0 \text{ if } \omega < \omega_j \qquad \text{Eqn (2.13)}$$

where n_∞ is the refractive index of a material when energy tends to infinity, ω is the wave energy in eV, f_j is the fraction of electrons that oscillate at resonant energy strength ω_j, Γ_j is the damping coefficient that gives rise to the phenomena of optical absorption. The constants B and C are given as follows:

$$B = \frac{f_j}{\Gamma_j}\left[\Gamma_j^2 - (\omega - \omega_j)^2\right] \qquad \text{Eqn (2.14)}$$

$$C = 2f_j\Gamma_j(\omega - \omega_j) \qquad \text{Eqn (2.15)}$$

The imaginary part of the refractive index $k(E)$ is also known as the extinction coefficient because it represents absorption or attenuation of an electromagnetic wave. Hence from $k(E)$, the absorption coefficient of the film can be extracted using the relation,

$$\alpha = \frac{4\pi k}{\lambda} = \frac{4\pi k\omega}{hc} \qquad \text{Eqn (2.16)}$$

where h is the Planck's constant and c is the velocity of the light.

Figure 2.17 explains the first two steps involved in modelling an ellipsometric spectra.

The measured (Ψ, Δ) spectra can be visualized in terms of n and k through internal calculations in the software. Therefore a model is built according to our structure under investigation also taking into account the possible surface roughness in the material as shown in Step 1. The parameters involved in the dispersion relation are adjusted to get an approximate shape of dispersion curve that matches with the standard material as shown in Step 2. Following this, a data fitting of the measured spectra with the theoretically obtained spectra is performed. The value of χ^2 is low if the extent of closeness between the two spectra is high. From this fitting, we deduce the optical constants from the new dispersion curve of the sample under investigation. These are represented as Step 3 and Step 4 in figure 2.18. The simulation results also include the thickness of the sample.

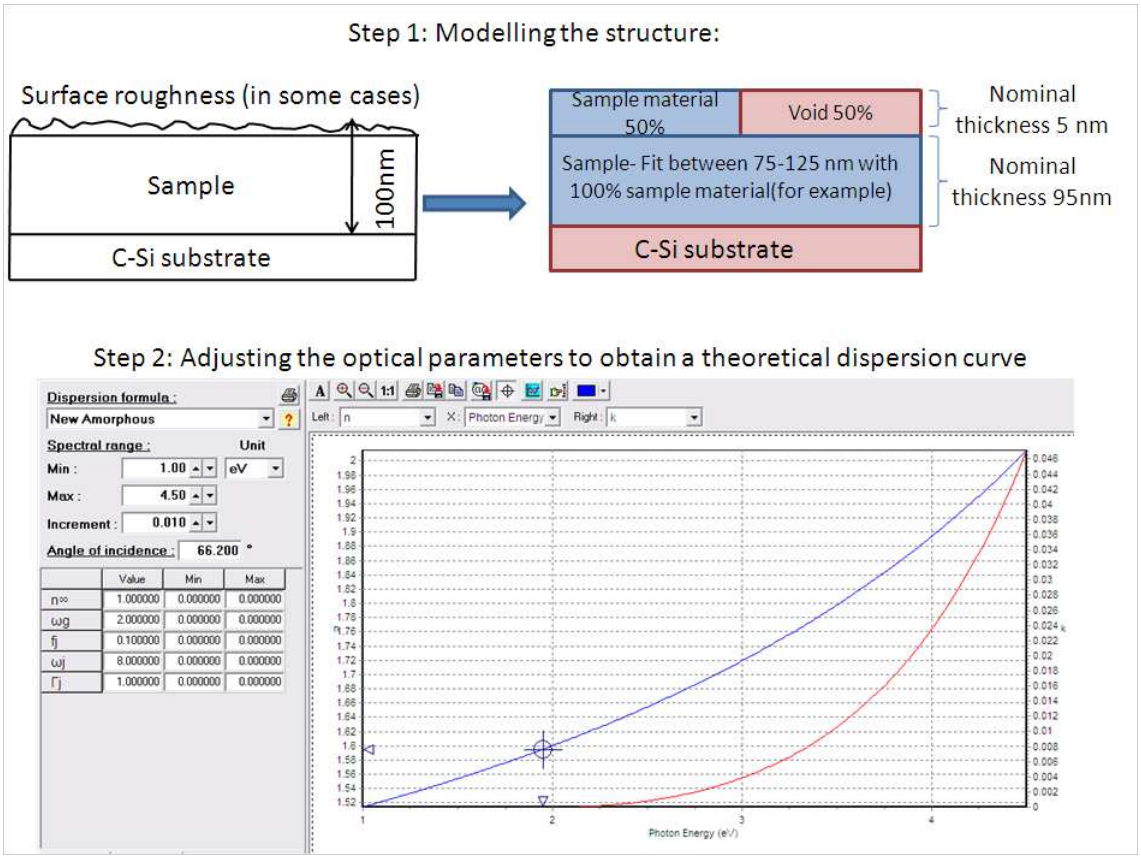

Figure 2.17: Step 1 and 2 of ellipsometry modelling.

Informations extracted in this thesis

- The refractive index of the thin film material is known from which we can estimate the composition of the film in terms of Si excess. Using this refractive index, Si excess in the material can also be evaluated by calculations involving Bruggeman effective medium approximation [Bruggeman 35]. Contrary to the FTIR technique, Bruggeman calculations account for the nucleated Si particles but do not consider the fraction of free unbounded Si atoms or smaller agglomerates.

- The thickness of the sample is determined to a good degree of accuracy (<5%) while modelling the ellipsometry measurements.

- The absorption coefficient of the material is calculated from the complex refractive index of the material from the imaginary part of refractive index (k) of the material.

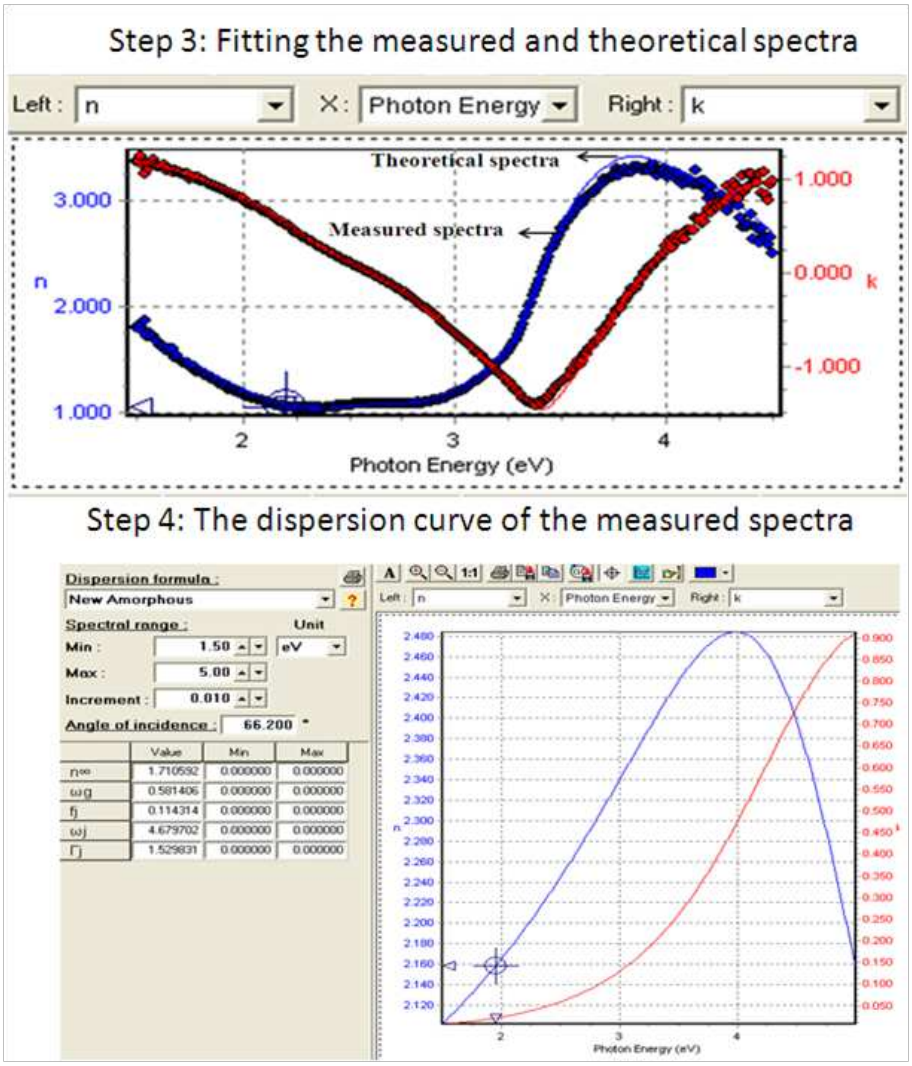

Figure 2.18: Step 3 and Step 4 of ellipsometry modelling.

2.2.8 Photoluminescence Spectroscopy

Principle

Photoluminescence (PL) spectroscopy is a non-destructive method that gives information on the electronic structure of materials. When a sample absorbs the incident photons, it gains excess energy and the electrons in the material get excited to permissible energy states (photo-excitation). When these electrons return to their ground states, the excess energy is released with (a radiative process) or without the emission of light (non-radiative process). The light emitted in a radiative process is called photoluminescence. Figure 2.19 illustrates the processes explained above for an incident light at 488 nm and emission between 700-900 nm range. The radiative transitions in semiconductors may also involve localized levels and defect states in addition to the bandgap transitions. In this case, the PL analysis also leads to the

identification of certain defects and impurities.

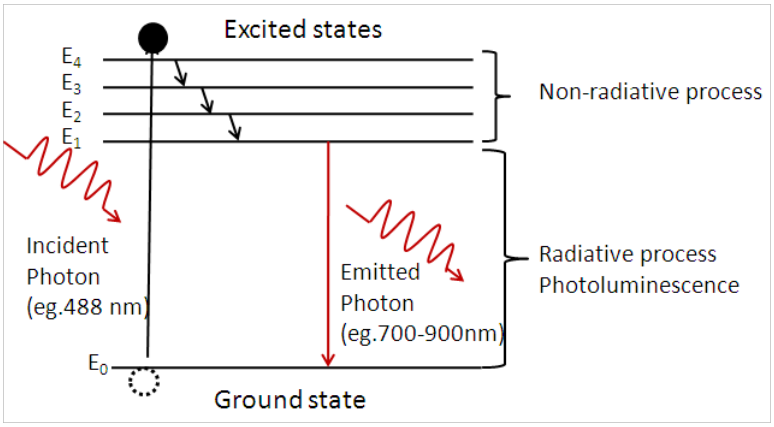

Figure 2.19: Illustration of excitation and de-excitation processes.

Experimental set-up and working

The schematic diagram of PL set-up used in our laboratory is as shown in figure 2.20. The optical excitation is provided by a continuous wave Ar laser source (Argon INNOVA CW 90C) operated at 488nm. The laser beam passes through a chopper (Thorlabs MC1000A) set for a chosen frequency (73 Hz). The lock in amplifier (SR830) is referenced to the chopper frequency. The laser beam is focussed on the sample at an angle of 45° using appropriate optical lenses. A part of the light emitted by the sample is collected through another set of lenses and is focussed on the entrance slit of the monochromator (TRIAX 180 HORIBA Jobin Yvon). The monochromator disperses the light emitted from the sample and reflects towards the exit slit. A photomultiplier tube (PM Vis PL R5108 HAMAMATSU) placed at the exit slit of the monochromator detects the dispersed light. An amplifier (AMPLI FEMTO DHPCA-100, DC-200 MHz) amplifies the detected signal and converts it into voltage. The signal consisting of all the detected frequencies is fed into the lock-in amplifier which selects signal at the reference frequency and filter other frequencies (room lighting electrical signal at 50 Hz). All the systems are LABVIEW interfaced. The power of the laser beam at the film surface was measured using a power meter from LOT-ORIEL.

All the PL spectra are standardized to a common reference sample, and corrected to spectral response of the PL set-up. The spectra before and after correcting to spectral response is as shown in figure 2.21.

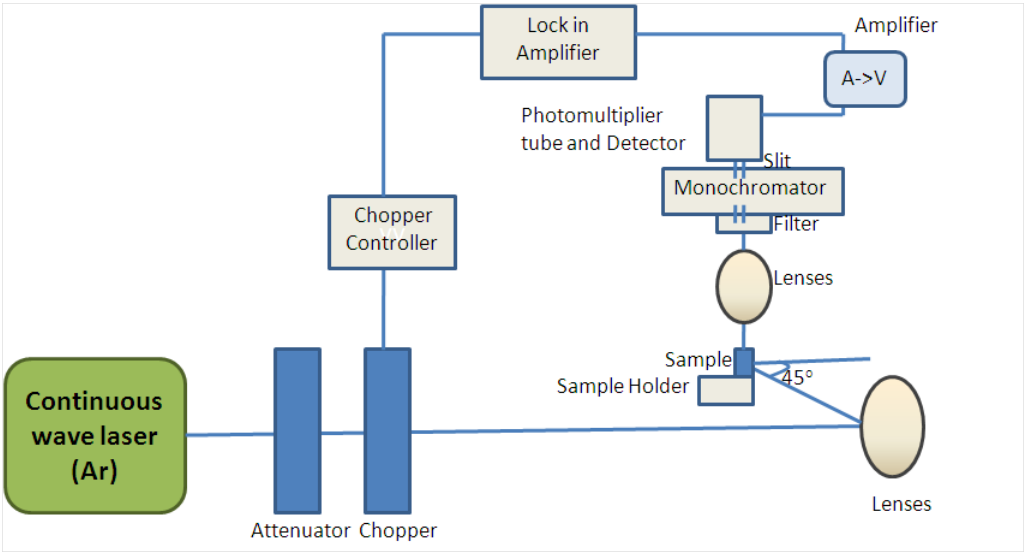

Figure 2.20: Schematic diagram of the photoluminescence experimental set-up.

Informations extracted in this thesis

- The information on the presence of Si-nps and radiative defects can be obtained from the position and shape of the luminescence peak.
- The shift of the PL peak position with varying deposition parameters yield information on the size of Si-nps
- The shape and the intensity of the PL spectra can be used to extract the informations such as the effect with annealing temperature, the sample thickness and interference phenomena especially in multilayers.

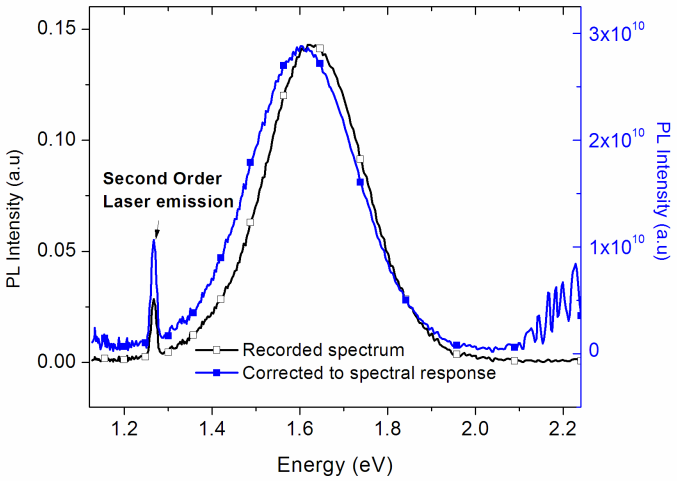

Figure 2.21: PL spectra before and after correcting to spectral response.$\lambda_{excitation} = 488$ nm.

Chapter 3

A study on RF sputtered SRSO monolayers and SRSO/SiO_2 multilayers

3.1 Introduction

One of the major aims of this thesis, as mentioned in chapter 1, is to increase the density of Si-nanoparticles (Si-np) with regard to the team's earlier obtained value of 9 x10^{18} np/cm^3 [Maestre 10]. Optimizing the growth parameters of SRSO[1] is an important step towards accomplishing this increase of density. Prior works on SRSO grown either by co-sputtering of SiO_2 target topped with Si chips placed at the target surface [Charvet 99] or by reactive sputtering [Ternon 02] have been done in our laboratory, using another RF magnetron sputtering unit 'MECA 2000'. With the sputtering unit AJA International used in this thesis, initial studies were performed with the values of plasma pressure controlled with butterfly valve, substrate-target distance and the substrate rotation speed of 3 mTorr, 38 cm and 20 rpm respectively. These values were confirmed by [Hijazi 09b] while studying SRSO: Er materials in which SRSO was grown by the co-sputtering of SiO_2 and Si. Hence these values have been adopted for all our depositions. Three methods using confocal sputtering technique are developed in our team to introduce excess Si to form SRSO. The first two methods are the same as those used by Ternon, (Reactive sputtering which will be investigated in AJA now) and Hijazi (co-sputtering) for their thesis in the references cited above. The third method, 'Reactive co-sputtering' is a newly introduced concept in this thesis, combining the advantages of the two other aforesaid methods. The SRSO monolayers grown using these three methods are studied with respect to deposition rate r_d, refractive index n and structural composition. Optimized

[1]SRSO will be occasionally denoted as SiO_x in the text

samples are investigated for their emitting and absorbing behaviours. The growth conditions of SRSO layers that exhibit desirable properties are extended for fabricating the SRSO/SiO_2 Multilayer structures (MLs). The effect of sublayer thicknesses on the structure and Si-np formation is analyzed. In addition, the influence of total thickness, sublayer thickness and Si excess on the emission properties of the MLs are investigated.

3.2 Reactive sputtering - Method 1

3.2.1 Effect of deposition temperature

SRSO samples were grown by sputtering the SiO_2 target reactively with hydrogen at four different deposition temperatures, T_d ranging between 200°C-500°C. As mentioned in chapter 2, the power density applied on SiO_2 target was fixed at 7.4 W/cm^2. As previously mentioned, the hydrogen rate is given by,

$$r_H = \frac{P_{H_2}}{(P_{H_2} + P_{Ar})} \qquad \text{Eqn (3.1)}$$

where $(P_{H_2} + P_{Ar})$ is the total pressure in the plasma. The total gas flow f_{tot} in the plasma was fixed to be 10 sccm (i.e.) Ar = 5 sccm and H_2 = 5 sccm. The respective partial pressures are P_{Ar} = 8.1 mTorr and P_{H_2} = 2.9 mTorr. Therefore, from equation 3.1, we obtain $r_H = 26\%$ which is the value used for the growth of SRSO samples discussed in section 3.2.1.

(a) Deposition rate (r_d) and Refractive Index ($n_{1.95eV}$)

The effect of T_d on averaged deposition rate (r_d) is represented in figure 3.1a. The thicknesses of the as-grown samples are estimated by ellipsometry from which r_d (nm/s) is deduced. The time of deposition was fixed by trial and error method to obtain approximately the same thicknesses (of about 300 nm) for comparison. The inset in figure 3.1a shows the thicknesses of the samples and the time required to grow such thicknesses at each T_d. The r_d decreases with increasing T_d and becomes the lowest at 500°C.

The refractive index at different energies are estimated from ellipsometry measurements; n at 1.95 eV is chosen for representation (Fig. 3.1b). The variation of refractive index with T_d shows an opposite trend as compared to r_d. It can be seen that $n_{1.95eV}$ steadily increases with T_d and reaches the highest at 500°C.

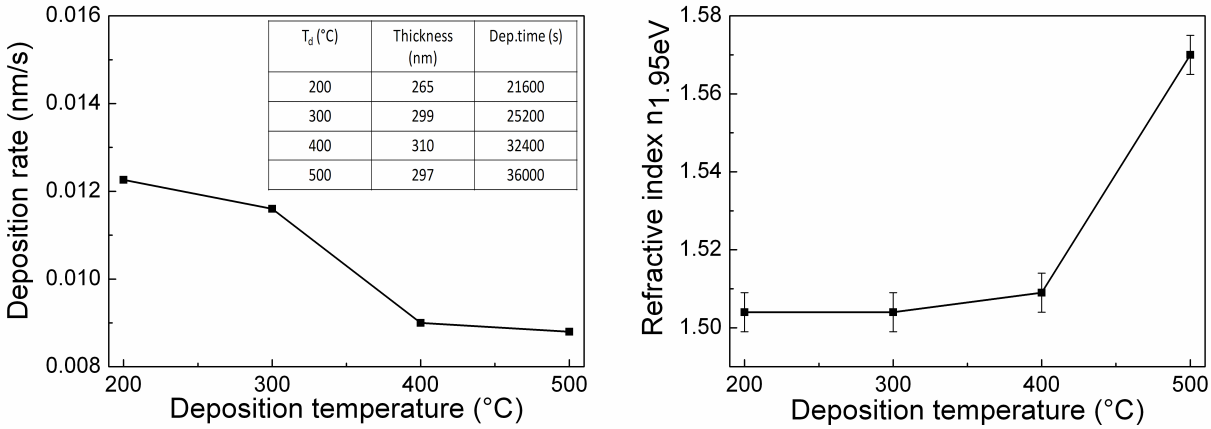

T_d (°C)	Thickness (nm)	Dep.time (s)
200	265	21600
300	299	25200
400	310	32400
500	297	36000

(a) Deposition rate. **(b)** Refractive index.

Figure 3.1: Effect of deposition temperature on (a) Deposition rate (r_d) nm/s and (b) Refractive index ($n_{1.95eV}$).

(b) Fourier transform infrared spectroscopy

The structural changes in the SRSO films with respect to T_d are studied using FTIR spectroscopy between 700-1400 cm^{-1}. Figures 3.2a and 3.2b show the FTIR spectra of the as-grown samples, recorded at Brewster (65°) and normal incidences respectively. The TO_3 peak maximum is normalized to unity which helps in visualizing the frequency shift, υ (cm^{-1}) of the TO_3 peak and the evolution of LO_3 peak relative intensity with T_d. The insets in figure 3.2a show a zoomed view of the variations in hydrogen related peaks, and the LO_3 peak intensity with T_d.

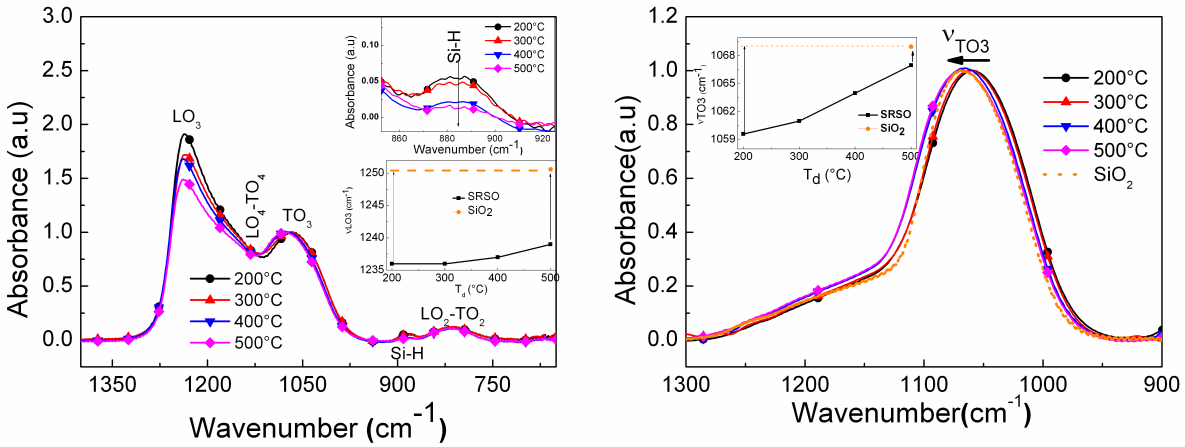

(a) Brewster incidence. **(b)** Normal incidence.

Figure 3.2: FTIR spectra - Effect of deposition temperature (T_d) on the SRSO film structure.

With increasing T_d, there is a progressive decrease in the LO_3 peak intensity. As seen from the insets, with increasing T_d, the Si-H peak decreases in intensity and the LO_3 peak position (ν_{LO_3}) shifts towards higher wavenumbers approaching the ν_{LO_3} of SiO_2. There is a similar shift in the TO_3 peak position (ν_{TO_3}) towards higher wavenumbers as can be seen from the normal incidence spectra. The inset in figure 3.2b clearly shows this variation in TO_3 peak positions. These results indicate that the sample becomes more ordered and the SiO_x matrix gradually shifts towards SiO_2 with increasing T_d.

(c) Si excess estimation

c1) From FTIR analysis

The phase separation of SiO_x into SiO_2 and Si particles can be initiated during the deposition process, or post-annealing treatment. This is represented by the following equation:

$$SiO_x = \left(\frac{x}{2}\right) SiO_2 + \left(1 - \frac{x}{2}\right) Si \qquad \text{Eqn (3.2)}$$

The value $x\,[= O/Si]$ is calculated using υ_{TO3} obtained in the FTIR spectra, from which the atomic percentage of Si excess is estimated using the formulae specified in section 2.2.1 of chapter 2.

c2) From Refractive index and Bruggeman model

The Si excess and the value of x can also be estimated from the values of refractive index obtained from ellipsometry using Bruggeman model (effective medium approximation-[Bruggeman 35]). In our case of SiO_x materials, the effective dielectric function (ε_e) is a combination of the dielectric functions of Si and SiO_2. The Bruggeman model gives a relationship of the effective medium as a volumic fraction of two different materials as follows:

$$f_1\left(\frac{\epsilon_{Si} - \epsilon_e}{\epsilon_{Si} + 2\epsilon_e}\right) + f_2\left(\frac{\epsilon_{SiO_2} - \epsilon_e}{\epsilon_{SiO_2} + 2\epsilon_e}\right) = 0 \qquad \text{Eqn (3.3)}$$

where,

$\epsilon_e = n_e^2$ is the relative permittivity of the effective medium

ϵ_{Si} and ϵ_{SiO_2} are the relative permittivity of Si and SiO_2 respectively, and f_{Si} and f_{SiO_2} their volumic fractions.

Thus, by knowing the refractive index from ellipsometry, concentration and the volumic fractions of the chemical species, the atomic percentage of excess Si can be estimated. The concentration of an element in a material can be estimated from the density d, molar mass M, and Avogadro number N. This leads to the following expressions, which result in the values indicated in table 3.2:

$$[Si]_{Si} = \{d_{Si}/M_{Si}\}\, N \qquad \text{Eqn (3.4)}$$

$$[Si]_{SiO_2} = \{d_{SiO_2}/M_{SiO_2}\}\, N \qquad \text{Eqn (3.5)}$$

$$[O]_{SiO_2} = 2\,\{d_{SiO_2}/M_{SiO_2}\}\, N \qquad \text{Eqn (3.6)}$$

Element x	Matrix y	Density d ($g.cm^{-3}$)	Molar Mass M (g)	$[x]_y (cm^{-3})$
Si	Si	2.33	28.09	$4.5\ 10^{22}$
Si	SiO_2	2.20	60.09	$2.18\ 10^{22}$
O	SiO_2	2.20	60.09	$4.35\ 10^{22}$

Table 3.1: Estimation of atomic concentration.

The concentration of Si and O in SiO_x are given respectively by

$$[Si]_{SiO_x} = f_{Si}\,[Si]_{Si} + f_{SiO_2}\,[Si]_{SiO_2} \text{ and } [O]_{SiO_x} = f_{SiO_2}[O]_{SiO_2} \qquad \text{Eqn (3.7)}$$

From equation 3.7, the Si excess (at.%) can be deduced by using the following equation:

$$\text{Si excess} = \frac{[f_{Si}\,[Si]_{Si}]}{\left[f_{Si}\,[Si]_{Si} + f_{SiO_2}\,[Si]_{SiO_2} + f_{SiO_2}\,[O]_{SiO_2}\right]} \qquad \text{Eqn (3.8)}$$

The values of n_{SiO_2} and n_{Si} used for estimating the Si excess are 1.457 and 4.498 respectively.

The values of Si excess (at.%) of the unbonded Si obtained from the FTIR analysis and of agglomerated Si estimated from refractive index obtained by ellipsometry using equation 3.8 (Bruggeman method) are given in table 3.2.

The results indicate that T_d influences the structural and compositional properties of the SRSO layer. The decrease of Si excess from FTIR analyses and its increase if deduced from equation 3.8, indicate the formation of Si-np with increasing T_d.

T_d(°C)	ν_{TO3}	$x = 0/Si$ from FTIR	Si excess (at.%) from FTIR (unbonded Si)	$x = 0/Si$ from ellip-sometry	Si excess (at. %) from ellipsometry (agglomerated Si)
200	1059.6	1.77	4.15	1.92	2.15
300	1061	1.79	3.8	1.92	2.15
400	1064	1.82	3.15	1.91	2.37
500	1067	1.86	2.539	1.76	4.98

Table 3.2: Si excess estimation by FTIR and refractive index (Bruggeman method- analysis with regard to T_d.

(d) Growth mechanism

It has been reported that r_d increases with increasing T_d [Gates 89, Kaiser 98]. Our results indicate a steadily decreasing r_d which can be related to a continuous increase in the etch rates. But, $n_{1.95eV}$ increases linearly with T_d indicating an increase in the Si content. This necessitates an understanding of the temperature dependent growth mechanism. The following mechanism is proposed based on the kinetic theory of gases and temperature dependence of SiH_x etch products. A diagrammatic representation of the proposed explanations are shown in figure 3.3.

According to classical mechanics, the kinetic energy is a function of the particle mass (m) and velocity (v) expressed as,

$$E_k = (1/2)mv^2 \backsimeq (3/2)kT \qquad \text{Eqn. (3.9)}$$

where $(3/2)kT$ is the averaged kinetic energy of a classical ideal gas per degree of freedom related to temperature T, and k is the Boltzmann constant. Considering our sputter gases, Ar is monoatomic having three degrees of freedom and hydrogen being a diatomic gas has 6 degrees of freedom.

It can be seen from equation 3.9 that an increase in temperature increases the average kinetic energy and therefore the velocity of the species in the sputter chamber. When the substrate is heated, it cannot be denied that a certain amount of energy is introduced in the plasma leading to the plasma temperature. Thus it can be said that with increasing T_d, $E_{k(avg)}$ and velocity of species in the plasma increases leading to an enhancement in the kinetics of sputtering process. Moreover, in a mixture of particles with different masses, the heavier atom will have a lower velocity than the lighter one but have the same average kinetic energy. Hence, at a given T_d hydrogen having the lowest mass acquires the greatest velocity.

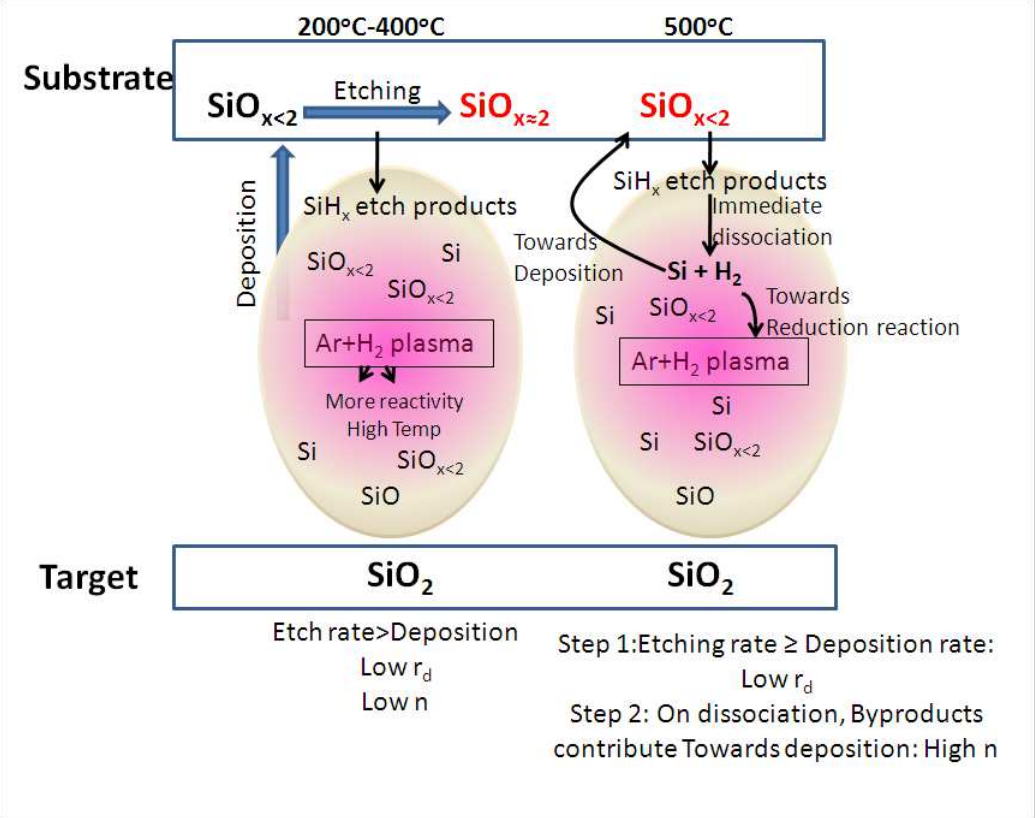

Figure 3.3: Proposed mechanism of temperature dependent reactive sputtering.

As a consequence of an increase in hydrogen velocity with increasing T_d as compared to other species, Si deposition is favoured. This is attributed to the increased reaction of hydrogen in reducing the sputtered oxygen species which move towards the substrate at a lower velocity. This explains the continuous rise in the $n_{1.95eV}$ as the Si content in SRSO layer increases with T_d. The role of hydrogen is not restricted to deposition, but also towards an etching mechanism since the weak and strained Si-Si bonds are broken leading to removal of Si atoms from the surface [Tsai 89, Akasaka 95]. Hence, with increased velocity, it is also probable that hydrogen reaches the film growing surface faster than the other Si or O atoms thereby forming Si-H bonds faster than Si-Si bonds. This leads to a continuous etching process resulting in a decreased r_d. Thus, the competing etching mechanism seems to be predominant at T_d ranging between 200°C to 400°C.

At elevated temperatures, between $T_d = 425$°C to 600°C, in addition to the process described above, the temperature allows the formation of Si-Si bonds since hydrogen from Si-H dissociates into Si and H_2 [Veprek 79]. This explains the decrease of r_d and concomitant increase of refractive index.

Increasing time and temperature of deposition facilitates the reorganization of the Si-Si bond into a network which could also lead to the agglomeration of few

Si-np. This phase separation process into Si agglomerates and SiO_2 is witnessed from v_{TO_3} and decreased intensity of $LO_4{-}TO_4$ peak in the FTIR spectra. This also explains the decrease of Si excess estimated by FTIR method in table 3.2.

We may also assume that with increasing T_d there is an increase in size of the Si agglomerates favoured by higher Si content and longer diffusion time. This could explain the progressive decrease in the LO_3 peak intensity which reflects the Si-SiO_2 interfaces since with increasing sizes, the number of the agglomerates and therefore the number of interfaces may decrease.

Since the decrease in LO_3 peak intensity indicates a lower total interface area at higher T_d and consequently a lower number of Si-agglomerates, we may write the following equation,

$$N_h S_h < N_l S_l \Rightarrow N_h(4\pi {R_h}^2) < N_l(4\pi {R_l}^2) \qquad \text{Eqn (3.10)}$$

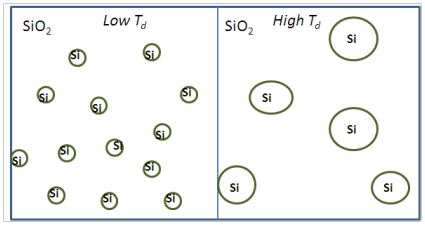

Figure 3.4: Illustration of SRSO layer at low and high T_d.

where N_h and N_l represent the number of agglomerates at the highest and lowest T_d, S_h and S_l their surface area and V_h and V_l their volumes.

Due to increase in sizes as well as refractive index at high T_d, the volumic fraction increases and can be expressed by,

$$N_l V_l < N_h V_h \Rightarrow N_l((4/3)\pi {R_l}^3) < N_h((4/3)\pi {R_h}^3) \qquad \text{Eqn (3.11)}$$

Thus, from Eqn. (3.10) & (3.11), we deduce,

$$\frac{R_l^3}{R_h^3} < \frac{N_h}{N_l} < \frac{R_l^2}{R_h^2} < 1 \qquad \text{Eqn (3.12)}$$

Equation 3.12 indicates that the radius of Si-np is lower at low T_d. This indicates that there is a high number of small Si-agglomerates and a few large Si-agglomerates in samples grown at low and high T_d respectively as illustrated in figure 3.4.

From the results obtained above, T_d=500°C is chosen for all the forthcoming investigations due to the high refractive index, Si excess and structural ordering favoured at this temperature.

P_{Ar}(mTorr)	P_{H_2}(mTorr)	r_H(%)
14.4	0.7	4.6%
10.5	1.4	11.7%
8.1	2.9	26%
4	5.3	57%

Table 3.3: Conditions used to obtain hydrogen-rich plasma.

3.2.2 Effect of hydrogen gas rate (r_H)

Four layers of SRSO with varying r_H were grown at T_d= 500°C. Table 3.3 shows the values of partial pressures of Ar and H_2 and the corresponding r_H.

Since the hydrogen in the plasma leads to two competing phenomena as described above, it becomes important to see how the hydrogen rate in the plasma influences the compositional and structural properties of SRSO layers.

(a) Deposition rate (r_d) and Refractive Index ($n_{1.95eV}$)

The evolution of r_d and $n_{1.95eV}$ with respect to r_H introduced into the plasma are shown in figure 3.5. It can be seen that there is a steady decrease in r_d with increase in r_H from 4.6% to 57%. On the contrary, $n_{1.95eV}$ value increases with increasing r_H.

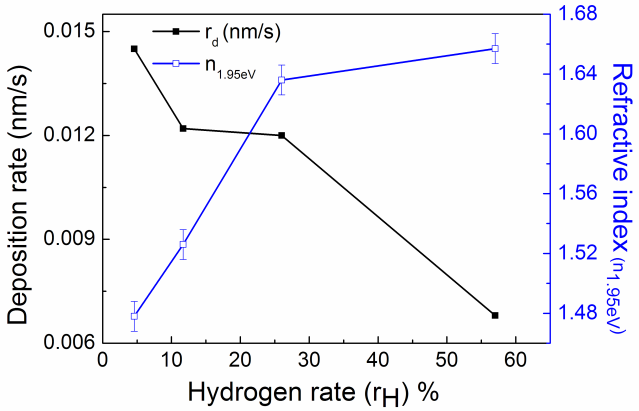

Figure 3.5: Effect of r_H% on the deposition rate (r_d) nm/s (left axis)and refractive index, $n_{1.95eV}$(right axis).

When hydrogen is introduced in the plasma,

- the Si-Si bonds are broken leading to the removal of Si atoms from the surface [Tsai 89, Drévillion 93, Akasaka 95]. This selective etching leads to a decrease in r_d on increasing r_H from 4.6%-57%.

- the hydrogen reacts with the oxygen species in the plasma which are sputtered from SiO_2 target, leading to the growth of a Si-rich suboxide at the substrate. Consequently, $n_{1.95eV}$ increases with r_H.

(b) Fourier transform infrared spectroscopy

Figure 3.6 shows the FTIR spectra of the as-grown SRSO samples with varying r_H in Brewster incidence and in the inset, the normal incidence spectra. The TO_3 peak is normalized to unity as in the previous analysis. The variation of LO_3 and TO_3 peak positions with regard to r_H are also shown in the inset.

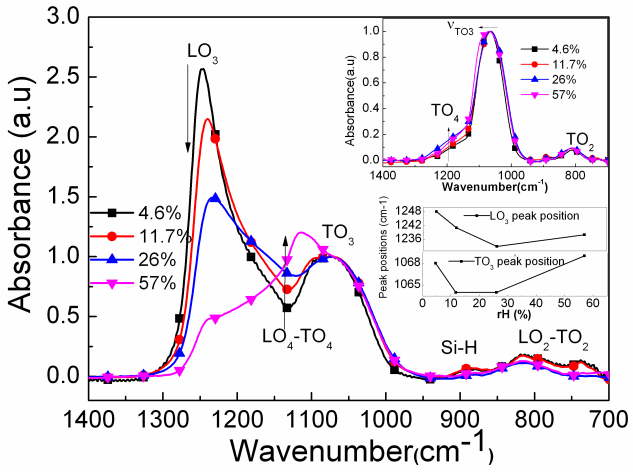

Figure 3.6: FTIR spectra - Effect of hydrogen rate on the SRSO film structure.

It can be seen from the Brewster incidence spectra that the LO_3 peak intensity decreases with increasing r_H. At $r_H = 57\%$, the LO_3 peak becomes the least intense, and a peak around 1107 cm^{-1} is observed. We also notice an increase in disorder with r_H from the increasing intensity of LO_4-TO_4 in Brewtser incidence spectra and TO_4 peak in normal incidence spectra. Traces of Si-H are seen in all the samples from the Brewster incidence spectra.

The decreasing LO_3 intensity can be attributed to the increase in Si excess and therefore agglomeration of Si-np leading to lower number of interfaces as discussed in previous section. The increase in Si excess with r_H also leads to an increase in structural disorder thereby enhancing the disorder induced modes. Similar effect with increasing Si excess by increasing RF power density on the target has been observed in our earlier reports [Hijazi 09a]. The huge decrease of LO_3 intensity and a higher enhancement of the LO_4-TO_4 mode due to Si excess may be a possible reason for the appearance of the peak around 1107 cm^{-1}. This peak position has also been reported as interstitial oxygen in Si substrates [Kaiser 56, Borghesi 91, Veve 96] and at Si/SiO_2 interfaces [Niu 07]. It has been proposed that interstitial oxygen in Si may have a structure similar to fused silica with Si-O-Si bond angle 100° which would result in a TO_{Si-O} stretching vibration around 1107 cm^{-1} [Kaiser 56] and

such a peak was witnessed in [Quiroga 09]. Therefore it may be supposed in our case, that while forming agglomerates oxygen may be trapped within the Si core resulting in such a peak. However, at this stage it is not possible to say certainly if the appearance of this peak with Si excess is due to an increase in disorder or formation of oxygen trapped Si agglomerates.

It can be seen from the inset of figure 3.6 that both LO_3 and TO_3 peak positions shift towards lower wavenumbers with increasing r_H except for the highest hydrogen rate. The shift towards lower wavenumbers with increasing Si excess till r_H=26% may be explained with the force constant model. As the Si content increases, the bond angle of Si-O-Si decreases from 180° as per force constant model (Eqn. 3.13) and hence the LO_3 mode shifts towards lower wavenumbers [Pai 86, Lucovsky 87]

$$\nu^2 = (k/m_0)sin^2(\phi/2) \qquad \text{Eqn (3.13)}$$

where ν is the frequency of vibration, k is the nearest neighbour force constant, m_0 is the mass of oxygen and ϕ is the Si-O-Si bond angle. The shift of the peak positions towards higher wavenumbers (towards SiO_2) in the case of $r_H = 57\%$ may support the previous argument of oxygen trapped by the Si core while forming agglomerates.

(c) Si excess estimation

In order to consider a balance between r_d, $n_{1.95eV}$ and material composition, it is important to have an estimate of the Si excess. The Si excess was estimated from FTIR analysis (unbonded Si) within an uncertainity of ±0.2%, and ellipsometry (Bruggemann method-agglomerated Si) analysis within an uncertainity of ±3% as detailed before. Table 3.4 consolidates the value of Si excess obtained by these methods.

$r_H(\%)$	ν_{TO3}	$x = 0/Si$ from FTIR	Si excess (at.%) from FTIR (unbonded Si)	$x = 0/Si$ from ellipsometry	Si excess (at.%) from ellipsometry (agglomerated Si)
4.6	1068	1.86	2.33	1.99	0.217
11.7	1064	1.82	3.26	1.87	2.33
26	1065	1.82	3.26	1.64	6.76
57	1069	1.87	2.14	1.61	7.55

Table 3.4: Si excess estimation by FTIR and refractive index analysis with regard to varying r_H.

The trends of Si excess with r_H from FTIR is not well defined, but from results deduced from ellipsometry one can notice an increase in the formation of Si-np.

3.3 Co-Sputtering- Method 2

In order to improve r_d and $n_{1.95eV}$ obtained by reactive sputtering, another method of incorporating Si excess into the SiO_2 matrix was adopted. This method involves co-sputtering of the Si and SiO_2 targets in a pure Ar plasma at T_d=500°C.

The power density applied on the Si cathode was varied to see the influence on deposition rates, refractive index and structural changes. The power density of Si can be altered by changing the percentage of the power applied on the Si target with regard to the total power (= 300 W) in the experimental set-up. As before, the power density of SiO_2 was fixed at 7.4 W/cm^2 while power densities of Si were varied between 1.62 to 2.96 W/cm^2.

3.3.1 Deposition rate (r_d) and Refractive Index ($n_{1.95eV}$)

All the SRSO samples were grown with a fixed deposition time of 3600s. The influence of increasing P_{Si} on r_d and $n_{1.95eV}$ is represented in figures 3.7a and 3.7b. The inset shows the thickness variations with increasing P_{Si}.

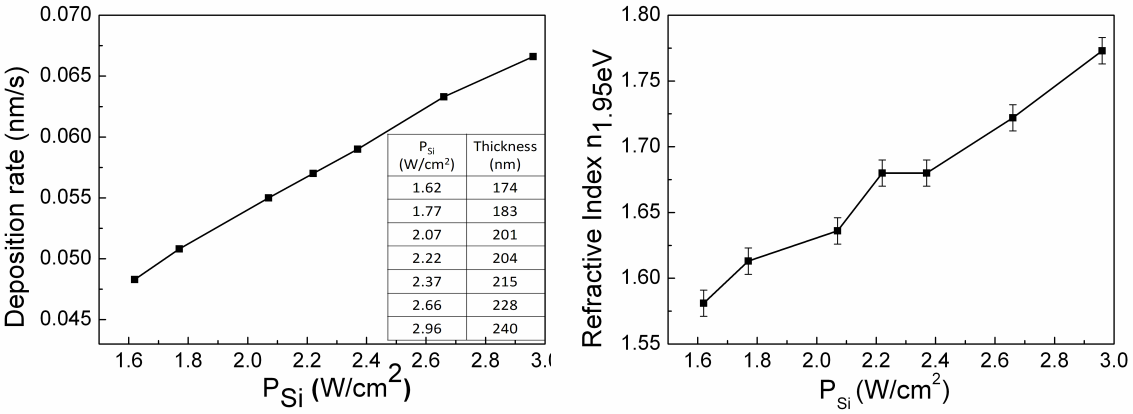

(a) Deposition rate.

(b) Refractive index.

Figure 3.7: Effect of P_{Si} on (a) Deposition rate (r_d nm/s); (inset) the thicknesses, and (b) Refractive index ($n_{1.95eV}$).

The thickness, deposition rate as well as the refractive index increase with increasing P_{Si}. Since there is no etching mechanisms due to the absence of hydrogen in this approach, there is an increase of the deposition rate and thickness with P_{Si}. Besides, the increase of Si power density favours the incorporation of Si excess in

the host SiO_2 matrix leading to an increase in $n_{1.95eV}$. This method is thus advantageous than method 1 since by controlling the ratio of power densities between Si and SiO_2 it is possible to incorporate higher Si excess at a higher r_d.

3.3.2 Fourier transorm infrared spectroscopy

Figures 3.8a and 3.8b show the FTIR spectroscopy of the co-sputtered SRSO samples recorded in Brewster and normal incidences respectively. In all the spectra the TO_3 peak position is normalized to unity for comparison.

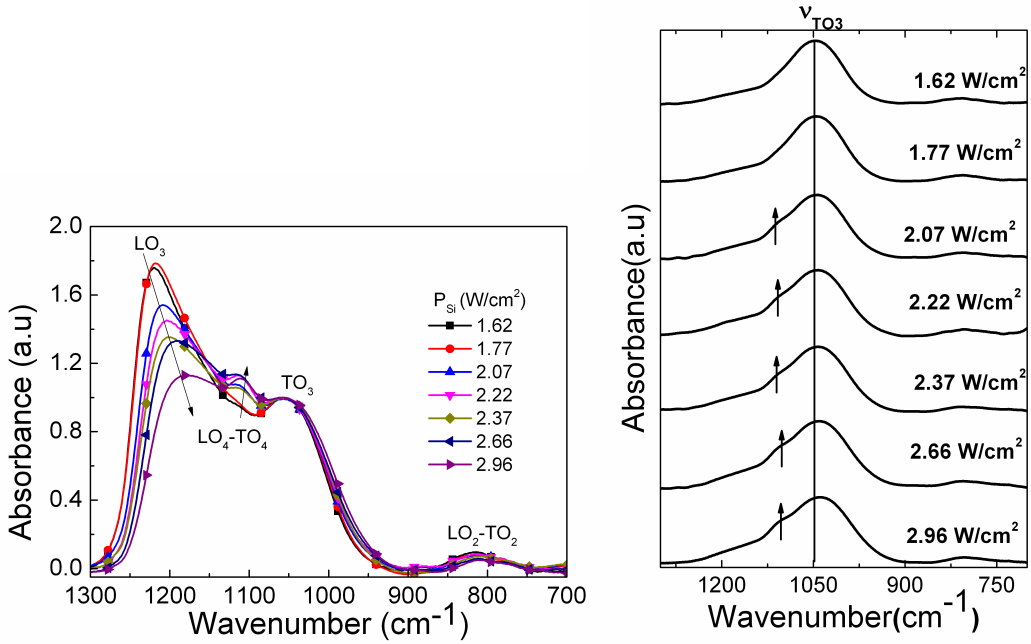

(a) Brewster incidence. **(b)** Normal incidence.

Figure 3.8: FTIR spectra of co-sputtered SRSO in (a) Brewster incidence and (b) normal incidence. The straight line in the normal incidence spectra helps to witness the shift of v_{TO3} and the arrows indicate the 1107 cm^{-1} peak.

With an increase in P_{Si}, the LO_3 peak position shifts from 1220 cm^{-1} to 1187 cm^{-1}, in addition to a progressive decrease of its intensity. The TO_3 peak position also shifts towards lower wavenumbers as can be seen from the normal incidence spectra. The FTIR spectra with increasing P_{Si} show the same behaviour as those shown when r_H was increased. Hence the same explanations as detailed in section 3.2.2 are valid. The only difference in these spectra as compared to method 1, is the absence of the Si-H peak between 870-890 cm^{-1} indicating these samples were fabricated under a pure Ar plasma. The increased Si incorporation as denoted by the high refractive index with increasing P_{Si} can also be seen from the FTIR spectra.

The LO_3 and TO_3 peaks approach each other, resulting in the increasing intensity of LO_4-TO_4 doublet. This is an indication that the increasing Si excess induces disorder in the deposited layer. Since the peak around 1107 cm^{-1} appears from P_{Si}= 2.07 W/cm^2 onwards and increases gradually with increasing power applied on Si cathode, we can confirm that this peak is associated with Si excess. This peak thus can be attributed to be a combined contribution of increasing disorder in the matrix and agglomeration of Si with interstitial oxygen.

(c) Si excess estimation

P_{Si}(W/cm^2)	ν_{TO3}	$x = 0/Si$ from FTIR	Si excess (at.%) from FTIR (unbonded Si)	$x = 0/Si$ from ellip-sometry	Si excess (at.%) from ellipsometry (agglomerated Si)
1.62	1046	1.62	7.25	1.75	5.4
1.77	1045	1.61	7.47	1.68	6.7
2.07	1042	1.57	8.2	1.64	7.6
2.22	1042	1.57	8.2	1.57	9.2
2.37	1041	1.56	8.45	1.57	9.2
2.66	1040	1.55	8.8	1.50	10.8
2.96	1039	1.54	8.96	1.43	12.57

Table 3.5: Si excess estimation by FTIR and refractive index (Bruggeman method) analysis with varying P_{Si}.

The Si excess estimated from FTIR (unbonded Si) within an uncertainity of ±0.2% and ellipsometry (Bruggeman method-agglomerated Si) analysis within an uncertainity of ±3% are given in table 3.5. Comparing with the results of previous deposition approach (ref. Tab. 3.2), it can be noticed that the increase of P_{Si} leads to an increase in Si excess estimated from both FTIR and ellipsometry methods. This can be attributed to the increasing RF power density applied on the Si target that favours the incorporation of isolated Si (i.e. unbounded Si) as well as the formation of Si-np (i.e. agglomerated Si).

3.4 Reactive Co-sputtering- Method 3

In order to take advantage of the above described two methods, in favouring the incorporation of Si excess within the SiO_2 matrix, reactive co-sputtering method is

initiated in this thesis, for the growth of SRSO layers. From the parameters analyzed above, T_d was chosen as 500°C, and r_H as 26% for this set of studies.

3.4.1 Effect of power density applied on Si cathode, (P_{Si})

The effect of varying the P_{Si} during the reactive co-sputtering is investigated. The same range of power densities and time of deposition as used in method 2 were employed.

(a) Deposition rates (r_d) and Refractive index ($n_{1.95eV}$)

The influence of P_{Si} on r_d and $n_{1.95eV}$ is shown in figure 3.9 with the values of sample thicknesses at each P_{Si}, in the inset. The time of deposition was fixed to be 3600s.

There is an increase of r_d with P_{Si}, similar to the trend observed in method 2. The deposition rate obtained by method 3 is higher than that obtained by method 1 (at $T_d = 500$°C) and lower than that obtained by method 2.

The comparison between thicknesses obtained from method 2 and 3 shows this decrease in r_d more evidently. For the same deposition conditions, the addition of hydrogen in the plasma decreases the thickness by about 70%.

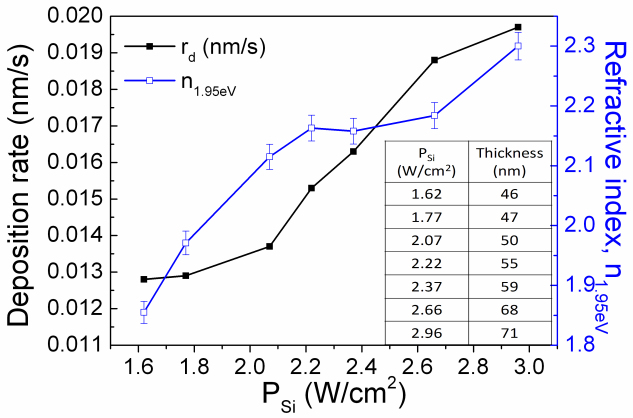

Figure 3.9: Effect of P_{Si} on deposition rate (left axis), refractive index (right axis), and thickness (Inset).

The variation of refractive index shown in the right axis of the figure 3.9 shows a steady increase with P_{Si}. Besides it can be noticed that the refractive index values have increased significantly as compared to the other two methods. This can be attributed to the combination of deposition methods 1 and 2 that allows in achieving higher Si incorporation in the film.

(b) Fourier transform infrared spectroscopy

Figure 3.10 shows the effect of P_{Si} as seen from Brewster and normal incidence FTIR spectra. In all the spectra, TO_3 peak is normalized to unity for comparison.

It can be seen from the Brewster incidence spectra (Fig. 3.10a), that the LO_3 peak intensity is very low as compared to the other two methods of SRSO growth,

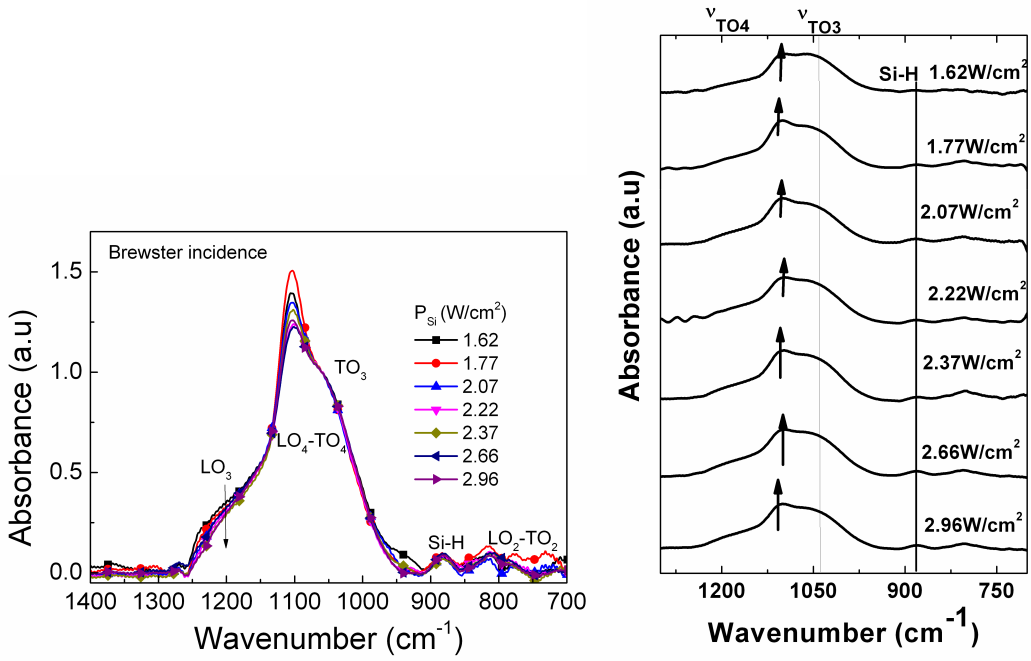

(a) Brewster incidence. **(b)** Normal Incidence.

Figure 3.10: FTIR Spectra- Effect of P_{Si} on the SRSO film structure.

and it decreases further with increasing P_{Si}. This indicates that the samples are more Si-rich as compared with the other two methods. The high refractive index achieved by this method proves that the host matrix is SiO_x rather than SiO_2. This explains the decrease of the LO_3 peak intensity. A curve fitting performed on each of these curves lead to three peaks around 1190 cm^{-1}, 1107 cm^{-1} and 1070 cm^{-1} respectively. The 1107 cm^{-1} peak intensity decreases which could be attributed to a lower interstitial oxygen formation with increasing Si excess that might favour pure Si agglomerates.

The normal incidence spectra in figure 3.10b shows the constant position of TO_3 peak. This indicates that most of the Si excess forms agglomerates even in the lowest P_{Si} case. The hydrogen-related peak is visible in all the cases as seen from Brewster incidence spectra, though in method 1 this peak almost disappeared for $T_d = 500°C$.

(c) Si excess estimation

The Si excess (unbonded Si) estimated by FTIR is around 5 at.%±0.2% in all the samples, due to the constant TO_3 peak positions. Table 3.6 consolidates the results estimated from refractive index using Bruggemann method within an uncertainity of ±3%.

P_{Si}(W/cm^2)	$x = 0/Si$ Bruggemann	Si excess (at.%) vol. fraction from refractive index (agglomerated)
1.62	1.33	15.28
1.77	1.2	18.89
2.07	1.08	23.08
2.22	1.04	24.34
2.37	1.04	24.34
2.66	1.029	24.9
2.96	0.943	28.18

Table 3.6: Si excess estimation (agglomerated Si) from Bruggemann method.

It can be seen that the Si excess values are high as estimated from Bruggeman method, than the other two methods. Besides, it can be seen that there is minimal variation in Si excess for cases of intermediate values of P_{Si}: 2.07 to 2.66 W/cm^2.

3.4.2 Effect of annealing

From the above investigations, it is clear that SRSO grown by method 3 incorporates the highest Si excess compared to the other two methods. The effect of annealing on the material properties has to be analyzed before finalizing the method 3 SRSO for multilayers. A high Si excess may result in formation of big Si-np leading to loss of the desired quantum confinement effects whereas a low Si excess would mean lower absorption coefficient which is not suitable for the objective of this work. Therefore SRSO sample with intermediate parameters of $r_H = 26\%$ and $P_{Si} = 2.22$ W/cm^2 were chosen in order to balance between deposition rate and Si excess. T_d = 500°C was chosen since it was demonstrated in this work that this temperature favours Si excess, and also forms some Si-np in the as-grown state as reported in [Hijazi 09a]. The SRSO sample with these optimized parameters are analyzed for structural and optical properties with regard to annealing. This sample will be referred as SRSO-P15 in the forthcoming discussions. The thickness and refractive index at 1.95 eV of this sample as estimated from ellipsometry are 565 nm and 2.02 respectively. According to RBS results[2], this sample is $SiO_{x=0.72}$ with 37 at.% Si excess. Five pieces of this sample were annealed at 1000°C during 1 minute, and at 700°C, 900°C, 1000°C and 1100°C during 1 hour in N_2 atmosphere. Unless stated otherwise, all the studies in this section are carried out on SRSO-P15.

[2]RBS analyses were made by J. Perriére at UNIV PARIS 06, INSP NANOSCIENCE PARIS, CNRS, UMR 7588, F-75015, Paris, France.

(a) Fourier transform infrared spectroscopy

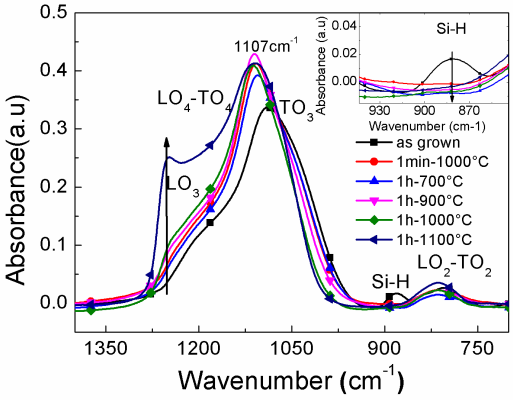

Figure 3.11: Effect of annealing on the FTIR spectra in Brewster incidence.

Figure 3.11 shows the FTIR spectra before and after annealing recorded using Brewster incidence. The inset in this figure shows an enlarged view of the Si-H peak variations with annealing.

It can be seen that the LO_3 peak intensity gradually increases with increasing annealing temperatures. Considering the effect of time, for a given temperature 1000°C (1min-1000°C and 1h-1000°C) there is no significant change in the LO_3 peak intensity whereas there is a drastic increase when the sample is annealed at 1h-1100°C.

This trend represents a gradual evolution towards the phase separation process upon annealing. A gaussian curve fitting performed on these spectra indicated a reduction in the peak widths of LO_3 and TO_3 peaks with increasing annealing temperatures. Such reduction in the peak width with increasing annealing treatment has also been observed in [Morales-Sanchez 08] and these changes are attributed to the phase separation processes. In addition, we also notice an increase of the $LO_4{-}TO_4$ mode upon annealing. This indicates the disorder in the matrix due to high Si excess. It can be seen that the Si-H peak appears only in the as-grown sample. The desorption of hydrogen occurs with increasing annealing temperatures leading to a disappearance of this peak.

(b) Raman spectroscopy

The evolution of Si-np formation between as-grown and 1h-1100°C annealed SRSO-P15 sample as reflected by FTIR spectra is confirmed through Raman spectroscopy following the procedure detailed in chapter 2 under section 2.4.4 (Fig. 3.12).

It can be seen that the as-grown sample shows a broad peak centered at 480 cm^{-1}, which decreases in intensity after 1h-1100°C annealing with the appearance of a new peak at 517.6 cm^{-1}. The Raman spectrum of the as-grown layer shows dominant features of amorphous Si, since SiO_2 is reported to have a very low scattering cross section [Kanzawa 96, Khriachtchev 99]. This confirms the formation of amorphous Si-np in the as-grown sample as indicated by ∼24 at.% of agglomerated Si estimated using ellipsometry (Bruggeman) method (Ref. Tab. 3.6).

After annealing, SRSO forms Si nanocrystals due to phase separation as seen from the sharp transverse optical (TO) mode appearing at 517.6 cm^{-1}.

It is known that when the Si crystalline size decreases, the optical TO mode of Si bulk downshifts in wavenumber [Ritcher 81, Sui 92]. Hence the observed peak at 517.6 cm^{-1} that appears on 1h-1100°C annealing confirms the formation of Si-nanocrystals. This is accompanied with a decrease of the amorphous Si mode at 480 cm^{-1}.

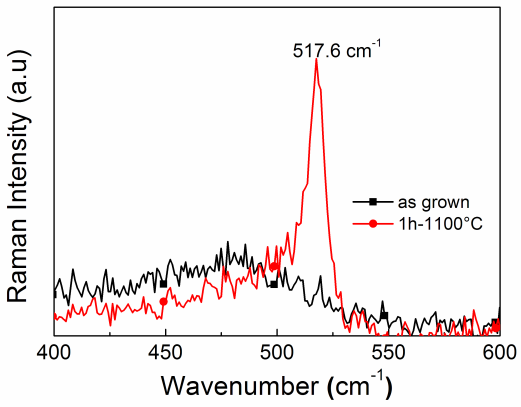

Figure 3.12: Raman spectra of SRSO-P15 grown on fused Si substrate. $\lambda_{excitation}$ = 532 nm and laser power density =0.14 MW/cm^2

(c) X-Ray Diffraction

In order to witness the formation of Si-np, their crystallization with annealing and to estimate the Si-np size, XRD studies were performed (Fig. 3.13).

It can be seen that the as-grown sample has a broad band between 20-30° which starts to peak around 28°. This confirms again that the as-grown sample already contains Si-np. With increasing annealing temperature, the crystalline phase of Si-np increases as can be seen by the distinct appearance of (111) peak corresponding to c-Si at 28.37°. After 1h-1100°C annealing, this peak becomes sharper and has a FWHM of 1.52°. The peaks at other orientations (220) and (311) also show their distinct presence which occurs only when there is a high crystalline volume in the material. From the (111) peak, the average Si-np size is estimated as 5.5nm using the Scherrer formula.

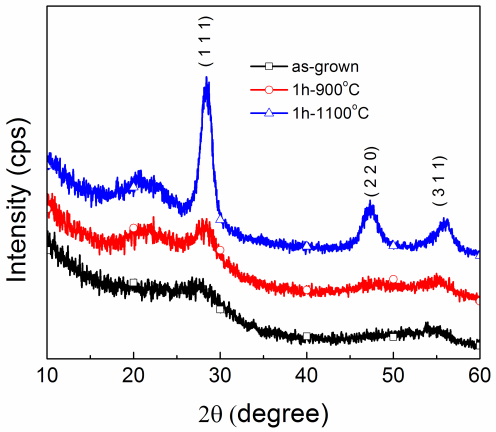

Figure 3.13: XRD spectra of SRSO-P15 grown on Si substrate.

(d) Photoluminescence

Figure 3.14a shows the PL spectra of SRSO-P15 at various annealing treatments.It can be seen that there is no emission whatever be the annealing conditions. The absence of PL may be attributed to high Si excess due to any/all of the following processes:

(i) an increase in the non-radiative paths in the matrix.

(ii) a higher disorder in the matrix as observed by FTIR investigations.

(iii) possible formation of oversized Si-np upon annealing, leading to the loss of quantum confinement effect.

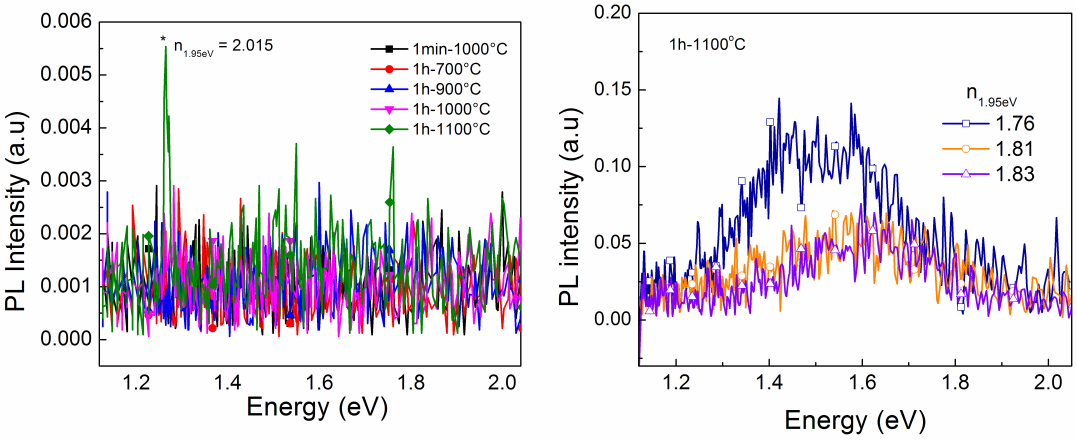

(a) PL spectra vs. annealing of SRSO-P15**(b)** PL intensity vs. $n_{1.95eV}$ of Method 3 SRSO.

Figure 3.14: PL spectra of (a) SRSO-P15 sample at various annealing and (b) Other SRSO samples grown by method 3 but with lower refractive index.(*) indicates second order laser emission.

This is confirmed by the presence of luminescence witnessed in other samples grown using method 3, that have lower refractive index and therefore lower Si excess in the matrix (Fig. 3.14b).

(e) Absorption coefficient

The values of absorption coefficients (α) between 1.5-4.5 eV were extracted from k values obtained by ellipsometry measurements as detailed in section 2.2.6 of chapter 2. Figure 3.15 represents the absorption coefficient curves of SRSO-P15 before and after different annealing treatments.

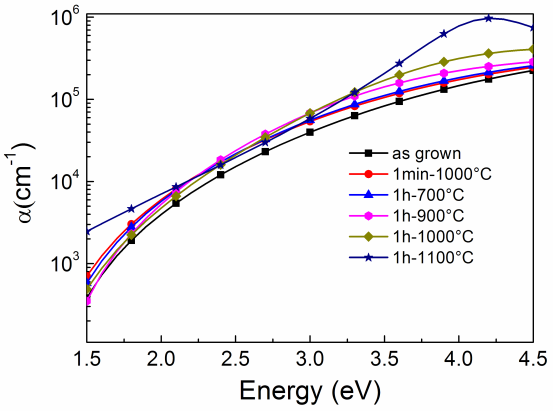

Figure 3.15: Absorption coefficient curves of SRSO monolayer with regard to annealing.

The absorption coefficient of even the as-grown sample is high of the order of 10^4-10^5cm^{-1} around 4 eV which meets the criteria for a solar cell material [Poortmans 06]. Besides, with increasing annealing treatment the absorption coefficient curves show a gradual increase till 1h-1000°C indicating the evolution of phase separation process. A dramatic increase at 1h-1100°C reflects the nanocrystal and Si-np formation which largely contribute towards absorption.

3.5 Summary on SRSO monolayers

- Three methods of incorporating Si excess into SiO_2 matrix to form Silicon Rich Silicon Oxide (SRSO) were investigated. Figure 3.16 summarizes the deposition rates and refractive index obtained on SRSO samples investigated.

- A temperature dependent growth mechanism is proposed depending on the velocity of the reaction species, desorption of SiH_x radicals and Si deposition-etching balance.

- From the investigations above,

  - $T_d = 500$°C is optimized as it favours Si clusterization and reorganization even in the as-grown sample.
  - Reactive co-sputtering is chosen for multilayer growth due to higher Si incorporation.
  - r_H=26% is chosen considering a balance between deposition rate and refractive index.

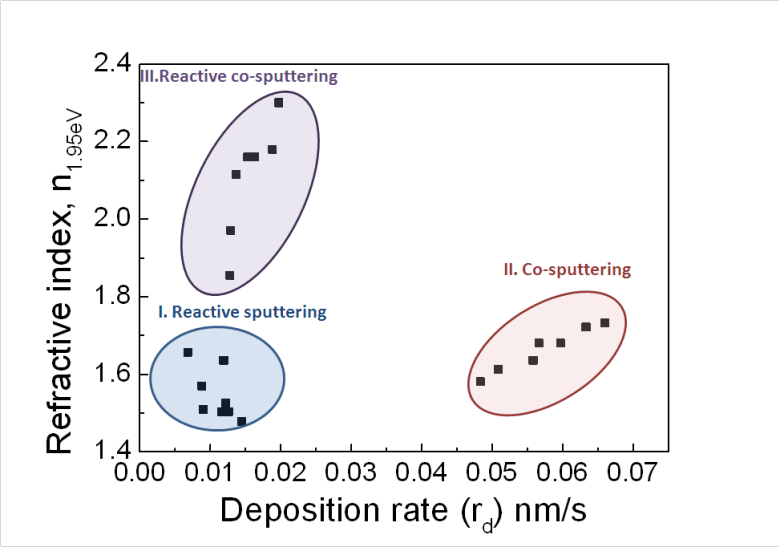

Figure 3.16: Summary of r_d(nm/s) and $n_{1.95eV}$ obtained with the three SRSO sputtering growth methods.

- FTIR spectra reveals the presence of a peak around 1107 cm^{-1} in samples with high Si excess. This is suggested to be he formation of interstitial oxygen within Si core during reorganization.
- An annealing at 1100°C during 1h is considered as the best condition for the formation of nanocrystals as confirmed by Raman and XRD spectra.
- Absence of visible emission from higher refractive index SRSO samples is related to the high Si excess.
- High absorption coefficient curves are obtained even with as-grown SRSO samples grown by reactive co-sputtering.
- To avoid the formation of bigger nanocrystals due to a very high Si excess within SRSO sublayer, a middle value of P_{Si}=2.22 W/cm^2 is chosen to be used for multilayer structures.

3.6 Role of the Hydrogen plasma

As seen from all the discussions above, there is a competition between etching and deposition due to hydrogen in the plasma. Therefore, before proceeding with investigations on multilayers, it becomes interesting to see the role of hydrogen plasma towards deposition. In order to compare its role during the deposition and after the deposition processes, a sample was merely placed in the hydrogen plasma by closing the shutter on the targets to avoid sputtering.

Aim of the study	Deposition / placing in hydrogen- rich plasma	t(nm)	$n_{1.95eV}$
To see the influence of hydrogen plasma	3h deposition (continuous)	236	1.76
	3h deposition + 1h placing in plasma without deposition	236	1.76

Table 3.7: Role of hydrogen plasma on the growth of reactively co-sputtered SRSO samples.

During multilayer fabrication we expect to alternate between hydrogen-rich plasma (Ar+H_2) and pure Ar plasma. Hence the residual hydrogen in the plasma might etch the next forming sublayers. Therefore, this study was made to get a deeper insight on the role of hydrogen plasma on the material growth. Table 3.7 shows the thickness and refractive index obtained on two samples: (i) SRSO layer deposited during 3h, and (ii) SRSO layer placed 1h in Ar+H_2 plasma after 3h deposition.

It can be seen that there is no change in the thickness or the refractive index of the samples after 3h continuous deposition or 3h deposition + 1h placing in the hydrogen plasma without deposition. This implies that the hydrogen does not participate in etching if Si and SiO_2 cathodes are closed, and plays a role on the material growth only if the deposition process is ongoing. The latter was confirmed by observing an increase in refractive index (1.82) and thickness (308 nm) when 3h deposited SRSO is placed 1h in plasma activating the Si cathode (i.e) deposited for an additional 1h. Therefore, during the multilayer growth it is wise to allow sufficient time to evacuate hydrogen before the deposition of next sublayer since Si cathode is active (open) during both SRSO and SiO_2 sublayer growth.

3.7 SRSO-P15 in a multilayer system: SRSO/SiO_2

The goal behind fabricating SRSO/SiO_2 multilayer configuration is to control the size and density of the Si-np within SRSO layer in accordance with the quantum confinement effect. PL measurements are indicative of the presence of Si-np (exciton) which are required for desirable absorption and carrier generation in a third generation PV device. Reducing the Si excess to attain smaller crystals significantly decreases the Si-np density in a monolayer. But in a multilayer (ML), the SRSO sublayer thickness controls the Si-np size without reducing their density and the SiO_2 barrier between the two consecutive SRSO sublayers prevent the overgrowth of

Si-np and their agglomeration. For this purpose, a ML composed of 50 patterns of 3 nm SRSO-P15 and 3 nm-SiO_2 was grown. All the MLs in the following discussions will be represented as 'Pattern number (t_{SRSOnm}/t_{SiO_2nm})'. Prior to the study on emission behaviours, the structure of our 50(3/3) ML is investigated to ensure the sublayer thicknesses are as expected to form Si-np. Most of the studies unless specified otherwise are done on the as-grown samples and the samples annealed at two chosen annealing treatments : 1min-1000°C and 1h-1100°C. These two annealing treatments are interesting since we assume that:

- a Short Time Annealing (STA) at 1min-1000°C allows the completion of Si seeds which grow with further annealing treatments and crystallize.
- the Classical Annealing (CA) at 1h-1100°C almost completes the formation of Si-np.

The intermediate annealing temperatures are analyzed if there is a need.

3.7.1 Structural analysis

(a) Fourier transform infrared spectroscopy and X-Ray Diffraction

The Brewster incidence FTIR and the XRD spectra of the test sample 50(3/3) are shown in figures 3.17a and 3.17b respectively.

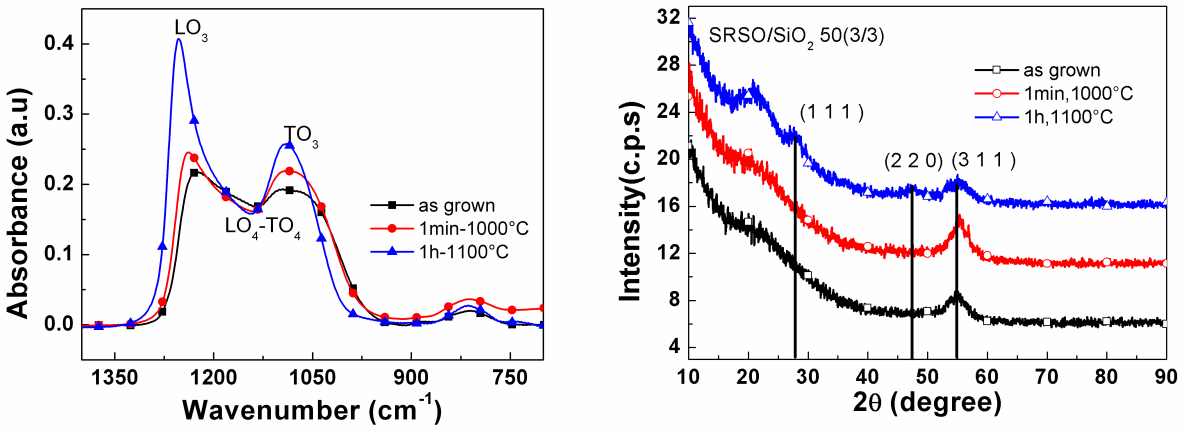

(a) FTIR spectra.

(b) XRD Spectra.

Figure 3.17: Structural changes in 50(3/3) ML with annealing as investigated by (a) Brewster incidence FTIR spectra and (b) XRD spectra.

It can be seen from the FTIR spectra that the LO_3 and TO_3 peaks shift towards higher wavenumber. The intensity of the LO_4 -TO_4 peak decreases indicating

a structural reorganization in the material. The XRD spectra also show that the annealing induces some structural changes in the film. Three peaks centered around 2θ= 28°, 47° and 55° represent the (111), (220) and (311) Si crystal planes respectively and the broad peak between 2θ= 20-30° correspond to the small amorphous nanoclusters [Torchynska 05].

It can be observed from FTIR and XRD analyses that the as-grown and STA samples are similar. However, in FTIR a higher ordering of the STA sample is seen from decreasing intensity of LO_4-TO_4 mode indicating the commencement of phase separation process. After CA, both FTIR and XRD spectra reflect the structural reorganization of the matrix into SiO_2 and Si. The increased intensity of LO_3 peak similar to that observed in SiO_2 (ref. Fig. 2.5 of chapter 2) is indicative of Si-np formation with phase separation process. This is confirmed by the XRD spectra where we can notice the appearance of Si (111) peak around 28°.

It is interesting to note that the peak around 1107 cm^{-1} attributed to interstitial oxygen in SRSO-P15 monolayer is absent in its multilayered configuration.

(b) Atom Probe Tomography

The density and size of the Si-np were estimated by Atom Probe Tomography (APT) measurements made by Dr. E. Talbot and M. Roussel[3] on CA 50(3/3) ML. Figure 3.18 shows the formation of Si-np and their size distribution in the SRSO sublayer. This technique provides a three dimensional chemical map of the sample at an atomic scale. Hence a very accurate and direct characterization of Si-np in SRSO can be made using APT.

The formation of Si-np in the SRSO sublayer can be seen. The APT studies revealed the average concentration of Si and O in SRSO sublayers to be 45.7% and 54.3% respectively indicating about 18.5% Si excess in the material. It can be noticed that this value of Si excess is lower than the one determined for SRSO-P15 monolayer (37 at.% by RBS). This can be attributed to the thickness of the SRSO sublayer and/or its growth on SiO_2 sublayers. After CA there is still $<$ 1-2% Si excess which is attributed to the limit of the experimental set-up. The Si-np density estimated from this method is 2.6$\pm$0.5 x 10^{19} np/cm^3 which is higher than our earlier reported [Maestre 10] Si-np density of 9 x 10^{18} np/cm^3 which was also estimated by APT [Roussel 11]. On the basis of the work of M. Roussel on our layers, the Si diffusion coefficient in SiO_2, D_{Si} is about 5.7 x 10^{-18} cm^2/s after CA. This implies that a minimum barrier length (l) to prevent diffusion in our layers is about 2.03 nm (using $l = \sqrt{D_{Si}.t_A}$, where t_A =annealing time). This value is very close to 1.5

[3]Groupe de Physique des Matériaux, Université et INSA de Rouen, UMR CNRS 6634, France.

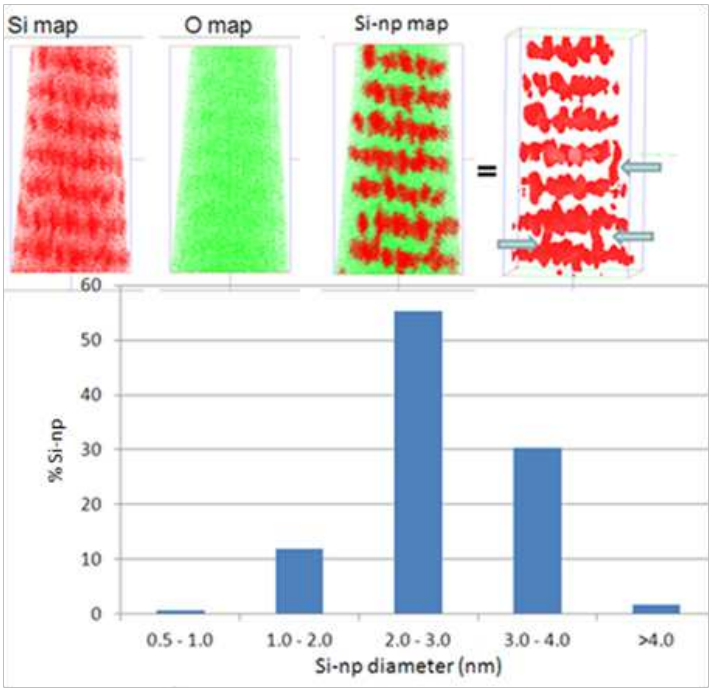

Figure 3.18: Formation of Si-np in SRSO sublayer of CA 50(3/3) ML and their size distribution.

nm barrier length estimated by [D.Tsoukalas 01]. Thus, a SiO_2 sublayer of 3 nm is at the limit to prevent diffusion from two consecutive SRSO sublayers, resulting in 30% of Si-np with sizes between 3-4 nm. However, most of the Si-np have sizes that are restricted to the 3 nm SRSO sublayer thickness and the mean size of the Si-np in our case is 2.7 nm.

3.7.2 Emission properties

The emission properties of 50(3/3) ML after CA is investigated (Fig. 3.19).

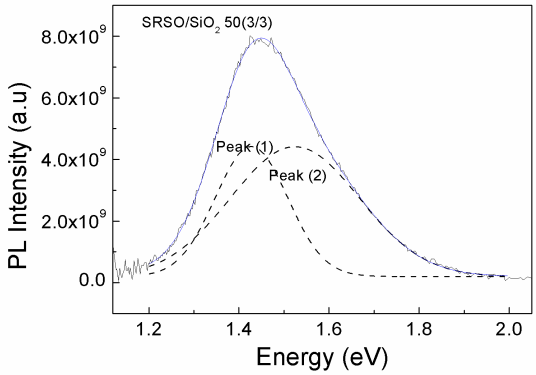

Figure 3.19: PL spectrum of CA 50(3/3) ML.

It can be seen that there is a significant emission from the material in the visible range, contrary to the absence of any emission in SRSO-P15 monolayer. This confirms that the absence of emission in a monolayered configuration at this annealing is due to the loss of quantum confinement of carriers. The agglomeration into big size particles is prevented in the ML leading to this emission. It is interesting to note that the curve is composed of two peaks, peak (1) and peak (2) at 1.41 eV and 1.53 eV respectively indicating there are more than one type of emitters. We can attribute the peak at higher energy (1.53 eV) to Si-np whose sizes range between 2-3 nm, which represent more than 50% of Si-np (ref. Fig. 3.18), since the mean size of our Si-np are only about 2.7 nm and cannot lead to a redshifted emission. Peak (1) at lower energy (1.41 eV) might be attributed to bigger sized particles that are formed due to overgrowth at interfaces as observed in APT.

3.8 Influence of sublayer thicknesses

In order to further explore the emission properties, the influence of the SRSO and the SiO_2 sublayer thicknesses on the formation of Si-np becomes the next subject of concern. To begin our investigations, five MLs with different thicknesses of SRSO and SiO_2 sublayers were grown as detailed in table 3.8. The total thickness of the samples were fixed around 500 nm to ensure uniformity in comparison. Since this part of the study is shared between this thesis and the thesis of M. Roussel[4], these sublayer thicknesses were chosen to suit the needs of both.

Notation	Patterns	t_{SRSO} (nm)	t_{SiO2} (nm)	Total thickness (nm)
28(8/10)	28	8	10	504
52(8/1.5)	52	8	1.5	494
36(4/10)	36	4	10	504
70(4/3)	70	4	3	490
90(4/1.5)	90	4	1.5	504

Table 3.8: SRSO/SiO_2 MLs-Sample details

3.8.1 Fourier transform infrared spectroscopy

Typical FTIR spectra of SRSO/SiO_2 ML with annealing is shown in figure 3.20a.

The FTIR analyses were made to witness the evolution of phase separation process from 1h-900°C to 1h-1100°C (CA). The as-grown spectrum is also included in

[4]Groupe de Physique des Matériaux, Université et INSA de Rouen, UMR CNRS 6634, France.

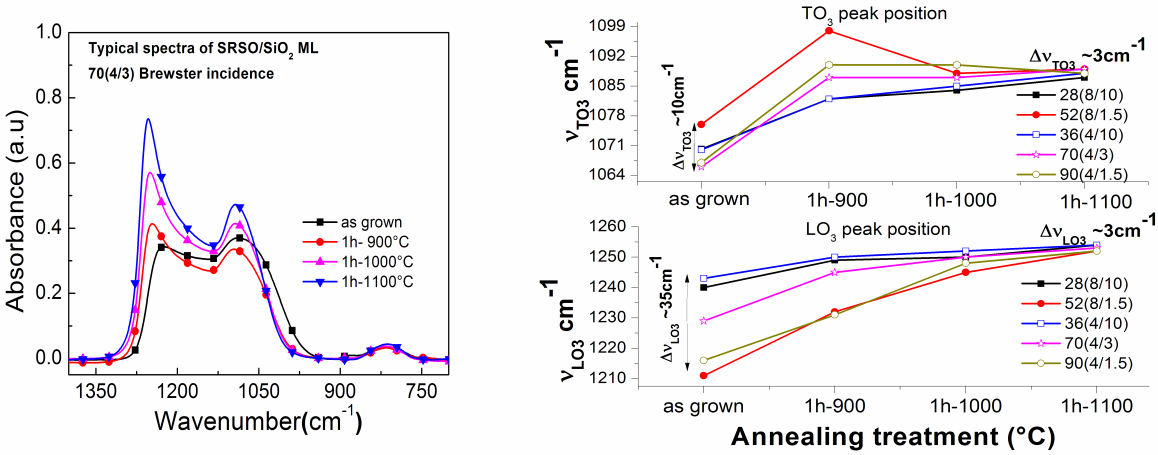

(a) Typical FTIR spectra.

(b) ν_{LO3} and ν_{TO3} vs. annealing.

Figure 3.20: (a) Typical FTIR spectra from 70(4/3) ML showing the effect of annealing and (b) LO_3 and TO_3 peak position variations with annealing.

the figure for comparison. The increasing intensities of LO_3 and TO_3 modes with annealing indicate the evolution of phase separation process.

Figure 3.20b shows the variation of LO_3 and TO_3 peak positions with annealing in all the MLs under investigation. Irrespective of the sublayer thicknesses, the LO_3 and TO_3 peak positions reach the same point after CA. This could be attributed to an almost complete phase separation process after such annealing treatment, in the view of the sensitivity of the experiment.

3.8.2 Atom probe tomography

The influence of the sublayer thickness (t_{SRSO}/t_{SiO_2}) as well as CA treatment on the formation of Si-np were investigated by APT on three samples with t_{SRSO}/t_{SiO_2}= 8 nm/10 nm , 4 nm/3 nm and 4 nm/1.5 nm respectively (Fig. 3.21). The as-grown samples were also analysed for comparison.

Special attention is laid on MLs with t_{SiO_2} = 1.5 nm and 3 nm in this study, to understand the diffusion and interlayer grain growth shown in section 3.8.2.

The presence of small clusters of Si is seen in the as-grown sample in support to all our previous discussions about high T_d and Si excess favouring such a formation. It can be also seen that the Si-np size is controlled along the growth direction after CA treatment. As expected, the size of Si-np is large in 8 nm thick SRSO sublayer but the 4 nm SRSO sublayer also shows big Si-np if separated by 1.5 nm SiO_2 sublayer. This is in agreement with the explanation above on diffusion length (about 2 nm) of Si in SiO_2 which results in the overgrowth of Si-np to form larger crystals. The Si-np are smaller with 3nm thick SiO_2 sublayer, but still there are few big crystals

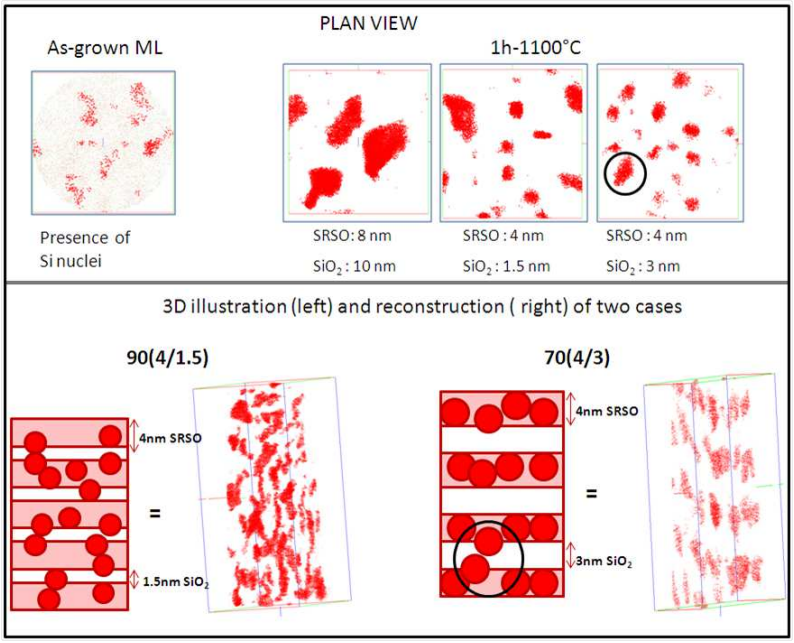

Figure 3.21: Influence of sublayer thicknesses on Si-np formation. Upper part of the figure shows the plan view of Si-np in SiO_x sublayers in as-grown and CA cases with regard to sublayer thickness. The bottom part of the figure shows a 3D illustration and a 3D volumic reconstruction of two specific cases of ML. (The plan view and volumic reconstructed images are given by M. Roussel from GPM).

as seen in 70(4/3) case (Fig. 3.21). These results confirm that the SiO_2 sublayer plays a strong role as a barrier layer in the formation of Si-np with controlled sizes.

3.8.3 Photoluminescence

The PL spectra of the samples after CA are shown in figure 3.22. In figure 3.22a the spectra are as recorded and in figure 3.22b the spectra is normalized to the pattern number. As mentioned before, all the curves are corrected to spectral response.

It can be seen in both the figures that there is no emission if $t_{SRSO} = 8$ nm which is attributed to the overgrowth of Si-np resulting in the loss of quantum confinement. In figure 3.22a it can be noticed that the most intense emission is obtained from 70(4/3) ML. Considering the MLs with 4 nm thick SRSO sublayers, we observe the lowest intensity for the highest number of emitters (green curve) and the highest emission for the intermediate number of emitters (pink curve). Consequently the number of emitters is not the only necessary parameter to achieve the highest intensity. This non-monotonous trend must be considered along with the t_{SiO_2} which may play a role on the emission intensity.

Since the total thickness of these samples are the same, the relevant parameter to compare the spectra would be to nomalize to one pattern of each ML. Therefore in

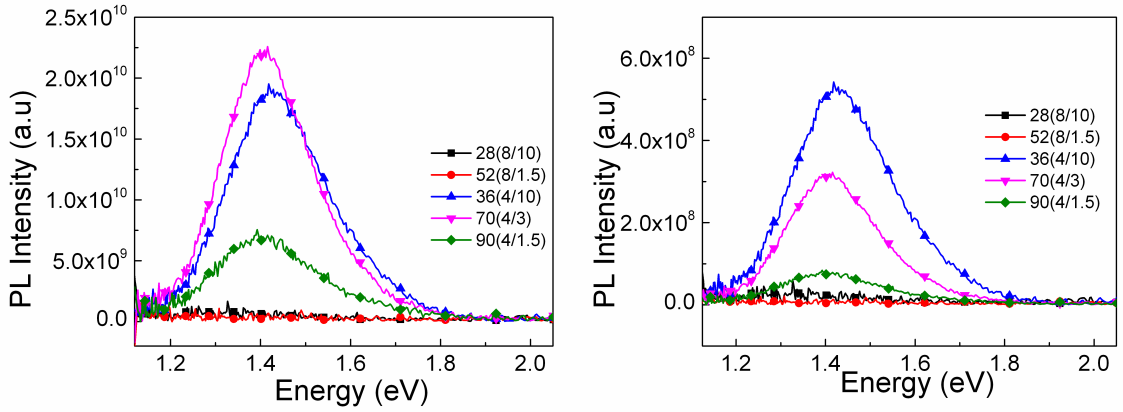

(a) As recorded. **(b)** Normalized to pattern number.

Figure 3.22: PL spectra to see the influence of SiO_2 barrier thickness by investigating (a) as recorded spectra and, (b) spectra normalized to pattern number.

figure 3.22b, the PL spectra are normalized to the pattern number. A monotonous trend of emission intensity with t_{SiO_2} is observed considering MLs with 4 nm thick SRSO sublayers. In the case of $t_{SiO_2} = 1.5$ nm, the Si diffusion between two consecutive SRSO sublayers are not prevented, leading to the overgrowth of Si-np. This might explain the low PL emission from 90(4/1.5) ML.

The PL spectra in both figures show that the emission peaks from 70(4/3) and 90(4/1.5) MLs are positioned at the same energy while a blueshift is observed with 10 nm SiO_2 sublayers. In order to confirm this, the curves of MLs with 4 nm thick SRSO sublayers were fitted using gaussian functions (Tab. 3.9).

Sample	Peak (1) eV	Peak (2) eV
36(4/10)	1.42	1.61
70(4/3)	1.40	1.57
90(4/1.5)	1.40	1.56

Table 3.9: Peak positions of MLs with 4 nm thick SRSO sublayer.

All the curves are composed of two peaks: peak (1) and peak (2). The blueshift of the peaks with increasing t_{SiO_2} is noticed. As seen from the structural analysis in section 3.8.2, it is clear that there is some interaction between two consecutive SRSO for lower barrier thicknesses, forming bigger Si-np. In the case of 10 nm barrier thickness, the SRSO layers are well separated and and the formation of Si-np is restricted only to the SRSO sublayers due to higher confinement offered by t_{SiO_2}. As a result, the formed Si-np are smaller leading to a blueshift of the PL intensity. In addition to all these microstructural effects, the emission might be influenced also by geometrical and optical effects which will be investigated in chapter 5.

3.8.4 Influence of SiO_2 barrier thickness

In order to understand better the role of t_{SiO_2}, the SiO_2 sublayer thickness was varied between 1.5 nm to 10 nm, while the SRSO sublayer thickness and total number of patterns were fixed to be 3 nm and 50 respectively. Figure 3.23 shows the as-recorded PL spectra from these layers.

It can be seen that the PL intensity obtained with t_{SiO_2} =1.5 nm is very low, which can be attributed to the overgrowth of particles due to a low barrier height. The emission intensity increases with barrier thickness which might be attributed to a better confinement within SRSO sublayer and/or to some optical and geometrical effects. But, the higher barriers that lead to better emission properties would on the contrary lower the conductivity. Hence considering a balance between optical and electrical properties needed for a PV device, t_{SiO_2} ranging between 3-3.5 nm can be an optimized barrier thickness.

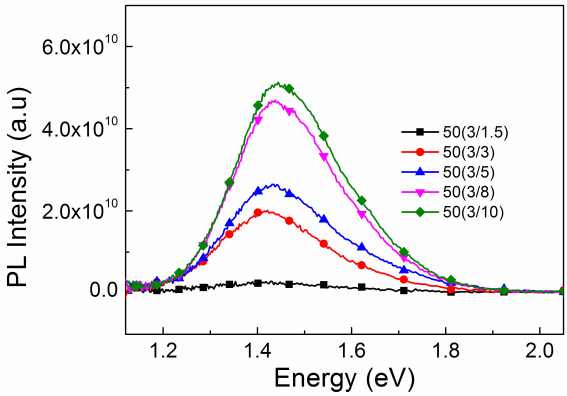

Figure 3.23: PL spectra of 50 patterned ML with $t_{SRSO} = 3nm$ and t_{SiO_2}varying between 1.5 nm to 10 nm to investigate the influence of SiO_2 barrier thickness.

3.9 Summary on SRSO/SiO_2 multilayers

- FTIR and XRD analyses indicate the formation of amorphous Si-np even in the as-grown state, a part of which crystallizes upon annealing.
- The peak attributed to interstitial oxygen (about 1107 cm^{-1}) in FTIR analysis of SRSO monolayers disappears in SRSO/SiO_2 multilayers.
- A high density of Si-np with a size control is achieved (about 3 x 10^{19} np/cm^3) in SRSO sublayer.
- APT analysis reveal that the diffusion of Si occurs in SiO_2sublayers with thicknesses lower than or equal to 3 nm.
- The SRSO-P15 when used in a ML configuration results in intense visible emission in comparison to the absence of emission in its monolayer configuration.

The PL spectra is composed of two peaks.

- The absence of emission in ML with 8 nm thick SRSO sublayer is related to the loss of quantum confinement effect.
- All the emission properties investigated above are expected to be influenced by optical/geometrical phenomena which will be analyzed in chapter 5.

3.10 Conclusions

A vast analysis of SRSO monolayer and SRSO/SiO_2 multilayer configurations have been discussed in this chapter. High refractive index in SRSO layer were obtained by developing a new deposition approach: Reactive co-sputtering. A deep insight on the deposition process, and the structural changes associated with each growth method is analyzed in the first part of this chapter. One of the major goals of this thesis is achieved by attaining a higher density of Si-np (2.6 ± 0.5 x 10^{19} np/cm^3) in SRSO/SiO_2 MLs than the earlier reported value of 9 x 10^{18} np/cm^3 using the reactive co-sputtering approach. It is demonstrated that the SiO_2 barrier thickness plays an important role in the formation of size controlled Si-np. For t_{SiO_2}lower than or equal to 3 nm, there is no effective prevention of Si diffusion. Considering a balance between diffusion barrier and carrier transport, it is estimated that the optimal barrier thickness is around 3-3.5 nm.

Chapter 4

A study on RF sputtered SiN_x single layers and $SRSO/SiN_x$ multilayers

4.1 Introduction

It was demonstrated in chapter 3 that a high density of Si nanoparticles (Si-np) with size control can be formed in $SRSO/SiO_2$ multilayers. But the high bandgap of SiO_2 materials ($\sim$ 8.5 eV) limits the performance of optoelectronic devices due to the difficulty in carrier injection [Franz 02, Wang 03]. Hence replacing SiO_2 with SiN_x insulating barriers which have a lower bandgap ($\sim$ 5 eV) is one of the best possible way to favour carrier transport [Park 01]. The first major step involves successful fabrication of such a material by optimizing various deposition parameters like the gas flow, pressure, power density etc. This chapter therefore focusses on understanding the influence of deposition parameters on the material properties of SiN_x(N-rich, Si_3N_4, Si-rich) single layers, which are then investigated in $SRSO/SiN_x$ MLs.

The single layers of SiN_x were prepared by two different approaches as mentioned in chapter 2:

- Reactive sputtering of Si cathode using N_2-rich plasma.
- Co-sputtering of Si_3N_4 and Si in Ar plasma.

The SiN_x monolayers and multilayers were grown at a total pressure of 3 mTorr and T_d = 500°C.

4.2 N_2-Reactive sputtering of Si cathode

The SiN_x layers were grown by sputtering Si cathode in a nitrogen rich plasma. The RF power density applied on the Si cathode (P_{Si}) and the time of deposition were fixed at 4.44 W/cm^2 and 3600s respectively. The reactive gas rate r_N was varied between 5.1%-16% in order to change the composition of the material (as indicated by the refractive indices) between stochiometric and Si-rich SiN_x layers. Table 4.1 details the conditions used in this thesis, for obtaining N_2-rich plasma.

P_{Ar}(mTorr)	P_{N_2}(mTorr)	r_N(%)
14.8	0.8	5.1
14.1	1.1	7.1
14	1.5	9.6
13.6	1.9	12
12.8	2.5	16

Table 4.1: Conditions used to obtain N_2- rich plasma.

4.2.1 Refractive index ($n_{1.95eV}$) and Deposition rates (r_d)

Figure 4.1 shows $n_{1.95eV}$ and r_d of the samples with regard to r_N.

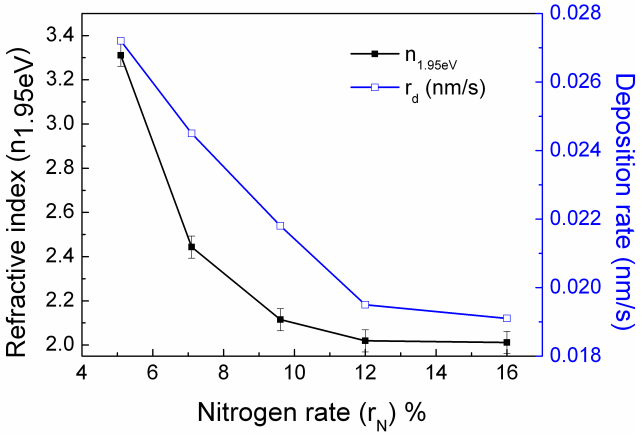

Figure 4.1: Effect of r_N on refractive index (left axis) and deposition rate (right axis).

The refractive indices increase with decreasing r_N, thereby making the material Si-rich. It can be seen that by varying r_N, $n_{1.95eV}$ changes between 2.01 to 3.3 which indicates that the composition can be tuned between Si_3N_4 and Si. The deposition rate can be seen to decrease with increasing r_N. This is attributed to the difficulty in sputtering the target when r_N is high, as observed in other sputtering set-ups in our team as well. The value, $n_{1.95eV}\sim$ 2.4 was chosen for most of the MLs to obtain a SRSN sublayer.

4.2.2 Structural analysis

(a) Fourier transform infrared spectroscopy

Figure 4.2 shows typical FTIR spectra of our SRSN samples, obtained from a 490 nm thick sample with $n_{1.95eV} = 2.44$. The spectra are recorded in both normal and oblique (Brewster = 65°) incidences.

The normal incidence spectrum contains only a single absorption peak around 840 cm^{-1}, whereas an additional peak centered around 1020 cm^{-1} appears when measurements are made in oblique incidence. In the whole spectral range between 4000-700 cm^{-1}, only these two absorption bands can be observed. This proves the absence of Si-O[1] or Si-H[2] or N-H bonds[3] that are usually observed in SiN_x materials due to oxygen or hydrogen contamination during the deposition process. Thus, the two peaks around 840 cm^{-1} and 1020 cm^{-1} observed in our samples can be unambiguously attributed to the TO and LO modes of asymmetric Si-N stretching vibrations respectively [Lin 92, Dupont 97, Bustarret 98, Batan 08]. The contribution of Si wafer from the interfacial oxide is noticed in thinner SiN_x samples around 1107-1105 cm^{-1}, whereas in thick samples this position is overlapped by the LO_{Si-N} mode as seen in figure 4.2.

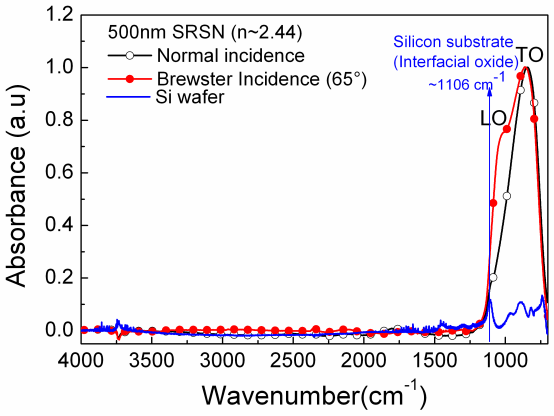

Figure 4.2: Typical FTIR spectra of our SRSN samples recorded in Brewster and normal incidence obtained from a SRSN sample with t=490 nm and $n_{1.95eV}$=2.44. The TO mode of Si-N is normalized to unity in the spectra.

The evolution of FTIR spectra in SiN_x monolayers as a function of refractive index (i.e. composition) was investigated on samples with thicknesses ranging between 70-100 nm (Fig. 4.3). In the Brewster incidence spectra, the curves are normalized to 100 nm thickness, and in the normal incidence spectra the TO_{Si-N} peak intensity is normalized to unity. The spectra is focussed in the region containing the Si-N bonds since these are the bonds we detect in our material in contrast to other deposition approaches [Aydinli 96, Wang 03, Vernhes 06, Scardera 08].

[1]Si-O (TO_4∼ 1200cm^{-1}, LO_4∼ 1160cm^{-1},TO_3∼ 1080cm^{-1},LO_3∼ 1250cm^{-1},TO_2∼ 810cm^{-1},LO_3 ∼ 820cm^{-1}) [Kirk 88, Bensch 90]

[2]Si-H (stretching∼2100 cm^{-1},wagging∼640 cm^{-1},∼890 cm^{-1}) [Shanks 80, Shanks 81, Satoh 85]

[3]N-H (stretching∼3320-2500cm^{-1}, bending∼1140-1200cm^{-1}) [Coates 00, Lin 02]

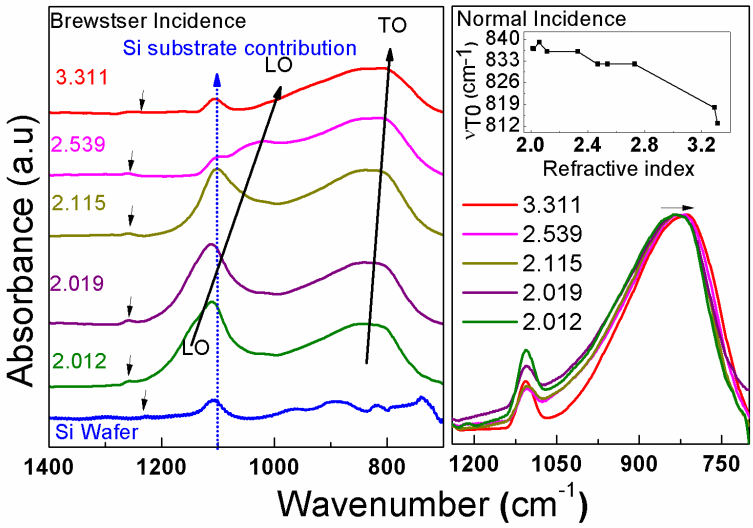

Figure 4.3: Evolution of FTIR spectra with refractive index as observed in Brewster and normal incidences; (Inset) TO_{Si-N} peak positions versus refractive index.

The peak around 1106 cm^{-1} prominently seen in samples with high refractive indices in Brewster incidence spectra and in all the samples in normal incidence spectra can be confirmed as Si substrate contribution for two major reasons:

1. The Brewster incidence spectra clearly shows the overlapping of LO_{Si-N} mode and the 1106 cm^{-1} peak at lower refractive indices. With increasing refractive indices, there is a shift of the LO_{Si-N} mode towards lower wavenumbers, whereas the peak at 1106 cm^{-1} remains unchanged and is distinctly seen. This peak position coincides with that observed in Si wafer.

2. A low intensity peak around 1250 cm^{-1} is observed in Brewster incidence spectra, suggesting a minimal contribution of Si-O bonds. Hence this peak can be attributed to the interstitial oxygen in Si substrate (similar to that witnessed at 1107 cm^{-1} in SRSO samples) or the thermal oxide on the substrate whose contribution is witnessed better with decreasing sample thickness.

It can be seen from both Brewster and normal incidence spectra that the LO_{Si-N} and TO_{Si-N} band redshifts with increasing refractive index. Similar shifts of the LO and TO bands were observed in hydrogenated SiN_x films and were reasoned as the hydrogen incorporation [Lin 92, Vernhes 06, Bustarret 98, Lucovsky 83]. Since our samples are hydrogen free, these shifts can be attributed to modification in the Si-N bonding configuration. A redshift of the TO mode with increasing refractive index, as observed in our case (Inset of Fig. 4.3) was reported in [Hasegawa 93] and attributed to a decrease in the Si-N bond length with changing composition of SiN_x.

The stress in the films induced by Si incorporation may also be a possible reason for these shifts as reported by [Huang 97]. Moreover, in addition to the redshift of the LO_{Si-N} peak, the peak intensity decreases and appears to merge with the TO_{Si-N} peak.

The increasing refractive indices denote a higher Si incorporation in the material resulting in a lower concentration of Si-N bonds. This may lead to the decrease of peak intensities. With varying refractive indices, the LO mode shows a more pronounced shift in the peak position than the TO_{Si-N} mode. This is in agreement to an earlier work [Huang 97] which showed that the LO_{Si-N} peak positions are better indicators of SiN_x composition than TO_{Si-N}. The LO-TO overlapping of the Si-N asymmetric stretching modes may be attributed to the disorder in the material that increases with higher Si incorporation similar to that reported in silicon oxide [Kirk 88].

Figure 4.4 shows the FTIR spectra of as grown and annealed SRSN samples ($n_{1.95eV} = 2.44$) recorded in Brewster incidence, and under normal incidence (inset). The structure of the as grown sample is compared with three parts of the sample annealed at 1min-1000°C (STA), 1h-900°C and 1h-1100°C (CA). It can be seen from the Brewster incidence spectra that the intensity of the LO_{Si-N} mode increases with annealing whereas the TO modes in all the annealed samples have similar intensities. The LO_{Si-N} and TO_{Si-N} modes shift towards higher wavenumbers with annealing, indicating a rearrangement towards stochiometric Si nitride with lower disorder. This may be due to a phase separation process into Si and Si_3N_4 as observed in the case of SRSO materials.

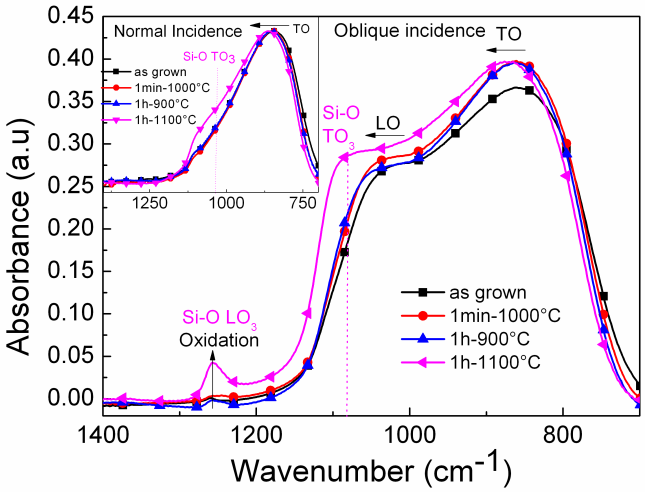

Figure 4.4: FTIR spectra of reactively sputtered SRSN as a function of annealing, recorded in Brewster incidence and (Inset) normal incidence.

It is interesting to note a sudden increase in intensity of the peak around 1250 cm^{-1} after CA. This peak position is attributed to the contribution from $(LO_3)_{Si-O}$ streching vibration. The drastic increase in intensity of this peak along with a broadened shoulder around 1080 cm^{-1} suggests the possible oxidation of the SiN_x

samples from atmosphere since this shoulder lies at the $(TO_3)_{Si-O}$ peak position.

The inset of figure 4.4 shows that the spectra recorded in the normal incidence also exhibits a similar behaviour with annealing. There is a shift of the TO mode between 843-864 cm^{-1} indicating a rearrangement of the Si and N atoms. The TO peak after CA shows an increased width which is attributed to an overlapping of TO_{Si-N} with $(TO_3)_{Si-O}$ modes due to oxidation.

(b) X-Ray Diffraction

The XRD spectra obtained from as-grown, STA and CA SRSN samples ($n_{1.95eV}$=2.44) are shown in figure 4.5. A peak around 28° corresponding to Si (111) plane appears after CA (1h-1100°C), indicating the formation of Si nanocrystals.

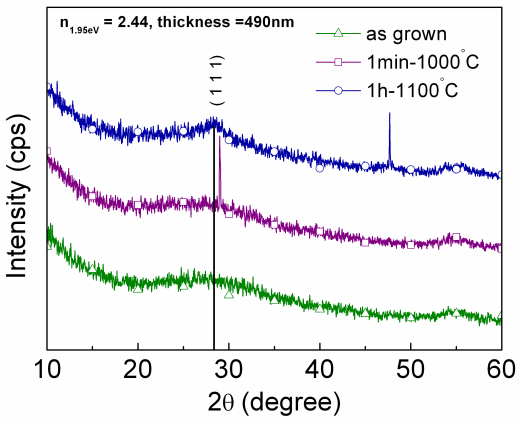

Figure 4.5: XRD spectra of as-grown and annealed SRSN samples grown by reactive sputtering.

The XRD spectra of the as-grown and STA samples are similar with a broad peak between 20-30°. This may be attributed to the presence of amorphous Si clusters that begin to form even during the growth process, due to the Si excess ($n_{1.95eV} \sim 2.44$) and high temperature of deposition (500°C). The investigations parallely conducted in our team on thinner samples (100-200 nm) revealed that despite a Si excess in SiN_x materials, the formation of Si nanocrystals were not observed for samples with $n_{1.95eV} < 2.4$ [Debieu 12]. The observation of nanocrystals in our case may suggest that we are at a value of refractive index close to the threshold to form nanocrystals. The peak around 56° in all the spectra is a contribution from the Si substrate, as mentioned earlier.

(c) Raman spectroscopy

The formation of Si-np was also analyzed by Raman spectroscopy on SRSN layers ($n_{1.95eV} \sim 2.44$) grown on fused silica substrate after subjecting to STA and CA treatments. The Raman spectra recorded by varying the laser power density between 0.14 and 0.7 MW/cm^2 are presented in figure 4.6. The Stokes shift in eV is marked on the upper scale in the figure. The inset shows the PL spectra obtained in the Raman set-up using a higher power density of 1.4 MW/cm^2.

Initially the laser power density was kept minimum (0.14 MW/cm^2) to avoid any possible influence of laser heating on the microstructure of our material. The two broad peaks around 150 and 480 cm^{-1} are attributed the presence of a-Si and their intensities suggest a significant density of amorphous particles in the material. It can be seen that even with a low power density, the width of the peak between 450-550 cm^{-1} in the CA film reduces as compared to its STA counterpart and a sharp peak around 510 cm^{-1} begins to appear. This latter peak attests the presence of nanocrystals in the material and its low intensity indicates a lower density of nanocrystals. There is no significant change in this peak on increasing the laser power densities implying the absence of laser annealing effect. This may be attributed to our sample whose refractive index 2.44, corresponds to the lower limit required for nanocrystal formation and to the lower diffusion coefficient of Si in SRSN as compared to SiO_2.

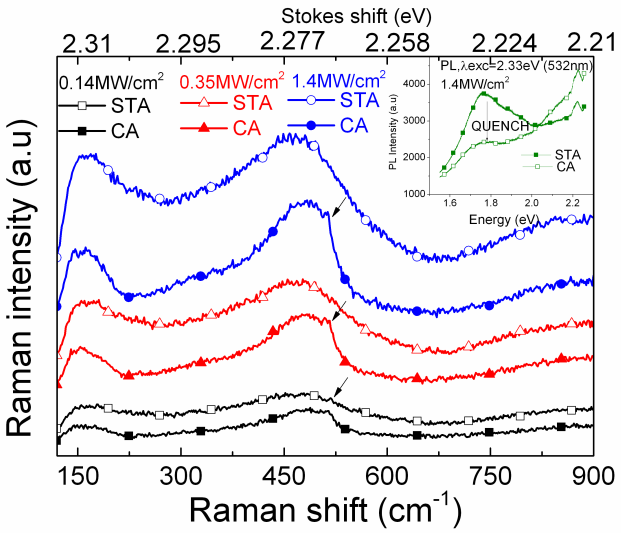

Figure 4.6: Raman spectra of STA and CA SRSN sample ($n_{1.95ev}$ =2.44) grown on fused silica substrate. (Inset) PL spectra obtained in Raman set-up with λ_{exc}=2.33eV (532 nm) and power density 1.4 MW/cm^2.

Considering the possible influence of the substrate on this crystallization, the presence of nanocrystals revealed by XRD from the same material grown on the Si substrate helps us confirm this sharp peak observed through Raman is from our SRSN layer. It is also interesting to note from the inset of figure 4.6 that the PL is quenched in CA sample despite the formation of nanocrystals, suggesting nanocrystals have a detrimental effect on emission.

4.2.3 Optical properties

The microstructural investigations reveal the presence of Si-np, and the Raman studies suggest a decrease in emission intensity associated with nanocrystal formation. In order to understand if such a suggestion is valid, investigations on the photoluminescence and absorption coefficients were made with regard to refractive indices and annealing.

The absorption coefficient studies were initially made on the thinner SiN_x as-

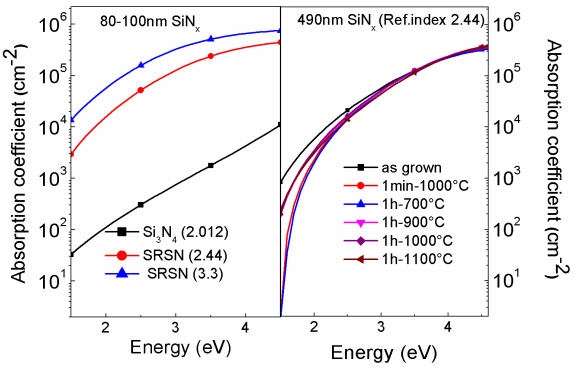

(a) Absorption coefficient curves.

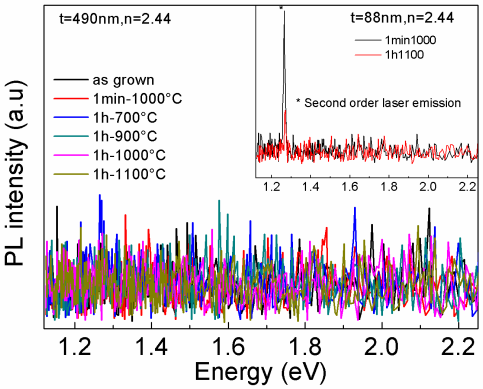

(b) PL spectra.

Figure 4.7: The absorption coefficient and photoluminescence spectra obtained from SRSN samples, with regard to refractive index and annealing.

grown samples (80-100 nm thick) with three different compositions (refractive indices 2.012, 2.44 and 3.3 that are close to Si_3N_4, SRSN and Si respectively). The left part of figure 4.7a shows that the absorption increases with increasing Si excess, which can be attributed to the higher density of Si-np formed in the material.

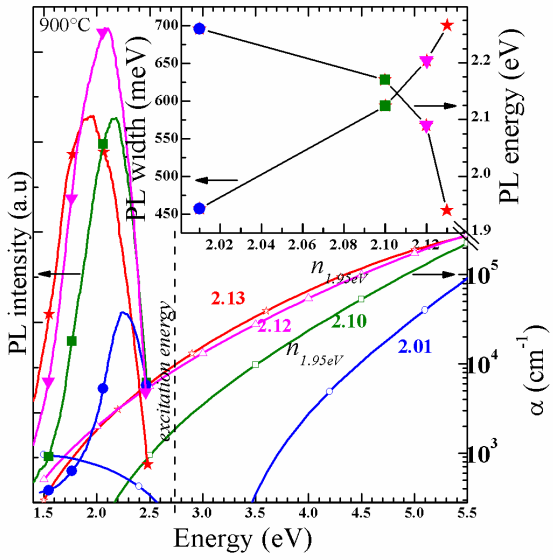

Figure 4.8: Optical investigations on SiN_x monolayers with $n_{1.95eV}$ between 2.01 and 2.13.

Comparing the SRSN samples with same refractive index in the left and right part of this graph, it is interesting to note that with increasing thickness the absorption coefficient of the material is lower, whatever be the annealing treatment. This difference cannot be explained at the moment. However the absorption does not vary with annealing for energies higher than 3 eV.

In the case of PL properties, both the thin and thick SRSN samples ($n_{1.95eV}$=2.44) do not exhibit any emission in their as grown or annealed state whatever the temperature or time of annealing as can be seen from figure 4.7b.

A detailed analysis by a fellow researcher in our team, Dr. O. Debieu revealed that emission is obtained only from samples that possess refractive indices between 2.0-2.13 when annealed at temperatures lower than CA. Figure 4.8 shows consolidated results of his optical investigations. These results also confirmed the absence of PL for $n_{1.95eV}$>2.4 whatever the annealing treatment.

The maximum PL was obtained after annealing at 900°C, and an increase in absorption coefficient with refractive indices is noticed. For the Si_3N_4 sample ($n_{1.95ev}$ = 2.01), a drop of α in the absorption spectra is noticed between 2.5-3.5 eV at the PL excitation energy which may explain the low emission intensity of this sample. For the other cases, the emission intensity increases with refractive indices till 2.12 and then begins to fall. This decrease is attributed to the increase in the non-radiative recombination rates with increasing disorder in the matrix brought by incorporating higher Si excess [Debieu 12].

4.3 Cosputtering of Si_3N_4 and Si cathodes

The SiN_x layers were grown at 3 mTorr and T_d=500°C by using Si_3N_4 and Si cathodes in pure Ar plasma. One sample of N-rich silicon nitride (NRSN) was also grown by sputtering the stochiometric target in N_2+Ar plasma to compare with Si_3N_4 and SRSN samples. The RF power density applied on Si_3N_4 cathode was maintained at 7.4 W/cm^2 while that on Si cathode was varied between 1.77 and 2.96 W/cm^2.

4.3.1 Refractive index ($n_{1.95eV}$) and Deposition rates (r_d)

Figure 4.9 shows the variation of refractive index (left axis) and deposition rate (right axis) with respect to P_{Si}. The refractive index increases from 2.3 to 2.82 with increasing P_{Si}. This is a signature of increasing the Si incorporation in the matrix with P_{Si}.

A direct sputtering from Si_3N_4 cathode in pure Ar plasma results in $n_{1.95eV} \sim 2.30$. This indicates that at our chosen conditions, the sputtering does not yield a stochiometric material. Hence a couple of samples were grown by sputtering Si_3N_4 cathode in N_2-rich plasma to obtain refractive indices relating to Si_3N_4 and N-rich SiN_x (pink and brown circles in the figure). Their values of $n_{1.95eV}$ are also indicated in the figure at P_{Si}=0W/cm^2, signifying only the Si_3N_4 cathode is sputtered for the growth of these layers. The deposition rate increases with P_{Si} which can be explained by the increase in the number of reacting species.

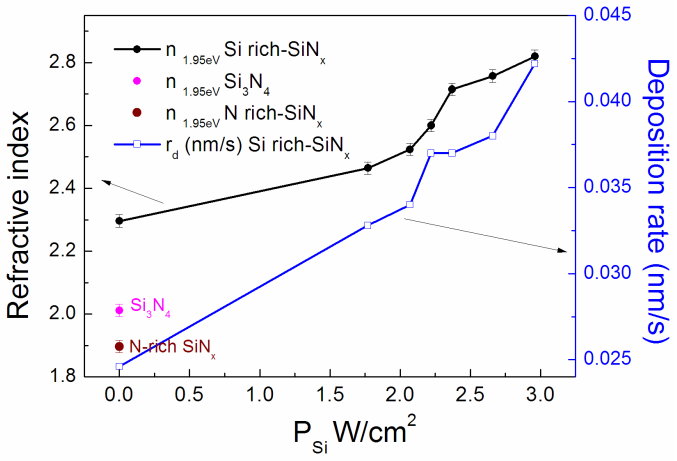

Figure 4.9: Effect of P_{Si} on refractive indices and deposition rates of co-sputtered SiN_x materials. (r_N=5.1% and 7.1% were used for $Si_3N_4$and NRSN layers respectively).

4.3.2 Structural analysis

(a) Fourier transform infrared spectroscopy

Figure 4.10a shows a typical FTIR spectra of NRSN, Si_3N_4 and SRSN samples obtained from layers with $n_{1.95eV}$= 1.9, 2.01 and 2.32 respectively. Similar to the samples obtained by the first deposition approach, these samples also possess only the Si-N bonds and hence the discussions in section 4.2.2 are valid here. The contribution from Si substrate is witnessed by a peak around 1107 cm^{-1} in the normal incidence, whereas in the Brewter incidence it is overlapped by the LO_{Si-N} mode. The LO_{Si-N} and TO_{Si-N} modes shift towards higher wavenumbers with increasing Si incorporation as indicated in the table of figure 4.10a. The evolution of FTIR spectra obtained from SRSN samples with varying refractive indices is shown in figure 4.10b. The decreasing LO_{Si-N}/TO_{Si-N} ratio with refractive index (increasing Si excess) can be well noticed. The trends observed in these samples are exactly similar to those observed in reactively sputtered SiN_x samples (ref. Fig. 4.3).

The effect of annealing on the structure of as-grown and annealed (STA, 1h-900°C and CA) Si_3N_4 (Fig. 4.11a) as well as Si-rich SiN_x sample (Fig. 4.11b) were investigated.

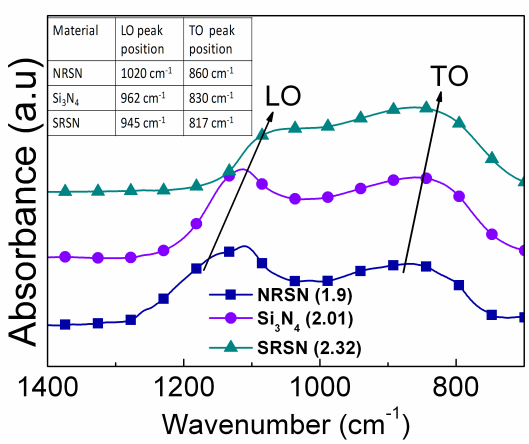

(a) FTIR spectra of NRSN, Si_3N_4 and SRSN.

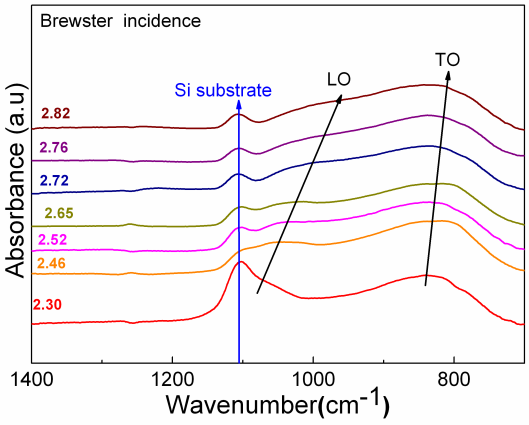

(b) Evolution of FTIR spectra with $n_{1.95eV}$.

Figure 4.10: FTIR spectra of SiN_x monolayers recorded in Brewster incidence. The table of sub-figure (a) shows the peak positions of LO_{Si-N} and TO_{Si-N} modes obtained by gaussian curve fitting.

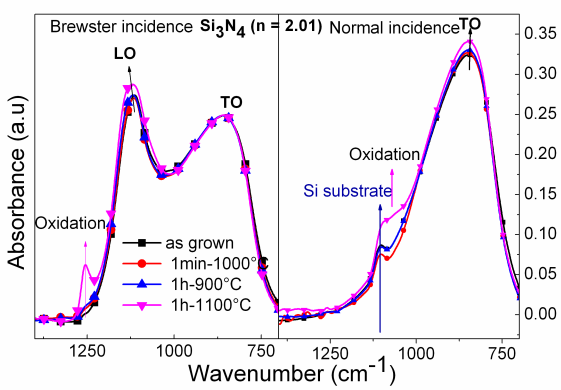

(a) Si_3N_4

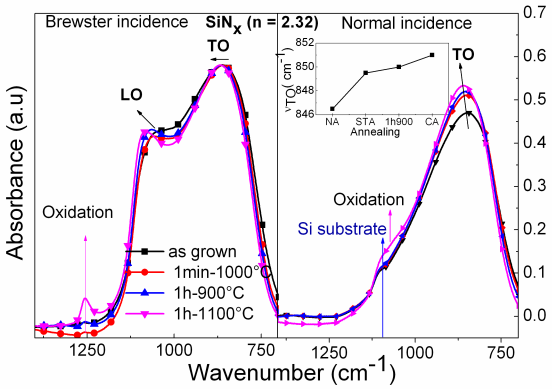

(b) SRSN

Figure 4.11: Effect of annealing on the structural properties as investigated by Brewster and normal incidence FTIR spectra on (a) Si_3N_4 and (b) SRSN.

Both the samples show a similar evolution with annealing as observed from samples grown by the first approach. The sample undergoes oxidation after CA, as can be seen from peaks around 1250 cm^{-1} and 1080 cm^{-1} in Brewster incidence and normal incidence spectra respectively, indicating the LO_3 and TO_3 modes of Si-O.

In the case of Si_3N_4 layers, the LO_{Si-N} peak intensity increases with annealing and shifts towards higher wavenumber whereas the TO_{Si-N} peak increases in intensity but remains at a fixed position. These increase in intensities may indicate a

structural rearrangement of the matrix, while the fixed TO_{Si-N} position indicates the quality of the stochiometric layer desposited, within the sensitivity of the instrument. In SRSN sample, annealing leads to an increase in the LO_{Si-N} and TO_{Si-N} peak intensities accompanied with a shift towards higher wavenumbers. This could be explained by the phase separation process in Si-rich material with annealing. From the FTIR analysis, it can be seen that the structural properties of SRSN samples depend only upon the composition (refractive index) and not on the deposition approach.

(c) Raman spectroscopy

The Raman spectroscopy was performed on Si_3N_4 and SRSN samples after annealing: STA (1min-1000°C) and CA (1h-1100°C). The Raman spectra obtained on these samples at different laser power densities ranging between 0.14-0.7 MW/cm^2 are shown in figures 4.12 and 4.13. The PL intensity of both the layers after STA and CA annealing were also recorded in the Raman set-up at a higher laser power density (1.4 MW/cm^2) and are shown in the inset. As mentioned in chapter 2, the excitation wavelength is 532 nm (2.33 eV) corresponding to the green laser and Raman shift of 0 cm^{-1} corresponds to 2.33 eV. The Stokes shift in eV is calculated from the relative Raman shifts recorded, and is given in the upper scale of the figure.

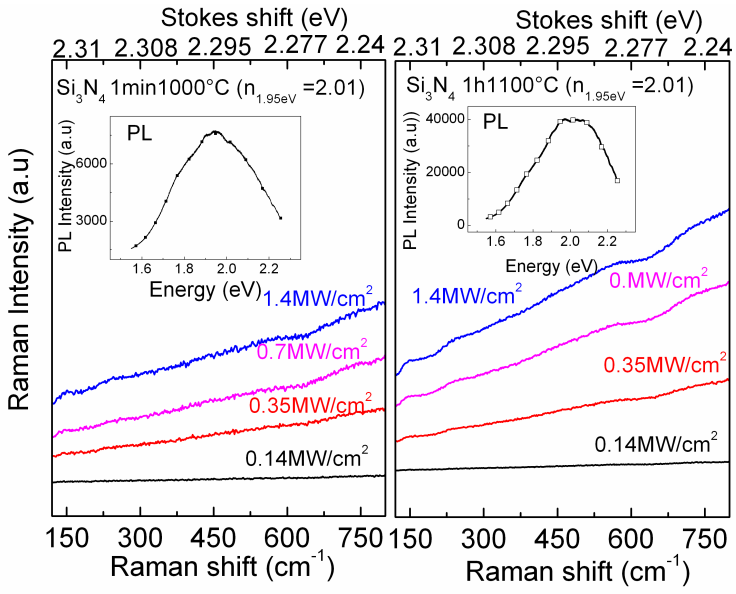

Figure 4.12: Raman spectra obtained with different laser power densities from 1min-1000°C and 1h-1100°C annealed Si_3N_4 layers. The inset contains the corresponding PL spectra [laser power density = 1.4 MW/cm^2 and $\lambda_{excitation}$=532 nm (2.33 eV)] in the Raman set-up.

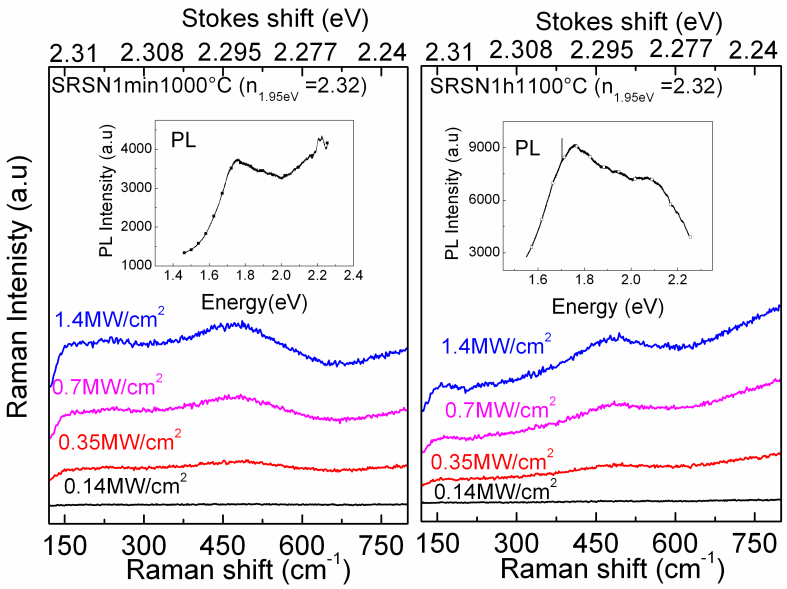

Figure 4.13: Raman spectra obtained with different laser power densities from 1min-1000°C and 1h-1100°C annealed SRSN layers. The inset contains the corresponding PL spectra [laser power density = 1.4 MW/cm^2 , $\lambda_{excitation}$=532 nm (2.33 eV)] in the Raman set-up.

The absence of broad a-Si TA and TO peaks around 150 and 480 cm^{-1} and sharp c-Si peak around 510 cm^{-1} in figure 4.12 confirms the stochiometry of this sample as indicated by ellipsometry measurements. An overall increase of the Raman curves is noticed in this figure, which can be related to the shoulder of the PL band. This argument is supported by the PL spectra obtained at a higher photon flux (laser power density = 1.4 MW/cm^2) in the Raman set-up, that shows emission centered around 2 eV (Inset of Fig. 4.12). Moreover, a larger shift of the Raman curve is noticed corresponding to a more intense emission in the CA sample than the STA layer.

The two peaks around 150 and 480 cm^{-1} of a-Si is evidently seen in SRSN sample attesting the presence of excess Si (Fig. 4.13). The absence of sharp c-Si peak indicates that the material is only composed of amorphous clusters. This confirms that refractive index alone rules the material properties and not the deposition approach, since according to our previous arguments with $n_{1.95eV}$ = 2.32, we are below the threshold of forming nanocrystals.

4.3.3 Optical properties

(a) Photoluminescence

The photoluminescence curves of Si_3N_4 and SRSN ($n_{1.95eV} = 2.32$) samples with regard to annealing are as shown in figure 4.11. It can be seen that the Si_3N_4 sample exhibits PL of very low intensity between 1.8-2.2 eV, which increases with annealing. This can be attributed to some radiative defects in the material. The spectrum was recorded with a 500 nm high pass filter and hence the curve is cut off after 2.2 eV. No emission is observed from SRSN sample whereas in the Raman set-up emission was observed from the same sample. The difference in emission intensities of these samples when measured in the PL and Raman set-up, can be attributed to the different excitation power densities used in the experiments (1.4 MW/cm^2 in Raman set-up versus 10 W/cm^2 in the PL set-up).

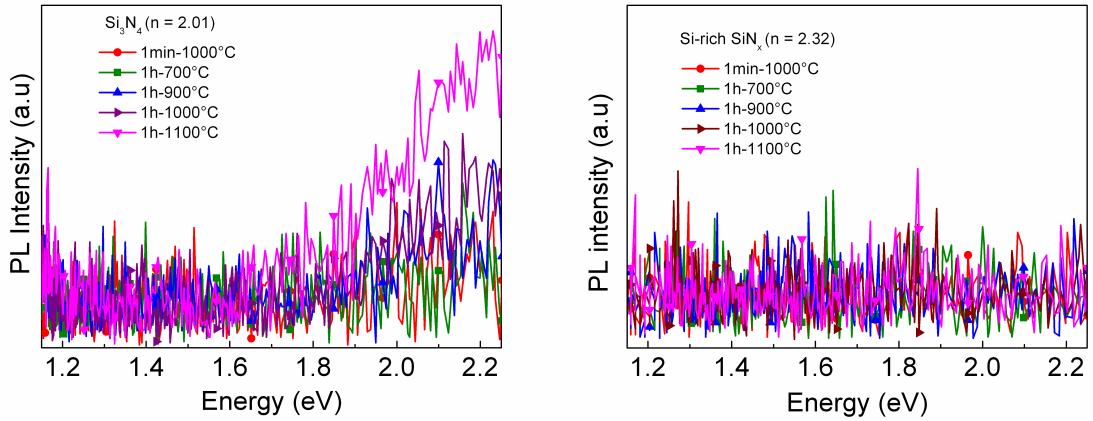

(a) Si_3N_4 **(b)** SRSN

Figure 4.14: Effect of annealing on photoluminescence of Si_3N_4 and SRSN layers. ($\lambda_{excitation}$=488 nm and laser power density= 10 W/cm^2).

(b) Absorption coefficient, (α)

The absorption coefficient curves obtained from Si_3N_4 and SRSN as-grown samples are as presented in figure 4.15.

It can be noticed from this figure that the trend of the absorption coefficient curves are similar to those obtained in samples grown by the first deposition approach. The Si_3N_4 sample has a low absorption in comparison to SRSN samples and all the curves show a steadily increasing α values with energy as well as with refractive index (increasing Si excess). The trend of α for this latter case is attributed to the increase of Si-np density with Si incorporation.

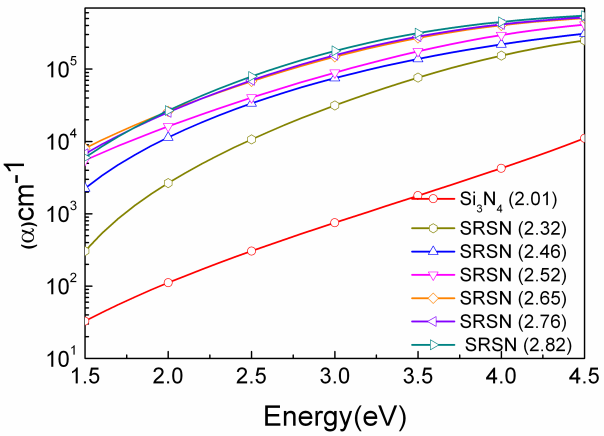

Figure 4.15: Absorption coefficient spectra of Si_3N_4 and SRSN samples.

4.4 Summary

SiN_x materials were grown by two different deposition approaches: Reactive sputtering and Co-sputtering. Three kinds of SiN_x layers were grown: N-rich silicon nitride (NRSN), Si_3N_4 and Si-rich silicon nitride (SRSN). It was demonstrated that the refractive index of the layer is the ruling factor and the deposition approaches do not influence the material properties of these layers.

NRSN:

NRSN material was grown by sputtering Si_3N_4 cathode reactively under N_2 plasma. FTIR and refractive index studies confirm this layer is N-rich.

Si_3N_4:

Stochiometric layer was grown by sputtering Si_3N_4 cathode reactively under N_2 plasma. The refractive index and FTIR investigations indicate that the grown layer is Si_3N_4. The material exhibits low PL emission which increases upon annealing reaching the highest for 1h-1100°C (CA). The material shows a low absorption that increases with energies.

SRSN:

SRSN layers with various refractive indices were investigated. It was shown that by using appropriate r_N in the first deposition approach orP_{Si} in the second one, we can tune SiN_x composition close to Si_3N_4 or pure Si layers. The SRSN layers grown by both the deposition approaches have similar trend in structural and optical

properties. The increasing Si incorporation with refractive indices is reflected in all the characterization techniques. Based on the investigations, the results on SRSN can be summarized under two categories:

(a) $n_{1.95eV} \leq 2.4$

- There is no formation of nanocrystals. For samples with low refractive indices ($n_{1.95eV}$=2.0-2.2) the absence of nanocrystals is attributed to the low Si excess and to the low D_{Si} in SRSN as compared to SiO_2. For samples with refractive indices between 2.3-2.4, this may be attributed to the low power density provided during thermal annealing, which does not favour crystallization.
- The material exhibits photoluminescence depending on the applied laser power density.
- With increasing refractive indices (Si excess), the emission decreases and the absorption coefficient increases.

(b) $n_{1.95eV} \geq 2.4$

- The threshold of refractive index for forming nanocrystals in SRSN matrix is demonstrated. XRD and Raman measurements confirm the presence of nanocrystals.
- No emission is observed from PL measurements whatever be the annealing, while from Raman measurements emission is witnessed. This emission is quenched after 1h-1100°C annealing. Correlation between formation of nanocrystals and quenching of PL suggest that nanocrystals might have a detrimental effect on emission in SRSN materials.
- The absorption coefficient decreases with increasing sample thickness.

4.5 SRSO/SRSN multilayer

The microstructural and optical analyses of SRSO/SRSN MLs grown by RF sputtering technique is demonstrated in the following sections. It was seen in chapter 3 that the best material properties in SRSO/SiO_2 MLs (formation of nanocrystals, emission, absorption etc.) are obtained after CA (1h-1100°C annealing). Hence the SRSO/SRSN ML is also subjected to CA for initial investigations. The material properties of CA sample are compared with those obtained from their as-grown MLs.

A multilayer composed of 100 patterns of 3.5 nm-SRSO and 5 nm-SRSN, (which will be referred as 100(3.5/5)) is chosen as a typical example for these initial investigations. The SRSN sublayers in this sample are grown using reactive sputtering approach.

4.5.1 Ellipsometry

The total thickness, roughness and pattern thickness of the 100(3.5/5) ML were analyzed using ellipsometry. Figures 4.16 and 4.17 show the results of ellipsometry simulations of the as grown and CA samples. The fits were performed assuming the SRSO/SRSN multilayer to be a constant refractive index homogenous layer.

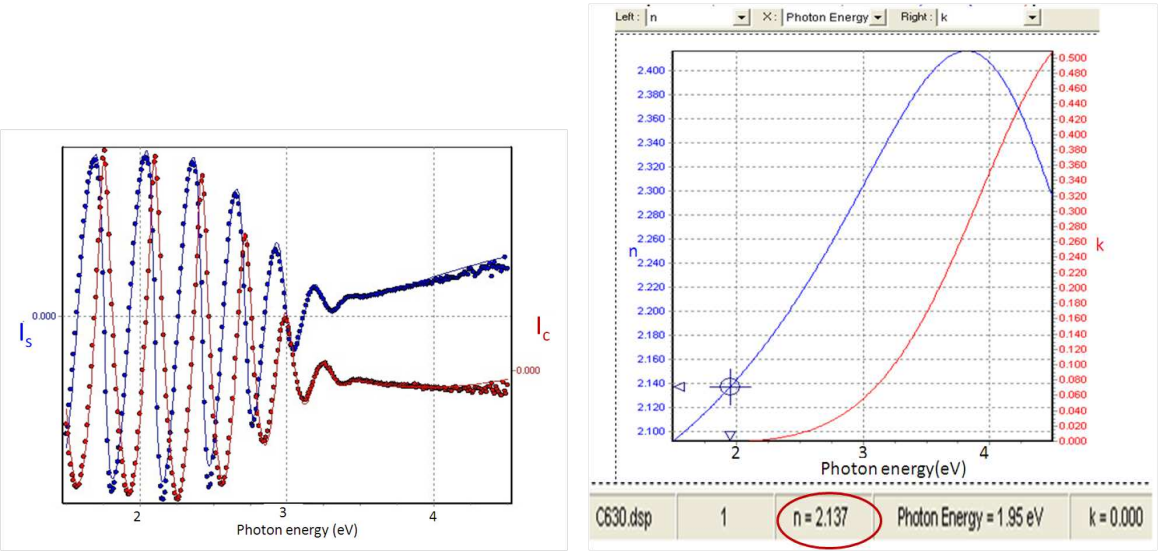

(a) **(b)**

Figure 4.16: As-grown 100(3.5/5) ML. (a)Fitting of the ellipsometric functions (Is & Ic as a function of photon energy). The circles relate to experimental spectra and the lines to the fitting, and (b) The dispersion curves, n_{eV} & k_{eV} of the real and imaginary parts of refractive indices respectively; $n_{1.95}eV = 2.137$ is highlighted in the figure.

It can be noticed in the results obtained from as-grown and CA 100(3.5/5) MLs (Fig. 4.16a and 4.17a) that with such an approximation the theoretical spectra well fit the measured ones. Moreover, the 832 nm thickness of the as grown sample deduced from ellipsometry closely relates to the expected thickness of 850 nm [$(100_{pattern}$ x $3.5_{t_{SRSO}}) + (100_{pattern}$ x $5_{t_{SRSN}})$]. As highlighted in figures 4.16b and 4.17b, the refractive index of the as-grown sample, $n_{1.95eV}$ =2.13 increases to 2.34 after CA. This increase is also accompanied by a reduction in thickness of the CA sample to 777 nm (as-grown sample = 832 nm) thereby indicating a densification process favoured by annealing.

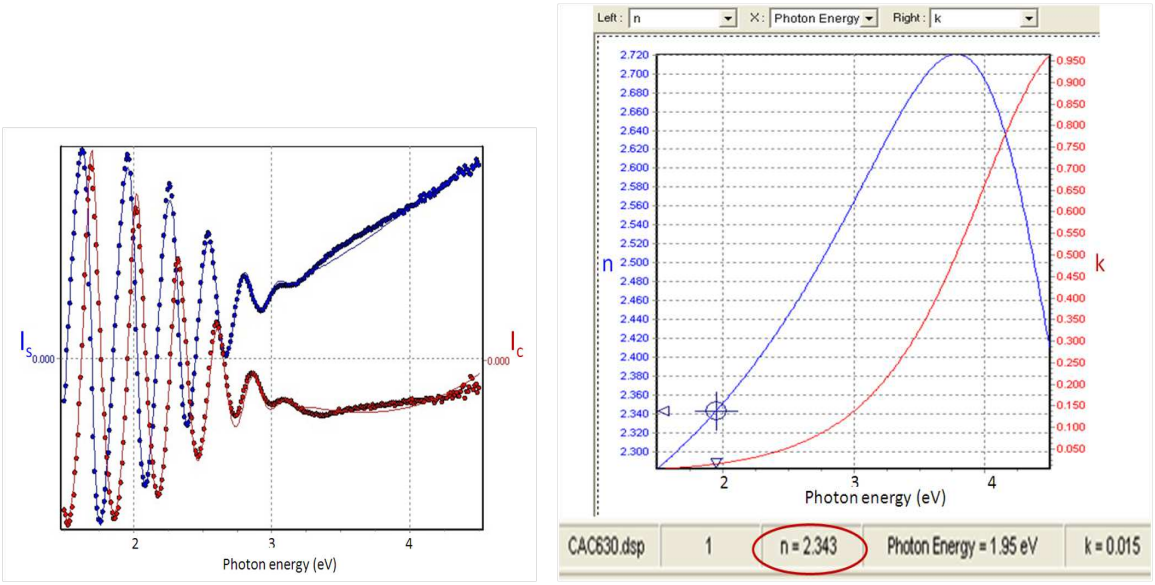

(a) . **(b)**

Figure 4.17: 1h-1100°C annealed (CA) 100(3.5/5) ML. (a)Fitting of the ellipsometric functions (Is & Ic as a function of photon energy). The circles relate to experimental spectra and the lines to the fitting, and (b) The dispersion curves, n_{eV} & k_{eV} of the real and imaginary parts of refractive indices respectively; $n_{1.95}eV = 2.343$ is highlighted in the figure.

4.5.2 X-Ray Reflectivity

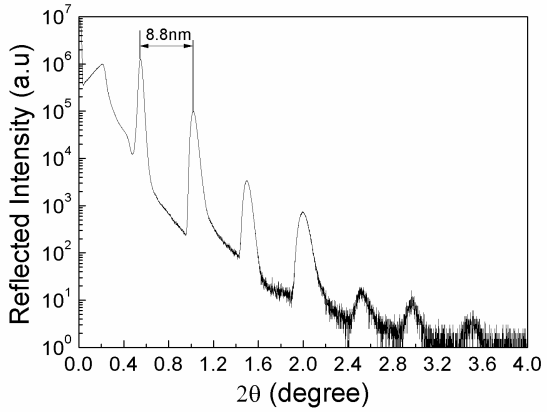

Figure 4.18: XRR spectrum of 100(3.5/5) ML.

The XRR technique was used to estimate the pattern thickness of the MLs. Figure 4.18 shows the spectrum obtained from CA sample which is similar to the one recorded from the as-grown sample (not shown). This figure clearly shows the repetitive peaks relating to the alternated SRSO and SRSN patterns in our

multilayered configuration. Therefore, the (SRSO+SRSN) pattern thickness of the multilayer was calculated and found to be 8.8 nm.

This value is close to the expected pattern thickness of 8.5 nm (3.5 nm + 5 nm) indicating that, the pattern thickness can be estimated from XRR technique to a high degree of accuracy. Hence most of the MLs in this thesis were investigated by XRR.

4.5.3 Fourier transform infrared spectroscopy

The FTIR spectrum of the as-grown ML recorded in Brewster incidence is showed in figure 4.19a. It can be clearly seen that the spectrum is composed of multiple peaks which overlap with each other due to the contribution of Si-O and Si-N bonds from SRSO and SRSN sublayers respectively.

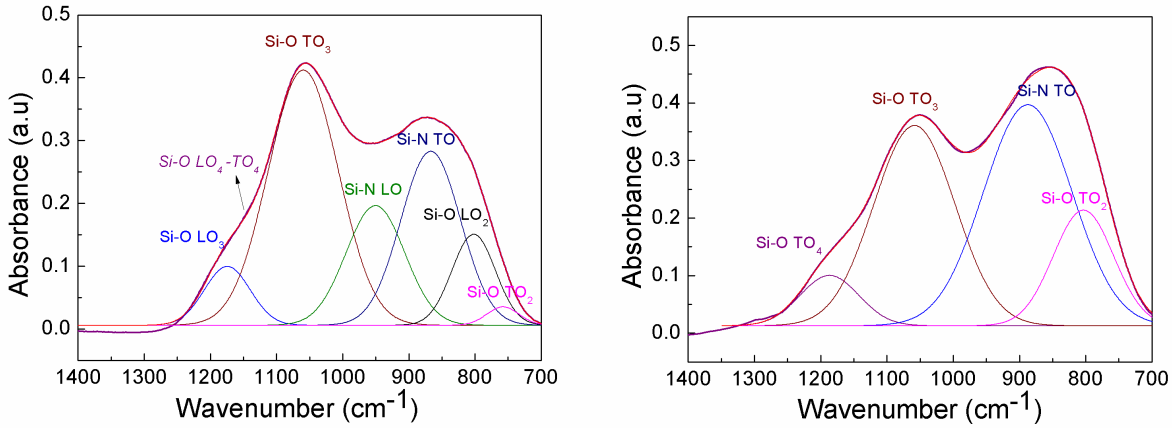

(a) Brewster incidence. **(b)** Normal incidence.

Figure 4.19: FTIR spectra (thick line) of as grown 100(3.5/5) ML. The spectra is decomposed into six gaussians and four gaussians in the Brewtser incidence and normal incidence spectra respectively.

The spectrum is fitted with six peaks, corresponding to the asymmetric stretching modes of SRSO and SRSN sublayers. The peaks centered around 1175 cm^{-1}, 1059 cm^{-1}, 802 cm^{-1} and 758 cm^{-1} can be attributed to the LO_3, TO_3, LO_2 and TO_2 peaks of Si-O bonds respectively while those at 954 cm^{-1} and 866 cm^{-1} can be ascribed to the LO & TO peaks of Si-N. All the peaks except TO_{Si-N} mode are shifted towards lower wavenumbers as compared to the (LO and TO)$_{Si-N}$ modes observed in monolayers (ref. FTIR in Sec. 4.2.2). There may be three possible reasons that induce this shift in the TO_{Si-N} mode towards higher wavenumbers in MLs:

1. Difference in bonding angles in monolayer and ML configurations.

2. Possible formation of Si-O-N bonds at the interface of SRSO and SRSN sublayers.

3. It has been reported in SiN_x monolayers that the presence of nitrogen atoms as the next nearest neighbours would induce a shift of the TO mode towards higher wavenumbers [Molinari 03]. The same proposition can be assumed in the case of SRSO/SRSN MLs.

In addition to these peaks, it also has to be remembered that the $(LO_4\text{-}TO_4)_{Si-O}$ modes may also contribute to the shape and peak positions of the FTIR spectra.

Similarly the normal incidence spectrum also shows the contribution of Si-O from SRSO and Si-N from SRSN layers (Fig. 4.19b) and is fitted with four peaks. The two major peaks centered around 1058 cm^{-1} and 887 cm^{-1} can be unambiguously attributed to the $(TO_3)_{Si-O}$ and TO_{Si-N} modes respectively.

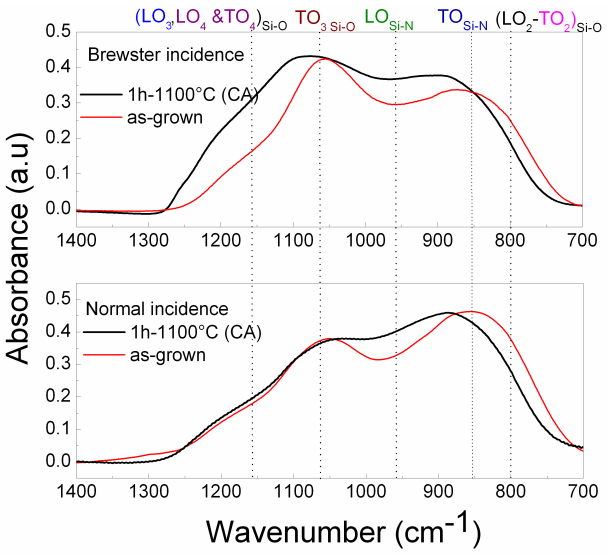

Figure 4.20: FTIR spectra of as-grown and CA 100(3.5/5) ML.

The presence of Si excess in SRSO sublayer is attested by the shift of the $(TO_3)_{Si-O}$ peak position towards lower wavenumbers as compared to that in SiO_2 ($\sim$1080 cm^{-1}). The less intense peaks around 1186 cm^{-1} and 806 cm^{-1} can be attributed to the TO_4 and TO_2 modes of Si-O respectively.

Figure 4.20 shows the the FTIR spectra of as-grown and CA 100(3.5/5) ML recorded in Brewster and normal incidences. The position and intensity of the FTIR bands is a result of an overlapping contribution from Si-O and Si-N modes thereby making the analysis complicated. Hence the identification of the peaks are very difficult after annealing and the fitting of peaks are therefore not appropriate. The approximate peak positions of the different vibration modes are indicated on the top part of the figure. From a comparison of the overall shape of the spectra obtained from the as-grown and CA samples, it can be seen that the Brewtser incidence spectra show a blueshift (towards higher wavenumber) of the peak maximas.

The blueshift of the Si-O modes with annealing is indicative of the formation of Si-np in SRSO sublayer. This is confirmed by the increase of $(LO_3)_{Si-O}$ mode

around 1250 cm^{-1}. The blueshift of the Si-N modes is evident from FTIR spectra recorded in both angle of incidences and can be ascribed to the evolution of SRSN sublayer towards Si_3N_4. Similar shifts have been observed in SiN_x monolayers when annealed at 950°C for $t_A >$ 1h under nitrogen atmosphere [Molinari 03].

4.5.4 Surface Microstructure

Preliminary surface microstructural investigations were performed using optical microscopy on the as-grown and CA 100(3.5/5) ML (Fig. 4.21).

The surface of the as-grown sample is completely smooth whereas the surface of the CA sample shows appearance of circular spots of varying diameters ranging between less than 1 µm to about 200 µm. The possible reasons for appearance of these circular spots can be attributed to the reactive growth process leading to gas (N,H) exodiffusion upon annealing. Consequently, the annealing procedure will be a key point for the achievement of a suitable film.

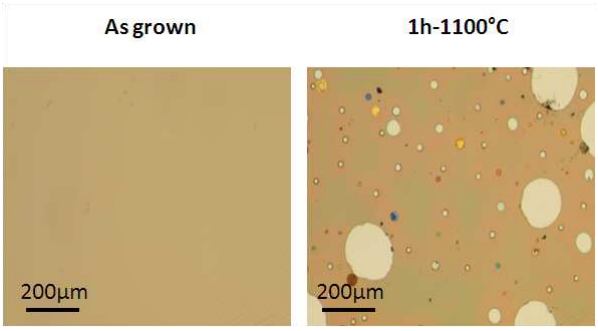

Figure 4.21: Surface microstructure of as-grown and 1h-1100°C annealed (CA) 100(3.5/5) ML.

4.5.5 X-Ray Diffraction

XRD analyses were performed on the as grown and CA samples (Fig. 4.22). The broad peak in the range between 20-30° seen in the as-grown sample relates to the presence of amorphous Si-np. The XRD spectrum of the CA sample exhibits a sharper peak around 28° referring to the Si (111) plane that can be fitted with a single gaussian peak confirming the presence of Si nanocrystals.

The high intensity of (111) peak and the clear presence of (220) peak which is not often witnessed, suggest a high density of Si-np formed in the SRSO and/or SRSN sublayers. Using Scherrer formula, the approximate Si-np size in the

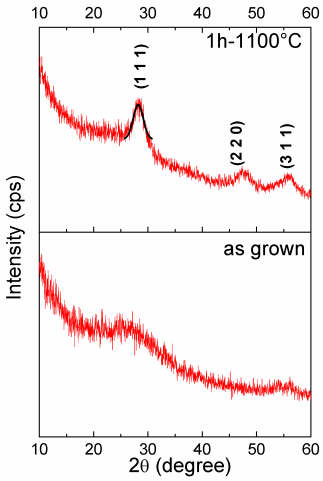

Figure 4.22: XRD spectra of as-grown and CA 100(3.5/5) ML.

CA sample is estimated as 4nm.

4.5.6 High Resolution-Transmission Electron Microscopy

In order to determine the location of nanocrystals, HR-TEM investigations were carried out on CA 100(3.5/5) ML. The microstructure displayed in figure 4.23a shows 100 patterns of perfectly alternated SRSO and SRSN sublayers deposited on a Si substrate (dark part on the bottom). The bright and dark contrasts observed in the film correspond to the SRSO and SRSN sublayers respectively. At this scale, it is not possible to correlate these observations to the ones performed above, on the surface of the film (ref. Fig. 4.21).

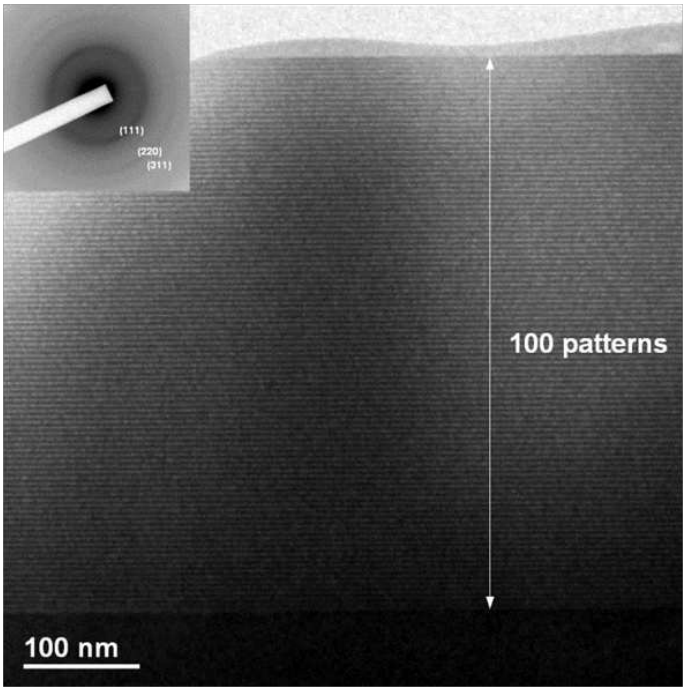

(a) General microstructure and electron diffraction pattern.

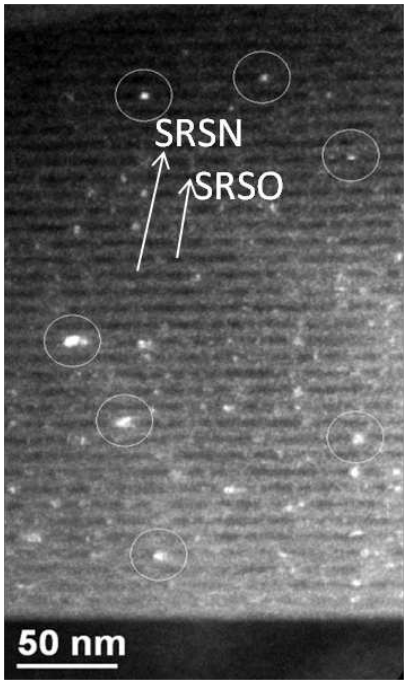

(b) Dark field image with Si(111) reflection. The Si-np are highlighted with a circle around them.

Figure 4.23: TEM images of CA 100(3.5/5) ML.

The inset of figure 4.23a corresponds to the electron diffraction pattern of the film. It reveals the presence of (111), (220) and (311) rings that are the signatures of Si nanocrystal formation in the ML. The corresponding (111) dark field image reveals that the Si nanocrystals are confined in the SRSO sublayers and the brighter SRSN sublayers are devoid of nanocrystals (Fig. 4.23b). A HR-TEM image of this ML (Fig. 4.24) shows the detailed microstructure of the film at the nanometer scale.

The thicknesses of the SRSO and SRSN sublayers are seen to be 3.7 nm and 5.1 nm respectively, confirming the pattern thickness of 8.8 nm deduced from XRR technique. The presence of Si nanocrystals are witnessed only in the SRSO sublayers and most of them were restricted to the 3.7 nm sublayer thickness, coherent with average size estimation from XRD. However, nanocrystals that show overgrowth in both the width and the height were also observed as shown in this figure. The presence of oversized Si nanocrystal could be the consequence of high temperature and time applied on a Si-rich (SRSO, SRSN) film during the annealing process. It can also be noticed that there are regular darker regions (arrows in Fig. 4.24) in the SRSO sublayers that lie along a line. This can be attributed to the path of gas exodiffusion during annealing, as suspected to be one of the reason for surface modifications in the optical microscopy analysis of the CA sample (ref. Fig. 4.21).

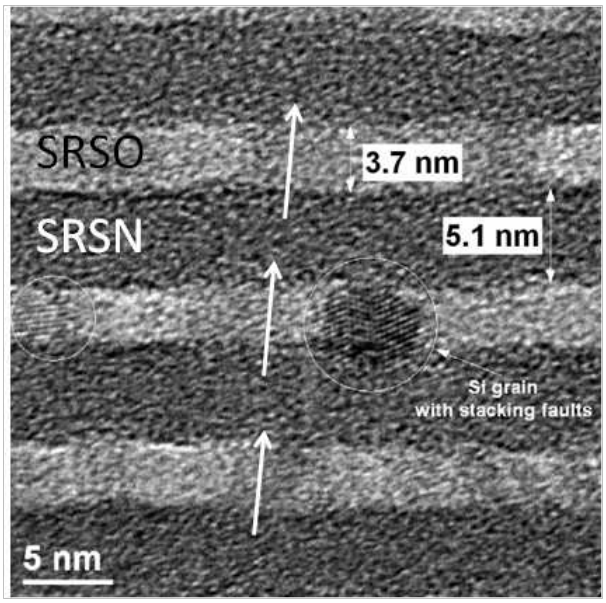

Figure 4.24: HR-TEM image of CA 100(3.5/5) SRSO/SRSN ML. The arrows indicate the possible exodiffusion paths.

4.5.7 Optical properties

(a) Photoluminescence

The PL spectra of as-grown and CA samples of 100(3.5/5) ML are shown in figure 4.25. The SRSO/SRSN as-grown sample shows PL emission contrary to SRSO/SiO_2 samples which did not show emission before annealing. This emission from the as-grown SRSO/SRSN ML achieved by the replacement of SiO_2 by SRSN sublayer suggests that the SRSO sublayer is emitting and the presence of defects in SiO_2 might have quenched the PL in SRSO/SiO_2 MLs.

The as-grown PL spectrum can be seen to contain three peaks centered around 1.41 eV (peak 1), 1.62 eV (peak 2) and 1.88 eV (peak 3). This suggests the presence of different emission centers in the material such as defects or amorphous Si-np in SRSO and/or SRSN sublayers. The position of peaks (1 and 2) might be ascribed to the electron-hole recombination in the Si-np within the frame of QCE [Kanemitsu 97, Ternon 04a, Gourbilleau 09]. Peak (3) closely relates to 1.9eV value reported for

$Si:Si_3N_4$ interfaces [Maria 75] and/or to various defect states in silicon nitride.

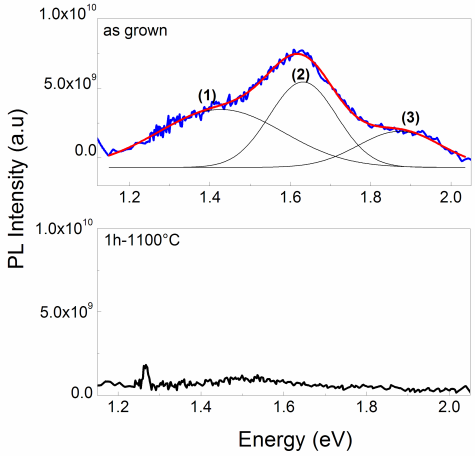

Figure 4.25: PL spectra of as grown and 1h-1100°C (CA) 100(3.5/5) ML.

However, these possibilities of different origins of emission will be analysed and confirmed in the forthcoming sections.

After subjecting to CA, the emission from SRSO/SRSN ML is quenched whereas in section 3.7.2 of chapter 3 it was seen that CA process enhances emission in SRSO/SiO_2 MLs. Since it was seen from XRD and HR-TEM that the average size of the nanocrystals in CA SRSO/SRSN MLs are about 3.8-4 nm, this quenching of PL cannot be attributed to the overgrowth of crystals. These results indicates that SRSN sublayers when annealed at high temperature show a detrimental effect on the emission from SRSN as well as SRSO sublayers.

(b) Absorption coefficient, (α)

The absorption behaviour of the CA 100(3.5/5) MLs were investigated by comparing α values of other Si-based layers investigated in this thesis (Fig. 4.26). The absorption coefficient curves of reference a-Si and c-Si are also presented by using the data from [Internet ta] to facilitate comparison between the absorption behaviours of the thin films.

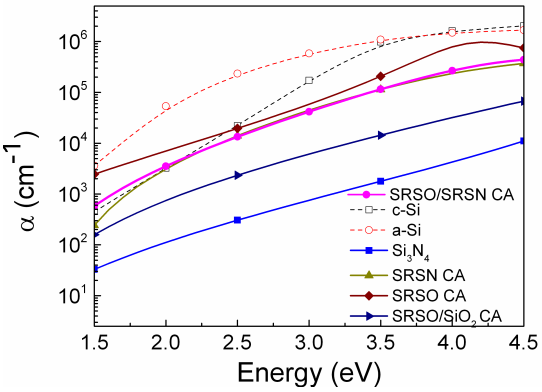

Figure 4.26: Comparison of absorption coefficient curves obtained from CA 100(3.5/5) ML with other CA Si-based thin films investigated in this thesis. The reference absorption curves of c-Si and a-Si are also plotted for comparison [Internet ta].

The absorption coefficient curves are similar in SRSN monolayer and SRSO/SRSN ML, from energies higher than 2 eV. It is interesting to note that the absorption coefficient values are about 10 times higher in SRSO/SRSN MLs as compared to the SRSO/SiO_2 ML, at energies greater than 2.5eV. Besides, in the range of emission energies also (typically 1.4-1.7 eV), the SRSO/SRSN MLs have a higher absorp-

tion but within a difference of one order of magnitude. It can also be seen that at high energies, the level of absorption in SRSO/SRSN ML approaches that of Si. This shows that the replacement of SiO_2 by SRSN sublayers in ML favours absorption.

Despite a higher pump absorption in CA SRSO/SRSN ML, in comparison to SRSO/SiO_2 ML, there is a quenching of PL from the former. This implies that CA SRSO/SRSN ML favours absorption but has a detrimental effect on emission.

4.6 Effect of annealing treatment under N_2 flow

It was seen in the previous sections that the SRSO/SRSN samples contain nanocrystals as SRSO/SiO_2 MLs, but the presence of SRSN sublayers create a detrimental effect on the PL emission after CA. However, both the as grown (not shown) and CA SRSO/SRSN MLs have high α values. These results indicate the possibility of intermediate annealing treatments that might favour PL emission. A detailed investigation on the effect of annealing treatments (temperature and time) was made to optimize the PL emission.

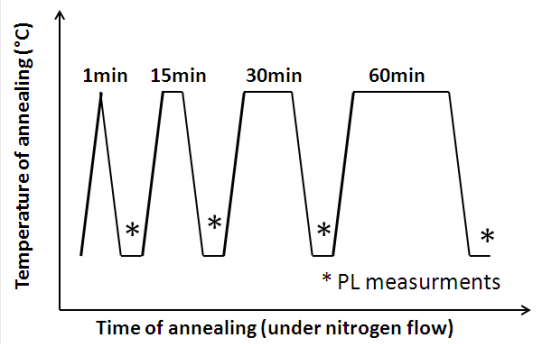

Annealing steps	Denoted as
1min	1min (1min 1000°C-STA)
1+15min	16min
1+15+15min	31min
1+15+15+30min	61min
1h continuous annealing	LTA (1h-1100°C-CA)

Figure 4.27: Pictorial representation of step by step annealing under N_2 flow. (Table) Details of annealing time used for investigation and their notations.

The 100(3.5/5) ML was annealed at various temperatures (T_A) between 400°-1100°C while the time of annealing (t_A) was varied between 1 minute to 61 minutes in steps as can be seen in the pictorial representation of figure 4.27. Continuous Long Time Annealing (LTA) of 1 hour at various temperatures were also performed. The emission obtained from LTA MLs were compared with MLs annealed for 61 minutes in steps. Table of figure 4.27 details the various annealing steps employed for these investigations and the way they are denoted in the forthcoming parts. The effect of T_A and t_A on the emission intensities of SRSO/SRSN ML are discussed below. (All the graphs in the discussions that follow in this section are comparable).

4.6.1 T_A=400°C:

Figure 4.28 shows the PL spectra of SRSO/SRSN MLs annealed at 400°C and their peak positions with respect to various time steps of annealing.

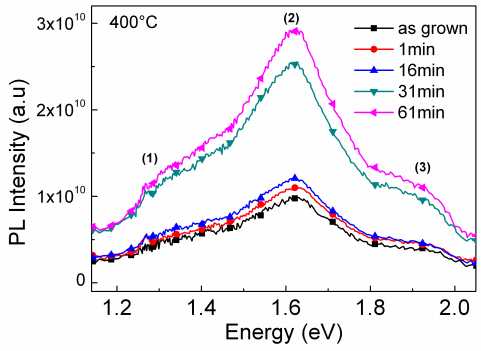

sample	peak 1 (eV)	peak 2 (eV)	peak 3 (eV)
as grown	1.41	1.62	1.88
1min	1.46	1.62	1.95
16min	1.41	1.62	1.91
31min	1.40	1.62	1.86
61min	1.38	1.62	1.87

Figure 4.28: PL spectra of 100(3.5/5) ML annealed at 400°C. The peak positions obtained after gaussian fitting are indicated in the table.

The three peaks obtained after gaussian fitting are indicated as peak (1), (2) and (3) in the figure and the table. It can be seen from the spectra that the emission intensity of all the three peaks increase with t_A. About twofold increase in the emission intensity is observed from the sample annealed at highest t_A as compared to the as-grown sample while the position of peak (2) is always centered at 1.6 eV. The shifts in the peak positions of (1) and (3) are not significant since their maxima are not well defined.

The increase in all the three peak intensities with annealing time may indicate a beginning of reorganization of the matrix and a decrease of the non-radiative defects. The fixed position of peak (2) indicates that there is no modification of Si-np size with increasing t_A due to the low annealing temperature applied here.

4.6.2 T_A=700°C:

Figure 4.29 shows the PL spectra and the peak positions of 100(3.5/5) ML annealed at 700°C.

The presence of three peaks is witnessed at all t_A at this temperature also. Contrary to the previous case, the PL intensity increases only till 16min and then starts to decrease with longer t_A. The previous comment on the shifted peak is still valid for peaks (1) and (3). Concerning the peak (2), its maximum being well defined, the shift is significant as a function of the annealing time. It can be seen that peak (2) is redshifted after 16min of annealing as compared to the as-grown

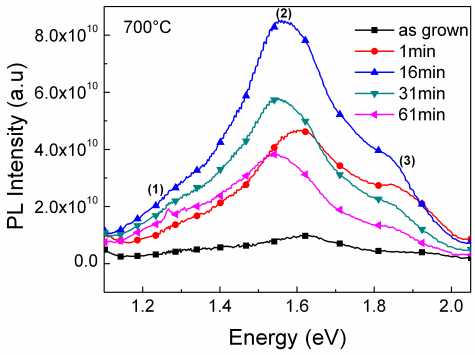

sample	peak 1 (eV)	peak 2 (eV)	peak 3 (eV)
as grown	1.41	1.62	1.88
1min	1.39	1.61	1.85
16min	1.41	1.57	1.80
31min	1.43	1.56	1.80
61min	1.33	1.55	1.80

Figure 4.29: PL spectra of 100(3.5/5) ML annealed at 700°C. The peak positions obtained after gaussian fitting are indicated in the table.

and 1min annealed spectra. This redshift may be attributed to the formation of bigger Si-np. Following the Delerue law [Delerue 93], this shift is linked to a size variation of 0.3 nm. Considering the maximum value of Si diffusion coefficient, $D_{Si} = 10^{-18}$ cm^{2}s^{-1} at this temperature [Nesbit 85], the maximum diffusion length ($l = D_{Si}$ x t_A) after an annealing time of 16min is estimated to 0.3 nm. Consequently, this PL shift can be attributed to the Si diffusion favouring the growth of Si-np. The quench of the PL intensity with further annealing time can be ascribed to this growth of the Si-np as well as the detrimental contribution of the SRSN sublayer.

4.6.3 T_A=900°C:

Figure 4.30 shows the PL spectra and the peak positions of 100(3.5/5) ML annealed at 900°C.

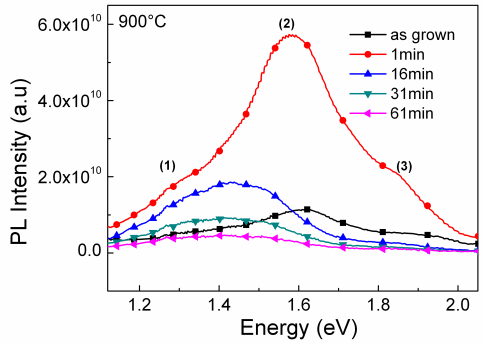

sample	peak 1 (eV)	peak 2 (eV)	peak 3 (eV)
as grown	1.41	1.62	1.88
1min	1.41	1.59	1.80

Figure 4.30: PL spectra of 100(3.5/5) ML annealed at 900°C. The peak positions obtained after gaussian fitting are indicated in the table.

The highest emission intensity is obtained after 1min when annealed at 900°C

and the intensity is gradually decreased for all other t_A. It has to be noticed that for annealing time longer than 1min, the three peak structure disappears. As in the previous case, the shift of the peak (2) with respect to the as-grown sample can be ascribed to the growth of Si-np. The observed decrease of PL intensity for time higher than 1min can be explained in the same way as that in the case of 700°C.

4.6.4 T_A=1000°C:

Figure 4.31 shows the PL spectra and the peak positions of 100(3.5/5) MLs annealed at 1000°C.

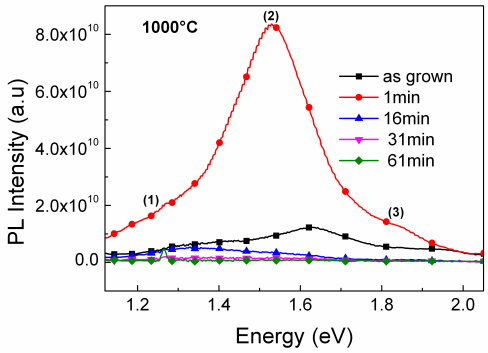

sample	peak 1 (eV)	peak 2 (eV)	peak 3 (eV)
as grown	1.41	1.62	1.88
1min	1.50	1.53	1.85

Figure 4.31: PL spectra of 100(3.5/5) ML annealed at 1000°C. The peak positions obtained after gaussian fitting are indicated in the table.

The behaviour at 1000°C follows a similar trend as the previous case but is more pronounced, with 1min-1000°C (STA) showing the highest intensity followed by a quenching of PL when t_A is long. This behaviour is already explained in the section above.

4.6.5 Influence of short time and long time annealing on emission

It can be noticed from previous discussions that the emission intensities from samples annealed during 1min-1000°C (STA) and 16min-700°C are similar. Considering the thermal budget and the maximum emission intensities, STA can be considered as the best annealing treatment from the analyses done above. In order to witness a possible enhancement of the emission intensity in these MLs with thermal budget, higher temperatures were employed for t_A= 1min. Figure 4.32a consolidates the PL intensities obtained from all the samples subjected to 1min annealing between 400°-1100°C.

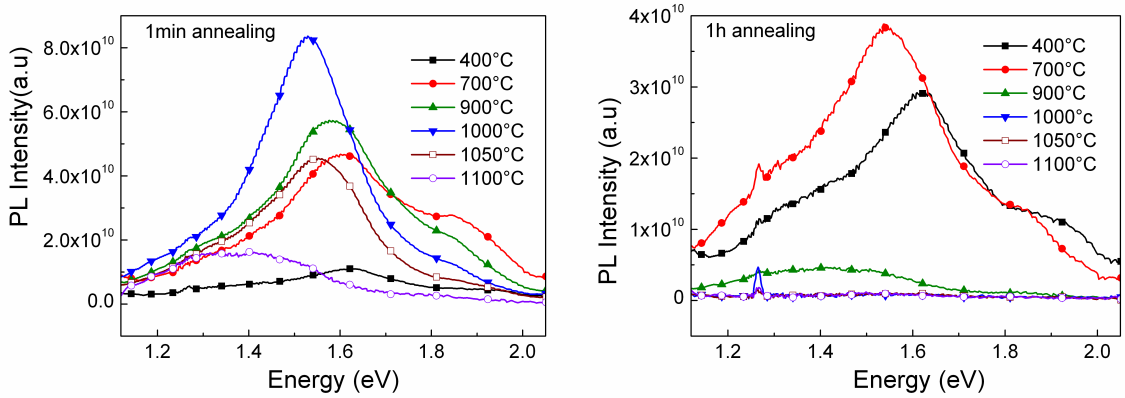

(a) 1min annealing vs. T_A.

(b) 1h annealing (LTA) vs. T_A.

Figure 4.32: Effect of time and temperature of annealing on the emission of 100(3.5/5) ML.

It can be clearly seen that the increase in emission intensity accompanied by a redshift occurs only till 1000°C. With further increase in temperature (1050°C), the PL is quenched and a blueshift is observed. The emission continues to decrease for the highest temperature employed, but the PL peak position is redshifted which could be due to the merging of peak (1 & 2). The intensity of peak (3) decreases with temperature and and completely disappears for the two highest temperatures. The increase in emission intensity with a redshift till 1000°C can be attributed to an increase in the density and size of the Si-np. Figure 4.32b shows the effect of LTA on the PL emission and it can be seen that the PL shape and intensities obtained by step annealing for 61min and continuous annealing (i.e. LTA) are the same. The PL quenches with high temperatures despite the formation of nanocrystals.

4.6.6 Structural analysis on STA SRSO/SRSN ML

In order to understand the reason behind the emission behaviour, structural investigations were performed on STA (1min-1000°C) 100(3.5/5) ML. Figure 4.33 shows the XRD spectrum of the sample. The peak between 20-30° is neither broad as in the as-grown sample, nor sharp as in the case of CA sample as observed in figure 4.22. This implies that the sample is a mixture of both amorphous and crystalline Si-np. Since after CA, there were no nanocrystals in SRSN sublayer as observed by TEM, the formation of crystalline Si-np as suggested by XRD should be only within the SRSO sublayer after STA.

But it was seen from SRSO/SiO_2 MLs that a minimum annealing treatment of 1h-900°C is needed to form Si-nanocrystals in SRSO sublayers. Therefore, in order

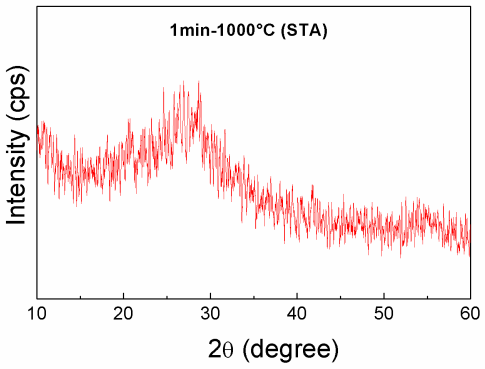

Figure 4.33: XRD spectra of SRSO/SRSN ML.

to confirm if replacing SiO_2 sublayer by SRSN ones could favour the formation of nanocrystals in SRSO/SRSN MLs even after such short time annealing of 1min, HR-TEM investigations were carried out. EF-TEM measurements were also done on this sample to estimate the density of Si-np considering the amorphous particles in SRSO sublayers and their possible presence in SRSN sublayers.

Figure 4.34 shows the microstructural investigations carried out on SRSO/SRSN ML. The dark field image taken under (111) reflection reveals the presence of nanocrystals indicating that STA treatment is sufficient for the formation of nanocrystals thus confirming the XRD results.

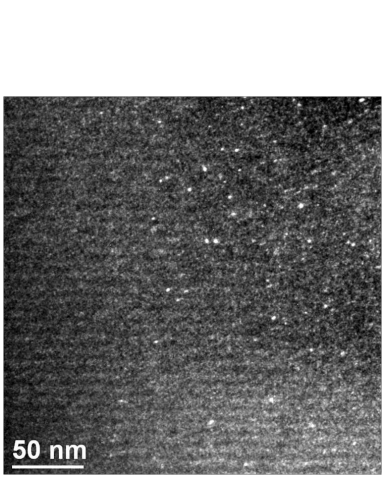

(a) Dark field with Si (111) reflection.

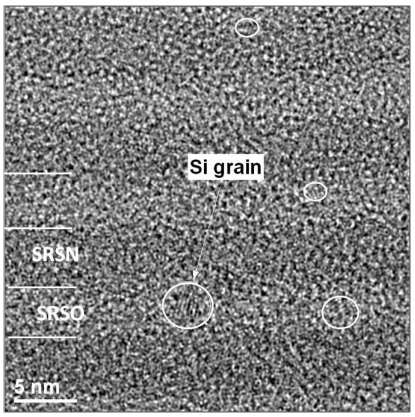

(b) HR-TEM image.

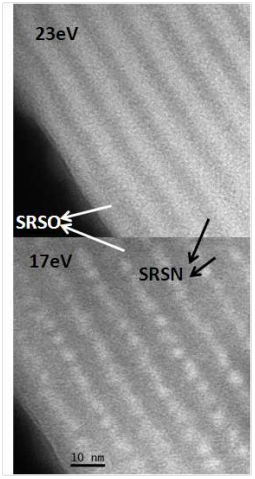

(c) EF-TEM image.

Figure 4.34: Microstructural investigations by (a) TEM, (b) HR-TEM and (c) EF-TEM imaged with Si (17eV) plasmon and O (23eV) plasmon.

The HR-TEM image evidences the presence of few nanocrystals in SRSO sublayer (highlighted with white circles). The EFTEM image obtained by inserting

an energy-selecting slit at the SiO_2 (23 eV) plasmon energy shows the bright and dark contrast of the SRSO and SRSN sublayers respectively. The image taken at Si (17eV) plasmon energy reveals the presence of a high density of Si-np (10^{13}np/cm^2) that are distributed all along the SRSO sublayers. There are no traces of even amorphous Si-np in SRSN sublayers which may be attributed to either the insufficient Si excess or the STA process which favours Si-np formation only in SRSO sublayers. However, it is interesting to note that the density of Si-np formed with STA in SRSO/SRSN MLs are similar to those in SRSO/SiO_2 achieved after a long time CA process.

Thus, these microstructural and optical investigations indicate that a strong PL emission can be achieved after STA. The absorption studies after such an annealing showed that the absorption coefficient curves lies between that obtained from as-grown and CA SRSO/SRSN MLs (not shown here). The STA and the as-grown sample follow a similar trend with low absorptions for energies lower than 2 eV and high absorptions for energies greater than 2.5 eV. A balance between emission and absorption behaviour is obtained from STA SRSO/SRSN MLs which is promising for device applications at a reduced thermal budget.

4.7 Effect of number of patterns on emission

In order to understand if the number of patterns (i.e. total thickness) of the ML has an influence on the emission intensity, three STA SRSO/SRSN MLs with 20, 50 and 100 patterns were compared (Fig. 4.35a).

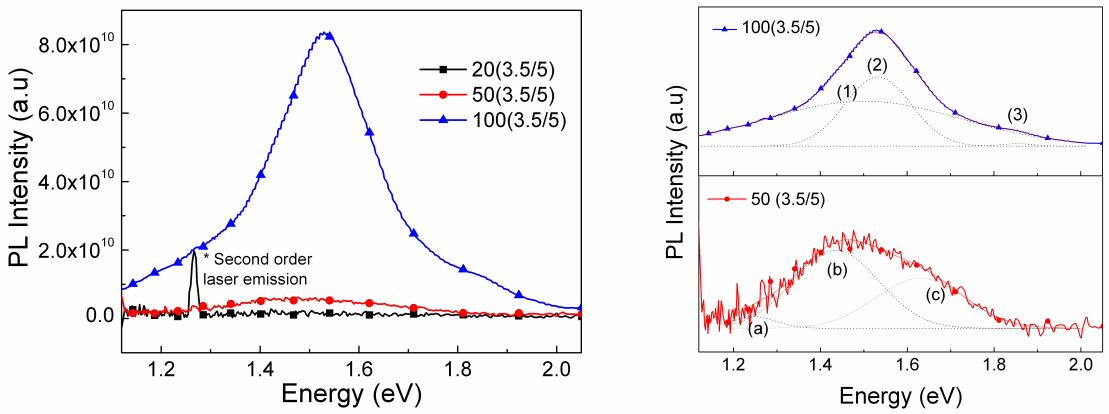

(a) Pattern number vs. emission intensity. **(b)** Curve fitting on 50 and 100 patterned ML.

Figure 4.35: Effect of pattern number on the emission of STA SRSO/SRSN MLs.

An increase in the PL intensity is noticed with increasing number of patterns. It

is interesting to note that doubling the number of patterns from 50 to 100 does not result in a doubling of PL intensity. Instead, the PL intensity shows a huge enhancement of about 7.4 times and suggests that besides the pattern number there might be other factors influencing the emission. The possible reasons will be systematically analyzed in the forthcoming sections and in chapter 5.

The 50 patterned ML also has three peaks (a, b & c) which are redshifted from peaks (1, 2 & 3) of the 100 patterned ML (Fig. 4.35b). The positions of peaks (b & c) fall within the range of peak (1) & peak (2) as seen in previous section and may be considered as a contribution of Si-np. The peak (3) disappears in 50 patterned sample, and a new peak (a) appears at lower energy. It is complicated to reason out:

- if peak (a) has a new origin and if the absence of peak (3) in 50 patterned sample might be due to a reduced volume of SRSN in the material. This is because peak (3) is assumed to be arising from Si:Si_3N_4 interface and/or defect states and even in 100 patterned ML (more SRSN sublayers than 50(3.5/5)), this peak intensity is too low.

- if these three curves in 50 patterned ML are only the redshifted (1, 2 & 3) peaks observed in the 100 patterned sample.

4.8 Effect of SRSN sublayer thickness on structural and optical properties

The influence of SRSN sublayer thicknesses (t_{SRSN}) on the structural and optical properties were investigated by growing 50(t_{SRSO}/t_{SRSN}) MLs, where t_{SRSO}= 3 nm and t_{SRSN} ranges between 1.5 to 10 nm.

Figure 4.36a shows the as-grown FTIR spectra of these set of samples recorded in Brewster incidence and normalized to 100 nm thickness.

A pronounced increase in the intensity of (LO and TO)$_{Si-N}$ modes can be seen when t_{SRSN} varies from 1.5 nm - 8 nm which is attributed to an increase in number of Si-N bonds with sublayer thickness. Such a trend is also observed in the asymmetric stretching modes of Si-O but to a lower extent. It can be observed in all these vibrating modes, that with further increase of t_{SRSN} (=10 nm) the peak intensities decrease. In the spectra recorded with normal incidence (Fig. 4.36b), the Si-O bonds are more pronounced for lower t_{SRSN}, due to lower amount of Si-N bonds in the material.

With increasing t_{SRSN}, the number of Si-N bonds in the material increases whereas the number of Si-O bonds remain constant. Therefore we notice an increase

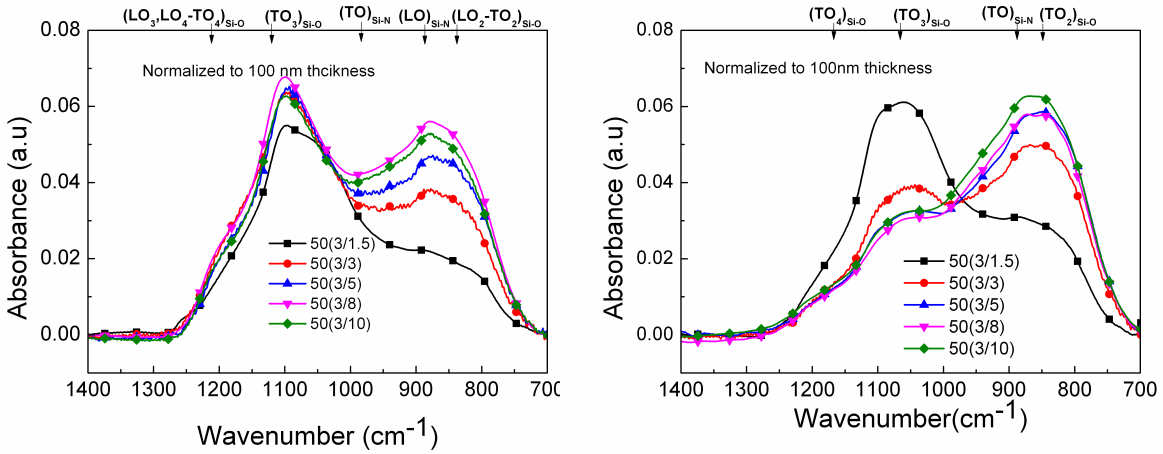

(a) Brewster incidence.

(b) Normal incidence.

Figure 4.36: FTIR spectra of as-grown SRSO/SRSN MLs grown by reactive approach as a function of SRSN sublayer thickness.

in the Si-N peak intensities with respect to those of Si-O ones (peak positions are marked in the upper axis of Fig. 4.36). Similar trend is observed for SRSO/SRSN MLs with SRSN grown by the co-sputtering method on varying the sublayer thicknesses.

The effect on the emission behaviour of STA SRSO/SRSN by varying t_{SRSN} is shown in figure 4.37.

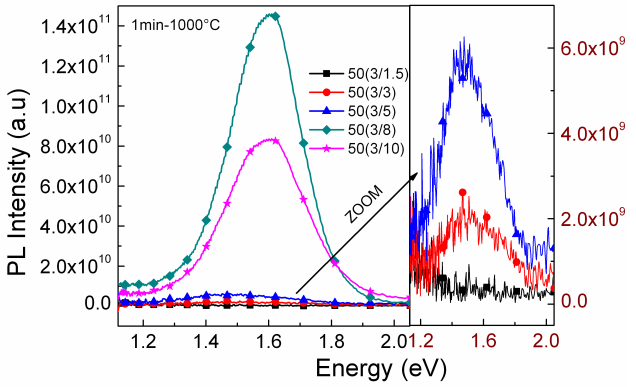

t_{SRSN}	peak (a) (eV)	peak (b) (eV)	peak (c) (eV)
1.5 nm	1.25	-	-
3 nm	1.21	1.48	1.72
5 nm	1.24	1.44	1.63
8 nm	1.43	1.59	1.85
10 nm	1.45	1.59	1.85

Figure 4.37: PL spectra and the peak positions of STA (1min-1000°C) SRSO/SRSN ML with varying t_{SRSN} grown by reactive sputtering approach. Table indicates the peak positions obtained after gaussian curve fitting on each of the PL spectra.

The PL intensity shows a non monotonous trend with increasing SRSN sublayer thickness. The intensity increases with increasing t_{SRSN}, reaching the highest at 8 nm and decreases for t_{SRSN} =10 nm. The table reports the values of the three peak maxima in all the samples under investigation. The results of gaussian curve fitting

on these PL spectra indicate that there is only one low energy peak when the t_{SRSN} is the lowest (=1.5 nm), and the presence of three peaks is observed for all other t_{SRSN}.

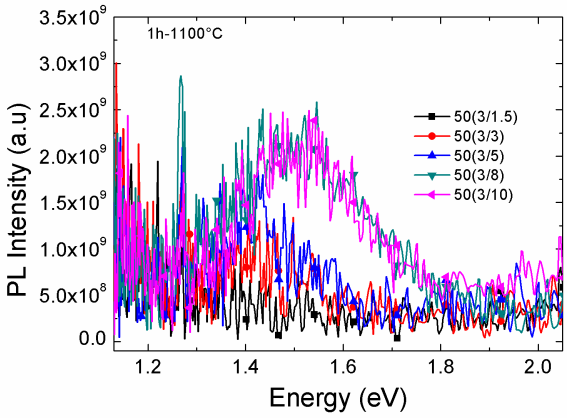

Figure 4.38: Influence of t_{SRSN} on the PL spectra of SRSO/SRSN ML grown by reactive sputtering approach, after CA (1h-1100°C).

The peaks are blueshifted with increasing t_{SRSN} and the positions of peak (b & c) reach the highest value for the two highest t_{SRSN}. Similar trend of PL intensities and peak shifts with varying t_{SRSN} is observed in MLs with SRSN grown by co-sputtering approach (not shown here). This blueshift may indicate a better confinement provided by SRSN barriers with increasing t_{SRSN} thereby preventing overgrowth of Si-np at the interface of SRSO and SRSN sublayers. The absence of peak (c) for the lowest t_{SRSN} and the gradually increasing appearance for higher t_{SRSN} confirms the attribution of this peak to SRSN sublayers. The samples were also subjected to CA to observe the influence of t_{SRSN} emission properties after such annealing (Fig. 4.38). The PL after CA is largely quenched, but t_{SRSN} plays a role in the emission intensity of CA MLs as well. The increase of PL intensity around 1.5 eV with increasing t_{SRSN} is seen accompanied by a blueshift of the peak position. Similar to our arguments on STA emission behaviour, this increase in peak intensity can be attributed to the SRSN barrier leading to a greater confinement of the Si-np formed within SRSO, with increasing t_{SRSN}. Consequently, the size of the Si-np decreases resulting in a blueshift and an enhanced emission.

4.9 Optimizing annealing treatments

It has been demonstrated in section 4.6 on nitrogen annealing that the SRSO/SRSN MLs are advantageous over SRSO/SiO_2 MLs by achieving higher emission properties at a lower thermal budget either by using short time annealing at high temperature (eg. 1min-1000°C [STA]) or longer time at low temperatures (eg. 16min-700°C). Besides, a high density of Si-np is formed after STA resulting in higher absorption behaviour than SRSO/SiO_2 MLs. It has been reported that the passivation of silicon

solar cells by forming gas (FG) annealing enhances the efficiency of low cost solar cells [Sana 94, Sopori 96]. This is due to the elimination of dangling bonds which act as trapping centres for charge carriers. Here, the hydogen atom plays a vital role in the activation of the radiative recombination centres. Hence a series of investigations were carried out by annealing under FG and also seeing the effect of preceding or succeeding this FG annealing by N_2 annealing.

Since the deposition temperature is high (500°C), we may reasonably suspect that one of the contributing factors to the enhancement (7.4 times) in intensity of the ML with 100 patterns as compared to 50 patterns after STA (ref. Fig. 4.35a) may be a consequence of the longer time spent in the deposition chamber. For instance, in a 100 patterned ML, the first 50 patterns are subjected to double the time inside the deposition chamber than the 50 patterned ML under the plasma which alternates between (argon + hydrogen) and (argon + nitrogen). It was calculated that 100(3.5/5) ML spent an excess time of 4.75h under high temperature (500°C) than 50(3.5/5) in the deposition chamber. This time spent in the chamber at 500°C may be considered as a low temperature annealing of the already deposited layers while the top layers are being deposited. Though the conditions in the deposition chamber for the excess time is not exactly the same in annealing chamber, long time annealing of 4.75h under forming gas flow at 500°C (4.75h-FG) was chosen to see if there could be any influence of such long time on emission intensity of 50(3.5/5) ML. The choice of FG annealing is also because it relates more closely to the deposition chamber ambience than annealing only under nitrogen flux. In addition, investigations on the influence of other shorter time FG annealing on enhancing the emission were also made.

4.9.1 Forming gas annealing versus annealing time

Figure 4.39a shows the PL spectra of 50(3.5/5) SRSO/SRSN ML obtained after annealing at 500°C under FG atmosphere with t_A between 0.5h-1.5h in steps and a continuous long time annealing (4.75h-FG).

As reported above for the case of annealing under N_2 flow (ref. Sec. 4.6), we observe the presence of the three emission peaks in the spectrum after FG annealing also. We focus our analyses on the most intense peak centered around 1.7 eV. An increase in annealing time favours emission with the highest intensity recorded after 4.75h-FG. Interestingly, it can be noticed that the STA and 4.75h-FG annealing treatments show similar intensities. This implies that an interplay between the coupled processes 'N_2-short time/high temperature' or 'FG-long time/low temperature' could result in similar emission intensities. Moreover, the annealing process allows

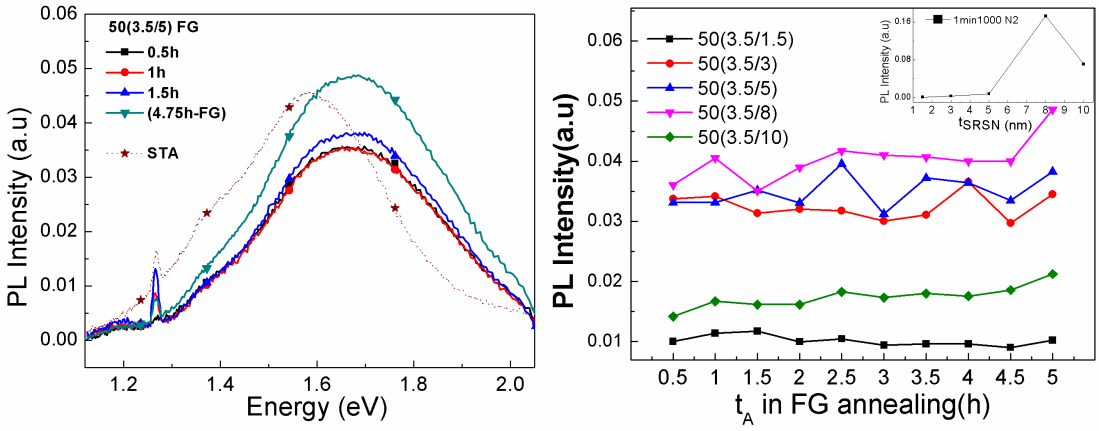

(a) PL spectra vs. FG annealing.

(b) PL peak maximum vs. t_A.

Figure 4.39: (a) Effect of annealing time under forming gas on the PL spectra of 50(3.5/5) SRSO/SRSN ML and, (b) PL peak maximum with regard to time of annealing in SRSO/SRSN MLs with different t_{SRSN}. (Inset) Recalling the influence of t_{SRSN} on PL from STA (1min-1000°C/N_2) samples.

the control over emission peak position.

Figure 4.39b shows the PL peak maximum of FG annealed 50(3.5/t_{SRSN}) MLs where t_{SRSN} varies between 1.5-10 nm. The samples were annealed sequentially between 0.5-5h. It can be observed that the time of annealing shows minimal influence on the PL intensity. Thus, 0.5h is a sufficient annealing time for achieving considerable emission.

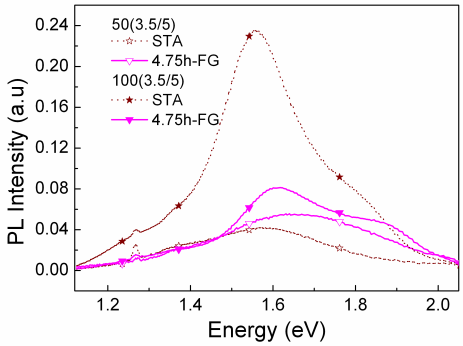

Figure 4.40: Comparing the PL spectra obtained after STA and 4.75h-FG annealing processes in 50 and 100 patterned SRSO/SRSN MLs.

Since T_A=500°C favours exodiffusion of hydrogen, further investigations under forming gas annealing were performed by reducing T_A, to understand the role of hydrogen in passivation of dangling bonds. Similar intensities were obtained even by reducing the T_A further down to 380°C (not shown here). It was observed in both the cases, that the intensities for a given time increase with t_{SRSN} till 8 nm and decreases with further increase in t_{SRSN} as observed in STA (Inset of Fig. 4.39b). Figure 4.40 shows a comparison of PL spectra between 50 and 100 patterned MLs after STA and 4.75h-FG. The emission intensity

increases for the 50 patterned sample after 4.75h-FG, whereas for the 100 patterned sample STA leads to the highest intensity. Moreover, one can notice a blueshift of the spectra between 4.75h-FG and STA

4.9.2 Short time annealing (STA) + Forming gas annealing

Since FG annealing results in emission equivalent to STA (1min1000°C-N_2) in 50 patterned ML, the next set of investigations focussed on enhancing the emission from STA sample by succeeding STA with a low temperature FG process.

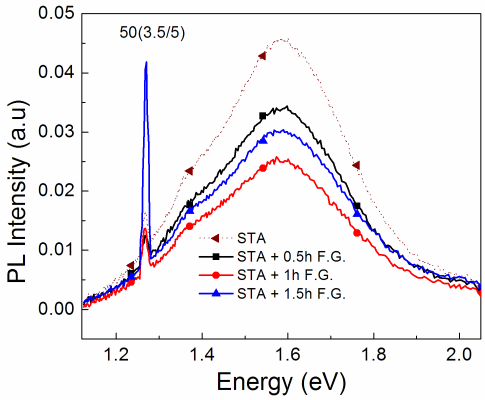

Figure 4.41: PL spectra obtained from 50(3.5/5) ML after STA + FG annealing.

Figure 4.41 compares the PL spectra obtained from 50(3.5/5) ML after STA+FG annealing with PL spectra obtained from STA sample. It can be seen from the figure that if STA treatment is done preceding FG annealing, it results in a detrimental effect on the emission intensity as compared to that obtained by FG annealing or STA alone.

It is interesting to note that the PL peak position remains the same, and is not blushifted as observed in the previous case with FG annealing. This can be attributed to the initial STA that almost completes the reorganization of the matrix with the formation of a high density of Si-np that would crystallize upon subsequent annealing treatments.

4.9.3 Forming gas annealing + Short time annealing (STA)

Figure 4.42 shows the PL spectra obtained from 50(3.5/5) SRSO/SRSN ML which was subjected to an initial annealing in FG and then succeeded by STA. The figure also presents the spectra obtained after annealing only by STA (1min-1000°C/N_2). Since it was seen that 0.5h in FG is sufficient to obtain considerable emission, such a treatment was first employed on SRSO/SRSN ML prior to STA treatment.

The emission intensity of 50 patterned ML annealed with 0.5h FG +STA treatment and only 0.5h in FG are similar (ref. Fig. 4.39a). Investigations were carried out, with varying t_A under FG flow followed by STA (not shown here) and it was

noticed that the intensity obtained after 4.75h-FG + STA is higher than that of 100(3.5/5) STA ML (Fig. 4.42). This suggests that the time spent under 500°C in 4.75h-FG process in 50(3.5/5) has a similar effect of the 4.75h excess time spent by 100(3.5/5) in the deposition chamber.

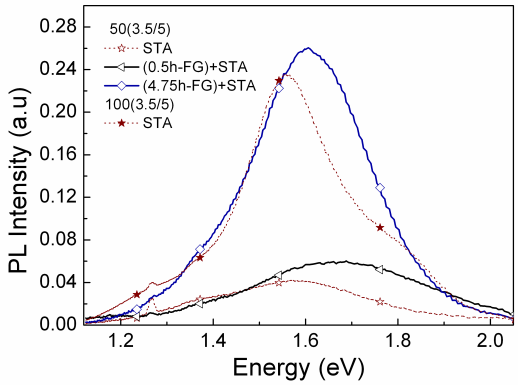

Figure 4.42: Investigating the PL spectra obtained from 50(3.5/5) SRSO/SRSN ML after FG+STA. (The PL spectra obtained after STA (1min-1000°C N_2) from 50 and 100 patterned MLs are also given in dotted lines for comparison).

One possible reason could be the exodiffusion of hydrogen at such high temperature (500°C) resulting in Si dangling bonds that reorganize to act as nucleating sites in the SRSO sublayers. Hence, a STA (1min-1000°C in N_2) treatment that follows after this time and temperature of exposure is sufficient to result in a high density of Si-np. Thus, we may say that the emission intensity increases with increasing density of nanoclusters resulting in emission enhancement of 50 patterned sample.

These results indicate that the time spent at high temperature (500°C-either in deposition chamber or in post fabrication process) prior to STA has a huge influence in favouring emission. The different peak positions of 100(3.5/5) STA ML and 50(3.5/5) 4.75h+STA ML, can be attributed to the different annealing processes employed on these two MLs. Thus, these studies demonstrate the possibility of enhancing the emission of a SRSO/SRSN ML by reducing the material (50 patterns vs. 100 patterns) subjecting to a pre-thermal treatment before STA.

4.10 Understanding the origin of photoluminescence

A detailed investigation on various annealing treatment on the PL spectra in the previous sections suggested various possible origins for emission. It was seen in section 4.6 that mostly all the PL spectra obtained from samples annealed under N_2 atmosphere had three peaks. From the peak positions in all the investigations above, we might attribute a range of positions for these peaks named as (1,2,3) in 100(3.5/5) ML and (a,b,c) in 50(3.5/5) ML. They are,

- Peak (1) (a) and (b) :1.2-1.45 eV
- Peak (2) and(c): 1.50-1.7 eV

- Peak (3) and (c): 1.8-1.95 eV

Different names are given for the three peaks in 100(3.5/5) and 50(3.5/5) ML since the origin of these three peaks in both the cases may be different. It can be seen that the position of peak (c) is sometimes the same as peak (2) or sometimes as peak (3) leading to confusions on the origin of this emission. Hence, further investigations were made in an attempt to understand the origin of PL emission

4.10.1 Role of defects in the matrix

In order to see the influence of SRSN sublayers on the emission of peaks, 50(3.5/3.5) SRSN/SiO_2 MLs were grown and subjected to STA, CA and FG annealing. The PL spectra obtained from SRSO/SRSN MLs can be compared with SRSN/SiO_2 and SRSO/SiO_2 MLs in order to identify the contribution of SRSO, SRSN and SiO_2 sublayers independently. Figure 4.43 compares the PL spectra obtained from SRSO/SiO_2, SRSO/SRSN and SRSN/SiO_2 MLs with 50(3.5/3.5) configuration after STA and CA. It can be noticed from the spectra of CA annealed samples that the SRSN/SiO_2 ML exhibits a weak PL around 1.9 eV while that from SRSO/SRSN ML is quenched as demonstrated before (ref. Fig. 4.25). This PL peak appears in a region usually related to the optical transitions in the SiO_2 matrix due to the presence of defects [Gourbilleau 09, Delachat 09].

The lower part of the figure 4.43 shows the PL spectra recorded from STA MLs. It can be noted that both SRSN/SiO_2 and SRSO/SiO_2 emit PL at the same peak position (around 1.9 eV), the latter being very weak. This indicates that besides SiO_2, SRSN sublayers also contribute to emission around 1.9 eV in SRSN/SiO_2 ML. The PL intensity of SRSN/SiO_2 increases with annealing temperature while the peak position remains fixed at 1.9 eV (See inset of Fig. 4.43). From figure 4.40 one can remark that that this peak around 1.9 eV is not seen in 50(3.5/5) ML, while in 100(3.5/5) it is significant. Moreover, even under N_2 annealed STA samples, this peak was noticed with increasing

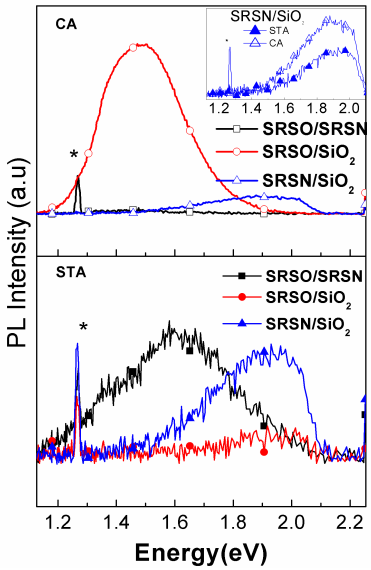

Figure 4.43: PL spectra from 50(3.5/3.5) SRSO/SRSN, SRSO/SiO_2 and SRSN/SiO_2 MLs after STA and CA treatments.

volume of SRSN in the material and was seen only in 100(3.5/5) ML (Ref. Fig. 4.35b) or 50(3.5/$t_{SRSN>5nm}$) after gaussian curve fitting (not shown here). In order to verify the influence of annealing under FG and SRSN volume on this PL peak intensity, SRSN/SiO_2 ML was also subjected to FG annealing (Fig. 4.44). The SRSN sublayer thickness in this ML is lower (=3.5 nm) than in SRSO/SRSN MLs investigated above in section 4.6 and still the peak around 1.9 eV is present.

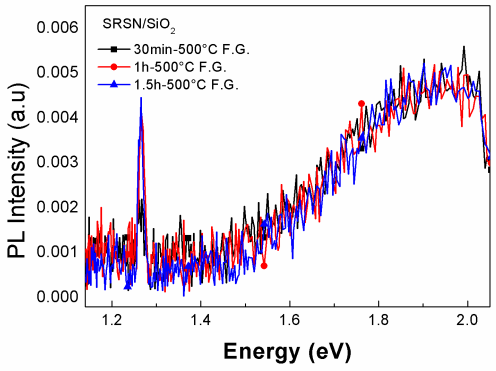

Figure 4.44: PL spectra obtained from FG annealed 50(3.5/5) SRSN/SiO_2.

In both figures 4.43 and 4.44, 1.9 eV peak is present in SRSN/SiO_2 MLs despite the two different annealing processes employed. In the case of N_2 annealing, since the SiO_2 defects are mostly passivated after CA, we can reasonably assume that the dominant contribution of this emission is from SRSN sublayers which also to emit in the same energy range as SiO_2. In the case of FG annealed samples the dominant contribution of luminescence comes from defects in SiO_2, since the temperature is lower for defect passivation. These observations help us to attribute the peak (3) of SRSO/SRSN PL spectra to be the contribution of SRSN sublayer.

The presence of nanocrystals were found neither in XRD spectra of SRSN/SiO_2 [Nalini 12] nor in the TEM images of SRSO/SRSN thereby indicating the emission from SRSN sublayer is not from Si-np. It can be seen that there is a blueshift in the central peak position from 1.57 eV after STA to 1.75 eV after FG annealing in 50(3.5/5) SRSO/SRSN ML (Ref. Fig. 4.39a), whereas for the two different annealing processes under N_2 or FG flow employed on SRSN/SiO_2 MLs there is no change in the peak intensity and the position remains fixed around 1.9 eV. Theoretical model has predicted that for a given defect, the peak position is fixed and cannot be controlled with ease [Kim 05]. This peak position around 1.9 eV can therefore be ascribed to the defects in SRSN sublayers.

Besides these defect related PL, it can be said that in a SRSO based ML, replacing SiO_2 by SRSN sublayers favours Si-np emission also, at a reduced thermal budget (STA in SRSO/SRSN versus CA in SRSO/SiO_2 MLs). Thus, SRSN sublayers contribute significantly towards emission around 1.9 eV (peak 3) and between 1.5-1.7 eV (peak 2) due to defects in the matrix, and by favouring the Si-np formation respectively.

4.10.2 Effect of Si-np Size distribution

The origin of peak (2) has been attributed to Si-np following the quantum confinement effect throughout our earlier discussions. In order to confirm this, investigations were done relating the experimentally obtained Si-np size with the Delerue law [Delerue 93]. The size of Si-np in a 3.5 nm SRSO sublayer has been estimated to be 3-4 nm from experiments in chapters 3 and 4, leading to a peak position of about 1.6 eV with the Delerue law. This peak position can be related to peak (2).

The peaks (1, a & b) between 1.2-1.45eV is seen mostly only in N_2 annealed samples. This peak is seen to redshift with increasing t_A, similar to peak (2). Since increasing t_A may lead to increasing Si-np size, we may suppose that these peaks also follow a quantum confinement model. Using the Delerue's law to identify the peaks between 1.2-1.45 eV range results in particle sizes ranging between 5.5-13.5 nm. Though, we may suppose the possible formation of 5.5 nm Si-np due to some overgrowth at the interfaces, but 13.5 nm for the lowest energy is impossible since we do not observe a breakdown of multilayer structure to result in such big Si-np. The TEM image of 100(3.5/5) ML which has peak (1) at low emission energy (1.24 eV) confirms that we have perfect alternations of the two sublayers, and EFTEM also confirms the presence of Si-np restricted to SRSO sublayer. Therefore, this peak cannot be attributed to such big Si-np even at SRSO interfaces. From our XRD, TEM and EFTEM observations, we have confirmed the absence of Si-np in SRSN either in crystalline or amorphous form. Thus, it can be said that this peak is not necessarily related to Si-np in SRSO or SRSN sublayers but has some other origin such as interference which will be analyzed in the next chapter.

4.10.3 Effect of surface microstructure

The surface microstructure of STA and FG annealed samples has been investigated by optical microscopy performed on 50(3.5/5) SRSO/SRSN ML (Fig. 4.45). It can be noticed that, with N_2 annealing the sample surfaces show the appearance of circular spots as already shown in figure 4.21 on 100(3.5/5) CA sample.

The surfaces of both STA and CA annealed samples are similar and show the appearance of circular spots after annealing. Moreover, there is no significant change in the size of these spots with annealing. The surface microstructure of STA 50(3.5/5) ML is similar to 100(3.5/5) ML, but the size of the circular spots increase for CA 100(3.5/5). The influence of STA and CA on the PL intensity are the same on the 50 and 100 patterned MLs, despite the pronounced surface difference after CA. Concerning the FG annealed samples, there is no difference on the surface structure

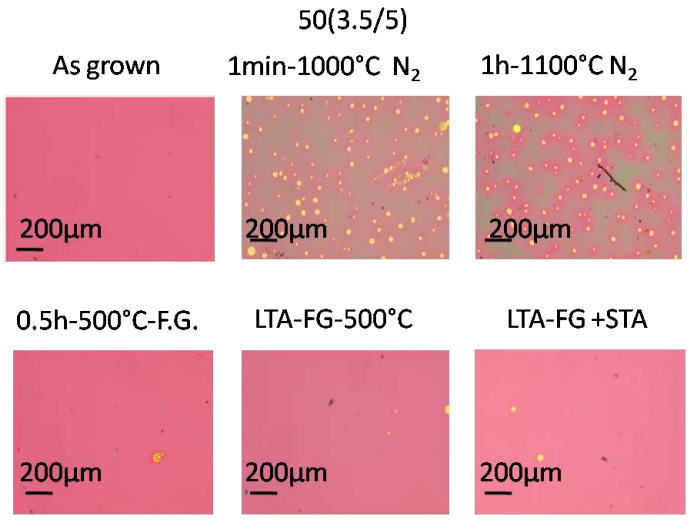

Figure 4.45: Surface microstructure of 50(3.5/5) ML after N_2 , FG and N_2+FG annealing as observed by optical microscope.

whatever the annealing time or the number of patterns (not shown here). Thus, we can say that the surface microstructural changes after annealing does not influence the emission intensity, and may only reflect the exodiffusion paths for gases.

To conclude on our analysis in this section on the possible origin of emission, we may attribute the peak between 1.50-1.7 eV (peak 2) to Si-np in SRSO sublayers and 1.8-1.95 eV (peak 3) to SRSN sublayer contribution due to some defects. However at this stage it is difficult to understand the type of defects in SRSN sublayers. The origin of the low energy peak still remains unclear. The possibility of interference effect or the presence of another kind of emission centers leading to this emission will be analyzed in chapter 5 by theoretical modeling and simulations.

4.11 Summary on SRSO/SRSN MLs

A detailed analysis on the structural and optical properties of SRSO/SRSN MLs was made. It was shown that the structures of the MLs obtained with SRSN grown by reactive sputtering approach and co-sputtering approach are the same, and exhibit similar trend in emission properties.

Ellipsometry : Results from ellipsometry simulation give the refractive indices and total thickness of the ML within 5% error and indicates the appearance of voids on the ML surface after annealing. An increase in refractive index accompanied by a decrease of the thickness on annealing suggests the densification process.

XRR and TEM: The XRR spectra shows the presence of repetitive patterns

in the ML and TEM images also reveal a perfect alternation of the SRSO and SRSN sublayers. The pattern thicknesses estimated from XRR and TEM are in agreement with each other thereby demonstrating XRR is a sufficient technique to estimate the pattern thickness of a ML. High density of Si-np even after STA (1min-1000°C/N_2 annealing) is witnessed from HRTEM and EFTEM images. The Si-np are formed only in the SRSO sublayers.

FTIR: The combined contribution of the longitudinal and transverse optical modes from SRSO and SRSN sublayers is seen in the FTIR spectra. The blueshift of the Si-N peak indicates an increase in Si-np and nitrogen content with annealing. Similar blueshift and changes in peak intensity associated with the formation of Si-np is observed in the Si-O related bonds.

XRD: The investigations on as-grown, STA (1min-1000°C) and CA (1h-1100°C) SRSO/SRSN MLs reveal the presence of Si-np in as-grown state crystallize upon annealing.

Absorption coefficient : The CA sample has absorption coefficient higher than that of as-grown or STA sample over the whole energy range. However, at 3eV the STA sample also possess high $\alpha \sim 10^4$ cm^{-1} comparable to the CA sample.

PL: An extensive investigation on the emission behaviour of the ML was made resulting in following observations and understandings:

- An interplay between time and temperature of annealing : low time/high temperature (1min-1000°C) & long time/low temperature (16min-700°C) lead to similar PL intensities. Among these STA (1min-1000°C) is identified to be better owing to a lower thermal budget than 16min-700°C.

- The highest PL is obtained after STA (1min-1000°C) and almost totally quenched after CA (1h-1100°C).

- The highest PL is attributed to the presence of a high density of amorphous clusters, and the quenching is related to the detrimental effect of SRSN sublayers on emission properties with annealing.

- Most of the PL spectra can be decomposed into three emission peaks whose origin were investigated. The central peak between 1.5-1.75 eV is attributed to the Si-np 1.9 eV to the defects in SRSN sublayers. The peak at the lower energies is still under investigation and the possible contribution of optical and geometrical effects on this peak is suspected.

- The pattern thickness, SRSN sublayer thickness as well as the time spent in the deposition chamber are found to be important factors that control the

emission intensity.

- It is found that significant PL intensities can be obtained by annealing under forming gas at temperatures as low as 380-500°C during 0.5h.

4.12 Conclusion

A thorough investigation of SiN_x materials indicated that the refractive index of the layer is the most important indicator of the material properties. It is possible to obtain similar structural and optical properties with the two kinds of deposition approaches for silicon nitride layers investigated here (reactive sputtering and co-sputtering). Significant emission intensities were obtained by using SRSN in a multilayer structure. A short time annealing treatment under nitrogen flow (STA, 1min-1000°C) on SRSO/SRSN MLs results in the highest emission intensities which is attributed the high density Si-np. The presence of Si-np and therefore emission after STA in SRSO/SRSN MLs contrary to SRSO/SiO_2 MLs reflect the advantages of SRSN in favouring the Si-np formation in SRSO sublayers with a faster kinetics. Similarly, it is shown in this chapter that annealing under forming gas even at low temperatures enhances emission intensity of the ML. Enhancing the emission intensity of the SRSO/SRSN MLs either by STA or by FG annealing reflects the advantages of this material over SRSO/SiO_2 which requires 1h-900-1100°C for Si-np formation leading to emission, with regard to thermal budget for photovoltaics or even photonic applications. The density of Si-np after STA in SRSO/SRSN ML (almost 10^{20} np/cm^3) is higher than the Si-np density achieved after CA in SRSO/SiO_2 ML.

Hence, a preliminary experiment to test these two samples for electrical conductivity was made. Figure 4.46 compares the dark current curves of (3.5 nm SRSO/5 nm SRSN) with our (3.5 nm SRSO/3.5 nm SiO_2) MLs.

The resistivity was calculated to be 2.15 and 214 MΩ·cm in the SRSO/SRSN and SRSO/SiO_2 MLs, respectively at 7.5 V. Since the thickness of the SRSO sublayer is the same in both cases (3.5 nm), this decrease in the resistivity of the SRSO/SRSN MLs can be ascribed to the substitution of SiO_2 by SRSN sublayers. This two-fold enhanced conductivity paves the way for further improvement of the SRSO/SRSN MLs' conductivity, for example, by decreasing the thickness of this SRSN sublayer. Thus, this chapter successfully demonstrates the advantages of SRSO/SRSN over SRSO/SiO_2 MLs with a control over thermal budget for device applications.

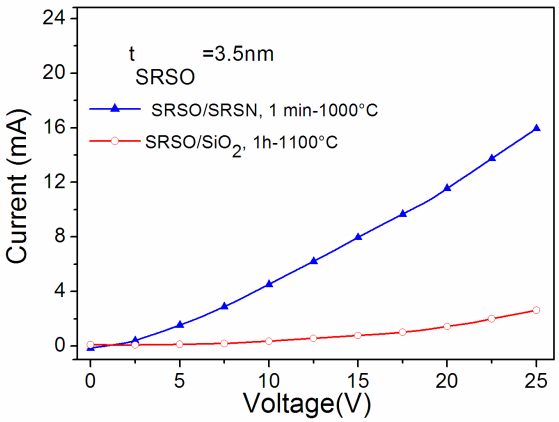

Figure 4.46: I-V curve of STA SRSO/SRSN versus CA SRSO/SiO_2.

Chapter 5

Photoluminescence emission modeling in Si-based thin films

5.1 Introduction

The emission properties of Si-based thin films can be tuned by playing with various factors such as refractive index, total thickness, sublayer thickness, type of emitters, concentration of emitters etc., as demonstrated in chapters 3 and 4. The results of the previous chapters suggested that there might be several kinds of emitters in the thin film that contribute to the position, intensity and shape of emission peaks. A thin film is assumed to be a multi-wave interferometer such as the plane parallel plate, of thickness d and a refractive index $\tilde{n}$. Therefore, the reflection and transmission coefficients at the air-film and film-subtrate interfaces, and the phaseshift due to the optical path within the thin film may lead to the interference effects in PL. Such effects were observed in cathodoluminescence studies of SiO_2 thin film on Si substrate and investigated as early as 1970s and 1980s [Mitchell 73, Holm 82]. It has been pointed out that oxide films thicker than 200 nm exhibit interference effects [Nesheva 02]. Besides, it has also been reported in SRSO films that thickness, refractive index, interface states, along with other experimental set-up parameters such as angle of the incident pump, its power density etc., also play a role in the photoluminescence spectra [Ternon 04b, Ferre 05]. Therefore, in this chapter emission modeling will be performed accounting for the following parameters that are broadly classified into two parts:

1. Incident pump: wavelength, amplitude, angle of incidence.

2. Emission: thin film thickness, refractive index, population profile of emitters in the ground and excited states, distribution of emitters in single layers and

multilayers, absorption and emission cross-sections.

For all the simulations, it is considered that the thin film is located between the semi-infinite Si substrate and semi-infinte air medium.

5.2 Incident pump profile

5.2.1 Methodology : Matrix formulation for Isotropic layered media

The incident Electro-Magnetic (EM) wave of the Ar laser is described by the electric field vector ($\vec{E}$), magnetic field vector ($\vec{H}$) and the wave vector ($\vec{k}$) perpendicular to each other (Fig. 5.1). The calculations are perfomed in the cases of TE wave ($E_y \neq 0, E_x = E_z = 0$). Figure 5.1 is a typical illustration of our thin films of thickness d, with two interfaces between the air and the substrate. The refractive indices of the three media (air, thin film and substrate) are denoted as n_1, n_2 and n_3 respectively. The incident angle of the propagation wave vector, $\overrightarrow{k}$ is denoted as θ_{inc}. The incident wave undergoes absorption, transmission and reflection phenomena and the intensity of the total EM wave that comes out of the sample is collected (in the PL set-up and in simulations) with an angle of collection in the range, $\theta_{collect}\pm 23°$.

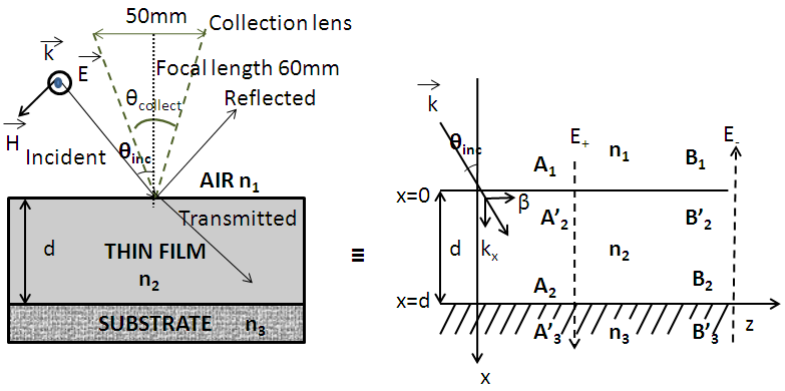

Figure 5.1: Schematic representation of external and internal components of our thin film samples under investigation. in TE mode. $\theta_{inc} = 45^o$ and $\theta_{collect}= \pm 23^o$.

The electric field amplitude of the incident plane wave is given by,

$$E_y(x) = E(x)e^{i(\omega t - \beta z)} \qquad \text{Eqn (5.1)}$$

where β is the z component of the propagation wave vector and ω is the angular frequency. The repartition of the incident pump field in this thin film is simulated using transfer matrix formulation [Yeh 88, Weber 91, Boucher 06] that relates the amplitude of the field on either sides of the thin film.

As seen from figure 5.1, a part of the incident light is transmitted within the thin film and a part is reflected back. Therefore the total electric field $\overrightarrow{E}(x)$ is a superposition of two waves travelling opposite to each other in the positive and negative directions of x with fields E_+ and E_-. This can be represented by,

$$E_y(x) = E_+e^{-ik_x x} + E_-e^{ik_x x} = A(x) + B(x) \qquad \text{Eqn (5.2)}$$

where $\pm k_x$ represent the x component of wave vector, $A(x)$ and $B(x)$ are constants in the positive and negative directions of x. We consider $A(x)$ and $B(x)$ at four positions for simplicity: top and bottom of interfaces at $x = 0$ and $x = d$ repectively as shown in figure 5.1. These can be written as,

$$A_1 = A(x = 0^-) \text{ and } B_1 = B(x = 0^-) \qquad \text{Eqn (5.3)}$$

$$A_2^{'} = A(x = 0^+) \text{ and } B_2^{'} = B(x = 0^+) \qquad \text{Eqn (5.4)}$$

$$A_2 = A(x = d^-) \text{ and } B_2 = B(x = d^-) \qquad \text{Eqn (5.5)}$$

$$A_3^{'} = A(x = d^+) \text{ and } B_3^{'} = B(x = d^+) \qquad \text{Eqn (5.6)}$$

Therefore, we can quantitatively describe the pump profile depending upon transmission and reflection of the incident wave using Fresnel's equations. For this, the components A_1 which corresponds to the incident pump field and B_1 the field of the reflected wave can be linked using the following equation, detailed in Appendix I,

$$\begin{pmatrix} A_1 \\ B_1 \end{pmatrix} = M \begin{pmatrix} A_3^{'} \\ B_3^{'} \end{pmatrix} \qquad \text{Eqn (5.7)}$$

where $B_3^{'}$=0, considering a semi-infinite medium (no wave travelling towards the negative direction of x) and M is a product of matrices that link the fields in medium 1 and 3. The ratio of A_1 to B_1 gives the reflected amplitude and A_1 to $A_3^{'}$ the transmitted amplitude. For a known input field A_1, the reflected amplitude B_1 can be calculated with the global reflection coefficient of all the structure (r_{glob}) due to the propagation of the wave inside the thin film.

The pump field repartition in the thin film is thus obtained by connecting each of the components mentioned in figure 5.1 as follows,

$$\begin{pmatrix} A_1 \\ B_1 \end{pmatrix} = D_1^{-1}D_2 \begin{pmatrix} A_2^{'} \\ B_2^{'} \end{pmatrix} = D_{12} \begin{pmatrix} A_2^{'} \\ B_2^{'} \end{pmatrix} \qquad \text{Eqn (5.8)}$$

$$\begin{pmatrix} A_2 \\ B_2 \end{pmatrix} = D_2^{-1}D_3 \begin{pmatrix} A_3^{'} \\ B_3^{'} \end{pmatrix} = D_{23} \begin{pmatrix} A_3^{'} \\ B_3^{'} \end{pmatrix} \qquad \text{Eqn (5.9)}$$

where D_α is the passage matrix whose shape depends on the polarization (TE and TM) and $\begin{pmatrix} A_2 \\ B_2 \end{pmatrix}$ is linked to $\begin{pmatrix} A_2' \\ B_2' \end{pmatrix}$ by propagation matrix $\begin{pmatrix} e^{ik_\alpha d} & 0 \\ 0 & e^{-ik_\alpha d} \end{pmatrix}$(refer Appendix I).

From equation 5.8, the reflected amplitude can be obtained for known A_1 since, $B_1 = r_{glob}A_1$. Hence,

$$\begin{pmatrix} A_2' \\ B_2' \end{pmatrix} = D_2^{-1} D \begin{pmatrix} A_1 \\ r_{glob}A_1 \end{pmatrix} \qquad \text{Eqn (5.10).}$$

From the values of $\begin{pmatrix} A_2' \\ B_2' \end{pmatrix}$, the stationary field of the pump is obtained with the following form:

$$E_p(x) = A_2' e^{-jk_2 x} + B_2' e^{jk_2 x} \qquad \text{Eqn (5.11)}$$

5.2.2 Incident electric field amplitude, A_1

A realistic value for the incident electric field amplitude has to be determined to be fed as an input for simulations. In the PL experiments, we have access to the intensity (I) of the laser which is the square amplitude of the incident electric field (Poynting vector). The intensity of the laser is calculated as 100 mW/mm^2= 10^5 W/m^2, in our case. This intensity is linked to the electric field amplitude $E_p(x)$ by,

$$I = \frac{c\varepsilon_o n \mid E_p(x) \mid^2}{2} \qquad \text{Eqn (5.12)}$$

From this, the amplitude of the incident electric field is calculated by,

$$E_p(x) = \sqrt{\frac{2I}{cn\varepsilon_0}} \qquad \text{Eqn (5.13)}$$

where, n = refractive index of air = 1, c = 2.99 x 10^8m/s is the speed of light and ε_o = 8.85 x10^{-12} C^2/N.m^2 is the dielectric constant.

Thus, the amplitude of the electric field calculated from equation 5.13 leads to a value of 8x10^3 V/m. This value is fed as input A_1 in the code developed by our team[1].

5.2.3 Pump profile in the thin film

The pump profile is simulated with regard to the angle of incidence, thickness of the film, and complex refractive index. The complex refractive index which vary as a

[1]Dr. J. Cardin and Prof. C. Dufour devoloped the code for simulations.

function of wavelength consists of the real part n and imaginary part k, known as the extinction coefficient. This is represented by,

$$\text{Complex refractive index } \tilde{n} = n(\lambda) - ik(\lambda) \qquad \text{Eqn (5.14)}$$

Figure 5.2 shows the shapes of simulated $n(\lambda)$ and $k(\lambda)$ by using the parameters from our ellipsometry results on the corresponding thin film, as the input.

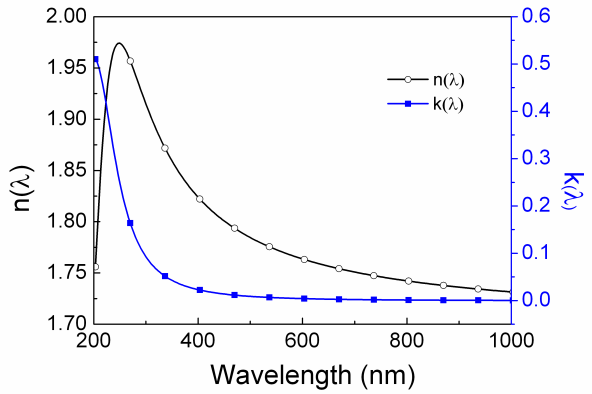

Figure 5.2: The variation of complex refractive index ($\tilde{n} = n(\lambda) - ik(\lambda)$) of a thin film, as a function of wavelength.

The pump wavelength was fixed at 488 nm in all the simulations, relating to the Ar laser used in the PL experimental set-up.

(a) Influence of Angle of incidence

The simulations consist of focussing the pump on a 500 nm thin film with complex refractive index described in figure 5.2. The pump profile is investigated as a function of depth (x) from the film surface, for two angles of incidence: normal incidence and 45° incidence (Fig. 5.3).

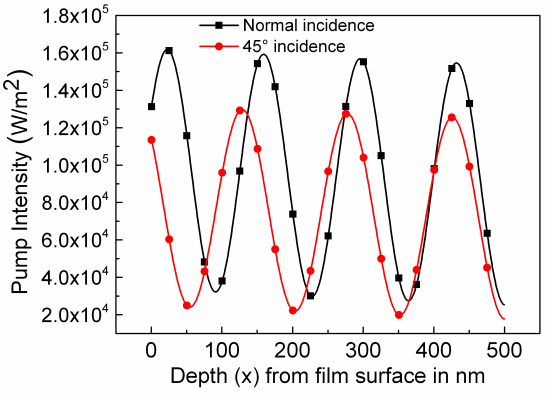

Figure 5.3: Pump intensity profile with regard to its angle of incidence on the thin film.

This figure clearly indicates that the incident pump intensity oscillates between maxima and minima along the depth (x). As a consequence, even if the emitters are homogeneously distributed within a thin film, they are subjected to a variable pump profile.

From the two cases shown in this figure, it can be noticed that the angle of incidence influences the intensity and position of the pump maxima. This indicates that with 45° incidence used in our PL experiments, the pump intensity is lower than that obtained in normal incidence.

(b) Influence of thickness

The influence of the film thickness (d) on the pump profile was investigated for three cases: $d = 300$ nm, 500 nm and 1000 nm (Fig. 5.4).

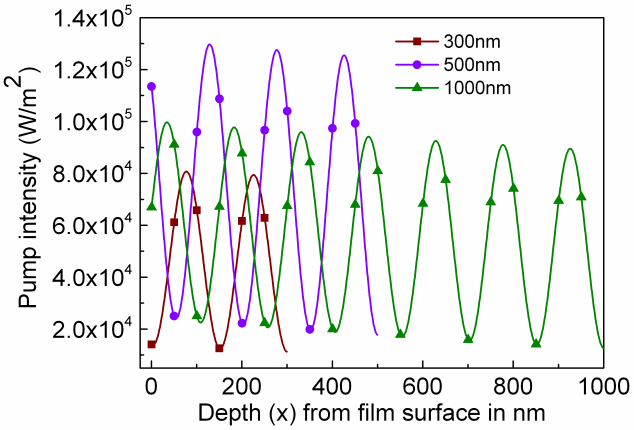

Figure 5.4: Influence of total film thickness on the pump profile.

In all the three cases shown in this figure, the angle of incidence was fixed at 45°, and the refractive index is as described before (ref. Fig. 5.2). It can be seen from figure 5.4 that only by varying the total thickness there is a change in the position and intensity of the pump profile. This can be related to the reflection in the film denoted as r_{glob} in equation 5.10, which is a function of film thickness. These results clearly indicate that the mean pump intensity varies non-monotonously with thickness (Tab. 5.1).

Thickness (d) nm	Pump intensity range W/m^2
300	1 x 10^4 - 8 x 10^4
500	2.5 x 10^4- 1x10^5
1000	2 x 10^4 - 9.5 x10^4

Table 5.1: The pump intensity range for the three thicknesses investigated.

(c) Influence of complex refractive index

The influence of the real part and imaginary part of the complex refractive index on the pump profile were investigated.

(c1) Real part (n_2):

To witness the contribution of n_2 on the pump wave that travels from medium 1 (air) to medium 2 (thin film), simulations are made by considering three SRSO monolayers with 500 nm thickness and three different refractive indices ($n_2 = 1.48$,

1.6 and 2.1). We assume that, there are no losses in the film due to absorption and hence set k_2=0. Figure 5.5 shows the pump profile variation with n_2, along the depth (x) from film surface.

The result indicates that the intensity of the incident pump and the position of maxima varies with the refractive indices of the material. The mean pump intensity varies monotonously with refractive index in the three cases investigated (Tab. 5.5). The lower index resulting in the highest intensity. The period of the pump profile also varies with n_2. We can thus suppose the variation of emission intensity with refractive index is not a sole contribution from Si-np density, but also the effect of the incident pump intensity that varies.

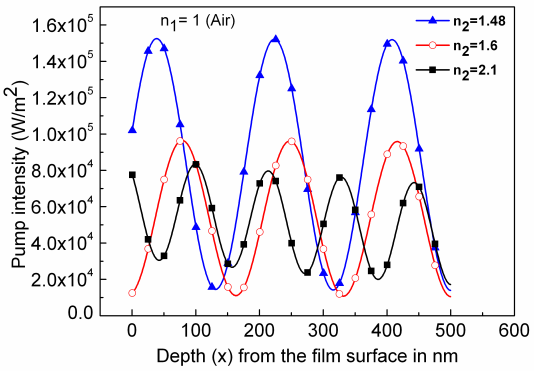

Figure 5.5: Pump profile versus real part of thin film refractive index (n_2).

Real part (n_2) of refractive index	Pump intensity range W/m^2
1.48	1.4 x 10^4 - 1.5 x 10^5
1.6	1.1 x 10^4- 9.5x10^4
2.1	2.3 x 10^4 - 7.9 x10^4

Table 5.2: The pump intensity range for the three thicknesses investigated.

(c2) Imaginary part (k_2):

In order to investigate the effect of losses, the extinction coefficient k_2 of the thin film was varied while keeping n_2 fixed at 1.6 (Fig. 5.6).

Figure 5.6a shows the pump profile for three cases : k_2= 0, 0.01 and 0.1 and figure 5.6b illustrates the envelope of the pump maxima and minima taking $k_2 = 0.1$ as a typical example. It can be seen from figure 5.6a that there are no losses when k_2=0 and the intensity of the pump maxima and minima are constant with depth (x). With increasing values of extinction factor k_2: (i) the envelopes of the pump maxima and minima decrease with depth (x) and (ii) the difference between $(\text{Envelope})_{max.}$ and $(\text{Envelope})_{min.}$ decreases. This indicates that with increasing losses, the pump intensity decreases. These factors would influence the excitation of emitters along the depth of the thin film, and consequently on the emission intensity.

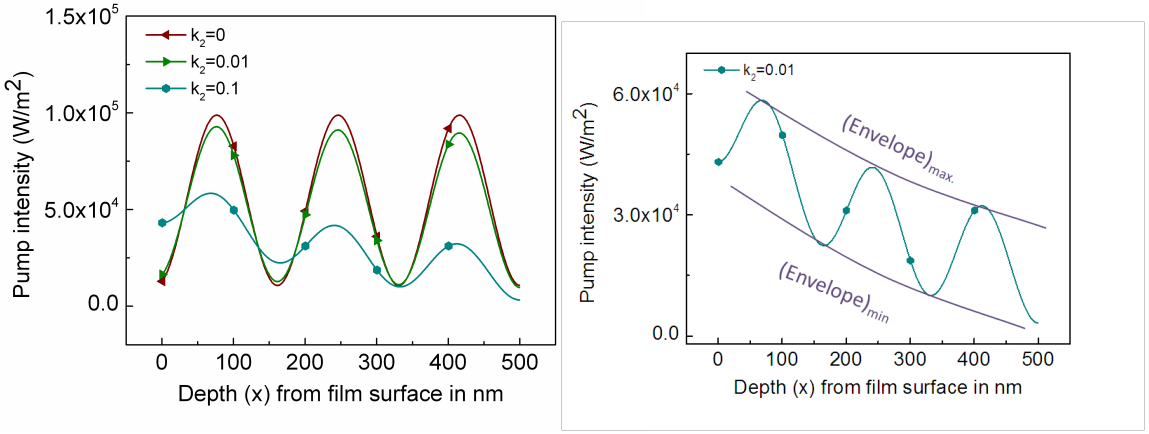

(a) $n_2 = 1.6$ and $k_2 = 0$, 0.01 and 0.1. **(b)** Envelope of pump maxima and minima: An illustration.

Figure 5.6: Pump profile versus imaginary part of thin film refractive index (k_2).

(d) Interplay between emitter distribution and pump profile for monolayer and multilayer configurations

In addition to the pump profile variation with various factors described above, the configuration of thin film (i.e. monolayers or multilayers) would also have a large influence on the distribution of excited emitters. In the case of a monolayer, we consider a uniform distribution of emitters (Fig. 5.7). As can be seen from the figure, in a SRSO monolayer with uniformly distributed Si-np, the emitters that are at the maxima of the pump are easily excited, whereas those are minima may be less excited. Consequently, the emission intensities also would vary depending on the location of emitters along the pump profile.

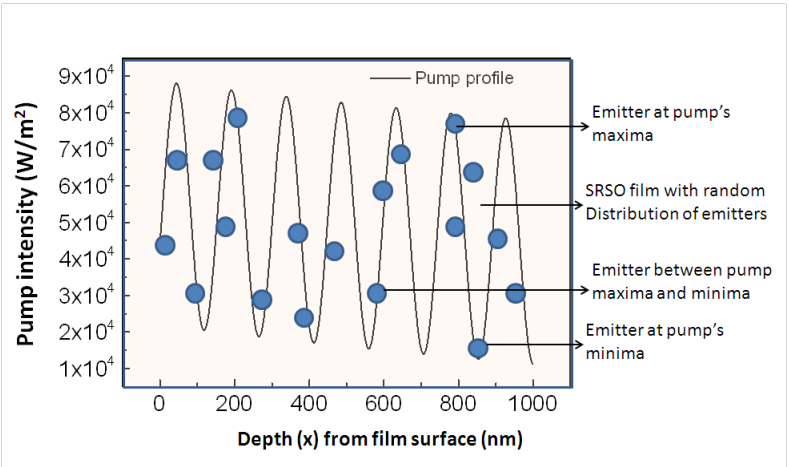

Figure 5.7: An illustration of the pump profile variation in a thin film of thickness d(nm) with distribution of emitters in monolayer configuration.

In the case of our multilayers, there is a periodical distribution of emitters since Si-np are restricted only to SRSO sublayers. Figure 5.8 illustrates the case of MLs comprised of alternative emitting sublayers and non-emitting sublayers.

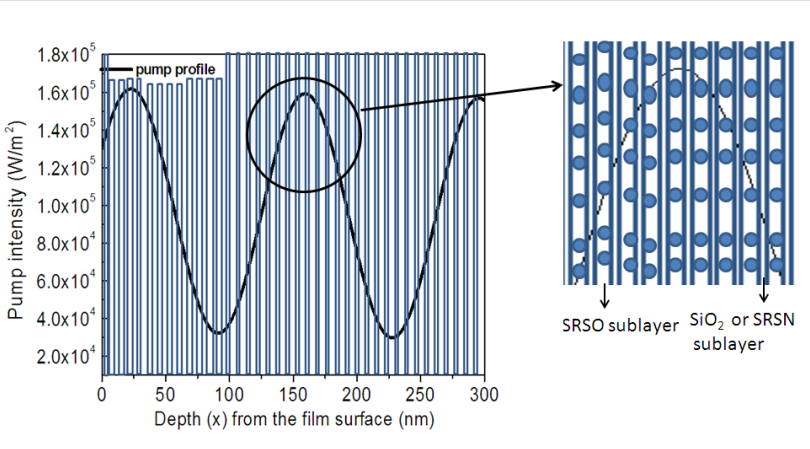

Figure 5.8: An illustration of the pump profile variation in a thin film of thickness d(nm) with distribution of emitters in multilayer configurations.

More emitters would be excited in those sublayers which experience a pump maxima. Depending upon the sublayer thicknesses, the number of emitters that are excited varies, as well as the emission intensity. This implies that the population of the excited state of emitters follows the shape of the incident pump profile, which will be discussed in the next sections.

As seen from the discussions in this section, modeling reveals that the incident laser intensity in the PL experiment depends upon various parameters such as the angle of incidence, thickness, refractive index, type of configurations etc. Since the pump profile contributes to the emission intensity, these results indicate that the variations in PL intensity cannot be directly linked to the emitter density in the thin film.

5.3 Emission modeling

Similar to the pump profile, the emission from thin film is also influenced by various components such as the thickness of the film, the distribution of emitters, their population density in the ground and excited states, lifetime of carriers, absorpion and emission cross sections. Experimental data and literature values are used to simulate PL curves in order to see the influence of our material parameters on emission intensity.

5.3.1 Single emitter modeling

In the same scheme as illustrated in figure 5.1 we now introduce a single emitter placed at position x_e below the sample surface (Fig. 5.9).

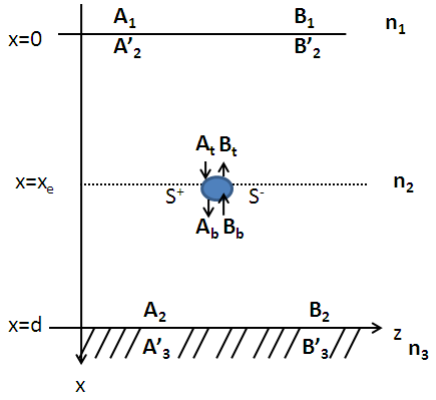

Figure 5.9: Schematic representation of the various components of the incident wave and the wave from a single emitter placed at a distance x_e in the thin film.

The emitter is considered as a source travelling in the positive and negative directions of x, the amplitude of which are given by S^+ and S^-respectively.

Let A_t= $A(x = x_e^-)$, $B_t = B(x = x_e^{-+})$ be the amplitude of the waves on top of the emitter and $A_b = A(x = x_e^+)$ & B_b= $B(x = x_e^+)$ the amplitudes below the emitter. Then at $x = x_e$, we may write,

$$A_b = A_t + S^+ \qquad \text{Eqn (5.15)}$$

$$B_b = B_t - S^- \qquad \text{Eqn (5.16)}$$

Equations 5.15 and 5.16 reflect that the total amplitude of waves travelling in the positive and negative directions is a combined contribution from the pump and the source.

The field amplitude at the top and bottom of the source can be linked using matrix formulation as follows:

$$\begin{pmatrix} A_t \\ B_t \\ 1 \end{pmatrix} = \begin{pmatrix} 1 & 0 & -S^+ \\ 0 & 1 & +S^- \\ 0 & 0 & 1 \end{pmatrix} \begin{pmatrix} A_b \\ B_b \\ 1 \end{pmatrix} \qquad \text{Eqn (5.17)}$$

The fields near the top interface in medium 2 can be linked to that near the bottom interface using a product of matrices between $x = 0$ and x_e, at x_e and between $x = x_e$ and d. This is written as,

$$\begin{pmatrix} A_2^{'} \\ B_2^{'} \\ 1 \end{pmatrix} = \begin{pmatrix} e^{ik_2x_e} & 0 & 0 \\ 0 & e^{-ik_2x_e} & 0 \\ 0 & 0 & 1 \end{pmatrix} \begin{pmatrix} 1 & 0 & -S^+ \\ 0 & 1 & +S^- \\ 0 & 0 & 1 \end{pmatrix} \begin{pmatrix} e^{ik_2(d-x_e)} & 0 & 0 \\ 0 & e^{-ik_2(d-x_e)} & 0 \\ 0 & 0 & 1 \end{pmatrix} \begin{pmatrix} A_2 \\ B_2 \\ 1 \end{pmatrix}$$

which on simplification gives,

$$\begin{pmatrix} A_2^{'} \\ B_2^{'} \\ 1 \end{pmatrix} = \begin{pmatrix} e^{ik_2d} & 0 & -e^{-ik_2d}S^+ \\ 0 & e^{-ik_2d} & e^{-ik_2d}S^- \\ 0 & 0 & 1 \end{pmatrix} \begin{pmatrix} A_2 \\ B_2 \\ 1 \end{pmatrix} \qquad \text{Eqn (5.18)}$$

Following the principles as detailed in section 5.2.1, the field amplitudes between medium 1 and medium 3 can be linked while taking into account the presence of source at $x = x_e$ now as follows,

$$\begin{pmatrix} A_1 \\ B_1 \\ 1 \end{pmatrix} = D_1^{-1}D_2 \begin{pmatrix} e^{ik_2d} & 0 & -e^{-ik_2d}S^+ \\ 0 & e^{-ik_2d} & e^{-ik_2d}S^- \\ 0 & 0 & 1 \end{pmatrix} D_2^{-1}D_3 \begin{pmatrix} A_3^{'} \\ B_3^{'} \\ 1 \end{pmatrix} \quad \text{Eqn (5.19)}$$

This global matrix formulation links the field amplitude at each wavelength and hence when we consider the case of emission wavelength (source wavelength) in medium 1, the input wave $A_1 = 0$ (since incident wavelength $\neq$ emission wavelength). The outgoing wave B_1 is only due to emission from the source which travels in the negative x direction towards medium 1. Therefore this can be represented as $B_1 = B_0^-$. In medium 3, the outgoing wave $A_3^{'}$ is a contribution only from source and hence $A_3 = B_s^+$. As described before, we consider a semi infinite medium as the substrate, therefore there is no wave reflecting back from the susbtrate ($B_3 = 0$). Using these conditions in Eqn 5.19, the two opposite travelling waves arising from the source, B_0^- and B_S^+ can be linked as follows:

$$\begin{pmatrix} 0 \\ B_0^- \\ 1 \end{pmatrix} = D_1^{-1}D_2 \begin{pmatrix} e^{ik_2d} & 0 & -e^{-ik_2d}S^+ \\ 0 & e^{-ik_2d} & e^{-ik_2d}S^- \\ 0 & 0 & 1 \end{pmatrix} D_2^{-1}D_3 \begin{pmatrix} B_s^+ \\ 0 \\ 1 \end{pmatrix} \quad \text{Eqn. (5.20)}$$

The intensities of the source waves travelling in opposite directions are then calculated with the following equations,

$$I_S^+ = \frac{c\varepsilon_0 n \mid B_s^+ \mid^2}{2} \text{ and } I_O^- = \frac{c\varepsilon_0 n \mid B_o^- \mid^2}{2} \qquad \text{Eqn (5.21)}$$

We now consider the amplitudes of the single source at x_e at the two opposite ends of medium 2 as $u^+$and u^-, then

$$u^+ = S^+ e^{-ik_2(d-x_e)} \text{ and } u^- = S^- e^{-ik_2 x_e} \qquad \text{Eqn (5.22)}$$

If there are $\mathcal{N}$ emitters placed at various positions x_i ($i = 1$ to $\mathcal{N}$), then the fields at the two ends of medium 2 becomes,

$$u^+ = \sum_{i=1}^{\mathcal{N}} S_i(x_i) e^{-ik_2(d-x_i)} \text{ at } x = d^- \qquad \text{Eqn (5.23)}$$

$$u^- = \sum_{i=1}^{\mathcal{N}} S_i(x_i) e^{-ik_2 x_e} \text{ at } x = 0^+ \qquad \text{Eqn (5.24)}$$

In order to calculate the emission intensity of $\mathcal{N}$ emitters, the population rate equations have to be known and are defined in the next section.

5.3.2 Population rate equations

In order to estimate the population density, the absorption and emission mechanisms are described by a four level system. This system as illustrated in figure 5.10 is chosen in order to relate to a Si-np system and to account for the difference in energy levels between the absorption and emission.

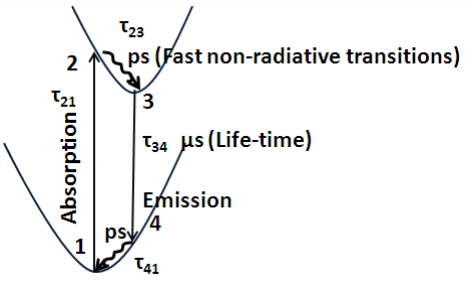

Figure 5.10: Four level system for modeling absorption and emission.

We assume the absorption of the incident photons (from laser) between energy levels 1 to 2, fast non-radiative transition in level 2 to 3, reaching of a stationary regime in level 3 where it stays for a time that defines the lifetime of the carriers, and finally deexcitation to level 1 either by spontaneous or stimulated emission. If N_i^- and N_i^+ represent the population density of level i at time t and $t + \Delta t$ respectively, the rate equations of each of the levels using the finite different method can be written as follows:

$$\frac{dN_1}{dt} = -\sigma_{abs.}\phi N_1 + \frac{N_4}{\tau_{41}} \qquad \text{Eqn (5.25)}$$

$$\frac{dN_2}{dt} = -\frac{N_2}{\tau_{23}} + \sigma_{abs.}\phi N_1 \qquad \text{Eqn (5.26)}$$

$$\frac{dN_3}{dt} = \frac{N_2}{\tau_{23}} - (\sigma_{em.}\phi + \frac{1}{\tau_{34}})N_3 \qquad \text{Eqn (5.27)}$$

$$\frac{dN_4}{dt} = -\frac{N_4}{\tau_{41}} + (\sigma_{em.}\phi + \frac{1}{\tau_{34}})N_3 \qquad \text{Eqn (5.28)}$$

where, $\sigma_{abs.}$ and $\sigma_{em.}$ represent the absorption and emission cross-sections respectively in m^2, τ_{21} is the transition time between levels 2 and 1 and τ_{23}, τ_{34} and τ_{41} represent the decay time from their respective levels and ϕ is the photon flux (photons/m^2).

The photon flux can be related to the emission intensity which in turn is dependent on the number of emitters in level N_3. From $N_3(x)$, the number of emitters, dn_e in a small region dx is considered by dividing the whole thickness of the thin film into numerous steps smaller than the period of the incident pump standing wave ($dx = T_{stand}/10$). The number of emitters in this small region is given as,

$$dn_e = N_3(x).\mathcal{A}.dx \qquad \text{Eqn (5.29)}$$

where $\mathcal{A}$ is the area of the laser beam. From this the square amplitude of source in this discretized small step of thickness dx is calculated as,

$$S^2(x)\ \alpha\ dn_e \qquad \text{Eqn (5.30)}$$

Using the rate equations, and using the initial population as $N_1^0 = 10^{26}$emitters/m^3, the photon flux as 8 x 10^3 V/m and refractive index described by figure 5.2, the distribution of emitters is visualized through theoretical modeling (Fig. 5.11).

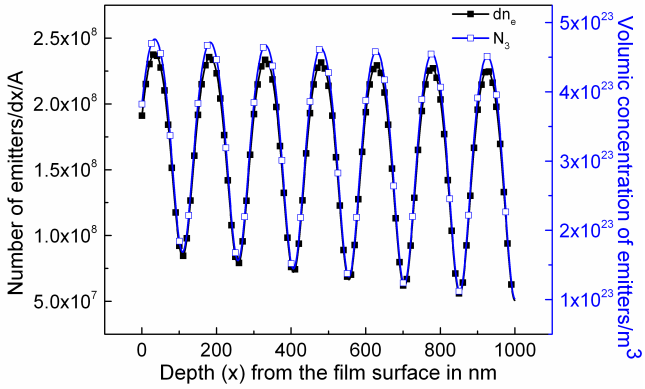

Figure 5.11: Distribution of emitters with depth in a film of 1000 nm thickness. Left axis: Number of emitters in a small thickness dx and Right axis: volumic concentration per m^3. (Simulated with Incident pump intensity: 10^5 W/m^2).

The number of excited emitters in a small thickness dx is given in the left axis and the volumic concentration of excited emitters/m^3 is given on the right axis of

figure 5.11. It can be seen clearly that the population in the excited state N_3 follows the pump profile with regularly alternating maxima and minima as suggested before.

5.3.3 Dynamical losses and gain

In the framework of this thesis, it is assumed that the real part of refractive index is a constant, while the imaginary part may depend on the absorption and gain dynamics according to the following equation,

$$\widetilde{n} = n(\lambda) - ik(\lambda, x) + ig(\lambda, x) \qquad \text{Eqn (5.31)}$$

where $n(\lambda)$ is the real part of refractive index which we assume to be unchanged with the absorption dynamics, $k(\lambda, x)$ accounts for the dynamic losses (absorption) and $g(\lambda, x)$ is the dynamic gain (emission).

Gain refers to an increase in the emitted electromagnetic intensity due to energy transfers within the medium as compared to the incident pump. When the gain is higher than the absorption in the thin film, we may expect to see emission. In order to simulate the gain and losses few assumptions are made:

- **Dynamic losses** $k(\lambda, x)$: The dynamic losses which depend on the population of emitters, can be expressed using the following equation,

$$k(\lambda, x) = \frac{\sigma_{abs}(\lambda).N_1(x).\lambda}{4\pi} \qquad \text{Eqn (5.32)}$$

where σ_{abs} is the absorption cross section, and N_1 is the population of emitters in the ground state.

In order to estimate the absorption cross section (σ_{abs}), and to give a shape to it, Lorentzian functions are used. Therefore σ_{abs} can be represented by,

$$\sigma_{abs} = \sigma_{abs.max.} \frac{1}{1 + \frac{\left(\omega^2_{ij(abs)} - \omega^2\right)^2}{\omega^2 \Delta\omega^2_{(abs)}}} \qquad \text{Eqn (5.33)}$$

where $\sigma_{abs.max}$ is the maximum value of absorption cross sections, $\omega_{ij(abs)}$ is the frequency of absorption between levels i to j, and $\Delta\omega$ is the width of the Lorentzian curve of absorption.

The parameters in equation 5.32 are obtained by giving a shape to $k(\lambda, x)$ by fitting the experimentally obtained $k(\lambda)$ with lorentzian function in the energy range of investigation (1.1 - 2.05 eV) of the emission behaviours (Fig. 5.12).

- **Dynamic gain** $g(\lambda, x)$: Similar to dynamic losses, dynamic gain can also be represented as a function of emission cross section (σ_{emis}) and the population of emitters in the excited state (N_3) as follows,

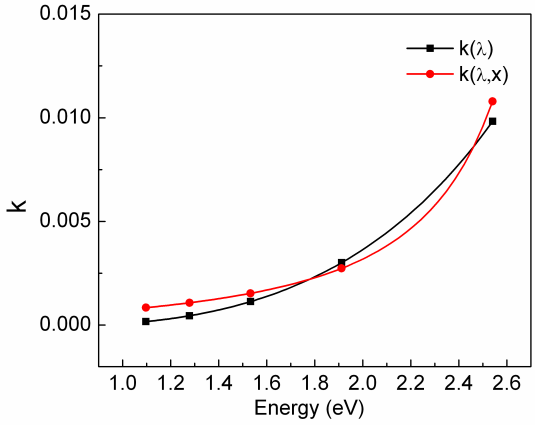

Figure 5.12: The shapes of $k(\lambda)$ and $k\,(\lambda, x)$. Lorentzian fit of the $k(\lambda)$ obtained through experiments, gives the shape of $k(\lambda, x)$.

$$g(\lambda, x)_{dynamic} = \frac{\sigma_{em}(\lambda).N_3(x).\lambda}{4\pi} \qquad \text{Eqn (5.34)}$$

For a transition between $i \rightarrow j$, the Lorentzian function for the emission cross sections is represented as,

$$\sigma_{em.} = \sigma_{em.max} \frac{1}{1 + \frac{\left(\omega^2_{ij(em.)} - \omega^2\right)^2}{\omega^2 \Delta\omega^2_{(em.)}}} \qquad \text{Eqn (5.35)}$$

where $\sigma_{em.max}$ is the maximum value of emission cross sections, $\omega_{ij(em.)}$ is the frequency of emission transitions and $\Delta\omega$ is the width of the Lorentzian curve of emission. Figure 5.13 shows the typical shapes of $\sigma(\lambda)_{abs.}$ and $\sigma(\lambda)_{em.}$

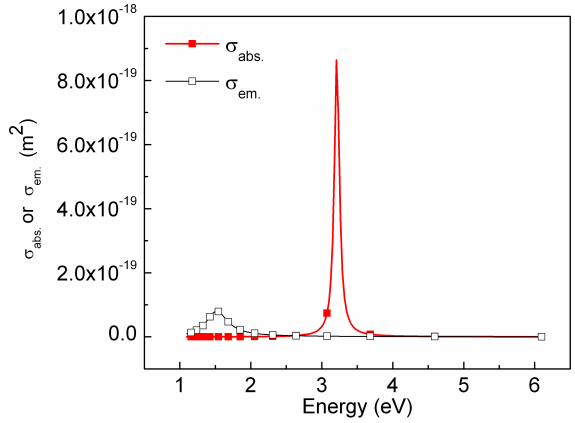

5

Figure 5.13: Illustration of emission and absorption cross-sections for arbitrary inputs.

In case of multiple emission bands in the material (n kind of emitters), the cross-sections are considered as a superposition of contribution of all the bands, as expressed by equation 5.36. In this thesis, the choice of a single absorption band is made.

$$\sigma_{em.} = \sum_{i=1}^{n} \sigma_{em.max} \frac{1}{1 + \frac{\left(\omega^2_{ij(em.)} - \omega^2\right)^2}{\omega^2 \Delta\omega^2_{(em.)}}} \qquad \text{Eqn (5.36)}$$

When the dynamic gain exceeds the dynamic losses, emission peak is evidenced in medium 1. Figure 5.14 shows the dependence of emission intensity on the thin film absorption (dynamic losses) and dynamic gain.

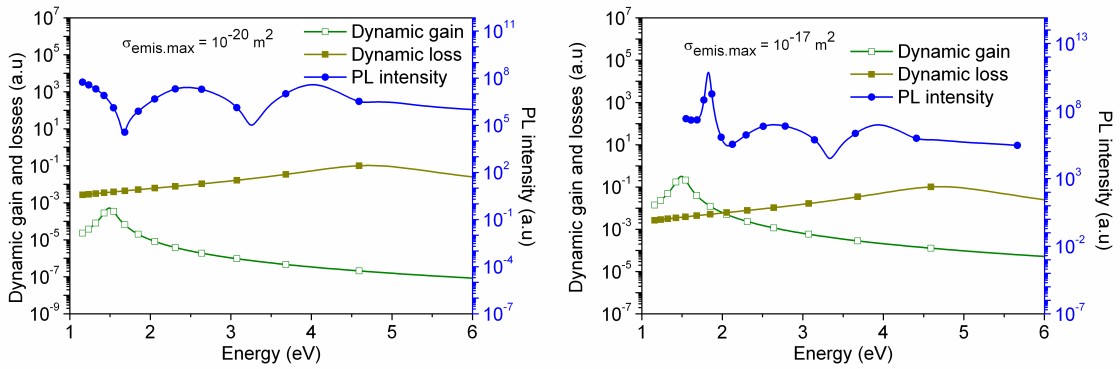

(a) $\sigma_{emis.max} = 10^{-20} m^2$ **(b)** $\sigma_{emis.max} = 10^{-17} m^2$

Figure 5.14: Dependence of emission intensity with dynamic gain and maximum emission cross-section obtained by simulations.

The graph is represented in energy scale to facilitate comparison with previous chapters. The simulation is done on a SRSO monolayer with arbitrary parameters for illustration: 1.5 refractive index, 500 nm thickness, 770 nm emission centre (1.61 eV) and $\sigma_{abs.max} = 10^{-20}$ m^2. Figure 5.14(a) shows that when $\sigma_{emis.max} = 10^{-20}$ m^2 $= \sigma_{abs.max}$ (arbitrarily fixed values), the loss is higher than the gain, and no emission is witnessed at 1.61eV. While increasing the emission cross-section to 10^{-17}m^2, the PL peak emission is evidenced as shown in figure 5.14(b), due to the positive net gain. This shows that the balance between absorption and gain plays a dominant role in the emission intensity.

The PL peak position maximum is located at 1.6 eV which differs from the position of the maximal gain. This difference in the maximum position of the peaks is attributed to the optical cavity effect of the thin film. In both the cases investigated, there are few alternating shoulders situated at similar positions which are indicative of interference mechanisms in the film.

5.4 Discussion on the choice of input parameters

5.4.1 Absorption and Emission cross-sections

We assume that the largest contribution towards emission in our SRSO/SiO_2 and SRSO/SRSN MLs is from Si-np. Since no Si-np were observed in SRSN, the SRSO layer is considered to be primarily responsible for emission. It has been reported that the absorption cross-section of Si-np usually ranges between 10^{-22} - 10^{-18} m^2 [Khriachtchev 02, Daldosso 06, Pavesi 00, Huda 09, Garcia 03]. From these literature values, we may assume our SRSO layers to have σ_{abs} in the above mentioned range.

The absorption intensity depends on the population of emitters in the ground state. Therefore, the ground state population N_1 is fixed at 10^{26} emitters/m^3 relating to the highest possible density of Si-np attainable in our SRSO layers. We keep the degree of freedom on emission cross-sections and do not link it with $\sigma_{abs.max}$ during these simulations. Various simulations were made and as illustrated in figure 5.14, it was observed that a higher emission cross-section is needed to obtain gain with our chosen σ_{abs} values and to witness emission peak in the modeled curves.

5.4.2 Lifetime of Si-np in different MLs

The lifetime of band to band recombinations of electron-hole pairs in Si-np is reported to be 10-100 µs [Wilson 93, Littau 93]. In order to have an estimate of carrier lifetime in our MLs, PL lifetime measurements[2] were made on SRSO/SiO_2 and SRSO/SRSN MLs after CA and STA treatments respectively since these annealing treatments resulted in the highest emission intensity as demonstrated in chapters 3 and 4.

Considering the emission peak around 830 nm ($\sim$ 1.5 eV) in CA SRSO/SiO_2, lifetime measurements were done by using this as the detection wavelength. Decay time was estimated to be 88 µs by fitting the experimentally obtained decay curve with a single exponential decay law.

It was discussed in chapter 4 that the PL spectra of SRSO/SRSN MLs mostly possess three peaks. The sample chosen for investigations had three emission peaks centered around 675 nm ($\sim$ 1.83 eV), 800 nm ($\sim$ 1.55 eV) and 900 nm ($\sim$ 1.37 eV). The decay time detected at each of these wavelengths were estimated to be 51 µs, 56 µs and 51 µs respectively by fitting the experimental and theoretical curves. These measurements give an estimate of the carrier lifetime, that well suits with

[2]Lifetime measurements were by Dr. J. Cardin and Prof. Christophe Labbé of our NIMPH team at CIMAP.

the values from literatures for band to band recombinations in Si-np. Therefore, the carrier lifetime (τ_{34}) is fixed as 50 µs in all the simulations. The time taken for fast radiative transitions to reach a maximum density of excited carriers (τ_{23}) and the time to deexcite to ground state (τ_{41}) are fixed arbitrarily as 100 and 500 ps respectively.

5.4.3 Absorption and emission wavelengths

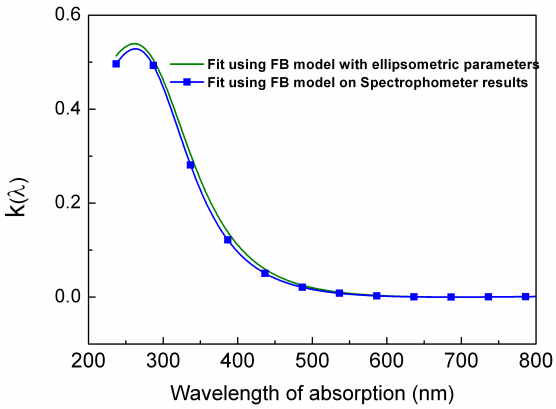

Figure 5.15: Extinction coefficient curves as a function of wavelength obtained from ellipsometry and UV-Visible spectrophotometry.

The absorption wavelength of Si-np was estimated by fitting the absorption $k(\lambda)$ curves (obtained from ellipsometry and UV-Vis spectrophotometry[3]) using Forouhi-Bloomer model [Forouhi 86]. Figure 5.15 shows the typical example of $k(\lambda)$ curves, obtained with SRSO/SRSN ML.

The maximum absorption of the material is centered around 260 nm (4.76 eV). Similar curves were obtained also with SRSO/SiO_2 MLs. Hence, it is valid to link this absorption wavelength at 260 nm to Si-np absorption as the SRSO sublayer containing Si-np is the common sublayer in both MLs.

The emission of Si-np mostly ranges between 720-830 nm (1.5 eV-1.7 eV) as demonstrated experimentally in our layers in the previous chapters. Hence in the modeling, the emission wavelength is fixed in this range when assuming the existence of a single peak in the PL spectra.

As mentioned in the previous sections, the other parameters such as the electric field amplitude of the pump (Ar laser) and the initial population of emitters are fixed at 8x10^3 V/m and 10^{26} Si-np/m^3 respectively.

5.5 Modeling SRSO/SiO_2 MLs

Figure 5.16 is shown to remind the PL spectra obtained experimentally from 50(3/3) SRSO/SiO_2 1h-1100°C annealed (CA) ML in chapter 3. As mentioned earlier, curve

[3]UV-Visible measurements were performed at "Matériaux et Instrumentation Laser" team of the CIMAP laboratory

fitting operations show the presence of two peaks centered around 1.4 eV and 1.5 eV in all the CA annealed PL spectra of this material. The second peak around 1.5 eV was explained to be a contribution from Si-np in SRSO sublayers as confirmed by XRD and APT measurements in chapters 3 and 4, while the origin of peak 1 was interpreted as a contribution from few overgrown Si-np at the interface. It was also suspected that there may be some optical phenomena such as interference that affects the shape of the emission spectra. Hence it needs to be confirmed if the two peaks are a contribution of two kinds of emitters in the material.

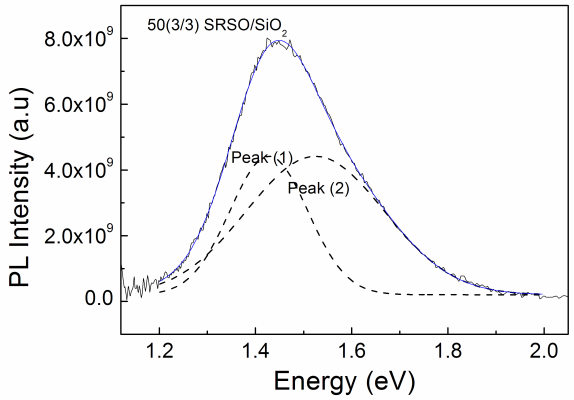

Figure 5.16: Experimentally obtained PL spectra of 50(3/3) SRSO/SiO_2 ML.

Moreover, it was seen in chapter 3 that the emission peak intensity follows a non-monotonous trend with increasing t_{SiO_2}. Therefore theoretical simulations are performed on SRSO/SiO_2 MLs to address the two major issues that arise from experimental observations:

(i) What is the origin of two emission peaks - Geometrical/optical effect or presence of two types of emitters?

(ii) What is the influence of t_{SiO_2} on PL intensity ?

5.5.1 Origin of two emission peaks

In order to understand the origin of peaks, PL curve of 50(3/3) ML was simulated with an initial assumption that only the emission peak at 1.5 eV (peak 1) is from the Si-np (i.e. only one kind of Si-np distribution). The factors that influence emission when there is only a single kind of emitter is investigated which is later extended to double kind of emitters. Simulations were made by varying thickness, refractive index, and cross-sections within the range of uncertainity, to compare the shape of the simulated curves with single and double kind of emitters with experimental PL curve.

(a) About photoluminescence from a single kind of emitter in multilayer configuration

The position and intensity of the emission peaks with regard to variation in thicknesses and refractive indices were analyzed, for the case of single kind of emitter in multilayers. Considering a typical example of a 300 nm film, the range of total thicknesses was chosen between 250 to 350 nm in steps of 10 nm for simulations. This was done to account for the influence of the possible uncertainity in the thickness determination, on the emission behaviour. Similarly, considering the uncertainity in refractive index estimation, the real part n_2 was varied between $n_2 \pm \Delta n$ for a given thickness, where Δn ranges between ± 0.05 in steps of 0.01.

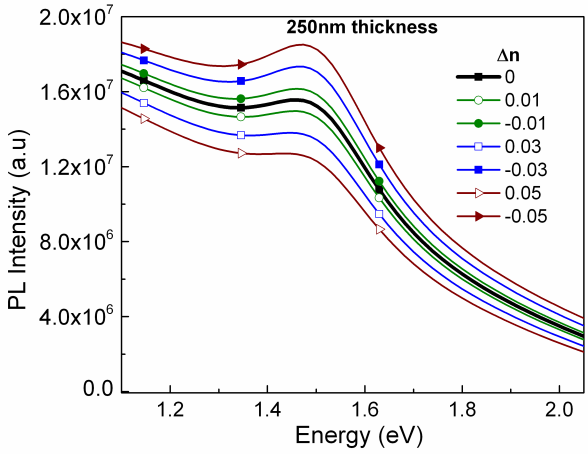

Figure 5.17: Influence of slight variations in refractive index, Δn on emission. Δn varies between ± 0.05 in steps of 0.01. [$\Delta n = 0$ corresponds to $n_{1.95eV}$ obtained by ellipsometry (here, $n_{1.95ev}$= 1.8)].

Figure 5.17 shows the emission spectra of a multilayer thin film with single kind of emitter leading to the appearance of peak (2) of the experimentally obtained spectra. The thickness of the film is fixed as 250 nm, and the influence of slight variations in refractive index is analyzed.

The results indicate that even with a slight variation of refractive index such as Δn=$\pm$0.01, there is an influence on the emission intensity. It can be seen from this figure, that with increasing refractive index, there is a drop in the emission intensity while the peak position remains fixed. This decrease of the emission intensity may be attributed to the profile of the pump within the film since the pump intensity decreases with increasing refractive indices.

Figure 5.18 shows the influence of refractive index variation on films with four different thicknesses ranging between 250 nm to 350 nm.

It is interesting to note that, the emission spectra exhibits a non-monotonous trend of refractive index influence, with varying thicknesses. For the case of 270 nm, the observations are similar to those from figure 5.17, while for 300 nm, Δn has a negligible change in the emission spectra and for 330 nm, the trend has reversed from what was observed for thicknesses lower than 300 nm. With further increase of total thickness to 350 nm, the emission spectra again show negligible variation with

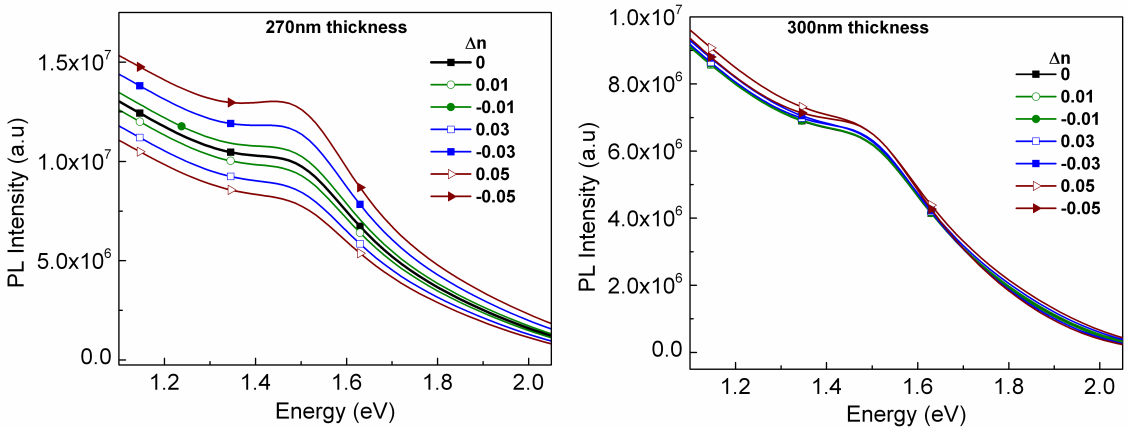

(a) 270nm. **(b)** 300nm.

(c) 330nm. **(d)** 350nm.

Figure 5.18: Effect of total thickness, and refractive index on the emission spectra.

refractive indices. This indicates that the influence of the thickness and refractive index of the thin film on the emission spectra is not straight-forward.

Figures 5.19(a and b) show the emission spectra and maximum emission peak intensity respectively, simulated from materials with same refractive index values but different thicknesses. It can be seen that there is a significant effect on the luminescence intensity by varying thicknesses in steps as small as 10 nm. These results caution us regarding the commonly used normalization to thickness for comparison of intensities in the PL analysis.

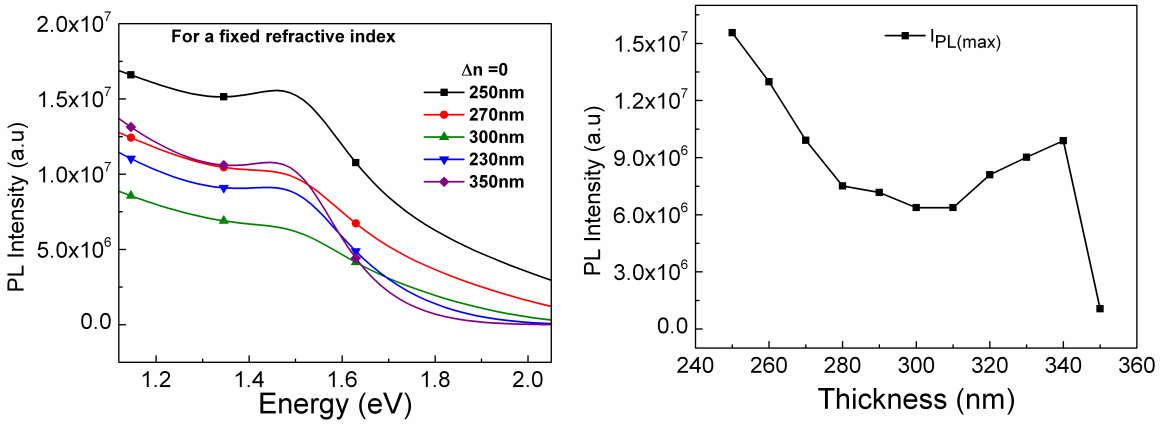

(a) Emission spectra

(b) I_{PLmax} vs. total thickness.

Figure 5.19: Influence of total thickness on the emission spectra, for a fixed refractive index.

(b) Influence of emission cross-section and emission width on the shape of the PL spectra

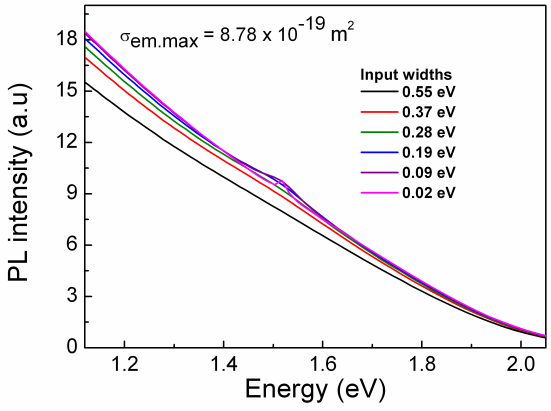

Figure 5.20: Simulating the width and intensity of PL spectra similar to experimental curve using single emitter. $\sigma_{emis.max}$ = 8.78 x 10^{-19} m^2.

It can be seen in all the figures above, that the PL peak intensity and width of the simulated curves are different from the experimentally obtained one. As mentioned earlier, the initial parameters are obtained from fitting $k(\lambda)$ and for SRSO/SiO_2 ML under discussion, the parameters are as follows: $\sigma_{abs.max}$= 8.78 x $10^{19}m^2$, with center at 3.21 eV and width 0.02 eV. Using similar parameters for emission in the case of 300 nm thick 50(3/3) ML, further simulations were made to obtain a PL shape similar to that of experimentally obtained one (Fig. 5.20). It can be seen from the figure that the PL peak is not well resolved with such conditions, despite varying the widths of the emission peak in the input. In order to increase the intensity and width (about 0.3 eV) to that of experimental curve, further simulations were made by varying the emission cross-sections and changing the theoretical width in the program (Fig. 5.21).

It can be seen from figure 5.21 that significant PL intensity is witnessed either

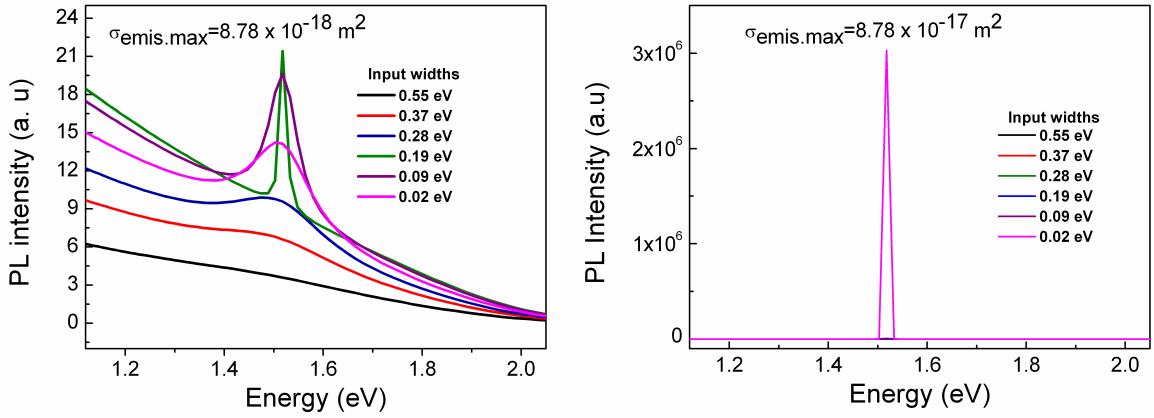

(a) $\sigma_{emis.max.} = 8.78 \text{ x } 10^{-18}\text{m}^2$ **(b)** $\sigma_{emis.max.} = 8.78 \text{ x } 10^{-17}\text{m}^2$

Figure 5.21: Simulating the width and intensity of PL spectra similar to experimental curve using single emitter and higher emission cross-sections.

by increasing the emission cross-section or by decreasing the input widths. However in all these cases, the width of the theoretical spectra is lower than the experimental one, and all the curves can be fitted with a single peak. These results suggest that the presence of another peak (peak 1) is not from interference or any other optical effects.

(c) Photoluminescence from double kind of emitters in multilayer configuration

In order to confirm the presence of two peaks to be a contribution from two kinds of emitters, simulations were performed using two emitters leading to two peaks at 1.4 and 1.5 eV in the input. Several trials were made by varying the emission cross-section parameters (see Eqn. 5.36), few of which are shown in figure 5.22a. The details of the six trials represented in this figure are given in Appendix 2. It can be seen that the intensity and width of the theoretically obtained spectra from few of the trials appear to match well with the experimental one. The PL spectra from trial 3, was chosen for further analysis (Fig. 5.22b).

The inset of figure 5.22b shows a lorentzian curve fit performed on the trial 3 simulated curve (obtained with $\sigma_{em.max}$= 8.78 x 10^{-17}m^2 for both kinds of emitters, emission peak centers for the two emitters at 1.55 eV and 1.38 eV, with widths 0.29 eV and 0.14 eV respectively). The results indicate that the broad peak of the simulated PL curve can be fitted with two peaks with positions and width similar to that of the experimentally obtained one. This fitting operation is not straight-forward, since the thin film acts as an optical cavity that filters the spectral distribution of

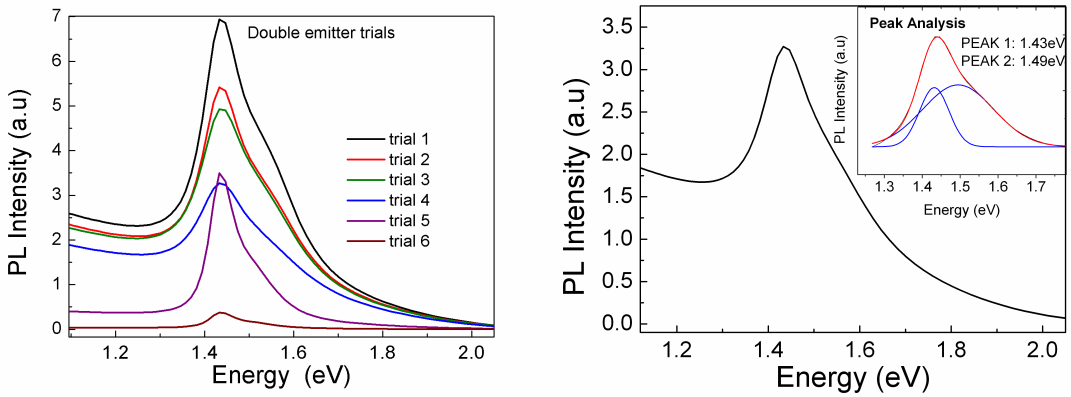

(a) Influence of various values for cross-sections and width on the PL spectra.

(b) PL spectra from trial 3.

Figure 5.22: Theoretically modeled spectra considering double kind of emitters. The inset of sub-figure (b) shows the lorentzian fit performed on the PL spectra from trial 3. The details of all the trials are given in Appendix II.

the PL band. Therefore, the fitting results on figure 5.22b confirm that, it is the existence of two kinds of emitters that lead to emission in SRSO/SiO_2 ML in the range of investigation.

5.5.2 Influence of t_{SiO_2} on the PL intensity

The role of SiO_2 as a barrier was explained in chapter 3, using which the PL spectra were also interpreted. Since it is shown in this chapter that the pump profile varies along the depth of penetration, it is clear that other factors also contribute to the emission intensity variation.

Figures 5.23(a-e) show the pump profile and the distribution of emitters in the excited state $N_3(x)$, with varying t_{SiO_2}. From $N_3(x)$, we can identify the SiO_2 sublayer positions where $N_3(x) = 0$. The five cases presented in this figure refer to SRSO/SiO_2 MLs with a constant density of emitters restricted within 3 nm SRSO sublayers. With increasing total thickness as a consequence of increasing t_{SiO_2}, the pump profile also evolves from almost two maxima to five maxima when t_{SiO_2} changes from 1.5 nm to 10 nm. It can also be seen from these figures that the distribution of emitters varies between maxima to minima in accordance with the pump profile.

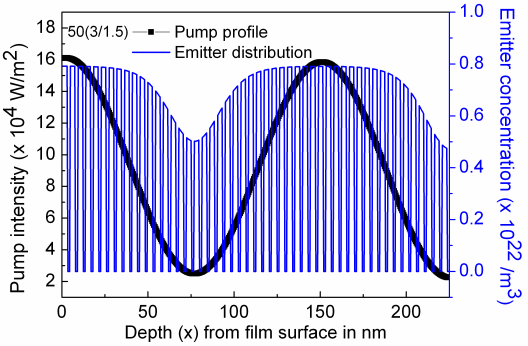

(a) 50(3/1.5)

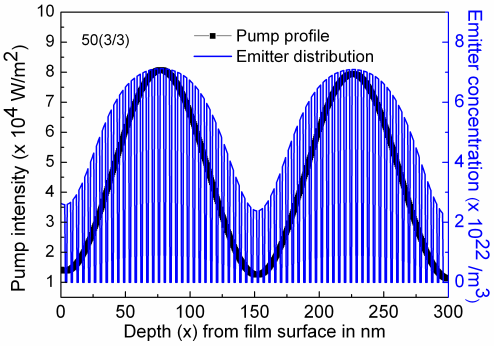

(b) 50(3/3)

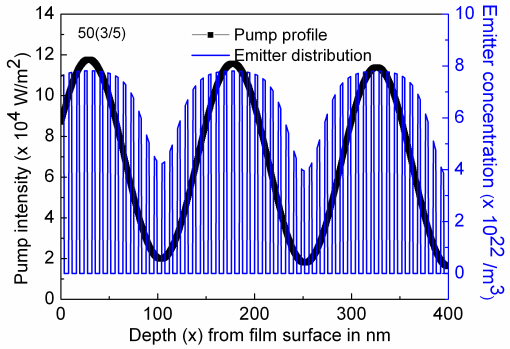

(c) 50(3/5)

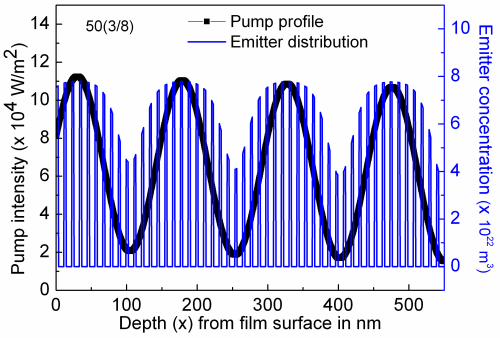

(d) 50(3/8)

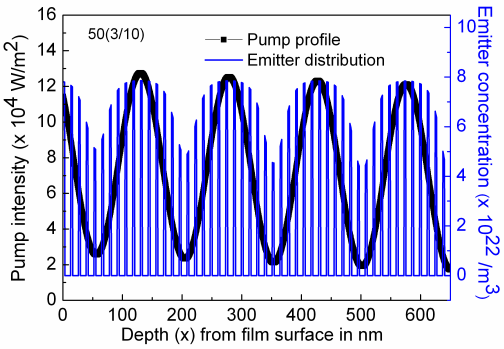

(e) 50(3/10)

Figure 5.23: (a)-(e) Simulated pump profile and excited state distribution of $50(3/t_{SiO_2})$ where t_{SiO_2}varies between 1.5 nm to 10 nm.

Figure 5.24a shows the maximum PL peak positions in MLs with varying t_{SiO_2}. The 50(3/1.5) ML shows a higher emission intensity than 50(3/3) and 50(3/5) in simulated curves, whereas in the experiments 50(3/1.5) has the lowest intensity (ref. Fig. 3.23 in chapter 3). This difference between the experimentally obtained and simulated curves may be attributed to the ideal case of ML considered in simulations, which does not account for overgrowth with lower barrier due to diffusion of Si within SiO_2. But, the non-monotonous trend of the emission intensities with increasing t_{SiO_2} indicate that the pump profile has also influenced this intensity since the emitter distribution varies with the pump profile.

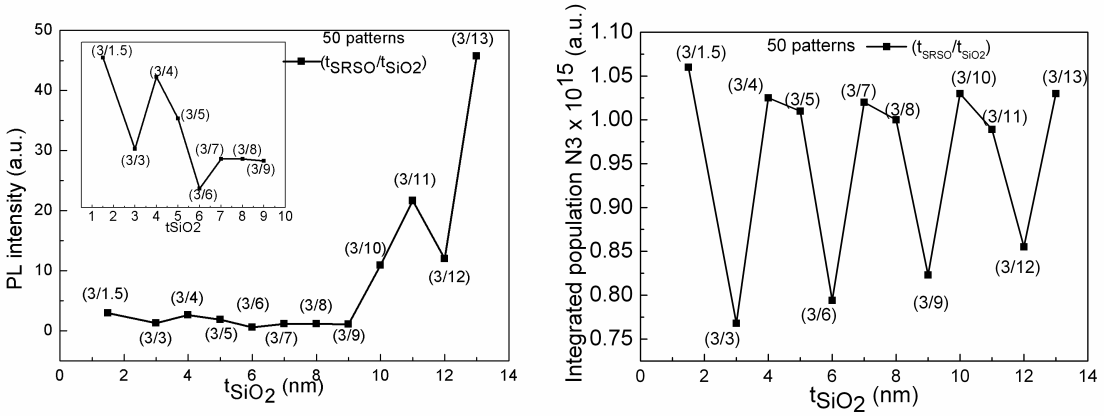

(a) $I_{PL.max}$ vs. t_{SiO_2} **(b)** Integrated population of excited emitters.

Figure 5.24: Variation of excited emitter population and maximum PL intensity with t_{SiO_2} in MLs with different total thicknesses.

In order to investigate the influence of the emitter distribution, the population of excited emitters integrated over the whole thickness (N_3^{int}) was analyzed in each case (Fig. 5.24b). It can be seen that N_3^{int} remains in the range 0.90 $\pm$0.20 x $10^{15}/m^2$ with varying t_{SiO_2}. The maximum PL intensity follows a similar trend to that of N_3^{int} upto t_{SiO_2} = 9 nm, after which it is no longer proprtional with N_3^{int} (Inset of 5.24a). This suggests the possible optical cavity effect, with increasing total thicknesses that approach the wavelength of emission. These results indicate that various other optical effects that arise with varying thickness, refractive index etc. also play a role besides the pump profile, and excited emitter distributions.

The emission intensity of MLs with different pattern numbers (36, 70 and 90) leading to similar total thickness with same t_{SRSO} and different t_{SiO_2} were also investigated in order to compare with figure 5.24 above and figure 3.22(a) (chapter 3). Figure 5.25 shows N_3^{int} and the simulated PL spectra from 90(4/1.5), 70(4/3) and 36(4/10) MLs.

It can be seen from this figure, that 90(4/1.5) which has the highest density

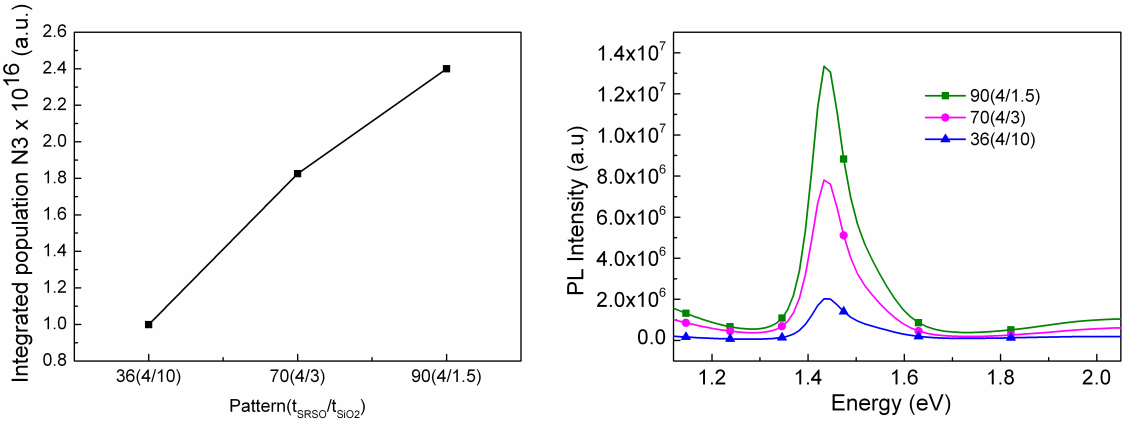

(a) Integrated population of excited emitters.

(b) PL spectra.

Figure 5.25: Variation of excited emitter population and maximum PL intensity with t_{SiO_2} in MLs with similar total thicknesses.

of excited emitters shows the highest intensity. The emission intensities of these MLs with similar total thicknesses follow a monotonous trend with N_3^{int} while in the experimental observations the 36(4/10) has higher emission than 70(4/3). Thus, we can hardly guess a trend depending on sublayer thickness or total thickness or pattern number since numerous factors influence the emission intensity.

5.6 Modeling SRSO/SRSN MLs

It was seen in chapter 4 that most of the SRSO/SRSN MLs contain three peaks whose origin was systematically investigated. However, the low energy peak (peak 1) was unattributed, and was suspected to be a contribution of interference phenomena or other such geometrical optical effects. Besides, the influence of sublayer thicknesses and pattern thicknesses on the emission intensity was also investigated experimentally but the influence of possible optical effects were suspected. Therefore, the two major issues on SRSO/SRSN MLs are similar to those in SRSO/SiO_2 MLs:

(i) Origin of low energy emission peak (peak 1).

(ii) Influence of sublayer thickness and pattern numbers.

A detailed investigation in the previous sections on SRSO/SiO_2 MLs gives an insight on the second issue that concerns the influence of sublayer thickness, pattern number, etc. on the emission intensity.

The analysis on the origin of emission from SRSO/SRSN MLs is a work in progress and the first results are discussed in this section. The curves are simulated with an assumption that the emitters are located only within SRSO sublayers.

Several trials were made to simulate PL spectra similar to those obtained from PL experiments. The typical case of 100(3.5/5) SRSO/SRSN ML was investigated by varying the three emission cross-section parameters related to three emission peaks - peak (1), (2) and (3). The three emission peak centers obtained from experiments were given as input.

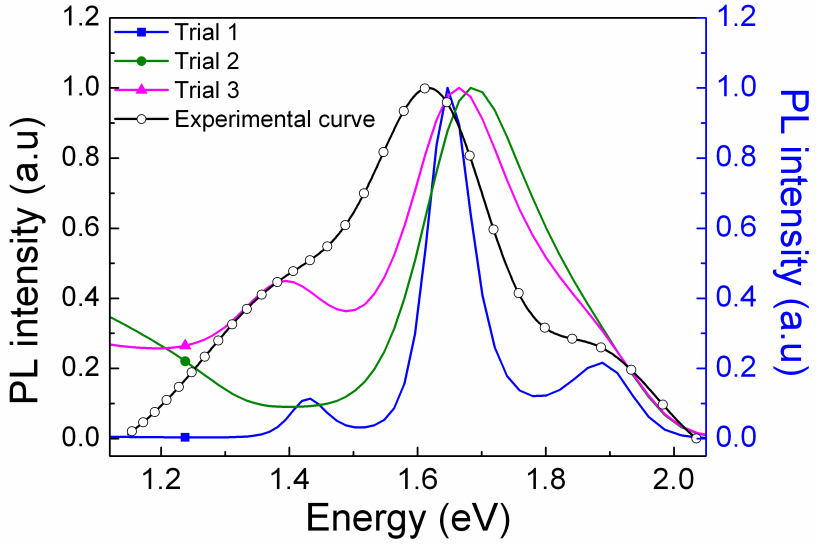

Figure 5.26: Experimental and simulated PL spectra of 100(3.5/5) SRSO/SRSN ML.

Figure 5.26 shows the experimental PL spectra and three selective trials (details in Appendix III) each resulting in different shapes of the simulated PL spectra. All the curves are normalized to unity to facilitate comparison.

It can be seen from the figure that the blue curve has all the three peaks, while in pink and green curves only two peaks may be seen. Despite the presence of three peaks, the simulated curve (blue curve) differs from the experimental PL shape. The impossibility to reproduce the experimental PL shape with our initial assumptions, suggests that the three kinds of emitters are not located within SRSO sublayer. Moreover, the position of the peak maximum in all the curves are shifted from that of experimental curve, though the input peak positions are the same as experiments. This shift clearly indicates the effect of optical cavity on the peak intensity, and emission width.

Previous results of simulations on SRSO/SiO_2 MLs show the presence of two peaks centered around 1.4 and 1.5 eV respectively (Sec. 5.5). These positions coincide with peak (1) and (2) of SRSO/SRSN MLs. Thus, we may say that the unattributed low energy peak (peak 1), in SRSO/SRSN MLs arises from second kind of emitters in SRSO sublayers. Further investigations are in progress considering

two kinds of emitters in SRSO sublayer and one kind of emitter in SRSN sublayers towards a deeper understanding.

5.7 Summary

This chapter deals with modeling the pump profile within the thin film, and emission from the thin film. The results obtained can be summarized as follows:

- The pump intensity varies with angle of incidence. With 45° incidence of Ar laser during PL experiments, the pump intensity is lower than that obtained from normal incidence.
- For a given condition, the position and intensity of the pump varies non-monotonously only by varying the thin film thickness. This is attributed to the thickness dependent reflections in the film.
- With increasing losses, the pump intensity decreases. The pump profile varies monotonously with refractive index.
- Even if the emitters are homogeneously distributed within the thin film, they are subjected to a variable pump profile. Consequently, the distribution of excited emitters follows the pump profile.
- When the dynamic gain exceeds the dynamic losses, emission peak is evidenced in medium 1.
- The emission spectra varies non-monotonously with thickness, and refractive index. Even slight variations of these parameters influence the shape of the curves.
- Simulation of SRSO/SiO_2 MLs confirms the presence of two kinds of emitters in SRSO sublayers.
- Simulation of SRSO/SRSN MLs indicates that both SRSO and SRSN sublayers contain emitters.
- The low energy peak (peak 1) is attributed to the second kind of emitter in SRSO sublayer.
- The effect of optical cavity is noticed on the emission spectra.

5.8 Conclusion

Theoretical investigations reveal various interesting facts about the numerous factors that influence emission. The simulations performed in this chapter clearly show the variation of pump profile with angle of incidence, thickness of the film and complex refractive index. These variations of the pump profile influence the excited emitter density, and therefore the emission intensity. The non-monotonous trend of emission intensity with total thickness, sublayer thickness, pattern number etc. caution us regarding the commonly used normalization to thickness of the PL intensity during analyses. Besides, the width and position of the emission peaks are influenced by the optical cavity effects. Therefore, the interpretation of emission peak position and intensity only on the basis of the density of emitters such as Si-np and their size-distribution is insufficient. A deep insight on the compexity of understanding the emission is detailed in this chapter. The presence of two emission peaks in SRSO/SiO_2 MLs is confirmed as the presence of two kinds of emitters. Following the analysis on SRSO/SiO_2 ML, the unattributed peak (1) in SRSO/SRSN is suggested to be the second kind of emitter in SRSO sublayer. Further investigations on SRSO/SiO_2 and SRSO/SRSN MLs are expected to reveal interesting informations on treating the PL spectra.

Conclusion and future perspectives

Fulfilled thesis objectives

A systematic study on the growth techniques and material properties was made towards fulfilling the four major objectives of this thesis. Therefore, the results of this thesis are also summarized into four parts as follows:

1. Material growth technique

The first major objective was to increase the density of Si-np in SRSO layers. This requires a higher incorporation of Si inside the SRSO layer during the sputtering process. In order to achieve this, two strategies were employed:

Strategy 1: Varying the deposition parameters such as deposition temperature, hydrogen rate and power applied on the Si cathode in the already established reactive sputtering and co-sputtering approaches.

Outcome: A temperature dependent growth mechanism was proposed, and it was shown that $T_d = 500$°C favours the agglomeration of Si even during deposition, which is confirmed by characterization studies performed on those layers. This agglomeration of Si will serve as seeds for Si-np formation on further annealing.

Strategy 2: Combining the advantages of reactive sputtering and co-sputtering approaches in favouring Si incorporation, and developing a new approach called as the "Reactive co-sputtering".

Outcome: High refractive indices were obtained, and the formation of Si-np in SRSO monolayers as well as SRSO sublayers in a ML configuration were witnesssed even in the as-grown state. It was seen that upon annealing, the Si-np density in SRSO reaches about 3 x 10^{19} np/cm^3 in SRSO/SiO_2 MLs and about 10^{20} np/cm^3 in SRSO/SRSN MLs thus fulfilling the first objective of this thesis.

2. Reducing the thermal budget of Si-np formation

The second major objective focussed on reducing the thermal budget of Si-np formation.

Strategy: Having established a suitable growth technique, the next investigations were focussed on the formation kinetics of Si-np in two different kind of multilayers : SRSO/SiO_2 and SRSO/SRSN by subjecting the layers to post fabrication annealing processes and analyzing the influence of the annealing time, temperature and ambience on the Si-np formation.

Outcome: The SRSO/SRSN ML exhibits a high density of Si-np after a short time annealing (STA) of 1min-1000°C which is almost a magnitude higher than that obtained from SRSO/SiO_2 MLs after annealing at 1h-1100°C (CA). The results indicate that the formation kinetics of Si-np in SRSO/SRSN is faster.

3. Demonstrating the advantages of SRSO/SRSN ML over SRSO/SiO_2 ML

The third major objective concerns the understanding of the two kinds of ML, and comparing their absorption and emission properties.

Emission properties: It was shown in this thesis that the SRSO/SRSN ML besides favouring a high density of Si-np, also exhibits intense emission at a low thermal budget (1min-1000°C) in comparison to SRSO/SiO_2 ML that needs 1h-1100°C. Besides in SRSO/SRSN ML, an interplay between time and temperature under nitrogen annealing lead to similar PL intensities (eg. 1h-700°C and 1min-1000°C). Similarly, an interplay between short-time/N_2 annealing and long-time/Forming Gas annealing also lead to similar PL intensities while the peak positions obtained by the two annealing processes are shifted. These results indicate the possibility of tuning the emission energies by using appropriate annealing treatments. Significant emissions were also obtained when SRSO/SRSN MLs are annealed for 0.5h at temperatures as low as 380°C - 500°C.

Absorption coefficients: The absorption coefficients obtained from SRSO/SiO_2 MLs even after CA annealing are lower than those obtained from SRSO/SRSN MLs after such annealing. The absorption coefficients of SRSO/SRSN MLs in its as-grown state or after STA are also significant (10^4 cm^{-1} at 3 eV).

Besides the interesting results on optical properties of SRSO/SRSN ML at a reduced thermal budget, preliminary electrical investigations indicated a two fold enhancement in conductivity than SRSO/SiO_2 MLs thus demonstrating the advantages of replacing SiO_2 barrier by SRSN.

4. Investigating the origin of photoluminescence

The fourth major objective was to understand the origin of emission, with regard to microstructure and optical/geometrical effects. The experimentally obtained PL spectra consist of one broad band composed of two peaks in the case of SRSO/SiO_2 MLs and three peaks in the case of SRSO/SRSN MLs (as seen from curve fitting operations on the emission spectra).

Experimental investigations: The peaks (1 and 2) in the PL spectra of SRSO/SiO_2 ML is suggested to be a contribution of bigger Si-np at the interfaces and Si-np within the SRSO layer respectively. In the case of SRSO/SRSN ML, the origin of peak (1) is unknown, peak (2) is attributed to Si-np contribution and peak (3) to defects from SRSN.

Theoretical investigations: Simulations performed on typical PL spectra of SRSO/SiO_2 confirm the presence of two types of emitters. Investigations indicate that the optical and geometrical effects on the emission intensities and their peak positions are not straight-forward. The results caution us about the huge role played by the pump profile, optical cavity effect, distribution of excited emitters etc. on emission and demonstrate that the microstructure of the material (eg. density and size of Si-np) is not the only necessary parameter in achieving the desired emission.

Future perspectives

This thesis lays the foundation for understanding the material growth, structural and optical properties especially of the new type of ML: SRSO/SRSN. Therefore, there are a lot of issues that have to be explored in the future some of which are described below.

(i) It was demonstrated that SRSN enhances the Si-np density and also the emission from SRSO after short time annealing. It may be assumed that the excess Si in SRSN may favour this increase in density. However, the exact mechanism that favours Si-np formation has to be analyzed.

(ii) This thesis shows that SRSN layers when annealed at high temperatures have a detrimental effect on its emission and also quenches the PL from SRSO sublayer. The reason for this detrimental effect has to be analyzed.

(iii) Experimental analysis on the origin of emission peaks from SRSO/SRSN suggests the peak around 1.9 eV (peak 3) to be a contribution from defects in SRSN sublayers. The type of defects that might lead to emission from SRSN sublayers have to be investigated. Besides, the origin of low enegy peak is unattributed. PL life-time measurements may give a deeper insight on these.

(iv) Theoretical investigations on the origin of emission peaks from SRSO/SRSN ML is a work under progress. A new code has to be built which accounts for emitters in both SRSO and SRSN ML.

(v) Using SRSO/SiO_2 and SRSO/SRSN MLs in p-i-n configuration or stacking both kinds of MLs and investigating for material properties would be another interesting future work.

Bibliography

[Abeles 83] B. Abeles & T. Tiedje. Phys Rev. B, vol. 51, page 2003, 1983.

[Aberle 01] A. G. Aberle. Sol. Energy. Mat. Sol. Cell, vol. 65, page 239, 2001.

[Aceves 96] M. Aceves, C. Falcony, A. Reynoso-Hernandez, W. Calleja & A. Torres. Solid. State. Electron., vol. 39, page 637, 1996.

[Aceves 99] M. Aceves, C. Falcony, J. A. Reynoso, W. Calleja & R. Perez. Mater. Sci. Semicond. Process, vol. 2, page 173, 1999.

[AJA 1] AJA. http://www.ajaint.com/systemsorion.htm, 1.

[Akasaka 95] T. Akasaka & I. Shimizu. Appl. Phys. Lett., vol. 66, page 3441, 1995.

[Aydinli 96] A. Aydinli, A. Serpenguzel & D. Vardar. Solid State Commun., vol. 98, page 273, 1996.

[Balber 98] I. Balber & Y. Lubianiker. Phys Rev. B, vol. 48 (12), pages 8709–8714, 1998.

[Baran 05] M. Baran, L. Khomenkova, N. korsunska, T. Stara, M. Sheinkman, Y. Goldstein, J. Jedrzejewski & E. Savir. J.Appl.Phys, vol. 98, page 113515, 2005.

[Batan 08] A. Batan, A. Franquet, J. Vereecken & F. Reniers. Surf. Interface. Anal., vol. 40, pages 754–757, 2008.

[Beard 07] M. C. Beard, P. Kelly, Knutsen, Pingrong Yu, M.Joseph, Luther, Qing Song, Wyatt K. Metzger, J. Randy, Ellingson & Arthur J. Nozik. Nano Lett., vol. 7(8), page 2506, 2007.

[Beaucarne 02] G. Beaucarne, A. S. Brown, M. J. Keevers, R. Corkish & 345-353 M. A. Green Prog. Phot. Res. Appl. 10. Prog. Photovolt: Res. Appl., vol. 10, page 345, 2002.

[Bensch 90] W. Bensch & W. Bergholz. Semicond. Sic. Technol., vol. 5, page 421, 1990.

[Bergmann 99] R. B. Bergmann. Appl. Phys. A, vol. 69, pages 187–194, 1999.

[Berremann 63] D. W. Berremann. Phys Rev. B, vol. 130, page 2193, 1963.

[Boehme 10] C. Boehme. *Mapping of recombination mechanisms in hydrogentaed amorphous silcion with coherent spin control-a 21st century approach to unsolved 20th century solar cell efficiency challenges.* 55th Annual Report DNI10, acswebcontent.acs.org/prfar2010/reports/, 2010.

[Bonafos 04] C. Bonafos, M. Carrada, N. Cherkashin, H. Coffin, D. Chassaing, G. Ben Assayag & A. Claverie. J. Appl. Phys., vol. 95, page 5696, 2004.

[Borghesi 91] A. Borghesi, M. Geddo & B. Pivac. J. Appl. Phys., vol. 69, page 7251, 1991.

[Boucher 06] Y. G. Boucher. Journal of European Optical Society - Rapid publications, vol. 1, page 06027, 2006.

[Brown 09] G. F. Brown & J. Wu. Laser & Photon Rev. 3, vol. 4, page 394, 2009.

[Bruggeman 35] D. A. G. Bruggeman. Ann. Physik (Leipzig), vol. 24, page 636, 1935.

[Brus 83] L. E. Brus. J. Chem. Phys., vol. 79, page 5566, 1983.

[Bustarret 98] E. Bustarret, M. Bensouda, M. C. Habrard, J. C. Bruyere, S. Poulin & S. C. Gujarathi. Phys. Rev. B, vol. 38, page 8171, 1998.

[Canham 90] L. T. Canham. Appl. Phys. Lett., vol. 57, pages 1046–1048, 1990.

[Canham 91] L. T. Canham, M. R. Houlton, W. Y. Leong, C. Pickering & J. M. Keen. J. Appl. Phys., vol. 70, page 422, 1991.

[Carlson 76] D. E. Carlson & C. R. Wronski. *Amorphous SIlicon Solar Cells.* Appl. Phys. Lett., vol. 28, page 671, 1976.

[Chang 10] G. R. Chang, F. M., D. Y. Ma & K. W. Xu. Nanotechnology, vol. 21, page 465605, 2010.

[Chapin 54] D. M. Chapin, C. S. Fuller & G. L. Pearson. J. Appl. Phys., vol. 25, page 676, 1954.

[Charvet 99] Stephane Charvet. *Croissance et propietes d'emission dans le visible de nanograins de silicium dans une matrice de silice:analyse par ellispometrie spectroscopique.* PhD thesis, Universite de Caen/Basse-Normandie, 1999.

[Chausserie 05] S. Chausserie, N. Khalfaoui, C. Dufour, J. Vicens, P. Marie & F. Gourbilleau. Optical Materials, vol. 27, page 1026, 2005.

[Chen 04] X. Y. Chen, Y. lu, Y. Wu, B. Cho, W. Song & D. Dai. Appl. Phys. Lett., vol. 96, page 3180, 2004.

[Chittick 69] R. C. Chittick, J. H. Alexander & H. F. Sterling. J. Electrochem. Soc, vol. 116, page 77, 1969.

[Cho 07] E. C. Cho, M. A. Green, G. Conibeer, D. Song, Y. H. Cho, G. Scardera, S. Huang, S. Park, X. J. Hao, Y. Huang & L. Van Dao. Advances in optoelectronics, vol. Article ID 69578, 2007.

[Cho 08] E.C. Cho, S. Park, X. Hao, D. Song, G. Conibeer, S.C. Park & M. A. Green. Nanotechnology, vol. 19, page 245201, 2008.

[Chopra 04] K. Chopra, P. Paulson & V. Dutta. Thin Film Solar Cells: An overview: In: Progress in photovoltaics research and applications, vol. 12, pages 69–92, 2004.

[Coates 00] John Coates. Interpretation of infrared spectra: a practical approach. John Wiley & Sons, Ltd, 2000.

[Coffa 05] S. Coffa. *Light from Silicon.* spectrum.ieee.org, 2005.

[Conibeer 06] G. Conibeer, M. A. Green, R. Corkish, Y. Cho, E. C. Cho, C. W. Jiang, T. Fangsuwannarak, E. Pink, Y. Huang, T. Puzzer, T. Trupke, B. Richards, A. Shalav & K. Lin. Thin Solid Films, vol. 511-512, pages 654 – 662, 2006.

[Conibeer 07] G. Conibeer. Materials today, vol. 10, page 42, 2007.

[Conibeer 10] G. Conibeer, M.A Green, X. Hao I. Perez-Wurfl S. Huang, D. Di, L. Shi, S. Shrestha, B. Puthen-Veetil, Y. So, B. Zhang & Z. Wan. vol. Prog. Photovolt. Res. Appl. (Paper presented at 25th EU PVSEC WCPEC-5,Spain, 2010.

[Cooke 96] D. W. Cooke, B. L. Bennett, E. H. Farnum, W. L. Hults, K. E. Sickafus, J. F. Smith, J. L. Smith, T. N. Taylar, P. Tiwari & A. M. Portis. Appl Phys Lett, vol. 68, page 1663, 1996.

[Crabtree 07] G. W. Crabtree & N. S. Lewis. Physics Today, vol. 60, page 37, 2007.

[Credo 99] G. M. Credo, M. D. Mason & S. K. Buratto. Appl Phys Lett, vol. 74, page 1978, 1999.

[Cullis 97] A.G. Cullis, L.T Canham & P.D.J. Calcott. J. Appl. Phys., vol. 82, pages 909–965, 1997.

[Daldosso 06] N. Daldosso, M. Melchiorri, L. Pavesi, G. Pucker, F. Gourbilleau, S. Chausserie, A. Belarouci, X. Portier & C. Dufour. J. Lumin., vol. 121, page 344, 2006.

[Deak 92] P. Deak, M. Rosenbauer, M. Stutzmann, J. Weber & M. S. Brandt. Phys. Rev. Lett., vol. 69, page 2531, 1992.

[Debieu 12] O. Debieu, R. Pratibha Nalini, J. Cardin, X. Portier, J. Perriere & F. Gourbilleau. *Structural and optical characterization of pure Si-rich silicon nitride thin films.* (submitted), 2012. submitted 2012.

[Delachat 09] F. Delachat, M. Carrada, G. Ferblantier, J. J Grob, A. Slaoui & H. Rinnert. Nanotechnology, vol. 20, page 275608, 2009.

[Delerue 93] C. Delerue, G. Allan & M. Lannoo. Phys Rev. B, vol. 48, page 11024, 1993.

[Delerue 99] C. Delerue, G. Allan & M. Lannoo. J. Lumin, vol. 80, page 65, 1999.

[Deshpande 95] S. V. Deshpande, E. Gulari, S. W. Brown & S. C. Rand. J. Appl. Phys., vol. 77, page 6534, 1995.

[Di 10] D. Di, I. Perez-Wurfl, G. Conibeer & M.A. Green. Sol. Energy. Mat. Sol. Cell, vol. 94, page 2238, 2010.

[Drévillion 93] B. Drévillion, I. Solomon & T. M. Fangsuwannarak. Mater. Res. Soc. Symp. Proc., vol. 283, page 455, 1993.

[D.Tsoukalas 01] D.Tsoukalas, C.Tsamis & P.Normand. Mater. Res. Soc. Symp. Proc., vol. J3.7, page 669, 2001.

[Duan 95] J. Q. Duan, G. Q. Yao, H. Z. Song, B. R. Zhang, L. Z. Zhang & G. G. Qin. J. Appl. Phys., vol. 78, page 478, 1995.

[Dupont 97] G. Dupont, H. Caquineau, B. Despax, R. Berjoan & A. Dollet. J. Phys. D: Appl. Phys., vol. 30, pages 1064–1076, 1997.

[Ekimov 81] A. I. Ekimov & A. A. Onushchenko. JETP Lett., vol. 34, page 20, 1981.

[Ellingson 05] R. J. Ellingson, M. C. Beard, J. C. Johnson, P. Yu, O. I. MiLic & A. J. Nozik. Nano Letters, vol. 5, page 865, 2005.

[ellipso 1] ellipso. http://www.horiba.com/scientific/products/ellipsometers/software/, 1.

[Ferre 05] R. Ferre, B. Garrido, M. Peralvarez, C. Garcia & J. A. Moreno. J. Appl. Phys., vol. 98, page 084319, 2005.

[Folsch 95] J. Folsch, F. Finger, T. Kulesa, F. Siebke, W. Beyer & H. Wagner. Proceedings of the Materials Research Society Symposium, vol. 377, pages 517–522, 1995.

[Forouhi 86] A. R. Forouhi & I. Bloomer. Phys Rev. B, vol. 34, page 7018, 1986.

[Franz 02] G. Franz, A. Irrera, E. C. Moreira, M. Miritello, F. Iacona, D. Sanfilippo, G. Di Stefano & F. Priolo. Appl. Phys. A, vol. 74, pages 1–5, 2002.

[Garcia 03] C. Garcia, B. Garrido, P. Pellegrino, R. Ferre, J. A. Moreno, J. R. Morante, L. Pavesi & M. Cazzanelli. Appl. Phys. Lett., vol. 82, page 1595, 2003.

[Gates 89] S. M. Gates, R. R. kunz & C. M. Greenlief. Surf. Sci., vol. 207, pages 364–384, 1989.

[Ginley 08] D. Ginley, M. A. Green & R. Collins. Harnessing materials for energy, solar energy conversion toward 1 terawatt. MRS Bulletin,Materials Research Society, 2008.

[Gnutzmann 74] U. Gnutzmann & K. Clausecker. Appl. Phys., vol. 3, page 9, 1974.

[Goetberger 02] A. Goetberger, J. Luther & G. Willeke. Solar Energy Materials and Solar Cells, vol. 74, pages 1–11, 2002.

[Gourbilleau 00] F. Gourbilleau, P. Voivenel, X. Portier & R. Rizk. Microelectronics Reliability, vol. 40, pages 889–892, 2000.

[Gourbilleau 01] F. Gourbilleau, X. portier, C. Ternon, P. Voivenel, R. Madelon & R. Rizk. Appl.Phys.Lett., vol. 78, page 3058, 2001.

[Gourbilleau 09] F. Gourbilleau, C. Ternon, D. Maestre, O. Palais & C. Dufour. J.Appl.Phys, vol. 106, page 013501, 2009.

[Green 93] M. A. Green. Semicond. Sci. Technol., vol. 8, pages 1–12, 1993.

[Green 01a] M. A. Green. Prog. Photovoltaics. Res. Appl., vol. 9, page 49, 2001.

[Green 01b] M. A. Green. Prog. Photovoltaics, vol. 9(2), page 123, 2001.

[Green 01c] M.A. Green. Third generation photovoltaics. Bridge Printery, Sydney, 2001.

[Green 02] M. A. Green & 2002 A.S. Brown. J. Appl. Phys., vol. 92, page 1326, 2002.

[Green 05] M. A. Green, E. C. Cho, Y. H. Cho, E. Pink, T. Trupke, K. L. Lin, T. Fangsuwannarak, T. Puzzer, G. Conibeer & R. Corkish. Proceeding of 20th European Photovoltaic Solar Energy Conference, Barcelona, Spain (June), page 3, 2005.

[Green 06] M. A. Green, G. Conibeer, D. Konig, E.C. Cho, D. Song, Y. Cho, T. Fangsuwannarak, Y. Huang, C.Jiang, T. Trupke, R. Corkish & T. Puzzer. 21st European Photovoltaic Solar Energy Conference, Dresden (September), 2006.

[Gritsenko 99] V. A. Gritsenko, K. S. Zhuravlev, A. D. Milov, H. Wong, R. W. M. Kwok & J. B. Xu. Thin Solid Films, vol. 353, page 20, 1999.

[Guha 99] S. Guha & J. Yang. IEEE Transactions on Electron devices, vol. 46, pages 2080–2085, 1999.

[Guha 02] S. Guha & J. Yang. Proceedings of the 29th IEEE PVSEC, New Orleans, pages 1070–1075, 2002.

[Hanna 06] M. C. Hanna & A. J. Nozik. J. Appl. Phys., vol. 100, page 074510, 2006.

[Hasegawa 93] S. Hasegawa, L. He, Y. Amano & T. Inokuma. Phys. Rev. B, vol. 48, page 5315, 1993.

[Hegedus 97] Steven. S. Hegedus. Prog. Photovolt: Res. Appl., vol. 5, pages 151–168, 1997.

[Hijazi 09a] K. Hijazi, L. Khomenkova, J. Cardin, F. Gourbilleau & R. Rizk. Physica E, vol. 41, page 1067, 2009.

[Hijazi 09b] Khalil Hijazi. *Contribution a l'optimisation du couplage Erbium-nanograins de silicium pour des dispositifs photoniques compacts.* PhD thesis, Universite de caen/Basse-Normandie, 2009.

[Holm 82] R. T. Holm, S. W. McKnight, e. D. palik & W. Lukosz. Applied Optics, vol. 21, page 2512, 1982.

[Hong 10] S. H. Hong, J. H. Park, D. H. Shin, C. O. Kim, S.-H Choi & K. J. Kim. Appl Phys Lett, vol. 97, page 072108, 2010.

[Hong 11] S. H. Hong, Y. S. Kim, W. L., Y. H. Kim, J. Y. Song, J. S. Jang, J. H. Park, S.-H Choi & K. J. Kim. Nanotechnology, vol. 22, page 425203, 2011.

[Huang 97] L. Huang, K. W. Hipps, J. T. Dickinson, U. Mazur & X. D. Wang. Thin Solid Films, vol. 299, page 104, 1997.

[Huda 09] M. Q. Huda, S. Saha, M. S. Akter, M. T. Hasan, S. Subrina & F. M. Mohammedy. 4th International Conference on Computers and Devices for Communication, CODEC 2009., pages 1–4, 2009.

[Iacona 00] F. Iacona, G. Franzò & C. Spinella. J. Appl. Phys., vol. 87, pages 1295–1303, 2000.

[Ibaraki 84] N. Ibaraki & H. Fritzsche. Phys Rev. B, vol. 30, page 5791, 1984.

[Innocenzi 03] P. Innocenzi. J. Non. Cryst. Solids, vol. 316, page 309, 2003.

[Internet 01] Internet. www.hydrogen.co.uk, 01.

[Internet 02] Internet. http://www.alternate-energy-sources.com/how-does-solar-energy-work.html, 02.

[Internet 03] Internet. *World energy usage width chart.* http://it.wikipedia.org/, 03.

[Internet 04] Internet. www.wikipedia.org on thin film solar cells, 04.

[Internet 05] Internet. http://www.icarussolarpower.co.uk/solarpanels.html, 05.

[Internet 06] Internet. http://us.sanyo.com/Solar/SANYO-HIT-Technology, 06.

[Internet ta] Internet. http://refractiveindex.info, data.

[IPCC 07] IPCC. *The Intergovernmental Panel on Climate Change.* IPCC Fourth Assessment Report (AR4), 2007.

[Jackson 82] W. B. Jackson & N. M. Amer. Phys Rev. B, vol. 25, page 5559, 1982.

[Jiang 04] C. W. Jiang, M. A. Green, E. C. Cho & G. Conibeer. J. Appl. Phys., vol. 96, page 5006, 2004.

[Jiang 06a] C. Jiang & M. A. Green. J.Appl.Phys, vol. 99, page 114902, 2006.

[Jiang 06b] C.W. Jiang, C. Pakes, Y. Huang, G. Conibeer & M.A. Green. 21st European Photovoltaic Solar Energy Conference, Dresden, page 168, 2006.

[Kahler 01] U. Kahler & H. Hofmeister. Opt. Mater., vol. 17, page 83, 2001.

[Kaiser 56] W. Kaiser, P. H. Kech & C. F. Lange. Phys. Rev., vol. 101, page 1264, 1956.

[Kaiser 98] I. Kaiser, N. H. Nickel & W. Fuhs. Phys. Rev. B, vol. 58, page R1718, 1998.

[Kameda 98] E. Kameda, T. Matsuda, Y. Emura & T. Ohzone. Solid. State. Electron, vol. 42, page 2105, 1998.

[Kanemitsu 97] Y. Kanemitsu & S. Okamoto. *Photoluminescence from Si/SiO_2 single quantum wells by selective excitation.* Phys. Rev. B, vol. 56, no. 24, pages R15561–R15564, Dec 1997.

[Kanzawa 96] Y. Kanzawa, S. Hayashi & K. Yamamoto. J.Phys: Condens. Matter., vol. 8, page 4823, 1996.

[Khriachtchev 99] L. Khriachtchev, M. Rasanen, S. Novikov, O. Kipela & J. Sinkkonen. J.Appl. Phys., vol. 86, page 5601, 1999.

[Khriachtchev 02] L. Khriachtchev. Appl. Phys. Lett., vol. 81, page 1357, 2002.

[Kim 05] B. H. Kim, C. H. Cho, T. W. Kim, N. M. Park, G. Y. Sung & S. J. Park. Appl. Phys. Lett., vol. 86, page 091908, 2005.

[Kim 09] S. K. Kim, C. H. Cho, B. H. Kim, S. J. Park & J. W. Lee. Appl Phys Lett, vol. 95, page 143120, 2009.

[Kingsbury 52] E. F. Kingsbury & R.S. Ohl. Bell. Syst. Tech J, vol. 31, page 802, 1952.

[Kirk 88] C. T. Kirk. Phys Rev. B, vol. 38, page 1255, 1988.

[Konig 10] D. Konig, K. Casalenuovo, Y. Takeda, G. Conibeer, J.F. Guillemoles, R. Patterson, L. M. Huang & Green M. A. Physica E, vol. 42, page 2862, 2010.

[Kurokawa 06] Y. Kurokawa, S. Miyajima, Y. Yamada & M. Konagai. Jpn J Appl Phys 2006; 45: L1064-L1066, vol. 45, page L1064, 2006.

[la Torre 06] J. De la Torre, G. Bremond, M. Lemiti, G. Guillot, P. Mur & N. Buffet. Thin Solid Films, vol. 511-512, page 163, 2006.

[LeComber 85] P.G. LeComber, W. E. Spear & R. A. Gibson. J. Non. Cryst. Solids, vol. 77-78, page 1081, 1985.

[Lehmann 83] A. Lehmann, L. Shuhmann & K. Huebner. Phys. Stat. Sol. B, vol. 117, page 689, 1983.

[Lelievre 07] J. F. Lelievre, H. Rodriguez, E. Fourmond, S. Quoizola, J. De la Torre, A. Sibai, G. Bremond, P.J. Reberryorn, J. C. Loretz, D. Aroujo & M. Leviti. Phys. Stat. Solidi. C, vol. 4, page 427, 2007.

[Lim 08] K. S. Lim & O. Shevaleevskiy. Pure Appl. Chem, vol. 80, page 2141, 2008.

[Lin 92] K. C. Lin & S. C. Lee. J. Appl. Phys., vol. 72, page 5474, 1992.

[Lin 00] C. F. Lin, W. T. Teseng & M. S. Feng. J. Appl. Phys., vol. 87, page 2808, 2000.

[Lin 02] S. Y. Lin. J. Optoelect. Adv. Materials, vol. 4, page 543, 2002.

[Littau 93] K. A. Littau, P. J. Szajowski, A. J. Muller, A. R. kortan & L. E. Brus. J. Phys. Chem., vol. 97, page 1224, 1993.

[Lopez 11] J. Carrillo Lopez, J. A. Luna Lopez, I. Vivaldo de la Cruz, M. Aceves-Mijares, A. Morales-Sanchez & G. Garcia-Salgado. Sol. Energy. Mat. Sol. Cell (Article in press), vol. doi:10.1016/j.solmat.2011.04.029, 2011.

[Lucovsky 83] G. Lucovsky, J. Yang, S. S. Chao, J. E. Tyler & W. Czubatyj. Phys Rev. B, vol. 28, page 3234, 1983.

[Lucovsky 87] G. Lucovsky, M. J. Mantini, J. K. Srivastava & E. A. Irene. J. Vac. Sci. Technol., vol. B5, page 530, 1987.

[Luque 97] A. Luque & 1997 A. Marti. Phys.Rev.Lett, vol. 78, pages 5014–5017, 1997.

[Luque 05] A. Luque, A. Marti, N. Lopez, E.Antolin, E. Canovas, C. Stanley, C. Farmer, L. J., L. Cuadra & J. L. Balenzategui. Appl Phys Lett, vol. 87, page 083505, 2005.

[Maestre 10] D. Maestre, O. Palais, D. Barakel, M. Pasquinelli, C. Alfonso, F. Gourbilleau, M. De Laurentis & A. Irace. J.Appl.Phys, vol. 107, page 064321, 2010.

[Mandelkorn 62] J. Mandelkorn, C. McAfee, J. Kaspersis, L. Schwartz & W. Pharo. J. Electrochem. Soc., vol. 109, page 313, 1962.

[Maria 75] D. J. Di Maria & P. C. Arnett. Appl. Phys. Lett., vol. 26, page 711, 1975.

[Marti 96] A. Marti & G. L. Aranjo. Sol, vol. 43, page 203, 1996.

[Meier 94a] J. Meier, S. Dubail, R. Fluckinger, D. Fischer, H. Keppner & A. Shah. Ist World Conference on photovoltaic enegy conversion, pages 409–412, 1994.

[Meier 94b] J. Meier, R. Fluckinger, H. Keppner & A. Shah. Appl. Phys. Lett., vol. 65, pages 860–862, 1994.

[Min 96] K.S. Min, K.V. Shchegtov, C.M. Yang, H. Atwater, M.L. Brongersma & A. Polman. *Defect-related versus excitonic visible light emission from ion beam synthesized Si nanocrystals in SiO_2.* Appl. Phys. Lett., vol. 69, pages 2033–2035, 1996.

[Miritello 10] M. Miritello, R. L. Savio, P. Cardile & F. Priolo. Phys. Rev. B, vol. 81, page 041411, 2010.

[Miroslav] M. Miroslav. www.posterus.sk, vol. ISSN 1338-0087.

[Miska 10] P. Miska, M. Dossot, T. D. Nguyen, M. Grun, H. Rinnert, M. Vergnat & B. Humbert. J. Phys. Chem. C, vol. 114, page 17344, 2010.

[Mitchell 73] J. P. Mitchell & D. G. Denure. Solid-State Electron., vol. 825, page 16, 1973.

[Molinari 03] M. Molinari, H. Rinnert, M. Vergnat & P. Weisbecker. Materials Science and Engineering, vol. B101, pages 186–189, 2003.

[Morales-Sanchez 08] A. Morales-Sanchez, J. Barreto, C. Dominguez-Horna, M. Aceves-Mijares & J.A. Luna-Lopez. Sensors and Actuators A, vol. 142, page 12, 2008.

[Nalini 12] R. Pratibha Nalini, L. Khomenkova, O. Debieu, J. Cardin, C. Dufour, M. Carrada & Fabrice Gourbilleau. Nanoscale Research Letters, vol. 7, page 124, 2012.

[Negro 06] L. Dal Negro, J. H. Yi, J. Michel, L. C. Kimerling, T. W. F. Chang, V. Sukhovatkin & E. H. Sargent. Appl Phys Lett, vol. 88, page 233109, 2006.

[Nesbit 85] L. A. Nesbit. Appl. Phys. Lett., vol. 46, page 38, 1985.

[Nesheva 02] D. Nesheva, C. raptis, A. Perakis, I. Bineva, Z. ANeva, Z. Levi, S. Alexandrova & H. Hofmeister. J. Appl. Phys., vol. 92, page 4698, 2002.

[Nguchi 93] N. Nguchi & I. Suemune. Appl Phys Lett, vol. 62, page 1429, 1993.

[Niu 07] J. Niu, D. Yang, J. Sha, J. N. Wang & M. Li. Mater. Lett., vol. 61, page 894, 2007.

[Nozik 01] A. J. Nozik. Annu. Rev. Phys. Chem., vol. 52, page 193, 2001.

[Nozik 02] A. J. Nozik. Physica E- Low dimensional systems & nanostructures, vol. 14(1-2), page 115, 2002.

[Nozik 08] A. J. Nozik. Chemical Physics Letters, vol. 457, pages 3–11, 2008.

[Ohl 41a] R. S. Ohl. *Light sensitive device including silicon.* US Patent 2443542 filed May 27,1941, 1941.

[Ohl 41b] R. S. Ohl. *Light sesitive electric device.* US Patent 2402622 filed March 27,1941, 1941.

[Ono 98] H. Ono, T. Ikarashi, M. B. K. Ando & T. Kitano. J. Appl. Phys., vol. 84, page 6064, 1998.

[Pai 86] P. G. Pai, S. S. Chao, S. Takagi & G. Lukovsky. J. Vac. Sci. Tech, vol. A4, page 689, 1986.

[Palma 02] R. J. M. Palma, L. Pascaul, P. Herrero & J. M. M. Duart. Appl. Phys. Lett., vol. 81, page 25, 2002.

[Parida 11] B. Parida, S. Iniyan & R. Goic. Renewable and Sustainable Energy Reviews, vol. 15, pages 1625–1636, 2011.

[Park 01] N. M. Park, T. S. Kim & S. Park. J. Appl. Phys., vol. 78, page 2575, 2001.

[Pavesi 00] L. Pavesi, L. D. Negro, C. Mazzoleni, G. Franzo & J. P. Prolo. Nature, vol. 408, page 440, 2000.

[Peterson 88] M. W. Peterson, J. A. Turner, C. A. Parsons, A. J. Nozik, D. J. Arent, C. Van Hoof, G. Borghs, R. Houdre & H. Morkoc. Appl. Phys. Lett, vol. 53, page 2666, 1988.

[Pieters 08] B. E. Pieters. *Characterization of thin film silicon materials and solar cells through numerical modelling: Delft Dissertation Thesis*. 2008.

[Poortmans 06] J. Poortmans & V. Arkhipov, editeurs. Thin film solar cells, fabrication, characterization and applications. John Wiley & Sons, Ltd, 2006.

[Portier 03] X. Portier, C. Ternon, F. Gourbilleau, C. Dufour & R. Rizk. Physica E, vol. 16, page 439, 2003.

[Prokes 92] S. M. Prokes, O. J. Glembocki & V. M. Bermudez. Phys Rev. B, vol. 45, page 13788, 1992.

[Qin 93] G. G. Qin & Y. Q. Jia. Solid State Commun., vol. 86, page 559, 1993.

[Quan 11] Cao Quan, Ma Zhi-Hua, Xue Chun-Lai, Zuo Yu-Hua & Wang Yi-Ming. Chinese Physics B, vol. 20, page 097103, 2011.

[Quiroga 09] E. Quiroga, W. Bensch, Z. Yu, M. Aceves, R. A. De Souza, M. Martin, V. Zaporojtchenko & F. Faupel. Phys. Stat. Sol. (A), vol. 206, page 263, 2009.

[Reber 99] S. Reber & W. Wettling. Appl. Phys. A, vol. 69, pages 215–220, 1999.

[Ritcher 81] H. Ritcher, Z. P. Wang & L. Ley. Solid State Commun., vol. 39, page 625, 1981.

[Ross 82] R. T. Ross & A. Nozik. J. Appl. Phys., vol. 53, page 3813, 1982.

[Roussel 11] M. Roussel, E. Talbot, F. Gourbilleau & P. Pareige. Nanoscale Research Letters, vol. 6, page 164, 2011.

[Ruiz 94] F. Ruiz, C. Vazquez-Lopes, J. Gonzales-Hemandes, D. David & J. Allred. J. Vac. Sci. Technol.,A. Vac. Surf. Films, vol. 12, page 2565, 1994.

[Salvo 01] B. De Salvo, G. Ghibaudo, P. Luthereau, T. Baron, B. Guillaumot & G. Reimbold. Solid. Stat. Electron., vol. 45, page 1513, 2001.

[Sana 94] P. Sana, A. Rohatgi, J. P. Kalejs & R. O. Bell. Appl Phys Lett, vol. 64, page 97, 1994.

[Satoh 85] T. Satoh & A. Hiraki. Jap. J. Appl. Phys., vol. 24, page L491, 1985.

[Scardera 08] G. Scardera, T. Puzzer, G. Conibeer & M. A. Green. J. Appl. Phys., vol. 104, page 104310, 2008.

[Schuppler 95] S. Schuppler, S. L. Friedman, M. A. Marcus, D. L. Adler, Y. H. Xie, F. M. Ross, Y. J. Chabal, T. D. Harris, L. E. Brus, W. L. Brown, E. E. Chaban, P. F. Szajowski, S. B. Christman & P. H. Citrin. Phys. Rev. B, vol. 52, pages 4910–4925, 1995.

[Seifarth 98] H. Seifarth, R. grotzschel, A. Markwitz, W. Martz, P. Nitzsche & L. Rebohle. Thin Solid Films, vol. 330, page 202, 1998.

[Shanks 80] H. R. Shanks, C. J. Fang, L. Ley, M. Cardona, F. J. Demond & S. Kalbitzer. Phys. Stat. Sol. (B), vol. 100, page 43, 1980.

[Shanks 81] H. R. Shanks, F. R. Jeffrey & M. E. lowry. Journal de Physique, vol. C4, page 773, 1981.

[Shockley 61] W. Shockley & H. Queisser. Journal of Applied Physics, vol. 32, pages 510–519, 1961.

[Siltronix 1] Siltronix. http://www.siltronix.com, 1.

[So 11] Y. H. So, S. Huang, G. Conibeer & M. A. Green. vol. 519, page 5408, 2011.

[Song 08a] D. Song, E. C. Cho, G. Conibeer, Y. Huang, C. Flynn & M. A. Green. J. Appl. Phys., vol. 083544103, page 083544, 2008.

[Song 08b] D. Y. Song, E. C. Cho, G. Conibeer, D. Y.Huang, C. Flynn & M. A. Green. J.App, vol. 103, page 083544, 2008.

[Sopori 96] B. L. Sopori, X. Deng, J. P. Benner, A. Rohatgi, P. Sana, S. K. Estreicher, Y. K. Park & M. A. Roberstson. Sol. Energy. Mat. Sol. Cell, vol. 41/42, pages 159–169, 1996.

[Spear 72] W. E. Spear & P. G. LeComber. J. Non. Cryst. Solids, vol. 8, page 727, 1972.

[Staebler 77] D. L. Staebler & C. R. Wronski. Appl. Phys. Lett., vol. 31, page 292, 1977.

[Staebler 80] D. L. Staebler & C. R. Wronski. J. Appl, vol. 6, page 51, 1980.

[Stevens 93] P. D. Stevens & R. Glosser. Appl Phys Lett, vol. 63, page 8003, 1993.

[Street 78] R. A. Street, J. C. Knights & D. K. Biegelson. Phys. Rev. B, vol. 18, page 1880, 1978.

[Street 82] R. A. Street. Appl. Phys. Lett., vol. 41, page 1060, 1982.

[Sui 92] Z. Sui, P. P. Leong, I. P. Herman, G. S.Higashi & H. Temkin. Appl Phys Lett, vol. 60, page 2086, 1992.

[Svrcek 04] V. Svrcek, A. Slaoui & J. C. Muller. Thin Solid Films, vol. 451, page 384, 2004.

[Taguchi 00] M. Taguchi, K. Kawamoto, S. Tsuge, T. Baba, H. Sakata, M. Morizane, K. Uchihashi, N. Nakamura, S. Kiyama & O. Oota. Prog. Photovolt: Res. Appl., vol. 8, page 503, 2000.

[Ternon 02] Celine Ternon. *Nanostructures luminescentes a base de silice et de silicium: de l'elaboration par pulverisation magnetron reactive a la modelisation de la photoluminescence*. PhD thesis, Universite de Caen/Basse-Normandie, 2002.

[Ternon 04a] C. Ternon, C. Dufour, F. Gourbilleau & R. Rizk. Eur. Phys. J. B, vol. 41, page 325, 2004.

[Ternon 04b] C. Ternon, C. Dufour, F. Gourbilleau & R. Rizk. Eur. Phys. J. B, vol. 91, pages 325–332, 2004.

[Timmerman 08] D. Timmerman, I. Izeddin, P. Stallinga, W. Yassierich & T. Gregorekeiwicz. Nat. photonics, vol. 2, pages 105–109, 2008.

[Timmerman 11] D. Timmerman, J. valenta, K. Dohnalova, W. D. A. M. de Boar & T. Gregorkeiwicz. Nature Nanotechnology, vol. 6, pages 710–711, 2011.

[Torchynska 05] T. V. Torchynska, A. Vivas Hernandes, M. Dybiac, Yu. Emirov, I. Tarasov, S. Ostapenko & Y. Matsumoto. Phys. Stat. Sol. (C), vol. 2, page 1832, 2005.

[Trupke 02a] T. Trupke, M. A. Green & P. Wurfel. J. Appl. Phys., vol. 92, page 4117, 2002.

[Trupke 02b] T. Trupke, M. A. Green & P. Wurfel. J. Appl. Phys., vol. 92, page 1668, 2002.

[Tsai 89] C. C. Tsai, R. Thompson, C. Doland, F. A. Ponce, G. B. Anderson & B. Wacker. Mater. Res. Soc. Symp. Proc., vol. 118, page 49, 1989.

[Veprek 68] S. Veprek & V. Marecek. Solid State Electronics, vol. 11, pages 683–684, 1968.

[Veprek 79] S. Veprek & A. P. Webb. Proc. 4th. Int. Symp. on Plasma Chemistry, Zurich, page 79, 1979.

[Vernhes 06] R. Vernhes, O. Zabeida & M. J. Mantini. J. Appl. Phys., vol. 100, page 063308, 2006.

[Veve 96] C. Veve, M. Stemmer & S. Martinuzzi. Materials Science and Engineering B, vol. 36, page 200, 1996.

[Wagendristel 94] A. Wagendristel & Y. Wang. An introduction to physics and technology of thin films. World Scientific Publishing, 1994.

[Wang 92] J. Wang, H. B. Jiang, W. C. Wang, J. B. Zheng, F. L. Zhang, P. H. Hao, X. Y. Hou & X. Wang. Phys. Rev. Lett, vol. 69, page 3252, 1992.

[Wang 03] Y. Q. Wang, Y. G. Wang, L. Cao & Z. X. Cao. Appl. Phys. Lett., vol. 83, page 3474, 2003.

[Weber 91] J. P. Weber & S. Wang. IEEE Journal of Quantum Electronics, vol. 27, page 2256, 1991.

[Weng 93] Y. M. Weng, Zh. N. fan & X. F. Zong. Appl Phys Lett, vol. 63, page 168, 1993.

[Wilson 93] W. L. Wilson, P. j. Szajowski & L. E. Brus. Science, vol. 262, page 1242, 1993.

[Wolkin 99] M. V. Wolkin, J. Jorne, P. M. Fauchet, G. Allan & C. Delerue. Phys. Rev. Lett, vol. 82, page 197, 1999.

[Wronski 02] C. R. Wronski, J. M. Pearce, R. J. Koval, A. S. Ferlando & R. W. Collins. Progress in Amorphous Silicon based solar cell technology RIO 02- World Climate and Energy Event, pages 67–72, 2002.

[Wurfel 97] P. Wurfel. Sol. Energy. Mat. Sol. Cell, vol. 46, page 43, 1997.

[Xiao 93] Y. Xiao, M. J. Heben, J. M. McCullough, Y. S. Tsuo, J. I. Pankove & S. K. Deb. Appl Phys Lett, vol. 62, page 1152, 1993.

[Yang 94] J. Yang, A. Banerjee, T. Glatfelter, K. hoffman, X. Xu & S. Guha. Proceedings of the 1st world conference on photovoltaic energy conversion, pages 380–385, 1994.

[Yang 04] M. S. Yang, K. S. Cho, J. H. Jhe, S. Y. Seo, J. H. Shin, K. J. Kim & D. W. Moon. Appl Phys Lett, vol. 85, page 3408, 2004.

[Yeh 88] Pochi Yeh. Optical waves in layered media. John Wiley and Sons, 1988.

[Zacharias 02] M. Zacharias, J. Heitmann, R. Scholz, U. Kahler, M. Schmidt & J. Blasing. Appl. Phys. Lett., vol. 80, page 661, 2002.

[Zoubir 94] N. H. Zoubir, M. Vergnat & Ph. de Donato. Appl Phys Lett, vol. 65, page 82, 1994.

Appendix I

2 x 2 Matrix formulation for Isotropic Layered Media [Yeh 88]

Let us consider the case of a plane wave incident on an interface between two media with refractive indices n_1 and n_2 respectively. It is know that a part of the incident wave will be transmitted into medium 2 and a part reflected back at medium 1. If $E_i exp\left[i\left(\omega t - k_i.r\right)\right]$, $E_r exp\left[i\left(\omega t - k_r.r\right)\right]$ and $E_t exp\left[i\left(\omega t - k_t.r\right)\right]$ are the field amplitudes of the incident plane wave, reflected and transmitted waves respectively, following the boundary conditions all the three propagation vectors k_i,$k_r$and k_t must lie in a plane. This plane where the propagation vectors of incident, reflected and transmitted wave lie is known as the plane of incidence. In such a plane, the tangential components θ_i,θ_r and θ_t of the wave vectors with regard to the normal of the plane interface satisfy the following condition,

$$n_1 sin\theta_i = n_1 sin\theta_r = n_2 sin\theta_t \qquad \text{Eqn (i)}$$

These kinematic properties hold true for many types of propagation vectors such as light waves, sound waves, matter waves etc.,. But, the dynamical properties such as the intensity of the reflected and transmitted waves, phase changes and the polarization effect depend on the specific nature of wave propagation and their boundary conditions.

Extending the case above to TE polarization in a thin film with three interfaces at air, thin film and susbstrate, $\overrightarrow{E}(x)$ for the s wave is a continuous function of x. However when decomposed into the right and left travelling components (Ref. Fig.5.1), they are no longer continuous at the interfaces. The amplitude of the field at the left and right side of the interface at x = 0 can be represented as column vectors and linked by

$$\begin{pmatrix} A_1 \\ B_1 \end{pmatrix} = D_1^{-1} D_2 \begin{pmatrix} A_2' \\ B_2' \end{pmatrix} \equiv D_{12} \begin{pmatrix} A_2' \\ B_2' \end{pmatrix} \qquad \text{Eqn (ii)}$$

$$\begin{pmatrix} A_2' \\ B_2' \end{pmatrix} = P_2 \begin{pmatrix} A_2 \\ B_2 \end{pmatrix} = \begin{pmatrix} e^{i\phi_2} & 0 \\ 0 & e^{-i\phi_2} \end{pmatrix} \begin{pmatrix} A_2 \\ B_2 \end{pmatrix} \qquad \text{Eqn (iii)}$$

$$\begin{pmatrix} A_2 \\ B_2 \end{pmatrix} = D_2^{-1} D_3 \begin{pmatrix} A_3' \\ B_3' \end{pmatrix} \equiv D_{23} \begin{pmatrix} A_3' \\ B_3' \end{pmatrix} \qquad \text{Eqn (iii)}$$

where D_1,D_2 and D_3 are the dynamical matrix which relates the refractive index

and the tangential components of the wave vectors in medium 1,2 and 3 and is given by,

$$D_\alpha = \begin{pmatrix} 1 & 1 \\ n_\alpha cos\theta_\alpha & -n_\alpha cos\theta_\alpha \end{pmatrix} \qquad \text{Eqn (iv)}$$

where $\alpha = 1, 2, 3$ and θ_α is the EM wave angle in each of the media which is related to β and $k_{\alpha x}$ by,

$$\beta = n_\alpha \frac{\omega}{c} sin\theta_\alpha,\ k_{\alpha x} = n_\alpha \frac{\omega}{c} cos\theta_\alpha \qquad \text{Eqn (v)}$$

P_2 is the propagation matrix which acounts for the propagation of the EM wave through the thickness of the film and ϕ_2 is given by $k_{2x}d$. The matrices D_{12} and D_{23} may be regarded as the transmission matrices which link the amplitude of the field on the two sides of the interfaces as:

$$D_{12} = \begin{pmatrix} \frac{1}{2}\left(1 + \frac{k_{2x}}{k_{1x}}\right) & \frac{1}{2}\left(1 - \frac{k_{2x}}{k_{1x}}\right) \\ \frac{1}{2}\left(1 - \frac{k_{2x}}{k_{1x}}\right) & \frac{1}{2}\left(1 + \frac{k_{2x}}{k_{1x}}\right) \end{pmatrix} \qquad \text{Eqn (vi)}$$

$$D_{23} = \begin{pmatrix} \frac{1}{2}\left(1 + \frac{k_{3x}}{k_{2x}}\right) & \frac{1}{2}\left(1 - \frac{k_{3x}}{k_{2x}}\right) \\ \frac{1}{2}\left(1 - \frac{k_{3x}}{k_{2x}}\right) & \frac{1}{2}\left(1 + \frac{k_{3x}}{k_{2x}}\right) \end{pmatrix} \qquad \text{Eqn (vii)}$$

Similarly in the case of TM polarized waves,

$$D_{12} = \begin{pmatrix} \frac{1}{2}\left(1 + \frac{n_2^2 k_{1x}}{n_1^2 k_{2x}}\right) & \frac{1}{2}\left(1 - \frac{n_2^2 k_{1x}}{n_1^2 k_{2x}}\right) \\ \frac{1}{2}\left(1 - \frac{n_2^2 k_{1x}}{n_1^2 k_{2x}}\right) & \frac{1}{2}\left(1 + \frac{n_2^2 k_{1x}}{n_1^2 k_{2x}}\right) \end{pmatrix} \qquad \text{Eqn (viii)}$$

$$D_{23} = \begin{pmatrix} \frac{1}{2}\left(1 + \frac{n_3^2 k_{1x}}{n_2^2 k_{2x}}\right) & \frac{1}{2}\left(1 - \frac{n_3^2 k_{1x}}{n_2^2 k_{2x}}\right) \\ \frac{1}{2}\left(1 - \frac{n_3^2 k_{1x}}{n_2^2 k_{2x}}\right) & \frac{1}{2}\left(1 + \frac{n_3^2 k_{1x}}{n_2^2 k_{2x}}\right) \end{pmatrix} \qquad \text{Eqn (ix)}$$

The expressions for D_{12} and D_{23} are similar, except the fact that they are represented by suitable subscripts referring to their corresponding media. D_{12} can be formally written as,

$$D_{12} = \frac{1}{t_{12}} \begin{pmatrix} 1 & r_{12} \\ r_{12} & 1 \end{pmatrix} \qquad \text{Eqn (x)}$$

where t_{12} and r_{12} are the Fresnel transmission and reflection coefficients given by,

$r_{12} = \dfrac{k_{1x} - k_{2x}}{k_{1x} + k_{2x}}$ and $r_{12} = \dfrac{n_1^2 k_{2x} - n_2^2 k_{2x}}{n_1^2 k_{2x} + n_2^2 k_{2x}}$ for s wave and p wave respectively Eqn (xi)

$t_{12}= \dfrac{2k_{1x}}{k_{1x}+k_{2x}}$ and $t_{12} = \dfrac{2n_1^2 k_{2x}}{n_1^2 k_{2x}+n_2^2 k_{2x}}$ for s wave and p wave respectively Eqn (xii)

Knowing all these relations, the amplitude of the field from medium 1 to medium 3 can be simply expressed by,

$$\begin{pmatrix} A_1 \\ B_1 \end{pmatrix} = D_1^{-1} D_2 P_2 D_2^{-1} D_3 \begin{pmatrix} A_3' \\ B_3' \end{pmatrix} \qquad \text{Eqn (xiii)}$$

Thus the column vectors that represent the plane wave in each medium is related by a product of 2x2 matrices in sequence. Each side of the interface is linked by dynamical matric and within the thickness of the thin film by the propagation matrix. Such a recipe can be applied to a multilayer structure and also be extended to a (3 x 3) matrix.

Appendix II

Trials	$\sigma_{em.max}$ (x10^{-17}m^2) (Emitter 1)	Emission center (nm) (Emitter 1)	Emission width (nm) (Emitter 1)	$\sigma_{em.max}$(m^2) (Emitter 2)	Emission center (nm) (Emitter 2)	Emission width (nm) (Emitter 2)
Trial 1	8.78	800	140	8.78	867	80
Trial 2	8.78	800	150	8.78	867	80
Trial 3	8.78	800	150	8.78	867	90
Trial 4	8.78	800	170	8.78	867	90
Trial 5	0.878	816	130	0.878	867	60
Trial 6	0.0878	816	130	0.0878	867	60

Details of trials performed on the PL spectra of SRSO/SiO_2 MLs shown in figure 5.22a.

Appendix III

Trials	Kind of emitters	$\sigma_{em.max}$ (m^2)	Emission center (nm)	Emission width (nm)
Trial 1	Emitter 1	7.78 x 10^{-17}	655	100
	Emitter 2	8.78 x 10^{-17}	751	100
	Emitter 3	7.78 x 10^{-17}	868	100
Trial 2	Emitter 1	7.78 x 10^{-17}	655	200
	Emitter 2	8.78 x 10^{-17}	751	200
	Emitter 3	7.78 x 10^{-17}	868	200
Trial 3	Emitter 1	9.77 x 10^{-17}	655	160
	Emitter 2	6.77 x 10^{-17}	751	150
	Emitter 3	1.77 x 10^{-16}	868	230

Details of trials performed on the PL spectra of SRSO/SRSN MLs shown in figure 5.26

Résumé

L'association du concept de troisième génération de cellules solaires et de la technologie de fabrication des films minces ouvre la voie à l'élaboration de matériaux entrant dans le cadre des énergies renouvelables. Les effets de confinement quantiques observés dans les nanostructures de silicium sont exploités pour une intégration dans des dispositifs du type cellule tandem tout-silicium. Cette thèse vise à comprendre la formation de nanoparticules de silicium dans deux types de matrices diélectriques (SiO_2 et SiN_x) sous forme de mono- et multi-couches. La matrice de nitrure de silicium possède l'avantage de pouvoir intégrer une densité élevée de nanoparticules (10^{20} Si-np/cm^3) qui après recuit rapide (1min-1000°C) conduit à une émission intense dans le domaine visible. Une investigation théorique détaillée des mécanismes d'émission et des facteurs influençant la luminescence est mise en regard des résultats expérimentaux. Les simulations indiquent les caractéristiques d'émission (intensité et énergie) dépendent non seulement de la densité et de la taille des nanoparticules de silicium, mais également de la géométrie (épaisseur des couches et sous-couches, nombre de motifs alternés) et des indices dont le rôle crucial doit être pris en compte pour permettre une intégration dans les dispositifs finalisés.

Mots clé: Nanoparticules, couches minces, composites, photoluminescence, microstructure (physique), simulation (méthodes de), silicium, pulvérisation magnétron réactive.

Abstract

The combination of third generation solar cell concepts in second generation thin film materials has been identified as an efficient way to solve the global energy needs. The quantum confinement effects observed from Si nanostructures are promising towards integration in a third generation solar cell such as an 'All-Si tandem cell'. This thesis focuses on understanding the formation of Si quantum dots (i.e Si-nanoparticles) in two kinds of dielectric matrix: SiO_2 and Silicon nitride, in monolayer and multilayer (ML) configurations. The advantages of SRSO/SRSN ML over SRSO/SiO_2 ML are demonstrated. High density of Si-np (about 10^{20} Si-np/cm^3) and intense emission in visible range are obtained in SRSO/SRSN ML after a short annealing time (1min- 1000°C), which is promising for device applications at a reduced thermal budget. A detailed investigation on emission mechanisms and factors that influence emission is made experimentally and theoretically. Simulations indicate that the density of Si-np and their size are not the only parameters that influence the emission intensity and peak positions. The demonstrated influence of geometrical and optical effects on emission is very important towards proceeding with the next step of device integrations.

Key words: Nanoparticles, thin films, composite materials, photoluminescence, microstructure, simulation methods, silicon, reactive magnetron sputtering.